A study on physical property dependent EMI shielding effectiveness behaviour of some magnetic and conducting nanofillers incorporated PVDF nanocomposite system.

Thesis submitted to

Jadavpur University

By

Tanmoy Chakraborty

In partial fulfilment of the requirements for the degree of

Doctor of Philosophy (Ph.D.) in Science

Department of Physics

Jadavpur University

Jadavpur, Kolkata-700032

West Bengal, India

2024

যাদবপুর বিশ্ববিদ্যালয়
কলকাতা-৭০০ ০৩২, ভারত

*JADAVPUR UNIVERSITY
KOLKATA-700 032,INDIA

FACULTY OF SCIENCE : DEPARTMENT OF PHYSICS

Certificate from the Supervisor

This is to certify that the thesis entitled "***A study on physical property dependent EMI Shielding effectiveness behaviour of some magnetic and conducting nanofillers incorporated PVDF nanocomposite system***" Submitted by Mr. Tanmoy Chakraborty who got his name registered on 09/06/2022 (Index No.: **135/22/Phys./28** & Registration No.: **SOPHY1113522**) for the award of Ph.D. (Science) Degree of Jadavpur University, is absolutely based upon his own work under the supervision of Dr. Soumyaditya Sutradhar and that neither this thesis nor any part of it has been submitted for either any degree/diploma or any other academic award anywhere before.

Soumyaditya Sutradhar

09/07/2024

Dr. Soumyaditya Sutradhar
Assistant Professor
Department of Physics
Jadavpur University

Dr. Soumyaditya Sutradhar
Assistant Professor
Department of Physics
Jadavpur University
Kolkata-700032

যাদবপুর বিশ্ববিদ্যালয়
কলকাতা-৭০০ ০৩২, ভারত

*JADAVPUR UNIVERSITY
KOLKATA-700 032,INDIA

FACULTY OF SCIENCE : DEPARTMENT OF PHYSICS

Certificate of Similarity Check

This is to certify that the plagiarism checking for this thesis entitled "***A study on physical property dependent EMI Shielding effectiveness behaviour of some magnetic and conducting nanofillers incorporated PVDF nanocomposite system***" authored by Mr. Tanmoy Chakrabortyhas been performed using professional plagiarism prevention software iThenticate. According to the report generated after plagiarism checking there is 08 % similarity in this thesis, which is in the category "Level 0" (minor similarities) as per the "Promotion of Academic Integrity and Prevention of Plagiarism in Higher Education Institutions Regulations, 2018" of the University Grand Commission (UGC) of India. The common knowledge or coincidental terms up to 10 (ten) consecutive words [as prescribed in UGC Regulation up to 14 (fourteen) terms can be excluded] and own works of the candidate published in various peer-reviewed journals (those are attached in the thesis) are excluded from the similarity checking. It is certified that the present thesis submitted by Mr. Tanmoy Chakrabortyis plagiarism-free and has followed standard norms of academic integrity and scientific ethics.

Soumyaditya Sutradhar

09/07/2024

Dr. Soumyaditya Sutradhar
Assistant Professor
Department of Physics
Jadavpur University

Dr. Soumyaditya Sutradhar
Assistant Professor
Department of Physics
Jadavpur University
Kolkata-700032

Dedicated

To my

"Family" & "Supervisor"

ABSTRACT

A study on physical property dependent EMI shielding effectiveness behaviour of some magnetic and conducting nanofillers incorporated PVDF nanocomposite system.

Tanmoy Chakraborty

Index No.: 135/22/Phys./28 **Registration No.: SOPHY1113522**

Abstract: In the variety of applications where waves interact with matter, it is required to enhance the ability of the materials to shield the electromagnetic interference (EMI) in terms of reflection at the surface and absorption into the bulk structure of the materials. When EM radiation is absorbed, it is transformed into heat energy and released into the atmosphere, but when it is reflected and transmitted it remains unaltered. The continuous exposure of EM radiation on living object causes many long-term health hazards such as Alzheimer's disease, infertility and AUTISM etc. The main objective of this work is to increase the absorption of EM radiation in the microwave (MW) frequency region. It is possible to enhance absorption of MW radiation in numerous ways over reflection and transmission. In this report the incorporation of magnetic fillers into the polymer system, magnetic-conducting binary nanofillers incorporated polymer system and their further modifications in form of multi-layer as well as non-conducting polymer jacket coated multi-layer polymer nanocomposite structure has been developed to enhance the absorption of MW radiation. The presence of crystallographic phase of the nanocomposite films has been confirmed using XRD analysis. The surface morphology of the nanofillers and nanocomposite films estimated using FESEM micrographs. The role of magnetic response to modulate the absorption property has been investigated using M-H loop study of the magnetic nanofillers and nanocomposite films. The EMI shielding study has been carried out and the estimations of the attenuation percentage for absorption of the MW radiation by the nanocomposite

system has been done. The attenuation constant, which symbolizes the ability of integral attenuation of the incident EM wave inside the material has been calculated from the real and imaginary component of relative permeability and permittivity of the nanocomposite films in the MW frequency region. Therefore, the formation of these magnetic nanofillers incorporated and magnetic-conducting binary nanofillers incorporated nanocomposite films as well as their tailor-made multi-layer structure make them more efficient to come out as a unique concept of improving the absorption property (SE_A) and the total shielding effectiveness (SE_T) of these laminated nanocomposite films.

ACKNOWLEDGEMENT

After completing my Master's degree, I have started my PhD journey at Jadavpur University from 2020. From the first day I entered the campus, I was immediately drawn to the university's unique atmosphere, which combines culture, art, and science in a way that is rare in academia. This combination of these elements alongside the university's strong history of fostering world-renowned scholars, appealed me. I feel privileged to have had the opportunity to undertake my PhD at this prestigious institute. I extend my sincere thanks to Jadavpur University for providing me with an enriching academic environment, exceptional facilities, and opportunities for growth. The support and resources offered by the university have been instrumental in my academic journey.

My heartfelt thanks go to ***Dr. Soumyaditya Sutradhar***, Assistant Professor, department of Physics, Jadavpur University, my guide/supervisor/mentor, for his invaluable guidance, expertise, and unwavering support throughout this project. His mentorship and constructive feedback have been crucial in shaping the direction and content of my work. Throughout these years, he treated me as more than just a doctoral candidate. He not only shared his vast knowledge and experience but also provided invaluable advice during hardships and tough days. He has also introduced me to the biophysics lab of **Professor (Dr.) Sukhen Das**, department of Physics, Jadavpur University. I am always grateful to Sukhen Sir for sharing his knowledge, insights and for providing me all the essentials facilities in his labs. During that time, I had the honour of meeting Professor (Dr.) Papiya Nandy, Dr. Ruma Basu, and Professor (Dr.) Tarakdas Basu. Their guidance, wisdom, and extensive cooperation were incredibly valuable, providing essential support at every stage of my academic path. Their contributions have made a lasting impression, and I am deeply appreciative of their influence.

The Physics Department of Jadavpur University played a crucial role, providing essential facilities and sharing their extensive knowledge throughout the process. They consistently offered assistance and guidance whenever needed. Additionally, I have received invaluable support from Vice-Chancellor sir of Jadavpur University, Dean of the Faculty Council of Science, and Dr. Rajat Ray, Dean of Students. They assisted me with various official matters and encouraged my participation in numerous national and international competitions. As a result, our team secured the second position in Anveshan 2022 at the zonal level and third position in the same competition at national level.

A special thanks to my dedicated team members and colleagues Suman, Aliva, Subhojit, Shivam and Tanmay for their collaboration, support, and camaraderie. Their contributions have enhanced all our collective efforts, making our teamwork both effective and enjoyable. I want to express my heartfelt appreciation to each team member for their tireless efforts, creative ideas, and willingness to go above and beyond. Together, we have navigated challenges, celebrated achievements, and grown professionally and personally. The synergy within our team has been a cornerstone of our achievements, and I am truly thankful for the opportunity to work alongside such talented individuals.

I would like to express my gratitude to all my lab mates Dhananjoy, Jhilik, Saheli Di, Debmalya Da, Namrata Di, Anwesha Dey, Manisha Di, Somen Da, Souvik Da, Sanghita Di, Minarul Da, Indrajit, Piyali, Madhuchanda Di, Solanky and my juniors Neelanjana, Monisha Sarkar, Anwesha Mukherjee, Anuja, Sumana, Shriparna, Koustav and Shaaista, who have been a strong support for me during this time, standing by me and showing their love. I am deeply grateful to Mainak Da, Dhananjay Da, Mousumi, for their unconditional support whenever I needed them.

To my seniors, Tanumay Da, Shubham Da, Shilpa Di, Souravi Di, Debbithi Di, Biplab Da, Dheeraj Da were invaluable companions on this journey. I appreciate their

guidance, advice, and encouragement, which have been pivotal in navigating academic challenges. Moreover, they provided training in operating various advanced machines, which not only deepened my interest in research but also strengthened our bond.

I would like to acknowledge the support of our chemical suppliers Pathak Lab Solutions and other department members who provided technical assistance, resources, and expertise crucial for the successful execution of experiments and research. I would also like to express my gratitude to Dr. Kaustuv Das, Associate Professor at Jadavpur University, who served on my research advisory committee. His experiences and insights have been inspiring, and he provided crucial facilities for my research. Additionally, I am deeply thankful to Dr. Goutam Pramanik from UGC-DAE-CSR Kolkata Centre and Partha Sardar from SAMEER, Kolkata, for their invaluable support and provision of essential facilities. A special thanks to the administrative and technical staff of the department whose behind-the-scenes efforts ensured smooth operations and support services. I am grateful to SVMCM for it's financial support, which enabled me to focus on my studies and research without financial worries.

Furthermore, I want to express my deep gratitude to my family, Baba, Maa, Dada, Boudi, my stress buster niece (Tunai) and my uncle. Despite my busy schedule, they stood by me with understanding and encouragement. I owe a profound debt of gratitude to my parents (father and mother) for their unconditional acceptance, countless sacrifices, and unwavering support. Words cannot fully capture the depth of my appreciation for their role in my journey.

Thank you all!

Tanmoy Chakraborty

Tanmoy Chakraborty

CONTENTS

Chapter: 2 Experimental

ABBREVIATIONS

ATC: Air traffic control

C-band: A range of microwave radio frequencies from 4 to 8 GHz

CNT: Carbon Nanotube

dB: Decibels

DMF: N, N-Dimethylformamide

DNA: Deoxyribonucleic acid

DSC: Differential Scanning Calorimetry

EDX: Energy dissipative spectroscopy

EDS: Energy Dispersive X-rat Spectroscopy

EM: Electromagnetic

EMI: Electromagnetic Interference

EMR: Electromagnetic Radiation

ETFE: Ethylene tetrafluoroethylene

EVA: Ethylene vinyl acetate

FC: Field Cooled

FEP: Fluorinated ethylene propylene

FESEM: Field Emission Scanning Electron Microscopy

FFT: Fast Fourier Transform

FM: Ferrimagnetic

FTIR: Fourier Transform Infrared Spectroscopy

FWHM: Full Width at Half Maximum

GHz: Gigahertz

GPa: Giga Pascals

GSM: Global System for Mobile Communications

GNS: Graphene nanosheets

GO: Graphene Oxide

GPRS: General Packet Radio Service

H_c: Coercive field

HRTEM: High Resolution Transmission Electron Microscopy

ICD: Implantable Cardioverter Defibrillator

IoT: Internet of Things

IF: Infrared Waves

IR: Infrared

J-E: Current Density-Electric Field

JCPDS: Joint Committee on Powder Diffraction Standards

K_u-band: A range of microwave radio frequencies from 12 to 18 GHz

LTE: Long-Term Evolution

MA: Microwave Absorption

MD: Magneto dielectric

M_m: Maximum magnetisation

M_r: Remanence magnetisation

M-H: Magnetization vs. Magnetic Field

MW: Microwave

MWCNT: Multi-Walled Carbon Nanotube

MWR: Microwave Radiation

NRW: Nicolson-Ross-Weir

NZCF: Ni-Zn-Cu-Ferrite

PA: Polyacetylene

PANI: Polyaniline

PCB: Printed Circuit Board

PCTFE: Polychloro trifluoro ethylene

PM: Paramagnetic

PPy: Polypyrole

PVDF: Poly(vinylidene fluoride)

PVDF-HFP: Polyvinylidene fluoride-hexafluoropropylene

PT: Polythiopene

PTFE: Polytetrafluoroethylene

R&D: Research and Development

RL: Reflection Loss

RAMs: Radar Absorbing Materials

RF: Radio Frequency

RFID: Radio Frequency Identification

rGO: Reduced Graphene Oxide

RT: Room Temperature

RW: Radio Waves

S_{11}/S_{22}: Reflection Coefficient

S_{21}/S_{12}: Transmission Coefficient

SAR: Specific Absorption Rate

SE_A: Shielding Effectiveness due to Absorption

SE: Shielding Effectiveness

SE_{MR}: Shielding Effectiveness for Multiple Reflection

SE_R: Shielding Effectiveness due to Reflection

SE_T: Total Shielding Effectiveness

SHF: Super High Frequency

SPM: Superparamagnetic

SQUID: Superconducting Quantum Interference Device

SWNT: Single-walled carbon nanotube

tan δ: Loss Tangent

T_c: Curie Temperature

TGA: Thermogravimetric Analysis

TTTT: All Trans-Planar Zigzag Conformation of PVDF

TGTG: Trans-Gauche Conformation of PVDF

WIMAX: Worldwide Interoperability for Microwave Access

X-band: A range of microwave radio frequencies from 8 to 12 GHz

XPS: X-Ray Photoelectron Spectroscopy

XRD: X-ray Diffraction

ZFC: Zero Field Cooled

ε': Real Part of Dielectric Permittivity

ε'': Imaginary Part of Dielectric Permittivity

Ω: Ohms

σ_{ac}: Alternating Current Conductivity

LIST OF PUBLICATIONS

Thesis publications:

[1] Enhancement of EMI shielding effectiveness of flexible Co_2U-type hexaferrite ($Ba_4Co_2Fe_{36}O_{60}$)-poly(vinylidene fluoride) heterostructure composite materials: An improved radar absorbing material to combat against electromagnetic pollution.

T. Chakraborty, *T. Debnath, S. Bhowmik, A. Bandyopadhyay, A. Karmakar, S. Das, A.S. Mahapatra, and S. Sutradhar*.*

Journal of Applied Physics. 2020, 128, 095301.

[2] Superior EMI Shielding Effectiveness of Light Weight and Stretchable X-type Hexaferrite-Poly(vinylidene fluoride) Laminated Nanocomposite Materials.

T. Chakraborty, *S. Dutta, A. S. Mahapatra, K. Das, S. Das, A. Roy, M. Mukherjee, S. Das, S. Sutradhar*.*

Journal of Magnetism and Magnetic Materials. 2023, 570, 170508.

[3] Electromagnetic Shielding Effectiveness of X-type hexaferrite-C_3N_4 Binary Nanofillers Incorporated Poly(vinylidene fluoride) Multiphase Composites.

T. Chakraborty*, S. Sharma, A. Ghosh, A. S. Mahapatra, S. Chakrabarti, and S. Sutradhar*.*

Journal of. Physical Chemistry C. 2020, 124, 35, 19396–19405.

[4] Fabrication of heterostructure composites of Ni-Zn-Cu-Ferrite-C_3N_4-Poly (vinylidene fluoride) films for the enhancement of electromagnetic interference shielding effectiveness.

T. Chakraborty*, S. Sharma, T. Debnath, A. S. Mahapatra, A. Selvam, S. Chakrabarti, S. Sutradhar*.*

Chemical Engineering Journal. 2021, 420, 2, 127683.

[5] An effective microwave absorber using multi-layer Design of carbon allotrope based Co_2Z hexaferrite-Polymer nanocomposite film for EMI shielding applications.

***T. Chakraborty**, S. Saha, K. Gupta, S. Dutta, A. S. Mahapatra, D. Mondal, A. K. Pradhan, C. Chakraborty, S. Das, S. Sutradhar*.*

Chemical Engineering Journal. 2024, 487, 150323.

[6] A Novel Approach to Obtain Superior Microwave Absorption Using Non-Conducting Polymer Jacket Coated Multi-Layer Hexaferrite-TMDC Nanocomposite Film

***T. Chakraborty**, S. Saha, A. Saha, S. Sharma, G. Pramanik, S. Das, S. Sutradhar*.*

Communicated

Others publications:

[7] Shielding Effectiveness Study of CoZCF-MWCNT Nanocomposite Materials and its possible application as EM pollution reducer.

***T. Chakraborty**, S. Sharma, K. Das, A. S. Mahapatra, A. Saha, S. Das, S. Saha, S. Chakrabarti, S. Das, S. Sutradhar*.*

Physica Scripta. 2023, 98, 065914.

[8] Coupled magnetic and ferroelectric orderings in flexible Mn–Cu–Zn-ferrite-PVDF nanocomposite film for multiferroic applications.

***T. Chakraborty**, A. S. Mahapatra, S. Saha, A. Saha, A. Maity, S. Das, S. Hasan, S. Das, S. Sutradhar*.*

Solid State Sciences. 2024, 149, 107475.

[9] Ni-Zn-Cu-Ferrite-PVDF Multiphase Nanocomposite Material for the Application of Multiferroics and Improved EMI Shielding Effectiveness.

T. Chakraborty, *Shivam Sharma, Suman Saha, Sukhen Das, Abhik Sinha Mohapatra, Soumyaditya Sutradhar*.*

Materials Today: Proceedings. 2023.

[10] A multi-layer design of hexaferrite decorated graphene derivatives incorporated PVDF nanocomposite films; understanding the role of GO/rGO for outstanding electromagnetic wave absorption at microwave frequencies.

S. Saha, ***T. Chakraborty****, A. Saha, S. Das, G. Pramanik, A. K. P, C. Chakraborty, S. Das, S. Sutradhar*.*

Carbon. 2024, 220, 118829.

[11] Magnetoelectric coupling response of novel mullite coated Ni–Zn–Cu-ferrite nanocomposite.

S. Sutradhar, A. S. Mahapatra,* ***T. Chakraborty****, S. Adhikari, K. Das, S. Das, A. Saha, S. Saha, S. Singh, M. Mukhopadhyay, S. Das, P. K. Chakrabarti.*

Materials Chemistry and Physics. 2024, 312, 128607.

[12] The influence of Nd^{3+} *doping on the structural, optical, magnetic, and dielectric characteristics of nanoscale hexagonal wurtzite type ZnO.*

A. Karmakar, ***T. Chakraborty****, S. Chakravarty, M. Nath, S. Chakrabarti, S. Mitra, S. Sarkar, G. Mandal, S. Sutradhar*, A. Bandyopadhyay*.*

Journal of Magnetism and Magnetic Materials. 2024, 591, 171728.

[13] Site selective response of cationic dopants in ZnO nanomaterials: Optical, dielectric and magnetic behaviors.

T. Debnath, ***T. Chakraborty****, A. Bandyopadhyay, K. Das, S. Singh, S. Saha, A. Saha, R. R. Bhattacharjee, S. Das, S. Sutradhar*.*

Materials Chemistry and Physics. 2023, 296, 127284.

[14] Influence of different Cr concentrations on the structural and ferromagnetic properties of ZnO nanomaterials prepared by the hydrothermal synthesis route.

T. Debnath, A. Bandyopadhyay, ***T. Chakraborty****, S. Das, S. Sutradhar**

Materials Research Bulletin. 2019, 118, 110480.

[15] Effect of hydrothermal synthesis on physical property modulation and biological activity of ZnO nanorods.

S. Sutradhar, A. Bandyopadhyay, T. Debnath, T. Chakraborty, S. Majumdar, S. Chakraborty, S. Das.*

Materials Research Express. 2019, 6, 1250f7.

[16] Modulation of structural, morphological and electrical charge transport property of Cr-doped ZnO nanomaterials prepared by chemical process.

T. Debnath, ***T. Chakraborty****, A. Bandyopadhyay, S. Sharma, A. S. Mahapatra, S. Das, S. Sutradhar*.*

Materials Science and Engineering: B. 2022, 280, 115688.

LIST OF SEMINARS ATTENDED

*[1] A one-day seminar in "**Commemoration of Centenary Birth Anniversary Of Prof. Shyamal Sengupta**" at Jadavpur University, Department of Physics.*

***Presentation on:** Enhanced microwave absorption of multilayer structures for EMI shielding applications.*

*[2] Third prize in "**Engineering and Technology" category at ANVESHAN-2022-23**, National research convention, Oral and Poster: "Superior Microwave Absorption of Layered Structured for EMI Shielding Application" **Tanmoy Chakraborty**, Aliva Saha, Manisha Kundu at Ganpat University, Gujrat, 17th and 18th march, 2023.*

*[3] Second prize in "**Engineering and Technology" category at ANVESHAN-2022-23**, National research convention, Oral and Poster: "Superior Microwave Absorption of Layered Structured for EMI Shielding Application" **Tanmoy Chakraborty**, Aliva Saha, Manisha Kundu at Royal Global University, Assam, 1st and 2nd march, 2023.*

*[4] An international conference on "**Advances in Smart Materials, Chemical & Biochemical Engineering" (CHEMSMART-2022**) 16th to 18th December, 2022 at the Department of Chemical Engineering, National Institute of Technology (NIT), Rourkela, Odisha.*

***Presentation on:** Ni-Zn-Cu-Ferrite-PVDF Multiphase Nanocomposite Material for the Application of Multiferroics and Improved EMI Shielding Effectiveness.*

*[5] **29th National Conference on Condensed Matter Physics (CMDAYS 2021)**, 10th to 12th December, 2021, at the Department of Physics, Central University of Jharkhand, Ranchi, Jharkhand.*

***Presentation on:** Possible Health Issues of Electromagnetic Pollution and the Corresponding Remedies.*

[6] ***Third International Conference on Material Science (ICMS2020)****, 4th to 6th March, 2020 at the Department of Physics, Tripura University (A Central University), Tripura.*

Presentation on: *Multiferroic behaviour of multiphase Mn-Zn-Cu-Ferrite-PVDF heterojunction composite film.*

[7] International conference on ***Condensed Matter Physics (IEMPHYS-19)****, 14th to 16th November, 2019 at Institute of Engineering & Management, Kolkata.*

Presentation on: *Influence of the C3N4 conducting network inside the composite network of Ni-Zn-Cu-ferrite-PVDF films for the improvement of EMI shielding effectiveness.*

LIST OF FIGURES

Chapter 1

Chapter 2

Chapter 4

LIST OF TABLES

Chapter: 1

Introduction

Chapter: 1

Introduction:

A new era starts with the study which aims to address the challenges faced due to advancements in technology by exploring diverse strategies to minimize its negative effects while recognizing its importance in modern society. Due to evolution of technology, there has been a substantial increase in various forms of pollution, namely water pollution, air pollution, soil pollution etc. which as a whole aggravating many environmental issues such as global warming, loss of habitat etc. Industries, transportation, and energy production have contributed largely to these environmental problems. Technological advancements have led to deforestation and urbanization which have in turn worsened these issues by disrupting natural ecosystems leading to loss of habitat. Besides these prominent forms of pollution there is also a rise of global issue related to the excessive exposer of non-ionizing electromagnetic (EM) radiation called EM pollution. With the progression of technology there is an exponential increase in the number of electronic devices, wireless communication networks, and power lines, which emit electromagnetic radiations (EMR). Regardless of its potential impact on human health and the environment, the recognitions of harmful effects of EM pollution remain almost unrealised and ignored as compared to other forms of pollution. This discrepancy might be due to the invisibility of EM pollution, contrary to the visible and tangible effects of conventional pollutants like smog or contaminated water. It becomes all the more essential to concentrate on understanding the long-term effects of EM pollution on human health and ecosystems and focus on finding strategies to combat the harmful effects of EMR. In the following section, discussions on the definition of EMR, it's various types, application areas, advantages and disadvantages of EMR in microwave (MW) frequency region along with strategies to combat the harmful effects of EMR in MW frequency region have been made.

1.1 Electromagnetic radiation (EMR):

The direction of energy and wave propagation, together with coordinated oscillations of the electric and magnetic fields perpendicular to one another, make up electromagnetic radiation (EMR). These travel in the form of electromagnetic (EM) waves. X-rays, microwaves, radio waves, and visible light are examples of EMR. It has the ability to pierce solid things and travel across space. In addition, a variety of uses for EMR exist, including imaging, medical diagnostics and treatments, and communication [1]. These waves' distinctive properties are energy, wavelength, and frequency. Global communication has been completely transformed by technologies including 4G/5G cellular networks, GPS systems, Wi-Fi gadgets, Worldwide Interoperability for Microwave Access (WIMAX), long-term evolution (LTE), Radio Frequency Identification (RFID), and Internet of Things (IoTs). EMR are released by equipment that uses radio frequencies to receive and send data, such as satellite transponders, microwave lines, routers, switches, and Wi-Fi modems [2].

1.2 Types of electromagnetic radiation (EMR):

With the advancement of technology to grow more communication system the installation of cell phone towers, internet router etc. increase rapidly. There are already over 600 million cell phone subscribers and about 7.4 lakh cell phone towers in India have been constructed to provide communication services [3]. A wireless communication link between the user and the network is provided by a mobile tower. It has many radio transmitters, which are merged via cables to the base station antenna [4]. As a result, the total power that is radiated will be the same as the total output of all the transmitters. When all the channels are in use during peak hours, there will be the most exposure to radiations, and the sector with the most call traffic will also be the one most exposed to EMR [5]. Each mobile phone has a SAR (Specific Absorption Rate) rating with a limit of 1.6 W/kg so, a person should not use a mobile phone for no longer

than 24 minutes a day, considering the SAR limit [4, 6]. Unfortunately, most mobile phone users are unaware of this information, therefore many individuals use their phones for more than 2-3 hours a day without realizing the potential health risks associated with this practice. The biological system is negatively impacted by the thermal and non-thermal effects of the MW frequencies utilized in mobile communication. The cell structures of living objects are impacted by the microwave radiation (MWR) released by mobile antennas and various other electronics used at base stations and user-owned mobile phones. Over time, prolonged and continuous exposure to this radiation may have detrimental effects on the human biological system [7-9]. When EM wave interacts with matter, the wave energy is transferred into the medium and is absorbed. Human tissue absorbs varying amounts of EMR depending on exposure parameters such as frequency, intensity, polarization, and duration. The MWR propagates with both electric and magnetic waves in the form of photons. MWR comes in a spectrum with varying frequencies and wavelengths, which gives it distinct properties. There are two types of EM radiation which have been classified as:

1.2.1 Ionizing radiation:

EMR having enough energy (10 eV) that interact with matter and create ions is known as ionizing radiation. Such as, cosmic rays, γ-rays, X-rays, and UV radiation etc. Ionizing radiation mainly damages the living tissues and modifies molecular structure which further modifies cell genetic tissue (chronic effects) [10].

1.2.2 Non-ionizing radiation:

Radio frequency (RF) radiation is classified as non-ionizing radiation. Atoms and molecules cannot be ionized by RF electromagnetic waves due to insufficient photon energy. MW, infrared waves (IF), radio waves (RW), etc. are a few examples. The main way that non-ionizing radiation affects health is via heating bodily tissue [4]. In this study the focus has been given to

minimize the hazardous effects of MWR on living beings. There are various sources of MWR which uses various bands of MW frequency such as [11]:

Table 1.1: MW frequency band and their applications

Sl. No.	Microwave band	Frequency range	Applications
1.	UHF Band	300-3000 MHz	Television broadcasts, Microwave oven, Microwave devices, Communications, Radio astronomy, Mobile phones, Wireless LAN, Bluetooth
2.	L-Band	1-2 GHz	Military telemetry, GPS, Air traffic control (ATC) radar
3.	S-Band	2-4 GHz	Weather radar, Surface ship radar, Microwave ovens, Microwave devices, Communications
4.	**C-Band**	**4-8 GHz**	**Long-distance radio telecommunications.**
5.	**X-Band**	**8-12 GHz**	**Satellite communications, Radar, Terrestrial broadband, Space communications**
6.	**K_u-Band**	**12-18 GHz**	**Radar, Satellite communications, Astronomical observations, Automotive radar**
7.	K_α-Band	26.5-40 GHz	Satellite communications
8.	Q-Band	36-46 GHz	Satellite communications, terrestrial microwave communications, radio astronomy studies and automotive radars.
2.	U-band	40-60 GHz	Wireless high capacity, Line-of-Sight communications.

3.	V-band	40-75 GHz	Wireless backhaul and point to point/point to multi-point radio links.
4.	W-Band	75-110 GHz	Automotive radars, satellite communication, astronomy, defence, and security applications.

1.3 Telecommunication system and it's developments in modern technology:

A communication system's primary function is to send signals or information. As baseband signals, which identify the frequency band and represent the original signal as transmitted from the information source, are often referred to as message signals. Furthermore, a signal is typically not a single frequency sinusoid; rather, it consists of a range of frequencies known as the signal bandwidth [12]. There are two categories of communication systems:

1.3.1 Analog system:

Analog technologies use electronic signals with different frequencies and amplitudes to transfer data between devices or humans. The most prevalent applications of analog technology are radio transmission and the telephone [13].

1.3.2 Digital system:

There are two states in which information is generated and processed in digital technology: high and low. Data is stored and sent digitally as a series of 0 and 1 [13]. On the other hand, two different kinds of channels exist for communication: Wired and wireless; specially, the working of wireless communication is based on Ground wave communication, Skywave communication, Space wave communication, Satellite communication [14]. The evolution of communication technologies over the past 20 years has fundamentally changed how we live our daily lives.

To improve the internet communication system the 1G, 2G, 3G, 4G and 5G networking system has been introduced since early 1980s. Approximately every ten years from the introduction of 1G in the early 1980s, a new wireless mobile telecommunications technology has been released. They are all related to the mobile carrier's and the internet device's own technology. They are better than the previous generation in terms of features and speed variations. 1G technology only allows voice calls with its analog technology, and the phones that used it had low security, poor speech quality, short battery lives, and frequent call drops. 1G technology has a maximum speed of 2.4 Kbps [15]. The first significant advancement in cell phone technology came with the transition from 1G to 2G. This transition from analog to digital communications for cell phones happened in Finland in 1991 on GSM networks. 50 Kbps is the fastest 2G speed when using General Packet Radio Service (GPRS). The 2G telephone technology brought data services like MMS, SMS, and picture communications, as well as call and text encryption [16]. With the advent of 3G networks in 1998, which allowed for greater data transmission speeds, cell phones were used for increasingly data-intensive purposes, like mobile internet access and video calling. When 3G cellular technology was initially introduced, the phrase "mobile broadband" was used. For stationary devices, maximum speed of 3G was about 2 Mbps [16]. After that, 4G stands for fourth generation networking, which debuted in 2008. As compared to 3G, it enables high-speed capabilities including video conferencing, gaming services, HD mobile TV, and mobile web access. The 4G network can communicate at a maximum speed of 150 Mbps [16]. In order to improve such a broad variety of technologies, 5G must undoubtedly focus on a few factors that cause the network's capabilities and requirements to differ from those of previous generations. Early in 2020, 5G technology was put into place. 5G networks use radio millimeter bands in the 30 GHz to 300

GHz range. Results from millimeter Wave testing in the 5G range are obtained at 500 meters away from the tower. The implementation of 5G with millimeter wave-based carriers can increase the total coverage area by using tiny cells. Up to 20 gigabits per second is the theoretical speed of 5G connectivity is expected [17, 18].

1.4 Pros and cons of MWR (A comprehensive analysis):

1.4.1 Pros of using MW radiation:

Long-distance large data transmission via MW is effective and doesn't require physical connections. Because MW can pass through smoke, clouds, and light vegetation, they may be used for communication under a variety of circumstances. MW are a kind of radiation that does not ionize atoms or molecules in biological tissues, in contrast to gamma and X-rays. There are many uses for MW in cooking by the conversion of EM energy to thermal energy by rotation of water molecules with MW within the food. Moreover, due to high frequency of MW more data can be sent at same time, so the antenna size gets reduced, as the frequencies are higher.

1.4.2 Cons of MW radiation:

The living beings are constantly exposed to low-intensity radiation from the cell phone towers and high-tension power line or sources. Since MWR cannot be smelled, touched, or seen, it takes extensive exposure to detect their potential danger before biological illnesses appear. The strength and frequency of the radiation affect biological systems differently. A human body is 70% liquid, thus when it is subjected to EMR, it causes thermal heating effects due to radiation. Since the wavelength of the frequencies that cell towers transmit matches with that of a human, there will be a resonance in the human body, leading to localized heating effect. Over time, chronic low-intensity MWR exposure can lead to major health issues as well as the impact of MWR can also damage the plants growth. There are many harmful hazards that arise for living objects related to the MWR and some of the problems listed below.

1.4.2.1 Impact on Plants:

The immobility and continual exposure to RF/EM wave produced by cell towers, plants provide excellent models for studying the harmful effects of this radiation. Numerous laboratory investigations demonstrate that plants exposed to radiation undergo chemical and biological changes in a short amount of time. In a study on the impact of EMR on plant development, Jamie A. Dyvig found that exposure to EM radiation reduced plant growth. Continuous exposure to 2.4 GHz radiation has caused radish plants to grow 16.5% shorter, while wheatgrass has shown a mean height decrease of 5.1% [19]. Extended exposure to RF/MW can cause a plant's leaf to become yellow instead of green, which could limit the plant's ability to develop [18]. Since 5G mobile cells emit radiation using millimeter waves, which have a higher frequency band, a strong RF/MW radiation will affect the growth of plant and shorten plant lifetime.

1.4.2.2 Effect on bird species:

Long-term impacts of EMR are observed in birds, including sparrows, owls, and crows; however, the families of pigeons and crows are less damaged than those of sparrows. This caused a large number of bird families to move across areas free of radiation and unaffected by cell tower coverage. There are more birds in certain parts of the place where 3G mobile technology is still in use than in areas with access to 4G or 5G cell towers. According to some experts, RF/MW waves also disrupt the earth's magnetic field, which birds need to guide them, and exposure to EMR causes them to get disoriented and fly in various directions. In order to navigate, birds use their thin skulls and wings, which function as dielectric receivers. Birds are unable to procreate due to the harmful effects of radiation; the sparrow species is a prime example in India [20, 21].

1.4.2.3 Peril for Expectant Mothers:

Because these MWR constantly react with the growing embryo and growing cells, both the pregnant lady and the fetus are at risk. The placental barrier, which shields the fetus from some harmful substances by blocking their passage between the mother's and fetal blood, can be harmed by MWR.

1.4.2.4 Irreversible Infertility:

Research has shown that heavy mobile phone users have 30% less sperm and also have damaged sperm. Cell phone radiation can also induce DNA breakage in sperm cells, which can lead to mutations and can further cause cancer. In addition, damage to sperm DNA can carry genetic alterations to offspring. One of the main causes of tumors and cancer is damage to DNA. According to Phillips et al., exposure to MWR can harm DNA [22]. According to research by Hardell et al. and Muscat et al, exposures to MWR can result in chromosomal breakage and DNA damage [23, 24].

1.4.2.5 Effect on Pace Makers:

Implantable cardioverter defibrillators (ICDs), pacemakers, and impulse generators can all be negatively impacted by MW/RF exposure and can develop arrhythmias. Cell phone radiation or MWR sources can cause implanted pacemakers to malfunction and cease in producing pulses on a regular basis. It can also cause an external regulating pulse that might kill the patient [25].

1.4.2.6 Effect on eye:

Mobile phone usage on a regular basis can also harm the visual system by the increase the risk of uveal melanoma, or eye tumors. A rise in temperature around the eye's lens can cause lens opacities and a chance of getting cataracts, a condition marked by clouding of the natural lens of the eye and lens opacities. Long-term exposure to MWR can cause both the microscopic and macroscopic damage, some of which seems to accumulate over time and not heal [26].

Not only that, it has been demonstrated that EM fields alter brain physiology. Using a phone right before bed lowers and delays sleep, and it can also result in headaches, melancholy, and disorientation. The exposure of radiation directly correlates with the percentage increase in sleep disruption. According to reports, even at a radiation level of 10 $\mu W/m^2$, there is a 35% interruption in sleep [27].

So, to control the increasing effect of EM pollution by the quick increase of electronic devices and the steep rise in the need for wireless communication, the focus has been given towards to develop such kind of materials that helps to absorb the EM radiation. As a result, materials to protect against electromagnetic interference (EMI) have been created in an attempt to address the alarming issue of EM pollution. However, shielding materials now need to meet greater standards for EMI shielding performance, weight, flexibility, and compatibility with 5G communication technologies and structure of current electronic goods. The issue has recently attracted even more attention and grown more significant; thus, it is now more important than ever to look into it in the pertinent study. Therefore, the requirement of the materials for the application of EMI shielding study first need to understand about the mechanism of EMI shielding property:

1.5 Theory of electromagnetic interference (EMI) shielding property:

As per the MW absorption theory, when the EM waves strike the surface of the materials the incident energy undergoes absorption (SE_A), reflection (SE_R), transmission and multiple reflection (SE_{MR}). The transmitted wave passes through the outer surface of the material by undergoing many internal reflections [28, 29]. There are several reflections and surface reflectance that make up the EM wave's reflection. The dispersive impact of inhomogeneity within materials is the requirement for numerous reflections. Heat generated by incoming

MWR can be converted into thermal energy and then absorbed by the material through the interaction of the EM waves with its molecular and electronic structure [30].

$$SE_T\,(dB) = -10\log_{10}\left(\frac{P_t}{P_0}\right) = SE_A + SE_R + SE_{MR} \quad (1.1)$$

Where, P_t represents the transmitted power and P_0 represents the incident power of MWR. To improve the MW absorption of the materials there are two main EM characteristics related to the MW absorbers. The first characteristic is magnetic loss, while the second is dielectric loss. The feature of the electrical interaction between the nanomaterial and the electric field of the incident EM radiation that causes reflection loss is represented by the dielectric loss.

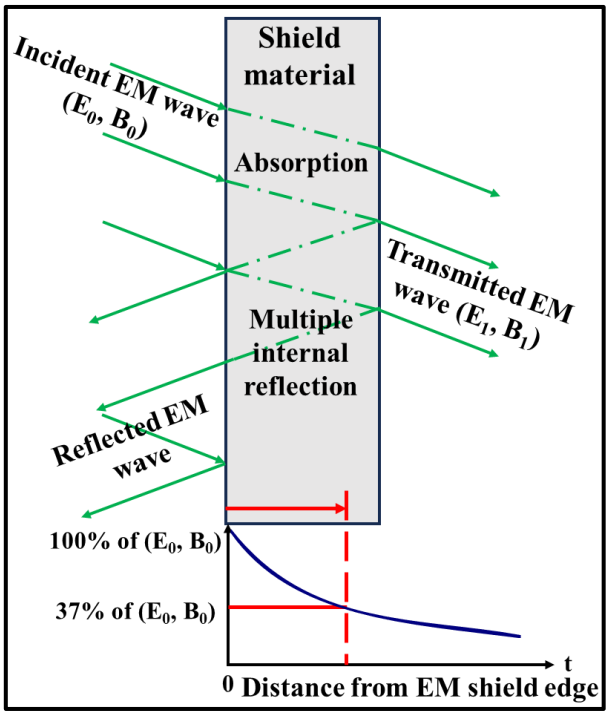

Figure 1.1: EMI shielding mechanism

Conversely, the magnetic loss is a measure of the magnetic interaction between the EM wave and the nanomaterial. The categorization of absorbers can be accomplished by applying standard measuring techniques, such as indirect assessment of their EM characteristics.

1.5.1 Shielding effectiveness due to absorption (SE_A):

It is known from the wave theory the amplitude of EM wave diminishes exponentially inside the material as it moves through it. Therefore, ohmic losses and material heating brought on by currents produced in the medium result in absorption loss. The SE_A value of the material can be written as [31, 32]

$$SE_A(dB) = 20\log e^{\frac{d}{\sigma}} = 8.7(f\pi\sigma\mu)^{1/2} \propto d\sigma\mu \propto \alpha d \quad (1.2)$$

Where, d represent thickness of the material, σ is conductivity, f is frequency, μ is permeability and α signifies the attenuation constant of the material. So, it is clear that the value of SE_A depends on conductivity (σ), permeability (μ) and thickness (d) of the material. The degree to which an EM wave's strength is diminished when it travels through a substance is indicated by the attenuation constant. This attenuation constant can be written as [33]

$$\alpha = \frac{\sqrt{2}\pi f}{c}\sqrt{(\mu''\varepsilon'' - \mu'\varepsilon') + \sqrt{(\mu''\varepsilon'' - \mu'\varepsilon')^2 + (\mu'\varepsilon'' + \mu''\varepsilon')^2}} \quad (1.3)$$

where, f is the frequency of the incident wave and c is the speed of light.

1.5.2 Shielding effectiveness due to reflection (SE_R):

The relative impedance mismatching between the EM waves and the surface of the EMI shielding material is the cause of reflection (SE_R) of MW. The SE_R value of the material can be expressed as [31]

$$SE_R(dB) = 20\log\frac{Z_0}{4Z_{in}} = 39.5 + 10\log\frac{\sigma}{2f\pi\mu} \propto \frac{\sigma}{\mu} \quad (1.4)$$

As may be observed, SE_R is determined by the ratio of conductivity (σ) to permeability (μ) of the shielding material. Therefore, SE_R falls with frequency (f) with constant conductivity (σ) to permeability (μ). In order to reflect EMR, materials need to have mobile charge carriers, such as electrons or holes.

1.5.3 Shielding effectiveness due to multiple reflection (SE_{MR}):

Because of multiple reflection, radiation is trapped between two barriers for thinner materials. Specifically, the EM waves reflect from the second boundary, return to the first boundary, and then re-reflect from the first to the second boundary, and so on. The SE_{MR} of the material can be calculated by [31]

$$SE_{MR} = 20log\ (1 - e^{\frac{-2d}{\delta}}) \quad (1.5)$$

Where, δ represent the skin depth, SE_{MR} is directly connected to absorption and is dependent on thickness (d). More active sites for EM wave scattering and multiple reflection are provided by the huge surface area and considerable empty space outside of the solid structure. However, the shielding effectiveness by multiple reflections (SE_{MR}) can be neglected of the materials when their thicknesses are more than the skin depth of the incident MW radiation as well as when the SE_A value of the material is above 10 dB.

1.5.4 Skin depth effect:

The near-surface area of an electrical conductor is penetrated by high frequency EMR this phenomenon is known as the skin depth effect (δ). The attenuation of EM waves in an electric field mostly takes place on the surface of the shielding materials. Consequently, the skin depth and the electrical conductivity or permeability of the materials have a negative relationship with the EM wave frequency. The effect of numerous reflections can be disregarded if the skin depth is smaller than the thickness of the material. The skin depth effect (δ) expressed as [31, 32]

$$\delta = \sqrt{(\pi f \mu \sigma)^{-1}} \tag{1.6}$$

Where, f is the frequency, μ represent the magnetic permeability, and σ represent the electrical conductivity.

1.6 Factors modulating the EMI shielding performance:

In different literature it has been found that the EMI shielding performance of different materials depends on various factors such as, size, permittivity, permeability, thickness and the mass ratio of the materials. The suitable modulation of one or more such physical property can modulate the EM shielding performance of the materials related to absorption, reflection and multiple reflection. The details discussion related to the modulation of the above mentioned physical quantity are listed below.

1.6.1 Size and morphological property:

To modulate the permeability of the material, dimensions of magnetic particle play a significant role. It is noticed that eddy current losses diminish when generated eddy voltage ($E_{eddy} \propto$ area) declines below a crucial small value of particle size. At the tiny scale of the nanostructures, anisotropy energy is thought to predominate because some exchange bonds are broken. Spin relaxation time or frequency are altered by the changes in anisotropy energy. Unlike inherent resonance, which predicts a constant permeability until relaxation, permeability in nanomaterials is determined by relaxation processes, with the exception of the bulk magnet scenario. Relaxation happens at higher frequencies in the superparamagnetic state because spin fluctuation stays extremely rapid because of its small size [33-38]. Furthermore, several interfaces were produced by some complex structures with high porosity and huge surface area, which accumulate bound charges at the interfaces, which leads to Maxwell-Wagner interfacial effect.

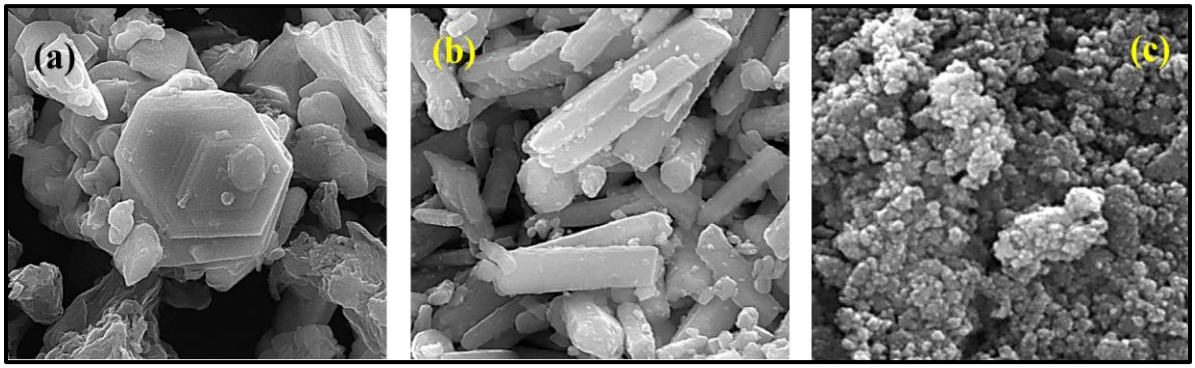

Figure 1.2: (a) Hexagonal shape, (b) Rod like shape and (c) Spherical shape

1.6.2 Permeability and permittivity:

An EM wave is a combination of oscillatory electric and magnetic field. Materials which interact with one or both of these fields can be utilized for fabrication of EMI shielding material. For effective MW shielding the most fundamental parameters are the complex permeability

($\mu_r = \mu' - j\mu''$) and permittivity ($\varepsilon_r = \varepsilon' - j\varepsilon''$). Here, μ' and μ''corresponds to the storing capacity and loss of magnetic energy respectively whereas, ε' and ε'' corresponds to the storing capacity and loss of electric energy respectively. The EM parameters like complex permittivity ($\varepsilon_r = \varepsilon' + j\varepsilon''$) and complex permeability ($\mu_r = \mu' + j\mu''$) of the material are determined from the scattering matrix calculated between the sample planes and are often tested using PNA series Network Analyzer. The Nicolson-Ross-Weir (NRW) approach is often utilized for conducting this calculation. This approach is noniterative and can be used with coaxial line and rectangular waveguides. The real and imaginary components of permeability, $\mu'$and μ'' strongly depends on the magnetization value of the magnetic material according to the following relation [39],

$$\mu' = 1 + \left(\frac{M}{H}\right)\cos\sigma \tag{1.7}$$

$$\mu'' = \left(\frac{M}{H}\right)\sin\sigma \tag{1.8}$$

Here, M is the magnetization, H is the external magnetic field and σ corresponds to the phase lag of magnetization with respect to the external magnetic field.

1.6.3 Thickness of the material:

When the thickness (t) of the absorber material is about a fourth of the propagating wavelength multiplied by an odd number, the minimal reflection of the MWR is detected.

$$t = n\left(\frac{\lambda}{4}\right) \tag{1.9}$$

Where, n = (1, 3, 5, …) and λ be the propagating wavelength. The incident and reflected waves at the absorber material's surface cancel out when the matching condition is met. Reflection of peaks therefore moved toward lower frequencies as sample thickness increased. The coating on the Fe component at the surface of the material alters the MW absorption characteristics in

addition to sample thickness. The rise in thickness due to coating can absorb the EM wave due to the matching of dimensions [31, 40].

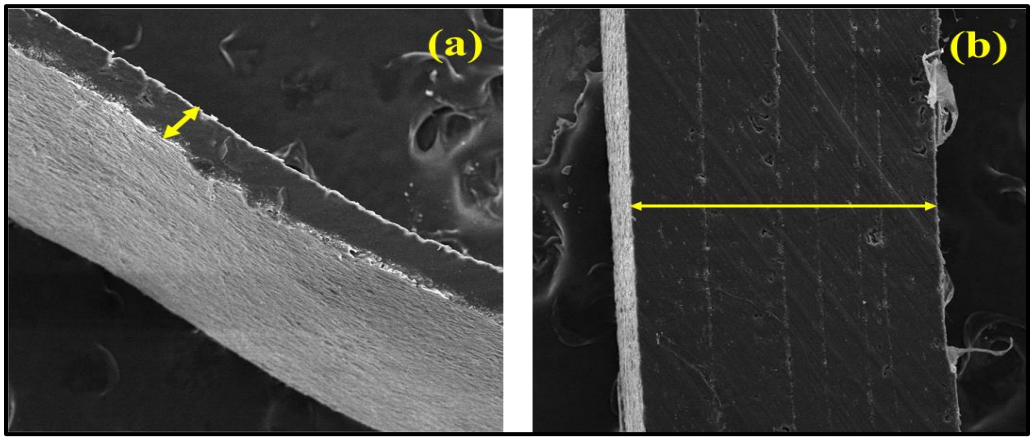

Figure 1.3: Thickness of the materials

1.6.4 Mass ratio of the material:

The electrical characteristics of any material are typically determined by the conductivity's percolation threshold value [41].

$$\sigma = \sigma_0 (V - V_c)^c \tag{1.10}$$

Here, σ represent the electrical conductivity, σ_0 is natural conductivity, V shows the volume fraction of materials, V_c denoted the volume fraction at the percolation threshold and c is the critical exponent. Conductive networks begin to develop inside matrices at the percolation threshold. The filler's conductivity, aspect ratio, and morphology are responsible to modulate the percolation threshold. Furthermore, it is contingent upon the dispersion, concentration, and compatibility of the filler with the host matrix. The characteristics of the composites begin to decline over the percolation threshold. For instance, a large volume proportion of filler in the host matrix (mainly metals) reduces the robustness of the composites.

1.7 Useful materials for EMI shielding:

There are two main EM characteristics of the MW absorbers. The first characteristic is magnetic

loss, while the second is dielectric loss. The feature of the electrical interaction between the nanomaterial and the electric field of the incident EM radiation that causes reflection loss is represented by the dielectric loss. Conversely, the magnetic loss is a measure of the magnetic interaction between the EM wave and the nanomaterial. The categorization of absorbers can be accomplished by applying standard measuring techniques, such as indirect assessment of their EM characteristics or direct measurement of reflection in free space. The useful magnetic materials for the study of EMI shielding property are:

1.7.1 Spinel ferrites:

When it comes to its crystal pattern, spinel ferrites are made up of cubic close-packed (FCC) oxides (O^{2-}), where M´´ cations occupy half of the octahedral holes and M´ cations one-eighth of the tetrahedral holes. Though they are often red, yellow, and brown, spinel ferrites can also be colorless. Octahedral and tetrahedral groups are the possible locations for metal ions. In contrast to Fe^{2+}, Ni^{2+}, and Mn^{2+} ions, which tend to occupy octahedral positions, Fe^{3+} and Zn^{2+} ions generally prefer tetrahedral sites. With part of the M´´ atom occupying the octahedral position and the M´ atom filling the tetrahedral site, inverse spinel structures are seen in MnZn and NiZn ferrites. These cations in the spinel structure give rise to tetrahedral and octahedral sublattices arranged in a close-packed manner through four- or six-fold coordination in the spinel system [31].

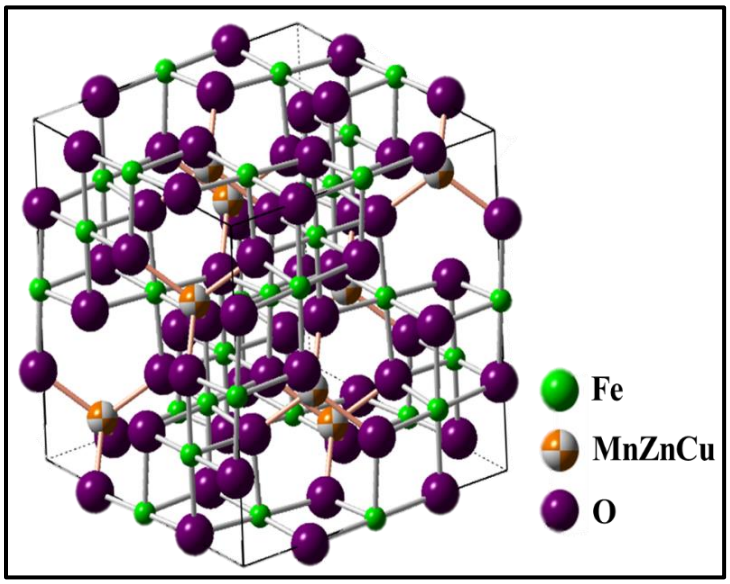

Figure 1.4: Structure of spinel ferrite ($Mn_{0.5}Cu_{0.2}Zn_{0.3}Fe_2O_4$)

1.7.2 Garnet ferrites

Garnet ferrites have the crystal structure of the silicate mineral garnet and are represented by the chemical formula $M_3(Fe_5O_{12})$, where M denotes either yttrium or a rare-earth ion. There is also dodecahedral sites in the structure of garnet, in addition to the tetrahedral and octahedral sites as found in spinel. The net ferrimagnetism arises from the combined outcome of antiparallel spin alignment among the three distinct sorts of sites. Garnets are hard magnets [42]. The garnet crystal structure is composed of a unit cell that is in a cubic form and consists of 160 atoms. The distribution of iron oxide ions is in a ratio of 3:2 between tetrahedral and octahedral sites. Yttrium Iron Garnet (YIG) is a widely recognized and frequently used type of iron garnet material that has distinct functional features that make it suited for applications involving magneto-optics and RF in the MW region. The chemical formula of the compound is $Y_3[Fe_2](Fe_3)O_{12}$. In this compound, the Y^{3+} ions are located in the dodecahedral sublattice sites, two of the Fe^{3+} ions are found in the octahedral sites, and the remaining three Fe^{3+} ions are situated in the tetrahedral sublattice sites. Several studies have shown that new types of garnet materials can be synthesized by replacing yttrium with transition-metal or rare-earth ions, such as Bi^{3+}, Ce^{3+}, Er^{3+}, Tb^{3+}, and others, in the dodecahedral sites. Additionally, the Fe^{3+} ions can be substituted with other elements (such as Ga^{3+}, Al^{3+}, or other metals) in the tetrahedral sublattice sites [43-46].

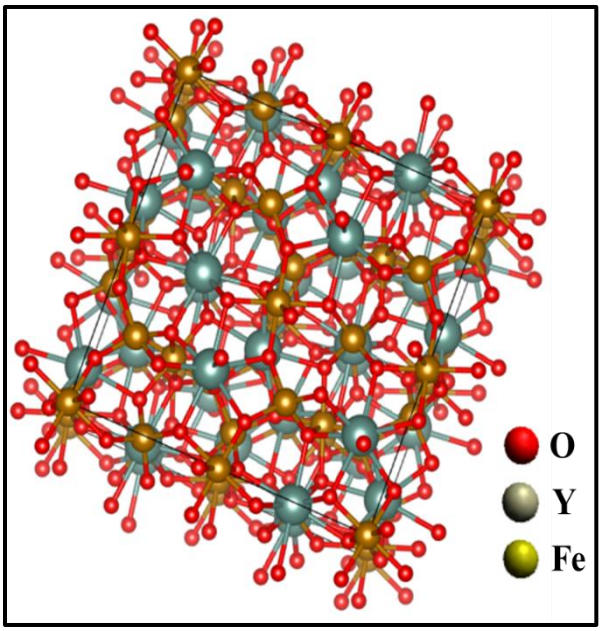

Figure 1.5: Structure of garnet ferrite ($M_3Fe_5O_{12}$)

1.7.3 Ortho-ferrites:

Ortho-Ferrites are chemical substances with a general formula of $RFeO_3$. R represents the group of rare earth elements. Their crystal structure is orthorhombic and they exhibit moderate ferromagnetism. Instead of using the letter R in the chemical formula of Ortho-ferrites, the letter M can also be used, which represents trivalent metal ions. The alignments inside the lattices of ortho-ferrites are anti-ferromagnetically linked. The material's properties are dependent on temperature, and the net magnetization of this material undergoes a 90º rotation. Ortho ferrite exhibits antiferromagnetic behaviour at temperatures below the Neel temperature. There are following few characteristics of $[(La)_{(1-X)}][(Ce)_X][(Fe)_{(1-X)}][(Cr)_X]O_3$ refers to the saturation magnetization M_s, remanence magnetization M_R, and the critical field H_C. Their susceptibility is contingent upon the Neel temperature. There is another type of ferrite called gadolinium ortho-ferrite, which has a single crystal structure and a magnetization temperature range of 78-295 K. Another type is Yttrium ortho-ferrite, which operates at an antiferromagnetic temperature of roughly 602 K. Ortho-ferrites have a face-centered cubic structure at a temperature of 310 K and a body-centered cubic structure at a temperature of 865 K [47,48].

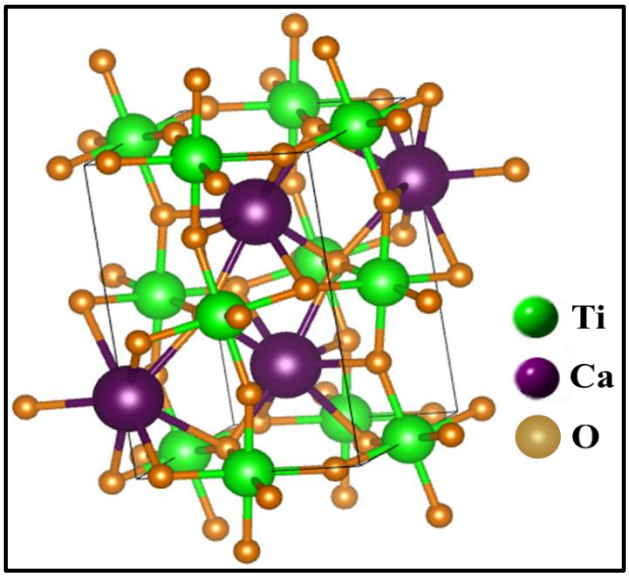

Figure 1.6: Structure of ortho-ferrite ($CaTiO_3$)

1.7.4 Hexaferrite materials:

The crystalline structures of the hexagonal ferrites are inherently related to their magnetic characteristics, as they are all ferrimagnetic materials. They are classified into two main groups: those with an easy axis of magnetization, called uniaxial hexaferrites, and those with an easy plane (or cone) of magnetization, called ferroxplana or hexaplana ferrites. They are all magneto crystalline anisotropic, meaning that induced magnetization has a preferred orientation within the crystal structure [49].

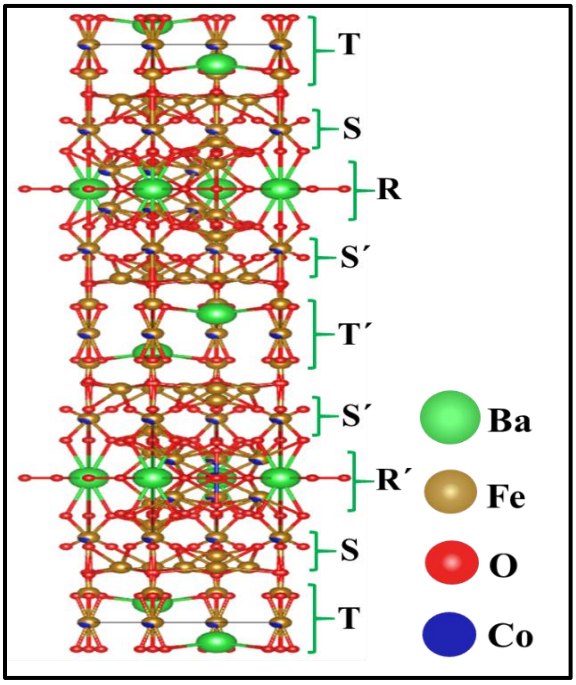

Figure 1.7: Structure of hexaferrite ($Ba_3Co_2Fe_{24}O_{41}$)

Generally, there are six types of hexaferrite has been reported now a days, such as:

1.7.4.1 M-type hexaferrite:

The stoichiometry ration of $BaFe_{12}O_{19}$ compound was long known to exist in 1936 with the melting point of 1390 ^oC was confirmed in 1936. But the structure was initially investigated and magnetically characterized in the early 1950s. It is less expensive to synthesize, had a high electrical resistivity of 10^8 Ω, and exhibited high magnetic uniaxial anisotropy along the c-axis, while having a lower saturation magnetization than the alloy magnets with a maximum density of 5.295 gcm^{-3}, and the molecular mass of 1112 g [49].

1.7.4.2 Y-type hexaferrite:

The Y-type hexaferrites are the first ferroxplana ferrites to be found. At room temperature (RT), almost all of them have a preferred plane of magnetization that is perpendicular to the c-axis.

The formula of Y-type hexaferrites is $Ba_2Me_2Fe_{12}O_{22}$, where Me is a divalent cation. The Y-type hexaferrite is composed of one S unit and one L unit, forming a total of six layers. The unit cell has three of these units and has a c-axis length of 43.56 Å. This hexaferrite belongs to the R_3m space group. When compared to ferrites with uniaxial anisotropy, Co_2Y-hexaferrite has lower magnetic permeability. However, it exhibits a significant magnetization at high frequencies because it benefits from having an easily rotatable magnetization plane [49].

1.7.4.3 W-type hexaferrite:

The formula for W ferrites is $BaMe_2Fe_{16}O_{27}$, where Me is often a transition metal or another divalent cation. In another composition two metal can be used in place of barium. W-type hexaferrite Fe_2W was discovered to have a substantially better electrical conductivity than M because of the Fe^{2+} ions, but it also had an easy axis of magnetization in the c-axis of the hexagonal crystal structure. In the c-axis, its computed hardness is 5.5 GPa [49].

1.7.4.4 X-type hexaferrite:

The X-type hexaferrites have the chemical formula $Ba_2Me_2Fe_{28}O_{46}$, where Me is a divalent transition metal or divalent cation. X-type hexaferrites were initially discovered in 1952 as a mixed phase with M and W-type hexaferrite. At RT, every X-type hexaferrite exhibits this uniaxial anisotropy, except of Co_2X (MW = 2688 g), which has a magnetization cone at 74^o to the c-axis. It has been mentioned specifically in many articles that the X-type hexaferrite polycrystalline nanoparticle has significant permeability and permittivity [49].

1.7.4.5 U-type hexaferrite:

The U-type hexaferrites, $Ba_4Me_2Fe_{36}O_{60}$, here, Me is a divalent cation, were discovered concurrently with the other hexagonal ferrites discussed here. From the study it has been observed that the densities of Co_2U is 5.44 g cm^{-3}, respectively. Co_2U-hexaferrite consist planar anisotropy at RT and a molecular mass of 3622 g. The presence of sufficiently high magnetic

response and dielectric permittivity of U-type hexaferrite nanoparticles or most of the hexaferrite nanoparticles could lead to a vast array of novel EM devices for applications [49].

1.7.4.6 Z-type hexaferrite:

The Z-type hexaferrites were found simultaneously with the ferroxplana Y-type hexaferrites and they contain the composition $Ba_3Me_2Fe_{24}O_{41}$. Co_2Z has a maximum density of 5.35 g cm^{-3} and a molecular mass of = 2522 g. All Z-type hexaferrites have a uniaxial anisotropy aligned with the c-axis, except for Co_2Z, which is planar at ambient temperature but possesses an intricate magnetic anisotropy. The Co_2Z hexaferrites exhibit magnetic permeability ranging from 12 to 15, with a resonance frequency of 1.5 GHz. The Co_2Z-type hexaferrite is highly intriguing for MW research due to its spontaneous polarization and planar magnetic anisotropy [49].

1.7.5 Conducting and semiconducting nanomaterials:

Along with these magnetic nanoparticles to improve the EMI shielding of the composite films by the improvement of the magnetic loss contribution, the dielectric loss also contributes to the SE due to absorption. In this regard the incorporation of conducting and semiconducting nanomaterials helps to enhance the dielectric loss of the material then any possible enhancement of any one of these two loss factors or the possible enhancement of both of them can enhance the EMI shielding of the materials with large bandwidth. Here in this study conducting and semiconducting materials has been chosen for their large aspect ratio, flexibility and its ability to modulate its charge conduction property depending on temperature and doping. Also, these type of materials acts as a charge source as a result of which there is more charge accumulation at the interfaces which enhances the dielectric response. Such kind of conducting and semiconducting materials are: Single-walled carbon nanotubes (SWNTs), Multi-walled carbon nanotubes (MWNTs), Carbon nitride (C_3N_4), Molybdenum disulphide (MoS_2), Reduced

graphene oxide (rGO), conducting MXene, Graphene etc [50].

1.7.6 Polymer materials:

The powder form of magnetic and conducting/semiconducting to study the EMI shielding property was a big challenge. Because, for different measurement purpose there is a requirement to hold the materials during measurement where a specific holder must be there, especially during the measurement of EMI shielding property. So, the selection of holding materials to hold the magnetic and conducting/semiconducting materials is an important part of this EMI shielding study. Also, the holding materials should be flexible, corrosive resistant, with controllable thickness and area. Such kind of materials are: Polyvinylidene fluoride (PVDF), Polyvinylidene fluoride-hexafluoropropylene (PVDF-HFP), Polytetrafluoroethylene (PTFE), Polychloro trifluoro ethylene (PCTFE), Fluorinated ethylene propylene (FEP), Ethylene tetrafluoroethylene (ETFE), polyacetylene (PA), polythiopene (PTs), polypyrole (PPy), polyaniline (PANI) etc. All the above-mentioned polymer are very good piezoelectric material and their additional contribution to the dielectric permittivity has been imparted in the resultant materials which is essential for EMI shielding [51].

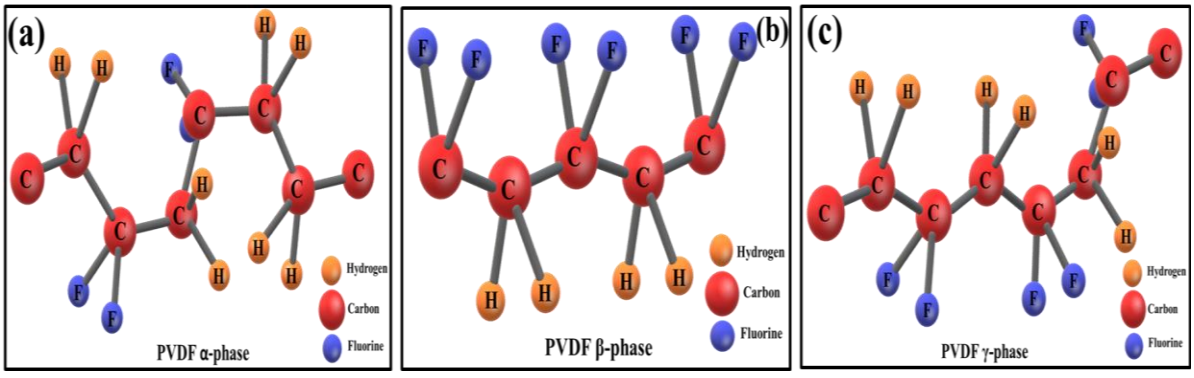

Figure 1.8: Structures of PVDF: alpha (α), beta (β), gamma (γ)

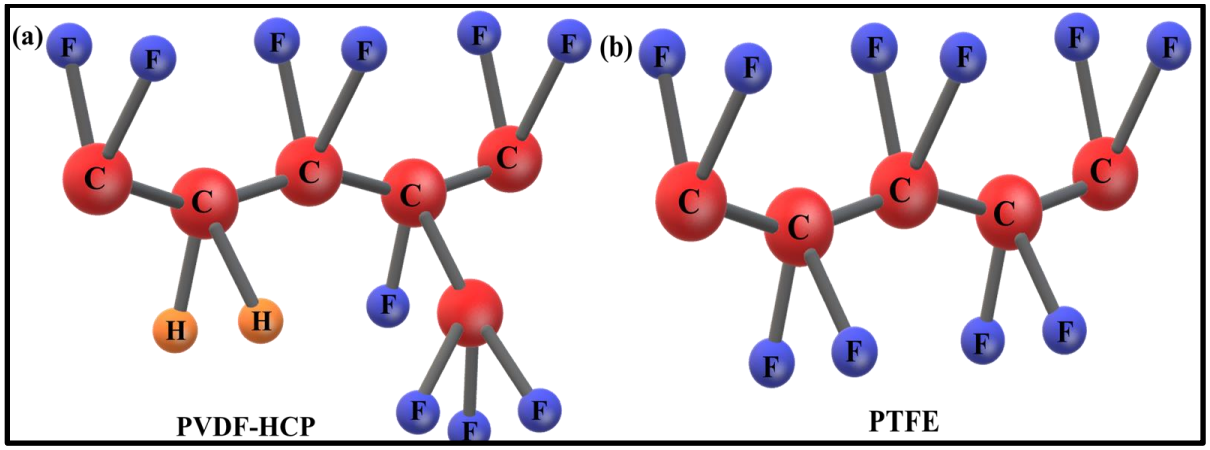

Figure 1.9: Structure of Polyvinylidene fluoride-hexafluoropropylene (PVDF-HFP) and Polytetrafluoroethylene (PTFE)

1.8 Selected materials for the EMI shielding property in this study:

MW absorbers work on an attenuation mechanism, which is characterised by the presence of dielectric and magnetic losses of the material, which are used in the measurement of the impedance matching and resonant frequency calculations, respectively. Hexaferrites can exhibit very high values of resonance frequency, ranging up to 100 GHz, making them very lucrative in the field of microwave-absorbing-based applications [49]. The presence of c-axis and c-plane anisotropy results in the creation of a suitable material for MW absorption [49]. In case of hexaferrite materials the unit cell is comprised of three layers or blocks namely the R-block which has the most significant hexagonal geometry consisting of the barium ions and two oxygen layers, the S-block, or the spinel geometry and lastly the T-block having the hexagonal geometry. On the other hand, it is expected to get a good magnetostrictive response from the magnetostrictive phase due to the presence of Ni-Zn-Cu-ferrite nanoparticles. The magnetic properties of Ni-Zn-ferrite can be greatly affected by the size of its particles/domains. Also, the partial replacement of Zn^{2+} with an optimum limit of 20% of Cu^{2+}, in Ni-Zn-ferrite enhances the density of copper ions in the resultant magnetic material which leads to increase in its

resistance to electricity and magnetic permeability.

According to recent studies, the X-type hexaferrite exhibits a high anisotropic field and saturation magnetization. In fact, the saturation magnetization of the W- and X-types is greater than that of any other types of hexaferrite. This X-type hexaferrite also possesses excellent chemical stability, low coercivity, small remanence, high m0icrowave magnetic loss, and is cost-effective. All of these characteristics contribute to its enhanced microwave absorbing properties [52-54]. Kyaw et al conducted a study where they synthesized X-type hexaferrites with a nominal composition of $[Ba_2(Zr_{0.5}Mn_{0.5})_xFe_{28-x}O_{44+0.25x}]$, where, x values of 0, 1.5, 2, and 2.5 were used. The synthesis was carried out using the solid-state reaction approach, and two distinct sintering settings of 1240 °C and 1300 °C for 5 hours were applied. The material with x = 2 exhibited the highest remnant magnetization, regardless of the sintering settings. The $Ba_2(Zr_{0.5}Mn_{0.5})_2Fe_{26}O_{44.5}$ sample with x = 2, which was sintered at a temperature of 1240 °C, exhibited a maximum absorption of -36.2 dB (99.975%) at a frequency of 15.4 GHz [55].

The U-type hexaferrite $Ba_4Me_2Fe_{36}O_{60}$ possesses the most intricate crystal structure and the greatest unit cell size. Lisjak et al. conducted a comprehensive investigation on the characteristics of this type of hexaferrite, focusing on phase formation, thermal stability, and microwave properties [56-62]. The increased complexity and larger size of the unit cell contribute to achieving greater absorption of EM waves across a wide range of frequencies. The anisotropic features of hexaferrites lead to a rise in the ferromagnetic resonance frequency, allowing them to be customized for the dissipation of EM energy in the MW frequency range. Polycrystalline samples of the U-type hexaferrite series, specifically $(Ba_{1-3x}La_{2x})_4Co_2Fe_{36}O_{60}$ with x ranging from 0.10 to 0.20 in increments of 0.05, are synthesized using the usual solid-state reaction method by Meena et al. The introduction of La^{3+} ions in place of some Ba^{2+} ions improve electron hopping and decreases magnetic interaction over the entire X-band

frequencies. As a result, the samples exhibit broad microwave absorption across all frequencies. The sample with a thickness of 1.8 mm and x=0.10 had a minimum reflection loss of RL= -27 dB, indicating a high absorption rate of 99.8% [63].

Z-type hexaferrite ($Ba_3Me_2Fe_{24}O_{41}$) is a ferrite with soft magnetic characteristics that make it highly valuable for absorbing MW, especially at higher frequencies. The saturation magnetization (M_s) of the material is 51 emu/g, and its Curie temperature (T_c) is 680 K. The Co_2Z type hexaferrites have a static magnetic permeability ranging from 12 to 15, and their resonance frequency is 1.5 GHz [64-67]. Magham et al., synthesized barium Z-type hexaferrites ($Ba_3Co_2Cr_{2x}Fe_{24-2x}O_{41}$ with x = 0, 0.3, 0.6 and 0.9) utilizing the solid-state reaction approach. The $Ba_3Co_2Cr_{1.2}Fe_{22.8}O_{41}$ sample, with a composition of x = 0.6, demonstrated a peak microwave absorption of 99.8% at a frequency of 5.34 GHz. All of the samples exhibited a wide absorption bandwidth ranging from 3 to 3.2 GHz, as well as a large reflection loss of -10 dB [68].

Y-type hexaferrites ($Ba_2Me_2Fe_{12}O_{22}$) exhibit a comparatively lower value of M_s when compared to other forms of hexaferrites. The Y-type hexaferrites with planar magnetic anisotropy have received attention due to their capacity to demonstrate higher magnetic permeability in the GHz frequency range compared to other hexaferrites with uniaxial magnetic anisotropy [69, 70]. Suthar et al. studied the synthesis of Y-type barium hexaferrite, $Ba_{2-x}La_xCo_{2-x}Mg_xFe_{12}O_{22}$, where x values of 0.1, 0.2, 0.3, 0.4, and 0.5 were used. The synthesis was done using the sol-gel auto-combustion method. The ceramics that were created were sintered to a temperature of 1050 °C for a duration of 2 h. The study of shielding efficiency demonstrated that the shielding efficiency due to reflection (SE_R) and overall shielding efficiency (SE_T) improved when the concentrations of La-Mg increased [71].

Zn-Ni ferrites have attracted significant attention among spinel ferrites because of their elevated electrical resistivity and reduced magnetic coercivity, resulting in decreased eddy current losses at high frequencies. It has excellent mechanical hardness, a high Curie temperature, and exceptional chemical stability. Zn-Ni ferrites possess features that make them suitable for a wide range of applications, including recording heads, antenna rods, microwave devices, telephony, and as a core material for power transformers in electronics [72,73]. Recently, it has been used in applications like radar absorbent materials (RAMs). Zinc-Nickel (Zn-Ni) ferrites, are employed in systems for the transmission and reception of EM signals. Singh et al. had synthesized Zn-Ni ferrite, Nickel ferrite, and Zinc ferrite using a solvohydrothermal technique assisted by sonochemistry. The Ni-Ferrite material achieved a SE_T of 28.5 dB, while the Zn-Ni-Ferrite material achieved a SE_T of 30.5 dB in the X band. The primary factor contributing to the shielding effectiveness in both cases was absorption. This indicates that the materials were able to successfully reduce the intensity of almost 99.99% of the incident MW [74].

The conducting/semiconducting fillers of in association with the magnetic materials can improve the EM shielding effectiveness (SE) of the nanocomposite nanomaterials just by allowing the flow of current loops inside the composite structures at RT, called eddy current, since conducting/semiconducting nanofiller can modulate its charge conduction property depending on temperature and doping [75]. This eddy current inside the nanocomposite structures may be appeared due to the magnetic flux linkages and it leads to the large absorption of EMR in the RF/MW frequency region. Among all the different nanofillers materials the selected conducting/semiconducting nanofiller material, such as rGO with a band gape of 1 to 1.6 eV, C_3N_4 with a band gap of ~ 2.7 eV and MoS_2 with a band gap of 1.2 eV can be the most interesting filler material because of its large aspect ratio and flexibility [75].

The extensively researched 2D nitrides mostly consist of C_3N_4 nanosheets and hexagonal boron nitride (BN) nanosheets. Nitrides are not utilized in isolation for MW attenuation in the literature. They are frequently used as an addition to create multipurpose microwave absorbers, either to improve thermal conductivity or to boost impedance matching. C_3N_4 is a semiconductor with low weight and moderate resistance, which reduces the conduction loss of electromagnetic waves and improves impedance matching to decrease surface reflection of EM waves. Lv et al. fabricated graphene/g-C_3N_4 composites for MW absorption by depositing g-C_3N_4 nanosheets onto graphene using a straightforward liquid-phase method. Due to its suitable resistance, the combination of g-C_3N_4 on graphene functions as a resistor, resulting in significant reduction in current when exposed to an EM field. This process converts EM energy into heat energy through the Joule effect. The optimal reflection loss (RL) was -29.6 dB at a frequency of 14.5 GHz for a thin coating layer with a thickness of 1.5 mm. The effective absorption bandwidth of 5.2 GHz (12.8–18 GHz) was achieved with a filling ratio of only 10 wt.%. [76].

rGO possesses excellent electrical conductivity, significant dielectric constant, substantial specific surface area, impressive mechanical strength, and low mass density. As a result, it provides remarkable benefits for the purposes of shielding and absorbing EM waves. Nevertheless, its effectiveness as a microwave absorber is limited due to its high conductivity, resulting in significant interfacial reflection caused by the impedance mismatch with the surrounding. Undesirable reflections can cause interference, information leakage, and signal loss in several scenarios, including anechoic chambers, stealth coating, and signal receivers. In order to enhance the MW absorption capabilities of materials based on graphene, such as reducing the reflection loss (RL) and increasing the range of frequencies absorbed, it is common practice to incorporate different dielectric or magnetic elements into the composite system.

Zhang et al. synthesized composites of reduced graphene oxide (RGO), copper sulfide (CuS), and polyvinylidene fluoride (PVDF) using wet chemistry and a hot-press technique. In this procedure, CuS complex microspheres of consistent size were included within the RGO layers, resulting in distinct core-shell nanostructures. These nanostructures were then hot-pressed into the PVDF matrix. Composites containing 15 wt.% filler demonstrated a dielectric constant of 36 at 2 GHz, which is ten times more than that of pure PVDF. Composites with 5 wt.% filler showed a minimum RL of -32.7 dB at 10.7 GHz when the thickness was 2.5 mm. The enhanced RL is elucidated by the Debye dipolar relaxation of the composites [77].

2D MoS_2 nanosheets exhibit exceptional MW absorption properties due to their unique 2D structure and appropriate EM characteristics. These properties result in significant losses through interfacial polarization and a multimode attenuation mechanism. MoS_2 nanosheets can serve several functions, such as impedance modulation, microwave attenuation, or structural support, when used in conjunction with other absorbers. Research was conducted on MoS_2-based multinary composites to enhance their EM performance. Quan et al. incorporated graphene into composites based on MoS_2 to modify the dielectric properties in order to achieve a more optimal balance between impedance matching and energy conservation. This is necessary because using only pure graphene or pure MoS_2 is not effective in attenuating EM waves due to either excessive surface reflection or inadequate dissipation. MoS_2/RGO composites were synthesized using a simple hydrothermal method. The dielectric constant of the composites was controlled by adjusting the mass ratio of the precursors, resulting in an ideal equilibrium between impedance matching and energy conservation. The RL reached a minimum value of -67.1 dB at a frequency of 14.8 GHz. The effective bandwidth for EM wave absorption, where the RL is less than -10 dB, was 5.92 GHz (ranging from 12.08 GHz to 18 GHz) were obtained using a thin material with a thickness of 1.95 mm. The study showed that

having better performance on one side alone does not ensure good microwave absorbing capabilities. To improve the microwave absorbing qualities, it is crucial to effectively combine impedance matching, attenuation ability, and absorber thickness [78].

Now, in order to hold the materials during EMI shielding measurement, a specific holder is required to contain all the powder materials. So, piezoelectric polymers PVDF and PVDF-HFP have been selected to not only have a laminated film structure to hold all the materials but also to incur dielectric losses in the GHz frequency range due to the enriched polar β-phase of PVDF and PVDF-HFP.

Although the above-mentioned materials have good EMI SE, their applicability are limited due to their poor mechanical properties and processing problems [79]. In order to prevent this issue, a potential solution is to include the fillers in engineering thermoplastics like poly (vinylidene fluoride) (PVDF). This technique offers the benefits of improved design flexibility, increased mechanical qualities, and excellent EMI SE. Polyvinylidene fluoride (PVDF)-based polymers have garnered ongoing interest in EMI shielding applications because of their inherent dipole and interfacial polarization effects. These properties contribute to the improved dissipation of EMR [80]. Zhao et al produce nanocomposite foams made of poly(vinylidene fluoride) (PVDF) and 10 wt% graphene nanoplatelets (GnP) that are lightweight and exhibit exceptional EMI SE. The foam thickness played a crucial role in determining the EMI shielding capabilities. The EMI SE of the PVDF/10 wt%-GnP foam, which has a void percentage of 48.7%, improved from 12.4 to 32.2 dB at 26.5 GHz and from 15.2 to 37.4 dB at 40 GHz when the thickness of the sample rose from 1.5 to 3.0 mm [81].

1.9 References:

1. M. Rouhi, Z. Hajizadeh, R. Taheri-Ledari, A. Maleki, M. Babamoradi, Mater. Sci. Eng. B 286, 116021 (2022).

2. T Tachibana, IEICE Transactions on Communications, 105 (2), 98–115 (2022).

3. Ministry of Communications; Year End Review 2022: Ministry of Communications; Launch of 5G Services in Oct 2022 by Hon'ble Prime Minister on 01.10.2022 Posted On: 16 DEC 2022 1:55PM by PIB Delhi.

4. R. Kumar, R. Geleta, A. Pandey, D. Sinwar, IOP Conference Series: Materials Science and Engineering 1099, 1, 012031 (2021).

5. T. Tarver, American cancer society (ACS) Atlanta, GA: American Cancer Society, 66 (2012).

6. A.Y. Owda, N. Salmon, A.J. Casson, M. Owda, Sensors, 20(5), 1480 (2020).

7. Rainer Nyberg, Lennart Hardell and Martin Pall, International Commission on Non-Ionizing Radiation, ch. 1,5,6 (2018).

8. E. Navarro, J. Segura, M. Portolés Claudio Gómez-Perretta de Mateo, Electromagnetic Biology and Medicine 22, 161 – 169 (2003).

9. Flint Richard, East Becky, Derbyshire Country Council (2019).

10. J.E. Olsen, S.B. Dineva, Appl. Forest Ecol. 5, 31–53 (2017).

11. Anne Marie Helmenstine, Microwave Radiation Definition, www.thoughtco.com (2021).

12. Ali Grami, Academic Press, 2015.

13. Nihad Ahmad Hassan, Data Hiding Techniques in Windows OS, 133-205 (2017).

14. Modes of Radio Wave Propagation in Wireless Communication, www.geeksforgeeks.org (2023).

15. Rahul Ahir, Difference Between 1G, 2G, 3G, 4G and 5G Technology, www.medium.com (2023)

16. Adam Fendelman, 1G, 2G, 3G, 4G, & 5G Explained, www.lifewire.com (2021).

17. T. S. Rappaport, Y. Xing, G.R. MacCartney, A.F. Molisch, E. Mellios, J. Zhang, IEEE Transactions on antennas and propagation 65.12, 6213-6230 (2017).

18. S. Verma, T. M. Tejaswini, D. Pradhan, Proceedings in IRAJ International Conference, Bengaluru, India page 71-75 (2019).

19. Jamie A. Dyvig, California State Science Fair 2012 Project Summary (2012).

20. Diana Kordas, Birds and Trees of Northern Greece: Population Declines since the Advent of 4G Wireless an Observational Study (2017).

21. Biplob Kumar Modak, Proceedings of the Zoological Society 70 (1), Springer, 21-27 (2017).

22. J.L. Phillips, N.P. Singh, H. Lai, Pathophysiology 16, 79–88 (2009).

23. L. Hardell, A. Nasman, A. Pahlson, A. Hallquist, M.K. Hansson, Int J Oncol., 15: 113-116 (1999).

24. J.E. Muscat, JAMA, 284 (23), 3001 (2000).

25. R. Beinart, S. Nazarian, Circulation 128(25): 2799-2809 (2013).

26. R.M. Lipman, B.J. Tripathi, R.C. Tripathi, Survey of ophthalmology 33(3): 200-210 (1988).

27. G. Kumar, Cell tower radiation, Mumbai, December (2010).

28. L.L. Adebayo, H. Soleimani, N. Yahya, Z. Abbas, F.A. Wahaab, R.T. Ayinla, H. Ali, Ceramics International, 46(2): 1249-1268 (2020).

29. V. Shukla, Nanoscale Advances, 1(5): 1640-1671 (2019).

30. C. Wang, V. Murugadoss, J. Kong, Z. He, X. Mai, Q. Shao, Y. Chen, L. Guo, C. Liu, S. Angaiah, Z. Guo, Carbon, 140: 696-733 (2018).

31. V. Shukla, Nanoscale Advances, 1(5): 1640-1671 (2019).

32. Y. Bhattacharjee, S. Bose, S., ACS Applied Nano Materials, 4(2): 949-972 (2021).

33. H. Lv, H. Zhang, J. Zhao, G. Ji, Y. Du, Nano Res. 9 (2016) 1813–1822 (2016).

34. D. L. Leslie-Pelecky and R. D. Rieke, Chem. Mater., 8, 1770–1783 (1996).

35. X. Zhang, P. Guan and X. Dong, Appl. Phys. Lett., 97, 033107 (2010).

36. R. Dosoudil, M. Usakova, J. Franek, J. Slama and A. Gruskova, IEEE Trans. Magn., 46, 436–439 (2010).

37. A. Habib, S. Xu, E. Walker, M. Ondeck, R. Swaminathanand, M. McHenry, J. Appl. Phys., 111, 07B305 (2012).

38. R. Kodama, J. Magn. Magn. Mater., 200, 359–372 (1999).

39. Y. Liu, S. Wei, B. Xu, Y. Wang,H. Tianand, H. Tong, J.Magn. Magn. Mater., 349, 57–62 (2014).

40. H. Lv, G. Ji, H. Zhang, M. Li, Z. Zuo, Y. Zhao, B. Zhang, D. Tang, Y. Du, Scientific Reports 5, 18249 (2015).

41. Y. Du, W. Liu, R. Qiang, Y. Wang, X. Han, J. Ma and P. Xu, ACS Appl. Mater. Interfaces, 6, 12997–13006 (2014).

42. O.M. Sanusi, A. Benelfellah, N.A. Hocine, Applied Clay Science, 185: 105408 (2020).

43. G.B. Scott, D. Lacklison, IEEE Transactions on Magnetics, 12(4): 292-311 (1976).

44. Y.H. Kim, J.S. Kim, S.I.Kim, M. Levy, J. Korean Phys. Soc., 43:400–405 (2003).

45. I. Nistor, C. Holthaus, I.D. Mayergoyz, C. Krafft, Journal of applied physics, 99(8) (2006).

46. P. Görnert, T. Aichele, A. Lorenz, R. Hergt, J. Taubert, physica status solidi (a), 201(7): 1398-1402 (2004).

47. S.M. Elhamali, N.B. Ibrahim, S. Radiman, J. Adv. Nanomater, 1: 11-20 (2016).

48. R. Dom, R. Subasri, K. Radha, P.H. Borse, Solid State Communications, 151(6): 470-473 (2011).

49. S.A. El-Molla, G.A. Fagal, N.A. Hassan, G.M. Mohamed, Research on Chemical Intermediates, 41: 679-689 (2015).

50. R.C. Pullar, Progress in Materials Science, 57(7): 1191-1334 (2012).

51. S. Kumari, J. Dalal, V. Kumar, A. Kumar, A. Ohlan, International Journal of Molecular Sciences, 24(15): 12267 (2023).

52. K.S. Kumar, R. Rengaraj, G.R. Venkatakrishnan, A. Chandramohan, Materials Today: Proceedings, 47: 4925-4928 (2021).

53. A.S. Džunuzović, N.I. Ilić, M.V. Petrović, J.D. Bobić, B. Stojadinović, Z. Dohčević-Mitrović, B.D. Stojanović, Journal of Magnetism and Magnetic Materials, 374, 245-251 (2015).

54. L. Li, K. Chen, H. Liu, G. Tong, H. Qian, B. Hao, Journal of alloys and compounds, 557, 11-17 (2013).

55. I. Sadiq, I. Ali, E. Rebrov, S. Naseem, M.N. Ashiq, M.U. Rana, Journal of magnetism and magnetic materials, 370, 25-31 (2014).

56. H.K. Ye, S.R. Shannigrahi, C.B. Soh, S.L.W. Yang, L.S. Li, D.V.M. Repka, P. Kumar, Journal of Magnetism and Magnetic Materials, 465, 716-726 (2018).

57. D. Lisjak, V.B. Bregar, A. Znidarsic, M. Drofenik, Journal of Optoelectronics and Advanced Materials, 8(1), 60 (2006).

58. D. Lisjak, M. Drofenik, Journal of applied Physics, 93(10), 8011-8013 (2003).

59. D. Lisjak, M. Drofenik, Journal of Magnetism and Magnetic Materials, 272, E1817-E1819 (2004).

60. C. Sudakar, G.N. Subbanna, T.R.N. Kutty, Journal of magnetism and magnetic materials, 263(3), 253-268 (2003).

61. D. Lisjak, D. Makovec, M. Drofenik, Journal of materials research, 19, 2462-2470 (2004).

62. Z. Haijun, L. Zhichao, Y. Xi, Z. Liangying, W. Mingzhong, Materials Science and Engineering: B, 97(2), 160-166 (2003).

63. D. Lisjak, P. McGuiness, M. Drofenik, Journal of materials research, 21(2), 420-427 (2006).

64. R.S. Meena, S. Bhattachrya, R. Chatterjee, Journal of magnetism and magnetic materials, 322(14), 1923-1928 (2010).

65. I.G. Chen, S.H. Hsu, Y.H. Chang, Journal of Applied Physics, 87(9), 6247-6249 (2000).

66. T. Nakamura, K.I. Hatakeyama, IEEE transactions on magnetics, 36(5), 3415-3417 (2000).

67. R. Tang, C. Jiang, H. Zhou, H. Yang, Journal of Alloys and Compounds, 658, 132-138 (2016).

68. J.J. Xu, C.M. Yang, H.F. Zou, Y.H. Song, G.M. Gao, Journal of Magnetism and Magnetic Materials, 321(19), 3231-3235 (2009).

69. S.B.S. Magham, M. Sharma, S.R. Shannigrahi, H.R. Tan, V. Sharma, Y.S. Meng, S. Idapalpati, R.V. Ramanujan, D.V.M. Repaka, Journal of Magnetism and Magnetic Materials, 441, 303-309 (2017).

70. Bai Y, Xu F, Qiao L and Zhou J, J. Alloys Compd. 473 505–8 (2009)

71. J. Jalli, Y.K. Hong, S. Bae, J.J. Lee, G.S. Abo, J.H. Park, B.C. Choi, T. Mewes, S.G. Kim, S.H. Gee, I.T. Nam, Journal of Applied Physics, 109(7) (2011).

72. M. Suthar, P.K. Roy, Materials Science and Engineering: B, 283, 115801 (2022).

73. M. Sertkol, Y. Köseoğlu, A. Baykal, H.Ü.S.E.Y.İ.N. Kavas, A.C. Başaran, Journal of Magnetism and Magnetic Materials, 321(3), 157-162 (2009).

74. M. Jalaly, M.H. Enayati, F. Karimzadeh, J. Alloy. Compd., 480 (2), 737-740 (2009)

75. H. Singh, S. Parmar, B. Ray, V.K. Lokku, D. Kumar, K.L. Bhavani, D. Nagaraju, D.V.N. Vo, A. Sharma, S. Datar, S. Banerjee, Journal of Alloys and Compounds, 906, 164199 (2022).

76. A.T. Sareshkeh, M.S.S. Dorraji, M.H. Rasoulifard, Progress in Organic Coatings, 125: 472-480 (2018).

77. X.J. Zhang, G.S. Wang, Y.Z. Wei, L. Guo, M.S. Cao, Journal of Materials Chemistry A, 1(39), 12115-12122 (2013).

78. B. Quan, X. Liang, G. Xu, Y. Cheng, Y. Zhang, W. Liu, G. Ji, Y. Du, New Journal of Chemistry, 41(3), 1259-1266 (2017).

79. Z. He, H. Xie, H. Wu, J. Chen, S. Ma, X. Duan, A. Chen, Z. Kong, ACS omega, 6(35), 22468-22477 (2021).

80. Li Ma, Mahdi Hamidinejad, Caiyun Liang, Biao Zhao, Saeed Habibpour, Aiping Yu, Tobin Filleter, Chul B. Park, Carbon,Vol. 179, 408-416 (2021)

81. B. Zhao, C. Zhao, M. Hamidinejad, C. Wang, R. Li, S. Wang, K. Yasamin, C.B. Park, Journal of Materials Chemistry C, 6(38), 10292-10300 (2018).

Chapter: 2

Experimental

(Materials, Methods and Instrumentations)

Chapter: 2 Experimental

2.1 Materials:

2.1.1 Required chemicals and apparatus used to synthesized nanoparticles and nanocomposite film:

Synthesis of nanoparticles and the fabrication of an effective nanocomposite film to study the EMI shielding property, the most important part is the selection of precursor chemicals of high degree of purity. For the synthesis of different ferrite magnetic materials such as, spinel ferrite (Ni-Zn-Cu-ferrite) and hexagonal ferrites (Co_2X, Co_2U, Co_2Z and Co_2Y) the required precursor salts or chemicals are Nickel (II) acetate tetrahydrate $Ni(CH_3COO)_2{\cdot}4H_2O$ (Sigma Aldrich, 99%), Zinc (II) acetate dihydrate $Zn(CH_3COO)_2{\cdot}2H_2O$ (Sigma Aldrich, 99%), Copper (II) acetate monohydrate $Cu(CH_3COO)_2{\cdot}H_2O$ (Sigma Aldrich, 99%), Iron (III) nitrate nonahydrate $Fe(NO_3)_3{\cdot}9H_2O$ (Merck Germany, 99%), Barium (II) nitrate $Ba(NO_3)_2$ (Merck Germany, 99%), Cobalt (II) nitrate $Co(NO_3)$ (Merck Germany, 99%), Strontium (II) nitrate ($Sr(NO_3)_2$) (Merck Germany, 99%), Citric acid ($C_6H_8O_7$), Acetone (C_3H_6O), and Ethyl alcohol (C_2H_5OH).

The semiconducting (C_3N_4 and MoS_2) and conducting (rGO) nanofillers acts as a charge source inside the PVDF matrix at the interfaces. In association with the magnetic nanofillers, the resultant composite can improve the shielding effectiveness due to absorption (SE_A), reflection (SE_R), and the total shielding effectiveness (SE_T). The required precursor chemicals to synthesize the semiconducting and conducting nanofillers are Melamine ($C_3H_6N_6$), Molybdenum Oxide (MoO_3) (Sigma Aldrich, 99%), Potassium thiocyanate (KSCN) (Sigma Aldrich, 99%), Graphite fine powder (Loba Chemie), Sodium nitrate $NaNO_3$ (Merck Germany, purified), Sulphuric acid (H_2SO_4) (98% concentrated, Merck), Potassium permanganate ($KMnO_4$) (Loba Chemie India, 99%), Hydrogen peroxide (H_2O_2) (30% concentrated, Merck),

Hydrochloric acid (HCl) (35% concentrated, Merck), Hydrazine hydrate (made in Germany, Sigma-Aldrich) and Milli-Q water.

Making a high degree of flexible, free standing and mostly cost-effective nanocomposite material is more important to conduct the whole EMI shielding property study without having any breakdown. To synthesize the nanocomposite film Poly(vinylidene fluoride)pellets (molecular weight Mn: 107,000, Mw: 275,000 (hpc), Aldrich, Germany), Poly(vinylidene fluoride-co-hexafluoropropylene) (PVDF-HFP) (average Mw: 455,000 Sigma Aldrich), N, N-dimethyl formamide (DMF, Merck, India) have been considered. Using these high quality and contamination free chemicals we have synthesized the required spinel ferrite-PVDF, hexagonal ferrites-PVDF (Co_2X-PVDF, Co_2U-PVDF) and the binary nanofillers-PVDF (NZCF-PVDF, Co_2X-C_3N_4-PVDF, Co_2Z-rGO-PVDF and Co_2Y-MoS_2-PVDF) nanocomposite films.

2.1.2 Apparatus used to fabricate the materials

During the synthesis of nanomaterials and nanocomposite films different types of apparatus have been used and the required apparatus are:

2.1.2.1 Recurring apparatus

The recurring apparatus are weighing machine (WENSAR), beaker (Borosil), petridish S-line (Borosil), micro pipet, spatula, glass rod (Borosil), teflon jacket, autoclave, glass vials (Borosil), centrifuge and hot air oven.

2.1.2.2 Non-recurring apparatus

The following non-recurring apparatus are micro tip (Tarsons), micro centrifuge tube (Tarsons, 2 ml), centrifuge tube (Thermo Fisher Scientifics, 50 ml), aluminium foil and tissues.

2.2 Methods:

2.2.1 Synthesis of magnetic hexaferrite and ferrite nanoparticles by sol-gel method:

The synthesis of hexaferrite (Co_2X, Co_2U, Co_2Z and Co_2Y) were prepared by the simple sol-

gel method [1]. The stoichiometry ration of different hexaferrite used to synthesized the nanoparticles are Co_2X: $Ba_2Co_2Fe_{28}O_{46}$, Co_2U: $Ba_4Co_2Fe_{36}O_{60}$, Co_2Z: $Ba_3Co_2Fe_{24}O_{41}$ and $C_{O2}Y$:$Ba_2Co_2Fe_{12}O_{22}$. In this method the required amount of precursor salts was taken in a beaker and as a solvent ethyl alcohol (C_2H_5OH) have been used. The mixture was then placed over magnetic stirrer for 2 hrs to get a homogeneous solution at 60 ^{O}C. After few hours the solution become dense and placed it inside the hot air oven at 70 ^{O}C. After 24 hrs the dense solution transform into dried flaky like structure and we have ground it using mortar pestle until the flaky like structure become powder. The details of the synthesis procedure has been shown in Figure 2.1. The as prepared hexaferrites was annealed in between 1100 to 1400 ^{O}C in hot air furnace for 6 hrs. Using the same above-mentioned method, the spinel ferrites nanoparticles $Ni_{0.50}Zn_{0.30}Cu_{0.20}Fe_2O_4$ (NZCF) have been synthesized and the as prepared nanoparticles annealed at 400 ^{O}C for 6 hrs. The annealing process is most important part because in order to get desired size and to ensure structural integrity, along with phase formation [2]. The growth of crystallites into grain can improve the magnetic domains present in the magnetic materials. The formation of large magnetic domains can further enhance the magnetization, remanence and magnetic loss of the finally prepared hexaferrite and ferrite nanoparticles [3].

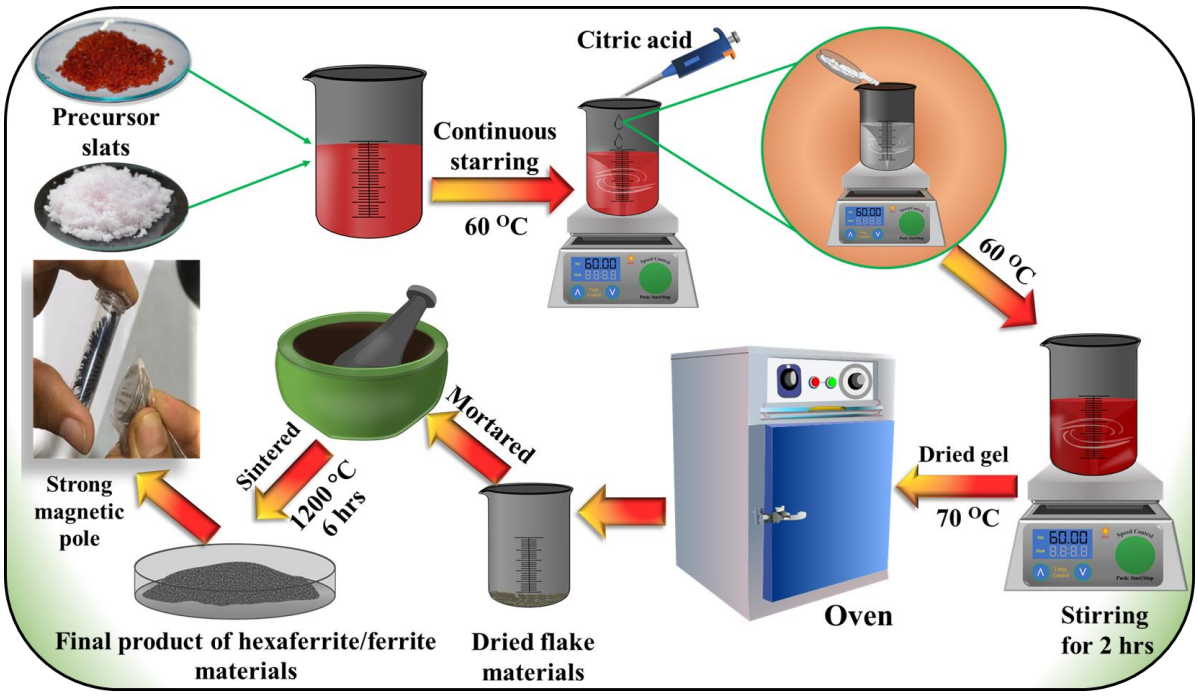

Figure 2.1: Synthesis of hexaferrite and spinal ferrite nanoparticles by sol-gel synthesis method.

2.2.2 Synthesis of semi-conducting and conducting nanofillers:

2.2.2.1 Synthesis of carbon nitrate (C_3N_4) by solid state reaction method:

The semiconducting C_3N_4 nanofillers was prepared by following one-step solid state reaction method. The desired product was obtained via heat treatment of 10 g melamine in a 7 ml curved bottom silica crucible and partially covering it with the cap. The crucible with the precursor was annealed in the presence of air using a hot air furnace at 500 ^oC for 4 hrs with a heating rate of 3 ^oC/min. The crucible containing C_3N_4 was then cooled to room temperature before collecting the powdered sample. A colour change was observed from white to faded yellow indicating the effective condensation of melamine resulting in a high yield of C_3N_4 with negligible loss in precursor [4]. The synthesized yellow sample was finely grounded using mortar pastel and the final form of C_3N_4 has been collected.

2.2.2.2 Synthesis of reduce graphene oxide (rGO) by modified Hummer's method:

Before getting the highly conducting rGO nano sheet graphene oxide (GO) has been synthesized using most effective modified Hummer's method. In this method, the precursor salts, namely graphite flakes and sodium nitrate ($NaNO_3$) were taken in stoichiometric ratios (1:1) in a beaker, wherein they were dissolved in 50 ml of 98 % concentrated H_2SO_4. The first phase of the reaction was carried out at low temperature conditions using an ice bath while stirring the suspension and maintaining the overall reaction temperature below 10 ^oC. This mixture was stirred for 2 hrs followed by the dropwise addition of freshly prepared 6 g of $KMnO_4$ solution, to promote oxidation. Using the mid-temperature phase of the reaction, constant stirring was maintained and the ice bath was removed, the reaction temperature rose upto 30 ^OC and the conditions were maintained till a partly brown colour solution was obtained, after that 100 ml of milli-Q was slowly added to the solution. The temperature got rapidly increased to about 98 ^oC, resulting in a brown coloured solution which was then diluted by adding 200 ml of milli-Q while maintaining constant stirring. In order to terminate the reaction process 10 ml of H_2O_2 was added to the solution and the solution turned yellow in colour. This sample suspension was subsequently washed multiple times with dilute HCl followed by milli-Q, decanting the supernatant each time, and eventually drying the washed sample in a vacuum oven, yielding a black coloured graphene oxide (GO) powder [5]. The dried GO powder was dispersed in milli-Q (1 mg/ml) and hydrazine hydrate (1 ml for 50 mg of GO) was added to the solution under continuous stirring and maintaining the temperature around 80 ^OC. After 12 hrs stirring, the resulting suspension was washed with distilled water to adjust the pH of the sample. The resulting sample was then finally dried in a hot air oven, and thus reduced graphene oxide (rGO) was obtained. Figure 2.2 represent the details synthesis procedure of reduced graphene oxide (rGO).

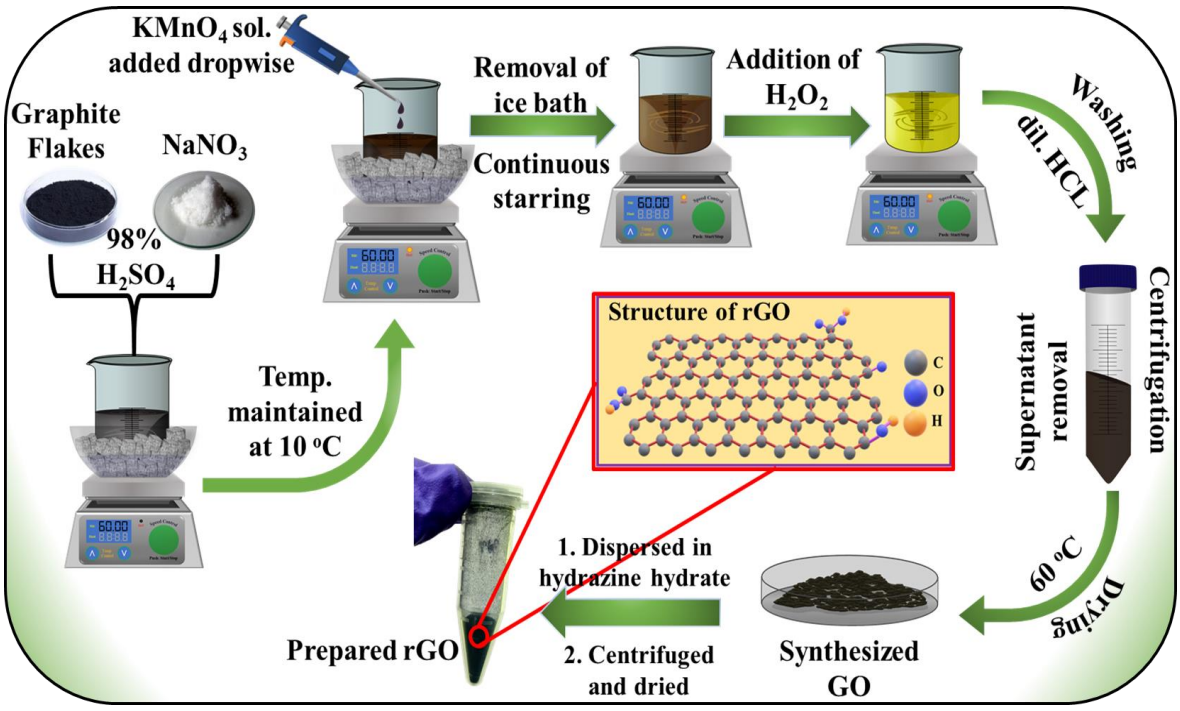

Figure 2.2: Synthesis of reduced graphene oxide (rGO) by modified Hummer's method.

2.2.2.3 Synthesis of molybdenum sulphide (MoS_2) by hydrothermal method:

MoS_2 nanoparticle synthesized via hydrothermal method. For the fabrication of MoS_2 precursor chemicals MoO_3 and KSCN are mixed in a 1:2 molar ratio with 60 ml of milli-q water. For an hour at 50 ^{O}C, the mixture is constantly agitated to ensure complete mixing and solvent dissolution of the precursors. The well-dispersed solution placed in stainless-steel autoclave with a Teflon jacket. After that, the complete system is put in an oven and heated to 200 ^{O}C for 24 hrs. Following completion of the process, the resultant suspension is carefully collected from the Teflon jacket and separated by centrifugation. The supernatant is effectively discarded by thorough washing and the pH level of the solution maintain at 7 in order to confirm that no unreacted species remain. Now, the sample has been collected and dried it using hot air oven at 70 ^{O}C and then mortared and the details synthesis procedure has been given in Figure 2.3 [6].

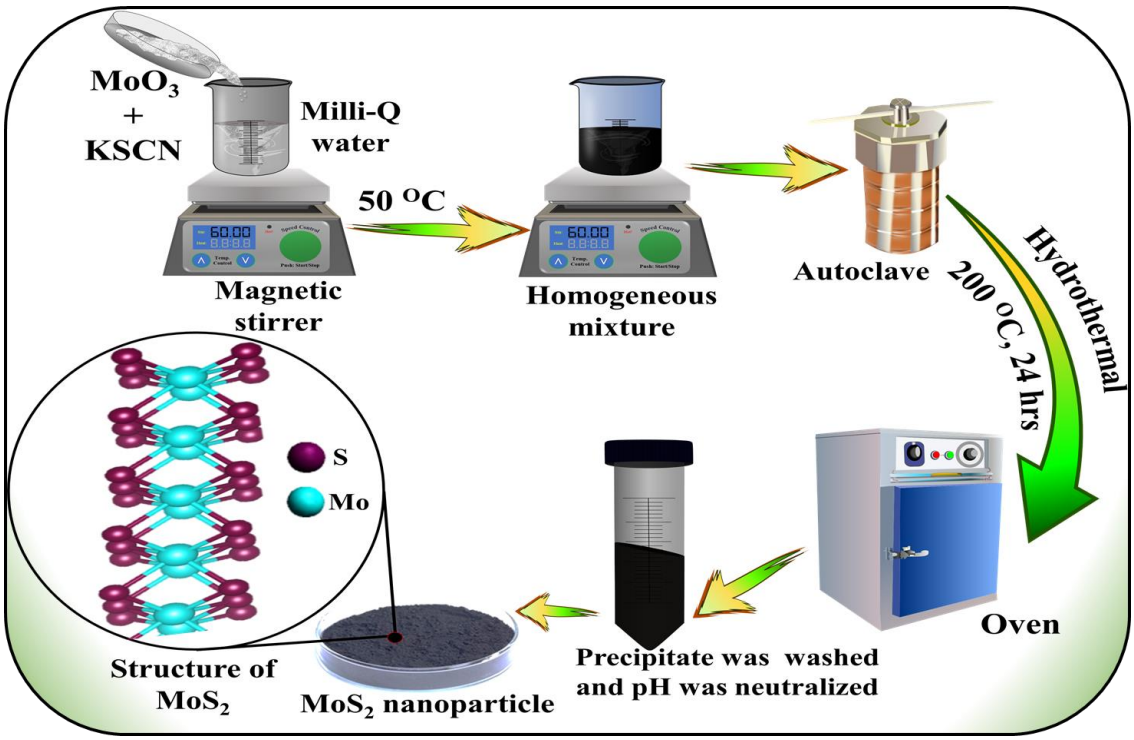

Figure 2.3: Synthesis of reduced semiconducting MoS_2 by hydrothermal method.

2.2.2.4 Synthesis of binary nanocomposite by grinding-mixing method:

The hexaferrite binary nanofillers (Co_2X-C_3N_4, Co_2Z-rGO, Co_2Y-MoS_2, and NZCF-C_3N_4) has been prepared by the one step solid-state reaction method [7]. At first, both the synthesized magnetic nanoparticles (Co_2X, Co_2Z, Co_2Y, and NZCF-C_3N_4) and semiconducting/conducting (C_3N_4, rGO, MoS_2) were mixed with proper proportion (mentioned in Table 2.1) in an organic solvent (acetone) and the homogeneous mixture of magnetic nanoparticles and semiconducting/conducting was prepared using ultrasonic bath sonicator. After several minutes of sonication process the homogeneous mixture was dried on a glass plate using hot air oven at 60 ^{O}C. The dried mixture was then grounded thoroughly in order to make the homogeneity of the mixture even better. After an hour of grinding process, the mixture was poured again in the organic solvent to make the well dispersed solution. This solution was then sonicated again and the entire process was repeated for 3-4 times. Finally, the dried and homogeneous mixture of

Co_2X-C_3N_4, Co_2Z-rGO, and Co_2Y-MoS_2 binary nanofillers has been collected.

Table 2.1: Specifications of binary nanofillers

Sl. No.	Sample name	Specifications
1.	NFC55	50:50 wt.% of NZCF:C_3N_4
2.	NFC73	70:30 wt.% of NZCF:C_3N_4
3.	XC73	70:30 wt.% of Co_2X:C_3N_4
4.	rZ55	50:50 wt.% of rGO:Co_2Z
5.	rZ37	30:70 wt.% of rGO:Co_2Z
6.	YM55	50:50 wt. % of Co_2Y:MoS_2
7.	YM91	90:10 wt. % of Co_2Y:MoS_2

2.2.2.5 Synthesis of nanofillers-polymer nanocomposite film by solution casting method:

The synthesis of binary nanofillers-polymer nanocomposite films synthesized using a cost-effective simple solution-casting method and the details procedure has been given in Figure 2.4. In this method the required amount of PVDF/PVDF-HFP pellets were initially taken in a glass vial with N, N-dimethyl formamide (DMF). After that, they were put on a magnetic stirrer at 50 ^{O}C to prepare the PVDF/PVDF-HFP gel. The PVDF/PVDF-HFP solution turned into a homogenous transparent gel. On the other hand, hexaferrite (Co_2X, Co_2U) and the binary nanofillers (NZCF-C_3N_4, Co_2X-C_3N_4, Co_2Z-rGO, and Co_2Y-MoS_2) were taken in another glass vial with DMF and the solution has been dispersed using vortex for an hour. Now, the thick, transparent gel of PVDF/PVDF-HFP was then supplemented with the hexaferrite and the binary nanofillers. For a one hour, the entire apparatus was submerged in a sonicator to ensure that the binary inside the PVDF/PVDF-HFP gel were evenly mixed. After that, the homogenous

mixture of Co_2X-PVDF, Co_2U-PVDF, NZCF-C_3N_4-PVDF, Co_2X-C_3N_4-PVDF, Co_2Z-rGO-PVDF, and Co_2Y-MoS_2-PVDF-HFP was substrate at dried and cleaned petridish and placed it at hot air oven at 70 ^{O}C for 6 hrs [8]. This slow evaporation is maintained to get the development of better interfacial area between the nanofillers and the polymer structure. After a slow evaporation process the casted mixture is now transform into a thick, free standing and flexible nanocomposite film. As mentioned the above process the bare PVDF and PVDF-HFP film has been synthesized. The details of the nanocomposite films discuss in the bellow mentioned Table 2.2.

Table 2.2: Specifications of nanocomposite films

Sl. No.	Sample name	Specifications
1.	NFCP552	20 wt.% of NFC55 in 80 wt.% of PVDF
2.	NFCP553	30 wt.% of NFC55 in 70 wt.% of PVDF
3.	NFCP732	20 wt.% of NFC73 in 80 wt.% of PVDF
4.	NFCP733	30 wt.% of NFC55 in 70 wt.% of PVDF
5.	XCP732	20 wt.% of XC73 in 80 wt.% of PVDF
6.	XCP733	30 wt.% of XC73 in 70 wt.% of PVDF
7.	rZP552	20 wt.% of rZ55 in 80 wt.% of PVDF
8.	rZP553	30 wt.% of rZ55 in 70 wt.% of PVDF
9.	rZP372	20 wt.% of rZ37 in 80 wt.% of PVDF
10.	rZP373	30 wt.% of rZ37 in 70 wt.% of PVDF
11.	YMP552	20 wt.% of YM55 in 80 wt.% of PVDF
12.	YMP553	30 wt.% of YM55 in 70 wt.% of PVDF

13.	YMP912	20 wt.% of YM91 in 80 wt.% of PVDF
14.	YMP913	30 wt.% of YM91 in 70 wt.% of PVDF

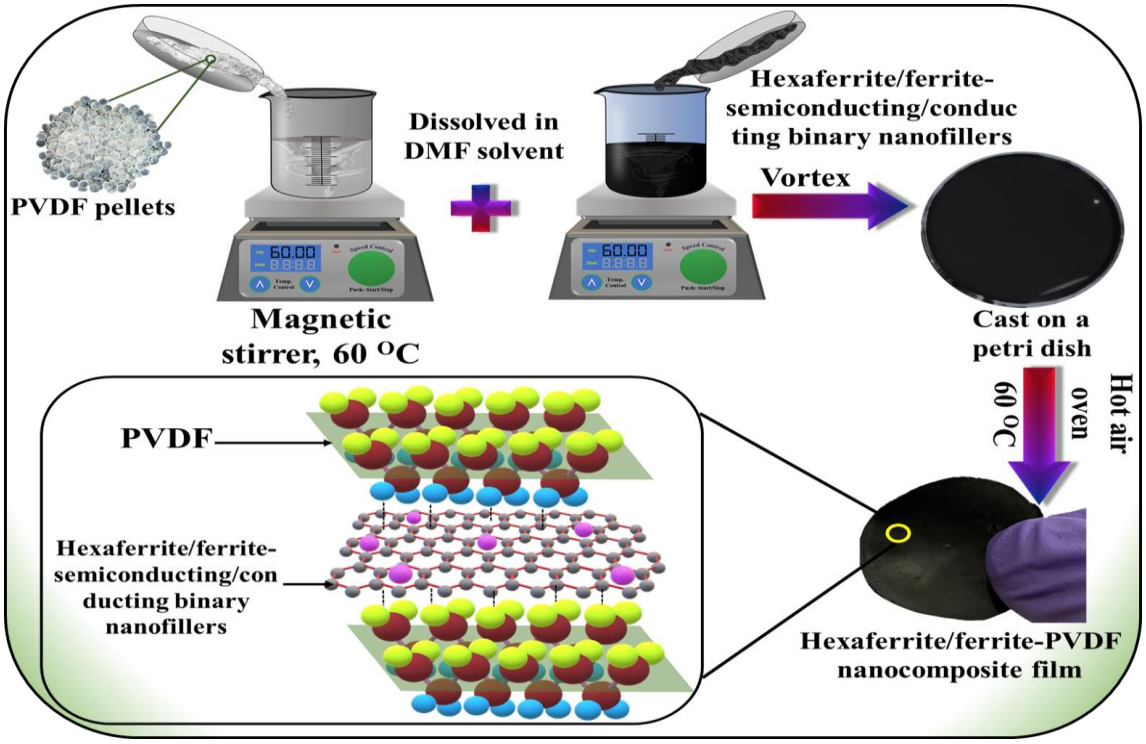

Figure 2.4: Synthesis of binary-hexaferrite-PVDF and binary-spinal ferrite-nanocomposite film by solution casting method.

2.3 Instrumentations:

In experimental research work on the most important part is uses of instruments starting from the synthesis of materials, characterization to fundamental study of the respective field. In this report to study the EMI shielding property of some magnetic fillers incorporated polymer or binary fillers incorporated polymer nanocomposite various type of measurement have been done. The details of the utilized instruments are mentioned in bellow:

2.3.1 Furnace

Muffle furnaces operate using the indirect heating concept, in which the material to be heated

is put inside a separate chamber known as a muffle and the heating sources are located outside the furnace chamber. Usually, a ceramic substance like alumina is used to make the muffle because it is resistant to chemical corrosion and high temperatures. The heating elements in the muffle furnace get an electric current when turning on, which causes them to heat up and radiate heat toward the muffle. A temperature controller regulates the temperature within the muffle by keeping an eye on it and modifying the power given to the heating components as necessary. This guarantees that the material will neither overheat or underheat when heated to the appropriate temperature. When material needs to be heated to temperatures of 1200 °C or more for high-temperature processes including sintering or calcination muffle furnaces are usually utilized. In this report the spinel ferrite (NZCF) and the hexaferrite (Co_2X, Co_2Z, and Co_2Y) nanomaterials sintered at 400 ^{O}C and 1200 ^{O}C respectively.

Figure 2.5: High temperature Muffle furnace.

2.3.2 Thermo Gravimetric Analyzer (TGA) and Differential Scanning Calorimetry (DSC):

The mass los of a sample is determined over time and temperature varies in a thermal analysis technique is called thermogravimetric analysis, or thermal gravimetric analysis (TGA). The measuring phenomena give us the information on both physical and chemical phenomena, such as thermal stability, and solid-gas interactions. Physical phenomena include phase changes, absorption, and desorption. The sample is heated at a controlled rate in a specific atmosphere (air, N_2, Co_2, He, Ar, etc.) for thermogravimetric analysis. The sample's weight variation is noted in relation to temperature and/or time. For a known beginning weight of the substance, the temperature is raised at a fixed pace, and weight variations are recorded as a function of temperature at various intervals. The thermo-gravimetric curve, sometimes known as the thermo-gram, is this plot of weight change versus temperature.

On the other hand, based on the temperature difference between the sample and the reference material, differential scanning calorimetry **(**DSC) estimates the amount of heat that the sample radiates or absorbs excessively during a temperature shift. For the better understanding of melting and crystallization behaviour of the material can be done by Differential Scanning Calorimetry (DSC) study. From this DSC study we have recorded the onset temperature (T_o), peak temperature (T_p), end temperature (T_e) and the enthalpy (ΔH) values of the material. The thermal properties of the materials were recorded using Perkin Elmer 6300 series thermoanalyzer (Perkin Elmer, Waltham, MA, USA).

Figure 2.6: Thermo Gravimetric Analyzer.

2.3.3 X-Ray Diffractometer:

X-ray powder diffraction (XRD) is most useful method to identify the phase of a crystalline material and the providing information related on unit cell dimensions. Also, the X-ray diffraction is used to study the atomic spacing and crystal formations. The incident X-rays interact with the sample to produce constructive interference, when conditions meet Bragg's Law ($n\lambda = 2d \sin\theta$), where, λ stands for incident X-ray wavelength, d stands for the average crystallite size, θ stands for Bragg's angle, which relates the wavelength of the electromagnetic radiation to its diffraction angle and lattice spacing in the crystalline sample. The X-rays are made up of several elements, K_α and K_β are the most common. One of the most common targets for single-crystalline diffraction is copper, the wavelength of CuK_α is 1.5418 Å of D-8 Bruker advanced. Using this X-rays study the individual phase of bare PVDF/PVDF-HFP, all the magnetic nanoparticles (Co_2X, Co_2Z, Co_2Y, and NZCF), conducting nanofillers (C_3N_4, rGO and MoS_2), multiphase nature in binary nanofillers (Co_2X-C_3N_4, Co_2Z-rGO, Co_2Y-MoS_2, and

NZCF-C_3N_4) and in nanocomposite films of Co_2X-PVDF, Co_2U-PVDF, NZCF-C_3N_4-PVDF, Co_2X-C_3N_4-PVDF, Co_2Z-rGO-PVDF, and Co_2Y-MoS_2-PVDF-HFP has been estimated.

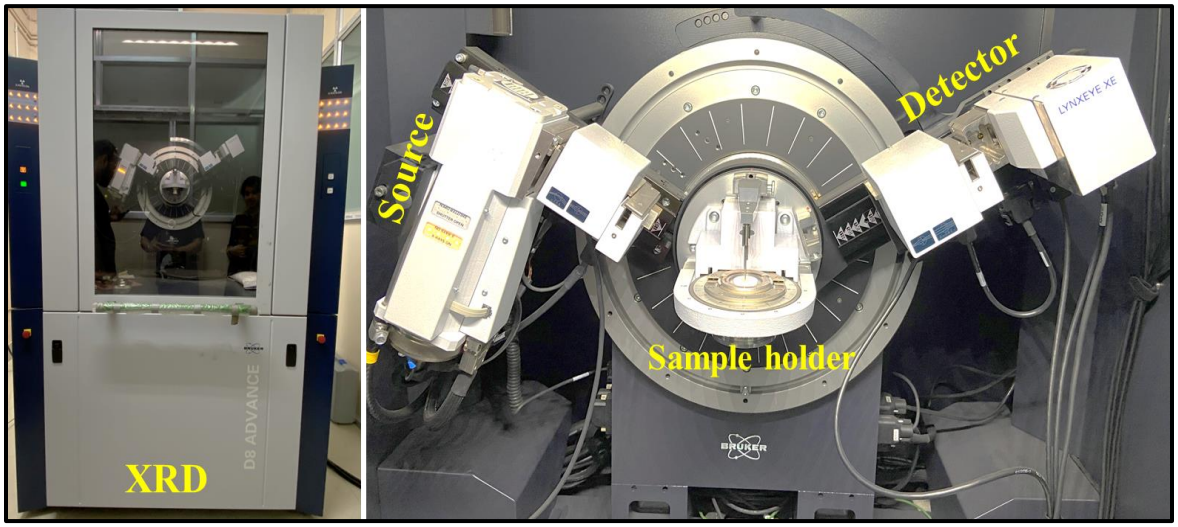

Figure 2.7: X-ray powder diffractometer.

2.3.4 Field Emission Scanning Electron Microscopy (FESEM):

The interaction between the electron beam and specimen, the losses of energy express in terms of various mechanism, such that:

1. Heat energy
2. emission of low-energy secondary electrons
3. high-energy backscattered electrons
4. light emission or X-ray emission.

By using a low-energy electron beam (usually between 1 and 30 keV) to scan the sample's surface and achieve resolutions in the low nanometer range, FESEM produces an image of the material. A picture is created by detecting the backscattered or secondary electrons that are generated when the incident electron beam is traversed across the sample's surface in a raster pattern. In this report using INSPECT-F50 (FEI, Netherland) the surface morphology of the nanoparticles and nanocomposite films has been collected. The EDS and elemental mapping

help to confirm the presence of existing elements inside the nanocomposite film and nanoparticles.

Figure 2.8: Field Emission Scanning Electron Microscopy (FESEM).

2.3.5 High resolution transmission electron microscopy (HR-TEM):

In High resolution transmission electron microscopy (HR-TEM) a positive electrical potential is used to accelerate an electron stream coming from an electron source, commonly referred to as the "Gun," in the direction of the sample. Then, using magnetic lenses known as "condenser lenses" and metal apertures, this stream is concentrated into a narrow, monochromatic beam. A portion of the beam is transmitted through the sample when it collides with it. The investigation of crystallographic phase, surface morphology and the presence of different elements in the nanoparticles have been carried out by the HRTEM analysis. Also, the Selected Area Diffraction (SAED) pattern use to confirms the structure of the nanoparticles and the elemental study (EDX) have been done to confirm the presence of all the elements of the nanoparticles. The HR-TEM study carried out using JEOL JEM 2100 HR, EELS microscope (Japan, accelerating voltage at 80–200 kV).

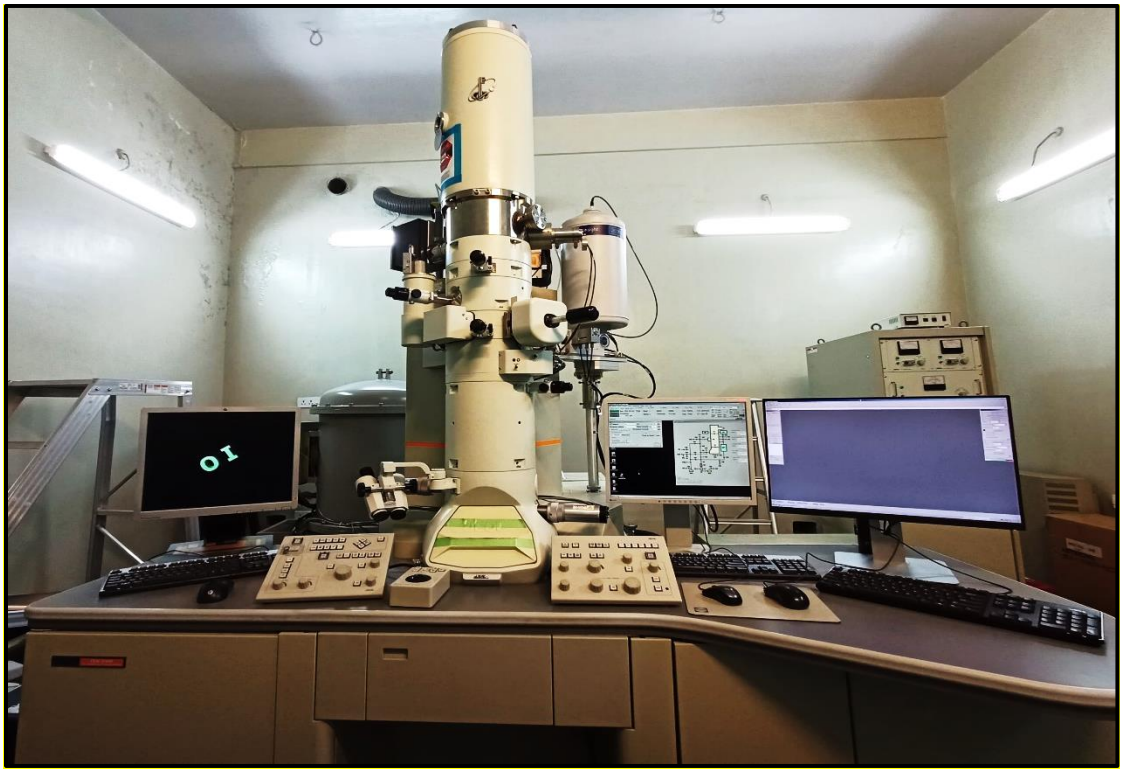

Figure 2.9: High-Resolution Transmission Electron Microscopy (HR-TEM).

2.3.6 Fourier Transform Infrared (FTIR) spectroscopy:

Using a Fourier transform infrared (FTIR) spectrophotometer and bonding network analysis, phase purity at the molecular level was examined. This experiment has been done using Shimadzu Infrared Spectrometer, the IR Affinity 900i. ATR (attenuated total reflectance) was used to perform the measurement where, the nanocomposite films were put over the path of infrared light and the data in a region of 400–1200 cm^{-1} wavenumbers. By this chemical property study, we will try to understand the polarization corresponding to the β-phase of the polymer matrix in the nanocomposite films.

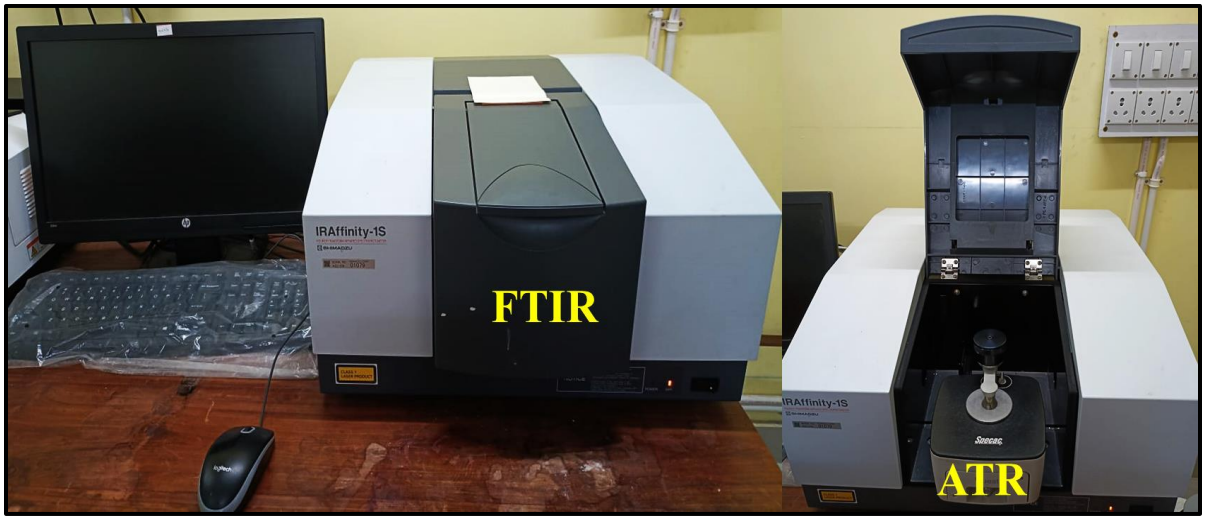

Figure 2.10: Fourier Transform Infrared (FTIR) spectrometer.

2.3.7 X-Ray Photoelectron Spectroscopy (XPS):

The elemental composition of a material, as well as its chemical state, overall electronic structure, and density of electronic states, can all be determined using X-ray photoelectron spectroscopy (XPS), a surface-sensitive quantitative spectroscopic method based on the photoelectric effect. The number of electrons found at a certain binding energy is plotted in an XPS spectrum. There are distinct XPS peaks produced by each element. The electron configurations of the individual atoms, such as 1s, 2s, 2p, 3s, etc., are represented by these peaks. Within the XPS sampling volume, the quantity of each element is precisely proportional to the number of electrons observed in each peak. A minimum of 10 to 200 micrometers can be used for data analysis and the maximum size of an X-ray monochromatic beam is 1-2 mm. Beams that are not monochromatic range in diameter from 10 to 50 mm.

Figure 2.11: X-Ray Photoelectron Spectrometer.

2.3.8 RAMAN Spectrometer:

An effective method for analyzing molecular structure is Raman spectroscopy, which is thought to be a supplement to infrared spectroscopy. Raman spectroscopy is working based on the Raman effect. The basis for the Raman effect is light scattering, which can be caused by molecular vibrations at various wavelengths or by elastic (Rayleigh) scattering at the same wavelength as the input light. Approximately a million times less strong than Rayleigh scattering is Raman scattering. Consequently, it is essential to keep Rayleigh scattering from outweighing the weaker Raman scattering in order to acquire Raman spectra. Using a high-intensity laser beam to excite a sample and then passing the scattered light via a spectrometer is how Raman spectra are determined. To find the spectroscopy band of conducting rGO, the Raman spectroscopy have been used.

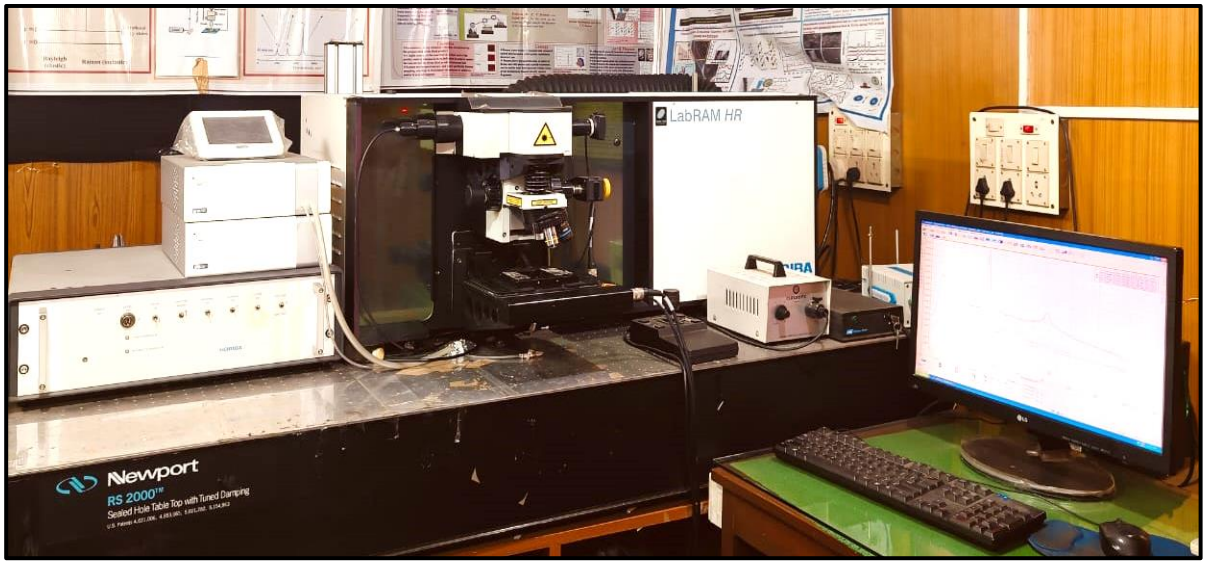

Figure 2.12: RAMAN Spectrometer.

2.3.9 Source measurement unit (Study of I-V characteristics)

Important quantities in an electrical network are electrical voltage and current. Since current cannot exist without voltage, voltage is the effort variable. An electrical circuit element or circuit branch is used to measure it. Voltmeter: The instrument that measures voltage. The net motion of charged particles (ions in a liquid, electrons in a solid) in a certain direction is represented by the flow variable called current. Instantaneous electrical power is obtained by multiplying the two. Impedance is defined as the voltage divided by current. It is an ammeter, sometimes known as an ammeter, that measures current. The current in the load is measured by connecting ammeters in series with it. The current must eventually be broken by the ammeters. To measure the I-V characteristics and J-E study followed by the I-V data Keithley 2450 Source measurement unit have been used.

Figure 2.13: Source measurement unit.

2.3.10 4-probe LCR meter (Study of dielectric property):

The capacity of a sample to store charge is reflected in its dielectric characteristic. The size of grain, temperature, humidity, the frequency of the external electric field etc. factors plays a significant role to modulate the dielectric property of a material. There are two functions that make up the total dielectric permittivity such as, real part of dielectric permittivity (ε′) and the imaginary part of dielectric permittivity (ε″). The real part shows the charge storage capacity and the imaginary part suggests the electrical dissipation factor. To study the dielectric property of the material 4294A Precision Impedance Analyzer has been used.

Figure 2.14: 4-probe LCR meter.

2.3.11 The Superconducting Quantum Interference Device (SQUID)/ Vibrating Sample Magnetometry (VSM):

The superconducting quantum interference device (SQUID) is made up of two parallel Josephson junctions formed by two superconductors that are separated by thin insulating layers. To detect extremely small magnetic fields, the gadget is set up as a magnetometer. The pick-up coil experiences an alternating magnetic flux as a result of the sample being moved up and down. A superconducting pick-up coil with four windings is used to obtain the sample's magnetic signal. To study the magnetic response of the material MPMS XL 7, Quantum Design SQUID has been used.

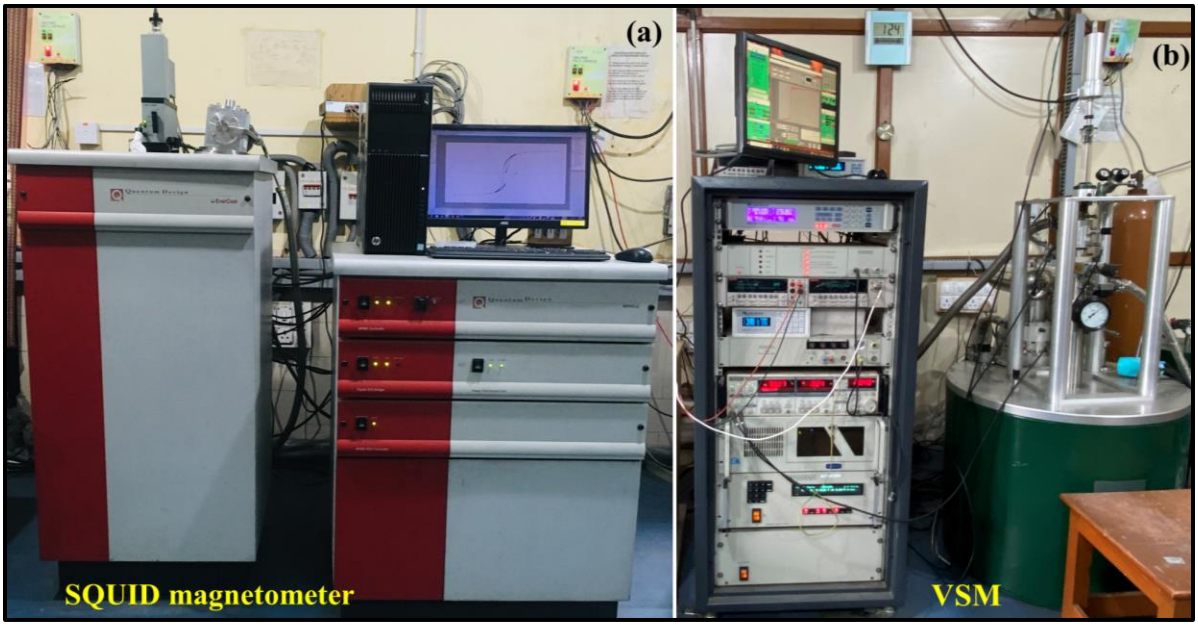

Figure 2.15: (a) The Superconducting Quantum Interference Device (SQUID) and (b) Vibrating Sample Magnetometry (VSM)

2.3.12 Vector Network Analyser (VNA):

Using Vector Network Analyser (VNA) both the amplitude and phase of the signal can be measured simultaneously. Their capacity to offer a thorough examination of intricate networks renders them indispensable in the creation, advancement, and upkeep of radiofrequency and microwave elements and structures. The transmission and reflection of RF signals is the fundamental function of a vector network analyzer. A test signal is sent via the device under test (DUT) by the analyzer, which then measures the signals at different frequencies that are reflected and transmitted. Important factors like the scattering parameters (S-parameters), which characterize the DUT's behavior in terms of reflection, transmission, and impedance, may be computed by the VNA by comparing the input and output signals. The shielding effectiveness of the nanocomposite films was measured by using Agilent E8363B PNA series Network Analyzer in the frequency range 8-12 GHz (X-band) and 12-18 GHz (K_u-band).

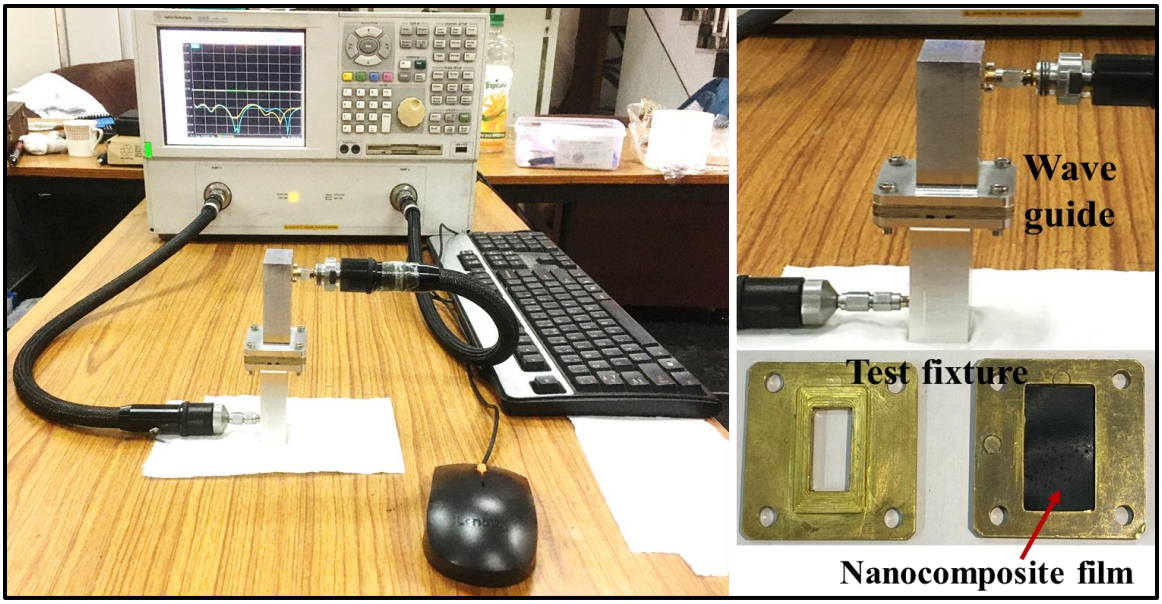

Figure 2.16: Vector Network Analyser.

2.4 References:

1. P. Saha, T. Debnath, S. Das, S. Chatterjee, and S. Sutradhar, Mater. Sci. and Eng.: B. **245**, 17-29 (2019).

2. G. Krauss, in Encyclopedia of Materials: Science and Technology (2001)

3. R. C. Pullar, Progress in Materials Science 57(7) 1191-1334 (2012).

4. Y. Zhang, Qiwen Pan, Guanqi Chai, Jianrong Qiu, 2013 Scientific Reports 3(1) (1943)

5. W. S. Jr. Hummers, R. E. Offeman, American Chemical Society 80(6) 1339 (1958).

6. L. Vieira, J. de R. M, Neto, O. P. Ferreira, R. M. Torresi, S. I. C. de Torresi, O. L. Alves, RSC Adv., 8, 30346-30353 (2018)

7. Mohan Lal Meena, Sudipta Som, Chung-Hsin Lu, Ranveer Singh Badgoti, Somrita Dutta, Rajan Kumar Singh, Shawn D. Lin , Hendrik C. Swart, Metal Oxide-Based Heterostructures Fabrication and Applications, Metal Oxides, 297-330 (2023)

8. Sutradhar S., Saha P., Chowdhury A. and Das S., Materials Research Express, 6(8), p.086424 (2019).

Chapter: 3

EMI shielding study of magnetic hexaferrite-PVDF laminated nanocomposite system to combat against electromagnetic pollution

Chapter 3:

3.1 Introduction:

The increasing usage of smartphones and other electronic devices increases the risk of several negative consequences on plant, animal, and human life. Silent and unseen EM pollution permeates our environment, affecting our brain and body. The overuse of numerous electronic devices, including FM radios, microwaves, cell phones, wireless LANs, Bluetooth, GPS, RADAR, and others in the microwave (MW) frequency range (300 MHz to 300 GHz), is causing this kind of pollution to appear in our surroundings [1, 2]. The detrimental impact of electromagnetic (EM) pollution is what causes a number of really problematic issues for living beings [3-7]. Here, in this study, the prime attention is given to identify potential possibilities to fix this issue. An attempt has been made to create an improved composite material with significant electromagnetic interference and EM pollution EMI shielding efficiency at microwave (MW) and radio frequency (RF) ranges. To control the exposer of EM radiation different types of magnetic nanofillers with proper domain size, magnetic moment, and weight percentage can be selected as the component materials. It is expected that, the hexagonal ferrite materials can be the most suitable component to get large magnetic loss factor from the laminated nanocomposite films [8,9]. In light of this, we have chosen to work with $Co_2U(Ba_4Co_2Fe_{36}O_{60})$ and $Co_2X(Ba_2Co_2Fe_{28}O_{46})$-hexaferrite. In addition to having a high magnetic moment at room temperature (RT), these Co_2U and Co_2X-hexaferrites are suitable for a wide range of applications involving electromagnetic radiation in the RF and MW region [9]. On the other hand, polar β-phase enriched Poly (vinylidene fluoride) (PVDF) matrix, which is a well know piezoelectric material, was chosen to impart additional dielectric permittivity to the nanocomposite films [10]. By interacting with the EM wave's electric field vector in the RF/MW region, the resulting nanocomposite systems' additional dielectric permittivity

enhances the overall dielectric loss effect. Also, the incorporation of PVDF giving a light weight, flexible and free-standing nature to the nanocomposite film that helps to conduct all the measurements without using any additional support (holder) to the nanocomposite films during measurement.

3.2 Experimental:

3.2.1 Materials:

The required chemicals to synthesize Co_2U and Co_2X-hexaferrite are barium (II) nitrate $Ba(NO_3)_2$ (Merck Germany, 99%), cobalt (II) nitrate $Co(NO_3)2$, iron (III) nitrate nonahydrate $Fe(NO_3)_3.9H_2O$ (Merck Germany, 99%), citric acid ($C_6H_8O_7$), and ethyl alcohol (C_2H_5OH). After prepared Co_2U and Co_2X-hexaferrite to get the Co_2U and Co_2X-hexaferrite-PVDF nanocomposite films poly(vinylidene fluoride) pellets (molecular weight Mw: 275,000 (hpc), Mn: 107,000, Aldrich, Germany), N,N-dimethyl formamide (DMF) (Merck, India have been used.

3.2.2 Synthesis of Co_2U- and Co_2X-hexaferrite:

Synthesis of Co_2U and Co_2X-hexaferrite with the stoichiometry ration of $Ba_4Co_2Fe_{36}O_{60}$ and $Ba_2Co_2Fe_{28}O_{46}$ has been done using simple sol-gel method. The details of the synthesis procedure have already been discussed in chapter 2 (**Section: 2.2.1** Synthesis of magnetic hexaferrite and ferrite nanoparticles by sol-gel method). After collecting the as prepared Co_2U and Co_2X-hexaferrite by sol-gel method, Co_2U-hexaferrite was annealed at 1400 °C and Co_2X-hexaferrite was annealed at 1200 °C in a hot air oven to get the proper crystallographic phase.

3.2.3 Synthesis of Co_2U- and Co_2X-hexaferrite-PVDF nanocomposite films:

To get the flexible, free-standing Co_2U and Co_2X-hexaferrite-PVDF nanocomposite films, cost effective solution casting method have been used. The detailed process of solution casting method is mentioned in chapter 2: (**Section: 2.2.2.5** Synthesis of nanofillers-polymer

nanocomposite film by solution casting method). The prepared UP1410, UP1420, XP1210, XP1215, and XP1220 nanocomposite films are cut into proper dimensions to conduct all the measurement.

3.2.4 Formation mechanism of Co_2U- and Co_2X-hexaferrite-PVDF nanocomposite films:

Figure 3.1 shows the structural mechanism of the Co_2U and Co_2X-hexaferrite-PVDF nanocomposite films. As previously indicated, solution casting was used to create the Co_2U and Co_2X-hexaferrite-PVDF nanocomposite films and Co_2U and Co_2X-hexaferrite, that were created using the sol–gel method. The presence of c-axis and c-plane anisotropy results in the creation of a suitable material for microwave absorption [11]. The Co_2U and Co_2X-hexaferrite unit cell is comprised of three layers or blocks namely the R-block which has the most significant hexagonal geometry consisting of the barium ions and two oxygen layers, the S-block, or the spinel geometry and lastly the T-block having the hexagonal geometry [9]. The β-phase PVDF (Polyvinylidene Fluoride) in an all-trans (TTTT) zigzag conflict form the basis of the X-type hexaferrite-PVDF nanocomposite. The CH_2 group has a positively charged hydrogen atom as a result of their differing electronegativity. The total negative surface charge of X-type hexaferrites interacts with this positively charged hydrogen atom. Co_2U and Co_2X-hexaferrite-PVDF nanocomposite films are formed when the hexaferrite binds to the PVDF matrix, forming a sandwich-like structure and this process is caused by electrostatic contact [12].

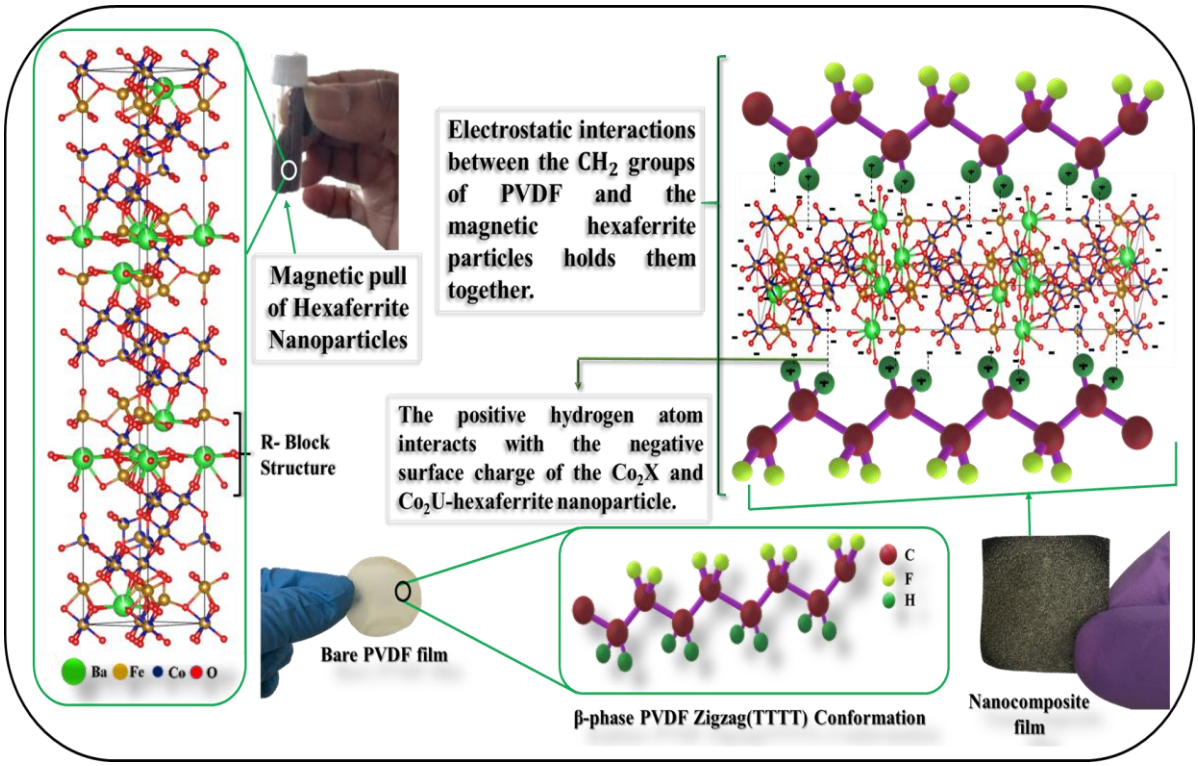

Figure 3.1: Formation mechanism of hexaferrite-PVDF nanocomposite films.

3.3 Result and Discussions

3.3.1 Crystallographic phase analysis:

Development of the crystallographic phases of Co_2U and Co_2X-hexaferrite calculated from the profile fitting that the Co_2U and Co_2X-hexaferrite has a hexagonal structure with a space group configuration of R-3 m:H [9]. The XRD has been observed for Co_2U and Co_2X-hexaferrite as well as UP1410, UP1420, XP1210, XP1215, XP1220 nanocomposite films and bare PVDF by using X-ray diffractograms and the corresponding images were depicted in Figure 3.2(a-f). The corresponding phases of getting from XRD analysis were confirmed from the JCPDS file. Co_2U and Co_2X-hexaferrite are basically the mixed phase of Co_2U = Co_2Z+Co_2M and Co_2X = Co_2W+Co_2M-hexaferrite, which are also significantly matched and we have observed a well-defined crystalline XRD pattern [9]. The average crystallite diameter of Co_2U and Co_2X-hexaferrite were calculated using the Debye-Scherrer equation from the broadening of 100%

intense XRD peak [13]

$$< D >= \frac{0.9\lambda}{\beta_{\frac{1}{2}}\cos\theta} \tag{3.1}$$

Here, D stands for the average crystallite size, λ stands for incident X-ray wavelength, θ stands for Bragg's angle for the peak (114) and $\beta_{\frac{1}{2}}$ stands forfull width at half maximum (FWHM). The average crystallite diameter of ~ 30 nm and 33 nm for Co_2U and Co_2X-hexaferrite has been observed in the XRD analysis, respectively. From Figure 3.2(a-f) it is quite clear that the different peaks corresponding to the combined phases of PVDF and Co_2U and Co_2X-hexaferrite present in UP1410, UP1420, XP1210, XP1215, and XP1220 nanocomposite films have been matched very well with the actual crystallographic phase of the respective components. As compare to bare PVDF, in case nanocomposite films it has been clearly visible that the polar phases such as β and γ-phase are quite prominent and the non-polar α-phase getting suppressed. This has also developed a large interfacial area between the hexaferrite and PVDF, which leads to the formation of the polymer chains with zigzag (TTTT) conformation [14]. This polymorph of PVDF improves the electroactivity of the PVDF matrix in the nanocomposite films (UP1410, UP1420, XP1210, XP1215 and XP1220) and it makes the nanocomposite films the most potential one for the magnetodielectric as well as shielding effectiveness applications [14, 15]. At the same time none of the given XRD patterns consist of any impurity phases other than the required phases of the component materials. This observation also signifies the coexistence of both the phases of PVDF, Co_2U and Co_2X-hexaferrite in each of the nanocomposite films (UP1410, UP1420, XP1210, XP1215, and XP1220) which is the signature pattern of any multi-phase nanocomposite material. Thus, all the nanocomposite films (UP1410, UP1420, XP1210, XP1215, and XP1220) reported in this study are multi-phase in nature.

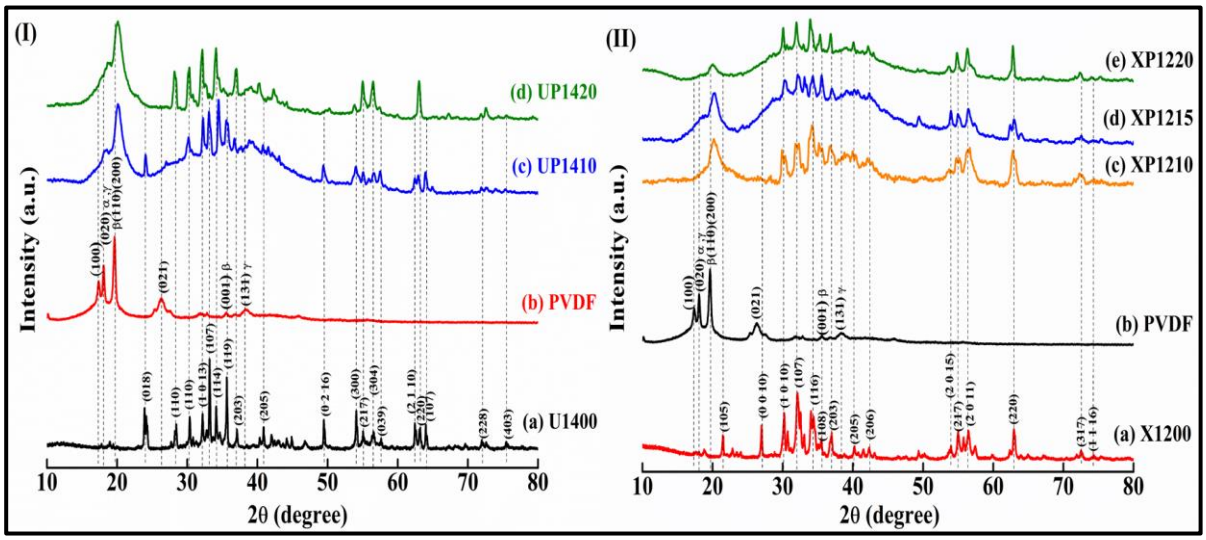

Figure 3.2: XRD patterns of (I)(a) PVDF, (b) UP1410, (c) UP1420, (II) (a) X1200, (b) PVDF, (c) XP1210, (e) XP1215, and (f) XP1220 nanocomposite films.

3.3.2 Study of surface morphology:

The surface morphology of the nanocomposite films (UP1410, UP1420, XP1210, XP1215, and XP1220) illustrated using FESEM analysis. Figure 3.3(a-j) represent the microstructural images of the PVDF, UP1410, UP1420, XP1210, XP1215, and XP1220 nanocomposite films. The spherulite bubble like structures has been observed for UP1410, UP1420, XP1210, XP1215, and XP1220 nanocomposite films, demonstrating their enhanced β-phase crystallization as a result of the Co_2U and Co_2X-hexaferrite being inserted into PVDF. It is also not possible to totally rule out the possibility of PVDF matrix α-phase present in the nanocomposite films [16]. Figure 3.3(a-j) clearly illustrates the existence and dispersion of Co_2U and Co_2X-hexaferrite within the PVDF matrix. The large-scale bubble-like structure found in nanocomposite films is an obvious. The creation of bigger polymer chains with zigzag (TTTT) conformation in nanocomposite films is the reason for the large size bubble-like structure, which is a clear sign of a larger fraction of β-phase crystallization of the PVDF matrix [17]. Furthermore, it is evident from this microstructural analysis that nearly all of the surfaces of the nanocomposite films

have bubbles similar to spherulite structures. Thus, all of the nanocomposite films (UP1410, UP1420, XP1210, XP1215, and XP1220) with bubble-like spherulite structures are significantly enhanced with electroactive nature, according to the FESEM analysis. Therefore, the PVDF matrix's enhanced β-phase crystallization and increased abundance in a wider range of surfaces inside the nanocomposite films make them the most promising candidate for different applications in the RF/MW frequency range. Figure 3.3(k, l) depicted the elemental mapping of the nanocomposite films, which prove the presences of all the elements (Ba, Co, Fe, F, C and O) in the nanocomposite films and distributed uniformly all around.

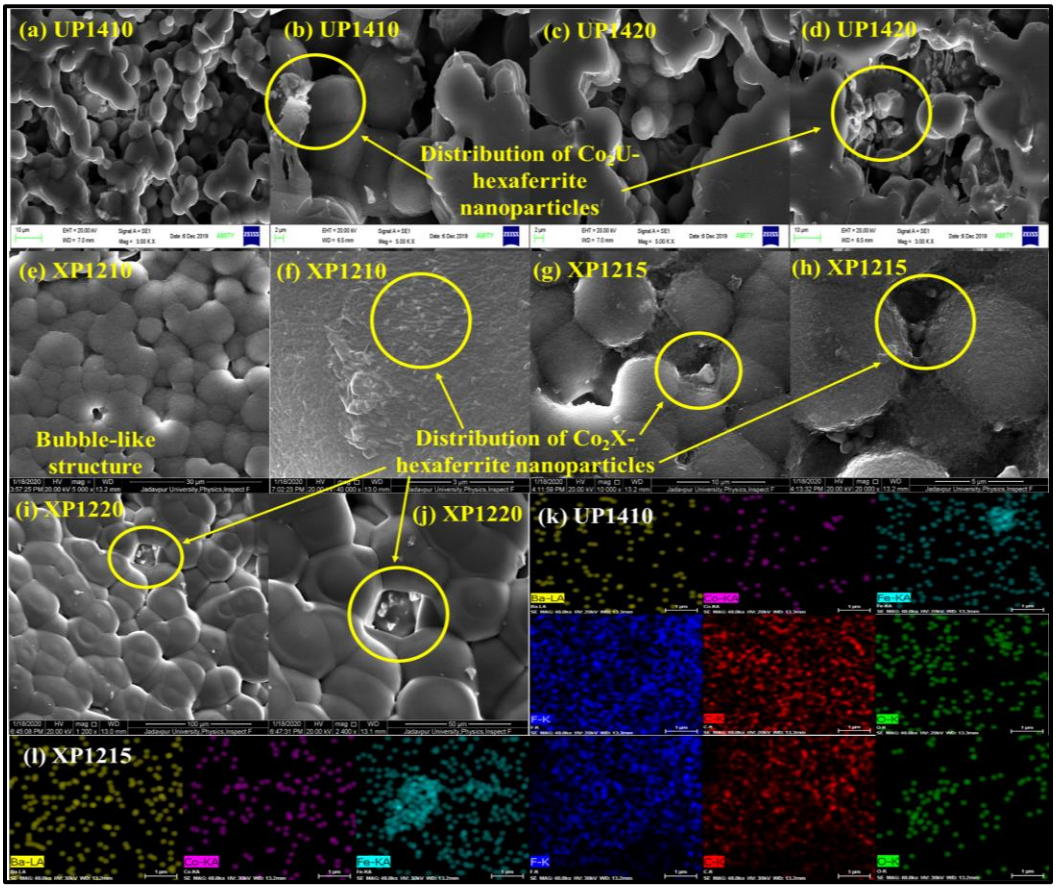

Figure 3.3: FESEM micrographs of (a, b) UP1410, (c, d) UP1420, (e, f) XP1210, (g, h) XP1215 and (i, j) XP1220 nanocomposite films and Elemental mapping image of (k) UP1410, and (l) XP1215 nanocomposite films.

3.3.3 HR-TEM analysis:

The HR-TEM analysis was used to examine the crystallographic phase, surface shape, and presence of various elements in the Co_2X-hexaferrite. The corresponding micrographs are shown in Figure 3.4(a-h). In the micrograph, the size of the Co_2X-hexaferrite has been approximated. A single hexaferrite has also yielded the selected area diffraction pattern (SAED), and the matching image. Furthermore, the hexagonal structure of the Co_2X-hexaferrite is confirmed by the SAED pattern [18]. The crystalline structure of the Co_2X-hexaferrite observed from the HR-TEM micrographs. The fringe pattern of the crystalline material indicates that the hexaferrites are structurally homogeneous with the corresponding group of atomic planes as shown in Figure 3.4(c, d). The fast Fourier transform (FFT) pattern of Co_2X-hexaferrite represent the perfect alignment of the planes in a specific direction that has been observed from Figure 3.4(e, f) [19]. Thus, the Co_2X-hexaferrite crystalline structure exhibits a noticeable periodicity. The EDX spectra confirms the presence of Ba, Co, Fe, and O in the Co_2X-hexaferrite shown if Figure 3.4(h).

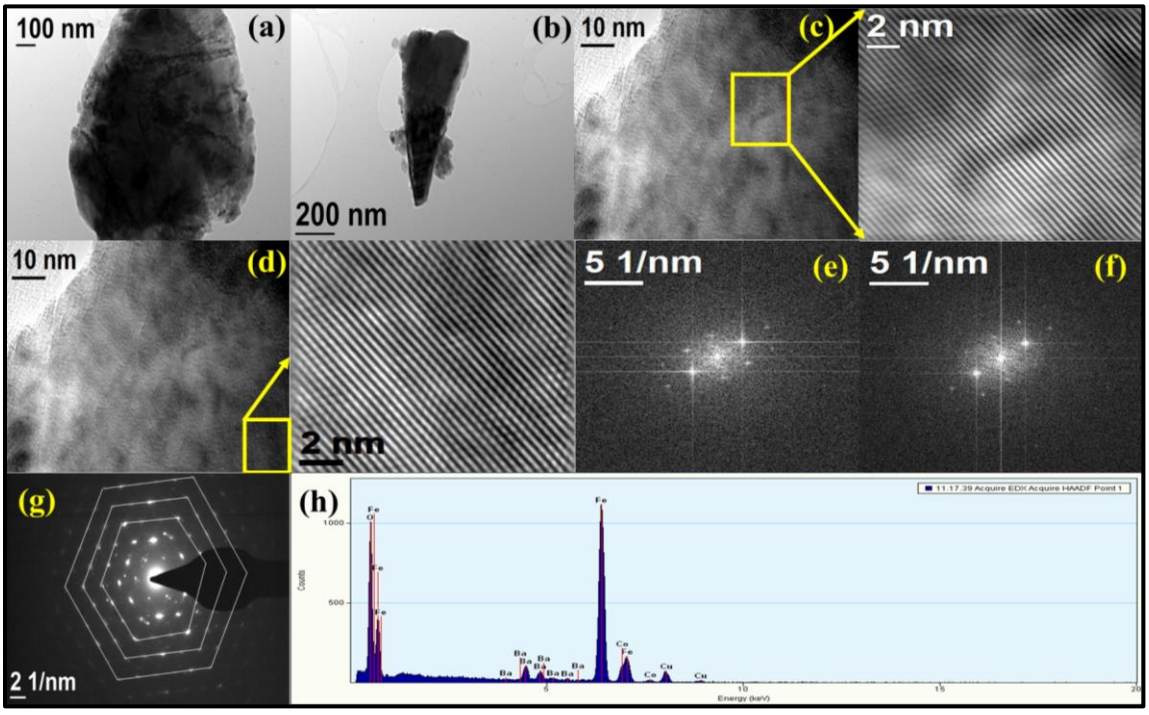

Figure 3.4: (a, b) HR-TEM image, (c, d) fringe pattern, (e-g) FFT pattern and (h) EDX study of Co_2X-type hexaferrite.

3.3.4 Thermal property study:

The thermogravimetric analysis (TGA) and differential scanning calorimetry (DSC) analysis have been used to evaluate the thermal stability of bare PVDF, UP1410, UP1420, XP1210, XP1215, and XP1220 nanocomposite films are shown in Figure 3.5(a). From TGA data, it has been noticed that the bare PVDF began to degrade earlier as compared to other nanocomposite films. This may happen due to the presence of Co_2U and Co_2X-hexaferrite inside the PVDF matrix. Also, the thermal stability of the nanocomposite films increases with the increase of wt.% of Co_2U and Co_2X-hexaferrite inside the PVDF matrix and it has been observed that in the case of nanocomposite films, the presence of surface electrostatic charge in the Co_2U and Co_2X-hexaferrite significantly enhances the β content with the decreasing α content. These mostly affect the UP1410, UP1420, XP1210, XP1215, and XP1220 nanocomposite films to get thermal stability [20].

On the other hand, Differential Scanning Calorimetry (DSC) studies can be used to gain a better knowledge of the melting and crystallization behavior of bare PVDF and Co_2X-PVDF nanocomposite. The DSC curves for PVDF, XP1210, XP1215, and XP1220 nanocomposite films are shown in Figure 3.5(b-e). Using the TGA data and a temperature in the range of 30 to 550 ^oC, a first-order differential computation was used to conduct to get the DSC data. The onset temperature (T_o), peak temperature (T_p), end temperature (T_e), and enthalpy (ΔH) values of PVDF, XP1210, XP1215, and XP1220 nanocomposite films observed from this DSC analysis. Here, it is evident that, in comparison to naked PVDF film, the melting point increased as the loading percentage of Co_2X-hexaferrite within the PVDF matrix has increased. However, the enthalpy (ΔH) readings has fallen simultaneously. Therefore, the presence of

nanocrystalline domains inside the crystallized nanocomposite and the morphological variations in the crystalline phase of nanocomposite XP1210, XP1215, and XP1220 films may be the cause of this change in enthalpy (ΔH) values [21]. The enthalpy data has been given in Table 3.1.

Table 3.1: DSC characteristic data of the nanocomposite films.

Sl. No.	Sample name	Onset Temperature (T_o) ^OC	Peak Temperature (T_p) ^OC	End Temperature (T_e) ^OC	Enthalpy (ΔH) J/g
1.	**PVDF**	415.93	437.22	454.34	13.52
2.	XP1210	425.15	444.68	456.59	9.20
3.	XP1215	443.28	459.96	473.58	8.40
4.	XP1220	436.10	455.72	468.60	8.14

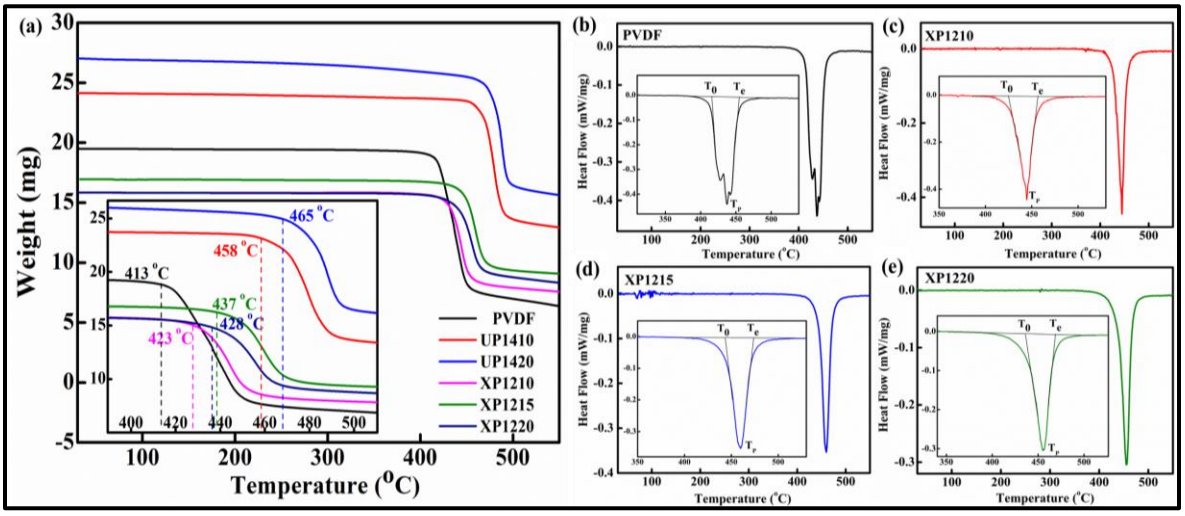

Figure 3.5: (a) TGA and DSC characteristic of (b) bare PVDF, (c) XP1210, (d) XP1215 and (e) XP1220 nanocomposite films

3.3.5 Chemical property study:

The chemical property study has been studied to understand how much polarization corresponding to the β-phase of the PVDF matrix in the nanocomposite films has been enhanced as compared to PVDF system. In this study, the IR spectra of all the nanocomposite films (PVDF, UP1410, UP1420, XP1210, XP1215, and XP1220) were measured and the various absorption bands of nonpolar α-phase and the polar β-phase of the host PVDF system have been recognized. The IR absorption spectra of nanocomposite films (PVDF, UP1410, UP1420, XP1210, XP1215, and XP1220) have been displayed in the Figure 3.6(I) and the details of corresponding absorption spectra has been mention in Table 3.2 [22, 23]. The β-phase fraction (F(β)%) of PVDF system and nanocomposite films have been done by using Lambert-Beer law and the values are displayed in the Figure 3.6(II) [24].

$$F(\beta) = \frac{A_\beta}{\left(\frac{K_\beta}{K_\alpha}\right)A_\alpha + A_\beta} \quad (3.2)$$

Here A_α and A_β are the absorbance at 773 cm^{-1} and 847 cm^{-1}, respectively, and K_α (6.1×10^4 cm^2mol^{-1}) and K_β (7.7×10^4 $cm^2.mol^{-1}$) are the absorption coefficients at their respective wavenumbers. the improvement of the β-phase of the nanocomposite films in comparison to the bare PVDF due the presence of electrostatic attraction between the negative surface charge of Co_2U and Co_2X-hexaferrite and the CH_2 groups of PVDF matrix. Due to this electrostatic attraction the effective amount of aligned chains inside the PVDF matrix having zigzag (TTTT) conformation has been enriched and it improves the *(F(β)%)* from 42% for PVDF system to the maximum of 46.5% for XP1215 and 45% for UP1210 nanocomposite films. Also, it has been observed that the *(F(β)%)* has been reduced due to further incorporation of the Co_2U and Co_2X-hexaferrite in the matrix of PVDF. The *(F(β)%)* has been reduced when the wt.% of Co_2U and Co_2X-hexaferrite is 20 wt.% inside the PVDF matrix. This phenomenon may be appeared due

to the restraint of the movement of elongation of the polymer chains in zigzag (TTTT) conformation for further loading of Co_2U and Co_2X-hexaferrite from 15 wt.% to 20 wt.% inside PVDF, which in turn reduces the β-phase crystallization in the nanocomposite films [24].

Table 3.2: FTIR peaks and corresponding data of bare PVDF, UP1410, UP1420, XP1210, XP1215, and XP1220 nanocomposite films

Sl. No.	Sample name	α-phase (cm^{-1})	β-phase (cm^{-1})	*(F(β)%)*
1.	**PVDF**	495 (CF_2 waging)	522 (CF_2 stretching)	42
		537 (CF_2 bending)	605 (CF_2 waging)	
		619 (CF_2 bending)	845 (CH_2 rocking, CF_2 stretching and skeletal C-C stretching)	
		771 (CF_2 skeletal bending)	1083 (CH_2 and CF_2 groups generated from the CH_2 rocking and CF_2 stretching)	
		801 (CH_2 rocking)		
		897 (CH_2 rocking)		
		980 (CH_2 rocking)		
2.	UP1410	same as above	same as above	45
3.	UP1420	same as above	same as above	44.6
4.	XP1210	same as above	same as above	46.2
5.	XP1215	same as above	same as above	46.5
6.	XP1220	same as above	same as above	42.5

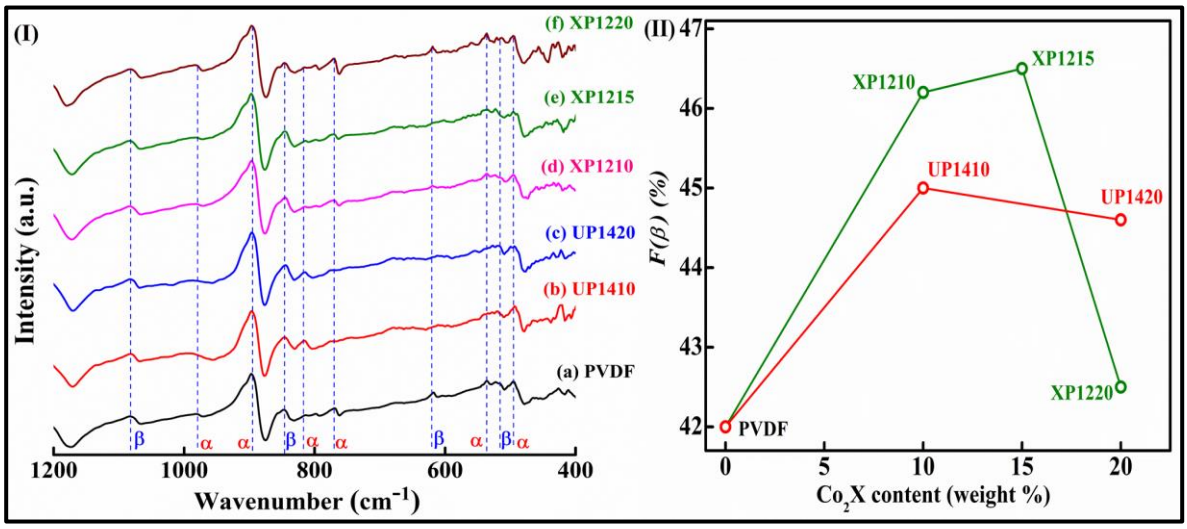

Figure 3.6: (I) FTIR spectra and (II) variation of *F(β)%* for (a) bare PVDF, (b) UP1410, (c) UP1420, (d) XP1210, (e) XP1215, and (f) XP1220 nanocomposite films.

3.3.6 Study of DC conductivity:

The electrical conductivity of the material has an impact on the EMI shielding study [25]. For a specific EMI shielding efficiency characteristic, conducting materials are typically employed for high reflection (SE_R) at the expense of absorption (SE_A) [25]. Here, for high absorption over reflection which is the primary goal of this study. The uses of Co_2U and Co_2X-hexaferrite-PVDF nanocomposite films to get better absorption property which is the main objective of this study. So, the enhancement of absorption (SE_A) in EMI shielding study we have used PVDF as a nonconducting polar polymer material and the Co_2U and Co_2X-hexaferrite are successfully encapsulated inside the matrix of PVDF to improve further the magnetic permeability and polarization loss. Now, to understand the electrical behaviour of the resultant Co_2X-hexaferrite-PVDF nanocomposite film (XP1215) we have attached current (I) vs. voltage (V) graph displayed in Figure 3.7. The nonlinear nature of the I-V characteristic in each case with very low magnitude of current confirms the nonconducting nature of the resultant nanocomposite film [26]. Therefore, this nonconducting nature of the resultant nanocomposite film plays the

most significant role for high EMI shielding effectiveness due to the absorption (SE_A) over EMI shielding effectiveness due to the reflection (SE_R).

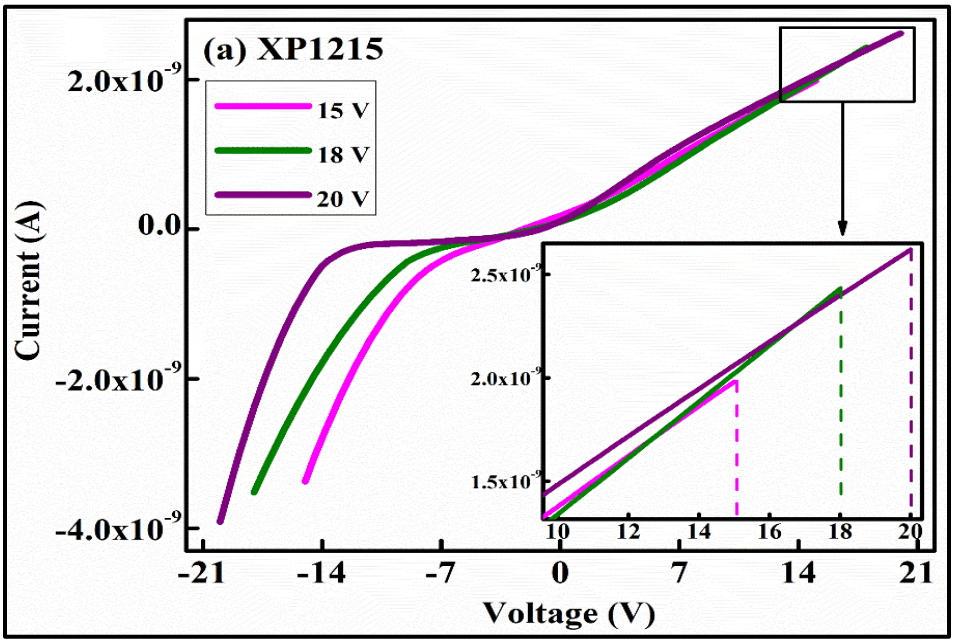

Figure 3.7: I-V characteristic of XP1215 nanocomposite films

3.3.7 Magnetic property study:

A static magnetic study of Co_2U and Co_2X-hexaferrite-PVDF nanocomposite has been performed at room temperature (300 K) with an applied magnetic field of 50000 Oe. This static magnetic study has been considered in this report to understand the presence of magnetic ordering in the nanocomposite films. The room temperature M-H loops of UP1410, UP1420, XP1215, and XP1220 nanocomposite films are displayed in Figure 3.8(I and II). The magnetic parameters such as magnetisation (M_m), high coercive field (H_c) and remanence magnetisation (M_r) of UP1410, UP1420, XP1215, and XP1220 nanocomposite films represent the presence of ferromagnetic nature of the nanocomposite films and the respective parameters mentioned in Table 3.3. With the increasing loading percentage of the Co_2U and Co_2X-hexaferrite inside the matrix of PVDF, the values of magnetization and coercivity of the composite materials have been increased. The values of maximum magnetization (M_m) of UP1410, UP1420, XP1215,

and XP1220 nanocomposite films. Thus, each of these UP1410, UP1420, XP1215, and XP1220 nanocomposite films with sufficiently high magnetisation (M_m), coercive field (H_c) and remanence magnetisation (M_r) can be considered the most potential materials for the specific application in the EMI shielding study.

Table 3.3: Various magnetic parameters of UP1410, UP1420, XP1215, and XP1220 nanocomposite films.

Sl. No.	Sample name	M_m (emu/g)	Hc (Oe)	Mr (emu/g)
1.	UP1410	7.21	1836	3.25
2.	UP1420	10.63	2026	5.24
3.	XP1215	9.7	1902	4.6
4.	XP1220	13.5	1979	6.2

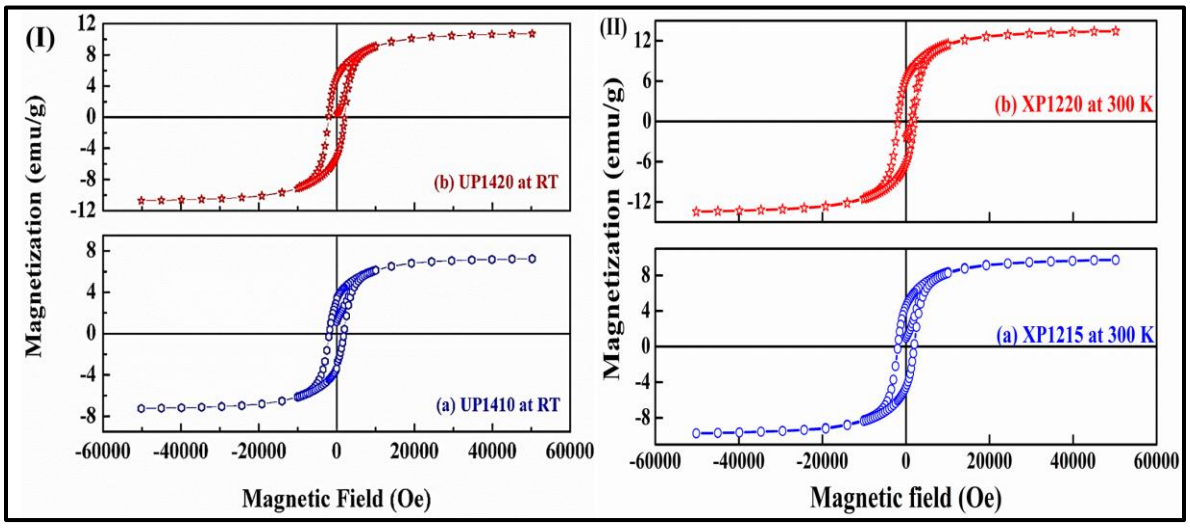

Figure 3.8: Static magnetic loops of (I) (a) UP1410, (b) UP1420, (II) (a) XP1220 and (b) XP1215 nanocomposite films at RT.

3.3.8 Dielectric response study:

The study of a dielectric response and the determination of complex dielectric permittivity is an important and integrated part for the study of the magneto-dielectric effect of the nanocomposite films. The dielectric response study and the determination of various dielectric parameters such as real dielectric permittivity (ε′), the imaginary dielectric permittivity (ε″), tangent loss (tanδ) factor and the ac conductivity (σ_{ac}) of the nanocomposite films. The value of both ε′ and ε″ of UP1410, UP1420, XP1210, XP1215, XP1220 and bare PVDF nanocomposite films have been calculated in the frequency range 40 Hz to 10^6 Hz using the equations [27]

$$\varepsilon' = \frac{Cd}{\varepsilon_0 A} \tag{3.3}$$

$$\text{and } \varepsilon'' = \varepsilon' \times tan\delta \tag{3.4}$$

Here, C stands for capacitance of UP1410, UP1420, XP1210, XP1215, XP1220 and bare PVDF nanocomposite films at applied frequency, d and A stand for thickness and area of each nanocomposite films and ε_0 stands for dielectric permittivity of free space. Usually, the frequency dependent dielectric permittivity of the PVDF based nanocomposite films can be explained by two major phenomena such as the improvement of electroactive β-phase crystallization of nanofillers-PVDF nanocomposite films and the second one is the Maxwell-Wagner-Sillers interfacial polarization effect [28-31]. In this synthesis procedure (the solution casting method, also known as doctor's blade method) the formation of space charge polarization and other types of polarization components at the interfaces inside the nanocomposite films are responsible for the variation of the electroactive β-phase crystallization of the nanocomposite films. The value of ε′ for all nanocomposite films shows enhancement as compared to the bare PVDF due to the improvement of the polar β-phase crystallization of the PVDF matrix in the nanocomposite films as well as the improvement of

space charge polarization at the interfaces of the nanocomposite films corresponding to the Maxwell-Wagner-Sillers interfacial polarization effect. It is clear to us that Co_2U and Co_2X-hexaferrite both are good dielectric material and it has a good frequency dependent dielectric response. Therefore, this could also help the nanocomposite films to improve its ε′ at the low frequency region as compared to bare PVDF. It is clear from Figure 3.9(a-c) that all the nanocomposite films and bare PVDF show a significant dielectric response in the low frequency region. Now, in some case the dielectric property study has been done at different temperature. As the temperature increases from 30 °C to 100 °C, the value of ε′ has been enhanced for UP1410 and UP1420 nanocomposite films. Therefore, it can be inferred that all the materials have significant amount of frequency response as well as temperature dependent dielectric polarizations due to the improvement of their electroactive β-phase crystallization as discussed in structural and chemical studies.

Figure 3.9(d-f) shows the variation of ε″ of UP1410, UP1420XP1210, XP1215, XP1220 and bare PVDF nanocomposite films. Here also, the high value of ε″ of UP1410, UP1420XP1210, XP1215 and XP1220 nanocomposite films has been found at low frequency region which confirms the greater polarization loss of the nanocomposite films as compared to bare PVDF. This improvement of ε″ of UP1410, UP1420, XP1210, XP1215 and XP1220 nanocomposite films due to the occurrence of effective area of interfaces between Co_2U and Co_2X-hexaferrite and PVDF matrix and the corresponding space charge polarization or interfacial polarization inside the nanocomposite films and the generation of larger heat energy at the cost of the external electrical energy corresponding to the external electric field by the dipoles of interfacial polarization effect. At the high frequency region, the inability of the dipoles to follow the frequency of the external electric field reduces the value of ε″ of the nanocomposite films, also, they do not obey the Maxwell-Wagner-Sillars interfacial

polarization effect. The same trend has been also observed with the increase of temperature for UP1410, UP1420 nanocomposite films.

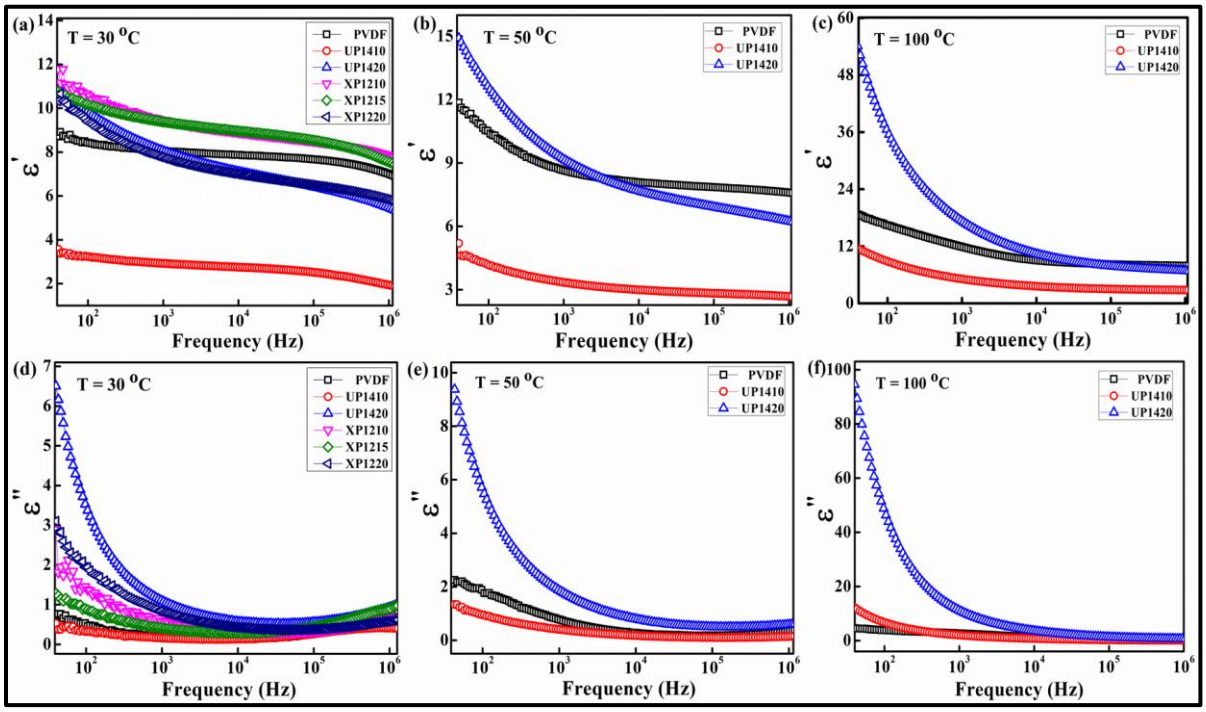

Figure 3.9: Variation of the real part of the dielectric constant (ε') with the frequency of at (a) 30 °C for bare PVDF, UP1410, UP1420, XP1210, XP1215 and XP1220 nanocomposite films, and (b) 50 °C, and (c)100 °C for bare PVDF, UP1410, UP1420 nanocomposite films and (II) variation of the imaginary part of the dielectric constant (ε'') with the frequency of at (a) 30 °C for bare PVDF, UP1410, UP1420, XP1210, XP1215 and XP1220 nanocomposite films, (b) 50 °C, and (c) 100 °C for bare PVDF, UP1410, UP1420 nanocomposite films.

The tangent loss (tanδ) factor of UP1410, UP1420, XP1210, XP1215, XP1220 and PVDF nanocomposite films within the frequency range of 40 to 10^6 Hz of the external electric field has been observed from Figure 3.10(a-c). The tangent loss (tanδ) factor of UP1410, UP1420, XP1210, XP1215, XP1220 and PVDF nanocomposite films have been calculated by using the equations.

$$tan\delta = \frac{\varepsilon''}{\varepsilon'} \qquad (3.5)$$

The high value of tangent loss (tanδ) factor of UP1410, UP1420, XP1210, XP1215, XP1220 and PVDF nanocomposite films has also been observed due to the occurrence of space charge polarization or interfacial polarization dependent polarization loss and the conduction loss [27, 32]. This conduction loss appears due to the drift motion of the induced charge carriers inside the nanocomposite films [32]. Now, the simultaneous existence of both these two loss factors inside the nanocomposite structure increases the value of tangent loss (tanδ) factor of UP1410, UP1420, XP1210, XP1215 and XP1220 nanocomposite films quite significantly as compared to PVDF system. It is to be mentioned here that inside the nanocomposite films the structural mismatch between Co_2U and Co_2X-hexaferrite and PVDF matrix induces localized carrier charges at the interfaces. The growth of charge carriers at the interface enhances dipole moment at the interfaces as well as the conductivity inside the Co_2U and Co_2X-hexaferrite grains of nanocomposite films (UP1410, UP1420, XP1210, XP1215 and XP1220) as compared to PVDF system and thereby the whole effect i.e., polarization loss due to induced dipole moment corresponding to interfacial polarization and conduction loss due to drift motion of carrier charges, increases the overall value of tangent loss (tanδ) factor of UP1410, UP1420, XP1210, XP1215 and XP1220 nanocomposite films. Also, the observed dielectric loss tangent has been increased with the increasing loading percentage of Co_2U and Co_2X-hexaferrite in the matrix of PVDF as well as with the increase of temperature (30 to 100 ^oC) in case of UP1410 and UP1420 nanocomposite films. This type of dielectric response can be explained partially by the high value of the dielectric loss tangent of the Co_2U and Co_2X-hexaferrite relative to those of the β-phase of the host PVDF due to the presence of a resistive factor called equivalent resistance (E_R) in series with the capacitive effect of the nanocomposite films and partially by the heterogeneous structure of the Co_2U and Co_2X-hexaferrite with the PVDF polymer.

In Figure 3.10(d-f) shows the variation of σ_{ac} response of UP1410, UP1420, XP1210, XP1215 and XP1220 nanocomposite films and bare PVDF. The ac conductivity of the nanocomposite films has been calculated by using the equation [27]

$$\sigma_{ac} = 2\pi f \varepsilon_0 \varepsilon' \tan\delta \quad (3.6)$$

Where, f is the applied frequency of external ac field. Now, it is to mention here that the nanocomposite films and bare PVDF are non-conducting in nature, so, the displayed σ_{ac} is short-range conductivity in nature. The short-range conductivity mostly appears when the induced charge carriers drifts inside the structure of these nanocomposite films under the influence of external electric field. In the low frequency region, all the samples show very low value of σ_{ac} and it remains constant throughout a very large variation of frequency and at very high frequency region this σ_{ac} increases very sharply. At a frequency region greater than 10^5 Hz the high value of σ_{ac} has been found due to the occurrence of various others dipolar polarization effects corresponding to the ionic polarization, electronic polarization etc. Also, the short-range σ_{ac} increases with the increasing temperature from 30 to 100 ^oC, and the cause behind this enhancement of this short-range σ_{ac} at higher temperature is the formation of more and more induced carrier charges at higher temperature inside the UP1410 and UP1420 nanocomposite films. Therefore, σ_{ac} of XP1210, XP1215, XP1220, UP1410, UP1420 and the bare PVDF in the frequency range of 40-10^6 Hz depends on various dipolar responses. Thus, the dielectric response study indicates that the incorporation of these Co_2U and Co_2X-hexaferrite inside the PVDF matrix can generate various dipolar effects which become helpful for the EMI shielding effectiveness of these nanocomposite films in the GHz frequency range.

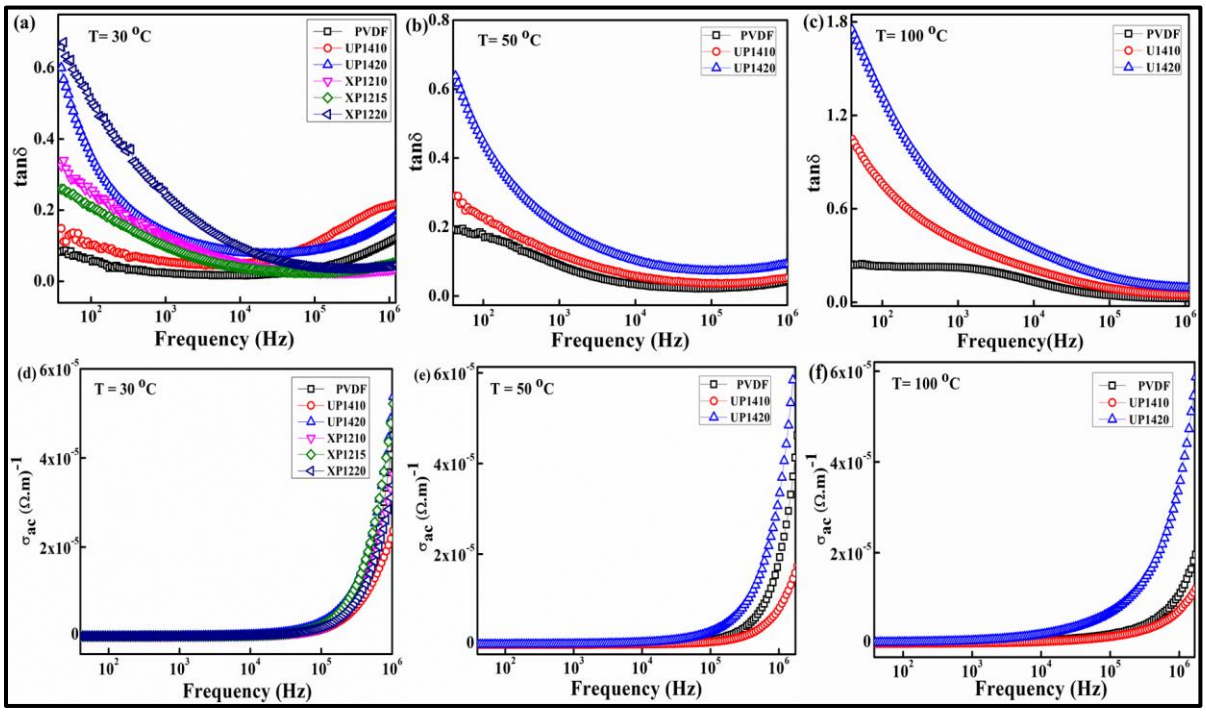

Figure 3.10: Variation of the tangent loss (tan δ) with the frequency at (a) 30 °C for bare PVDF, UP1410, and UP1420, XP1210, XP1215 and XP1220 nanocomposite films, (b) 50 °C, and (c) 100 °C for and bare PVDF, UP1410, and UP1420 nanocomposite films (II) variation of ac conductivity (σ_{ac}) with the frequency at (a) 30 °C for bare PVDF, UP1410, and UP1420, XP1210, XP1215 and XP1220 nanocomposite films, (b) 50 °C, and (c) 100 °C for bare PVDF, UP1410, and UP1420 nanocomposite films.

3.3.9 Impedance analysis:

The dielectric impedance study is important to understand some of the interesting electrical characteristics such as grain morphology, synthesis procedure, internal interfaces etc. corresponding to the simultaneous existence of both homogeneous and heterogeneous nanocomposite films as well as grain and grain boundary effects inside the nanocomposite films systems in a more comprehensive manner. So that, the complex impedance has been done for some of the nanocomposite films (XP1210, XP1215, XP1220 and bare PVDF) within 40-10^6 Hz frequency range at RT can be expressed as

$$Z^* = Z' + jZ'' = R + \frac{1}{j\omega C} \tag{3.7}$$

Here, Z' is the real part of complex impedance and Z'' is the imaginary parts of complex impedance within 40-10^6 Hz frequency range and these Z' and Z'' can be further represented as

$$Z' = \frac{1}{2\pi f C_0}\left[\frac{\varepsilon''}{(\varepsilon')^2+(\varepsilon'')^2}\right] \tag{3.8}$$

$$Z'' = \frac{1}{2\pi f C_0}\left[\frac{\varepsilon'}{(\varepsilon')^2+(\varepsilon'')^2}\right] \tag{3.9}$$

Here also, ε′ and ε″ have their usual meaning, f is the applied frequency of external ac field that varies within 40-10^6 Hz frequency range, C_0 is the geometric capacitance.

Also, these Z' and Z'' can be estimated further as [33]

$$Z' = \frac{1/R}{1/R^2 + \omega^2 C^2} = \frac{R}{1+ \omega^2 C^2 R^2} \tag{3.10}$$

$$Z'' = \frac{-\omega C}{1/R^2 + \omega^2 C^2} = \frac{-\omega C R^2}{1+ \omega^2 C^2 R^2} \tag{3.11}$$

Here, ω is the angular frequency, R and C are grain resistance and grain capacitance, respectively. Figure 3.11(a) represents the variation of Z′ of XP1210, XP1215, XP1220 and bare PVDF within 40-10^6 Hz frequency range at RT. The figure shows that in frequency region the values of Z′ decreases very first and after that this Z′ gets saturated. This comparatively high value of Z′ in the low frequency region appears due to the presence of non-conducting grain boundary effect and at higher frequency region it decreases due to either by the enhancement of polarization effect across the grain boundaries or due to the rise in electron hopping mechanism between the localized ions present inside the structure. Figure 3.11(b) shows the variation of Z′′ of XP1210, XP1215, XP1220 and bare PVDF within the frequency range of 40 Hz to 10^6 Hz at RT. This figure shows the gradual decrement of Z′′ with the rising frequency. It is also found that the value of Z′′ corresponding to XP1210, XP1215, XP1220

and bare PVDF gets saturated at high frequency region and this particular variation of Z′′ develops due to the growth of space charge carriers at the interfaces of the materials.

Figure 3.11(c) represents the Nyquist plot or the Cole-Cole plot of XP1210, XP1215, XP1220 and bare PVDF within 40-10^6 Hz frequency range at RT. The variation of Z′′ as a function of Z′ provides very important information regarding the electrical characteristics (grain, grain boundary and the interface etc.). It is clear from the Cole-Cole plot of the nanocomposite films that the electrode effect is not there in the dielectric polarization response and the present dielectric response is appeared due to the interfacial polarization at the interfaces of XP1210, XP1215, XP1220 and bare PVDF.

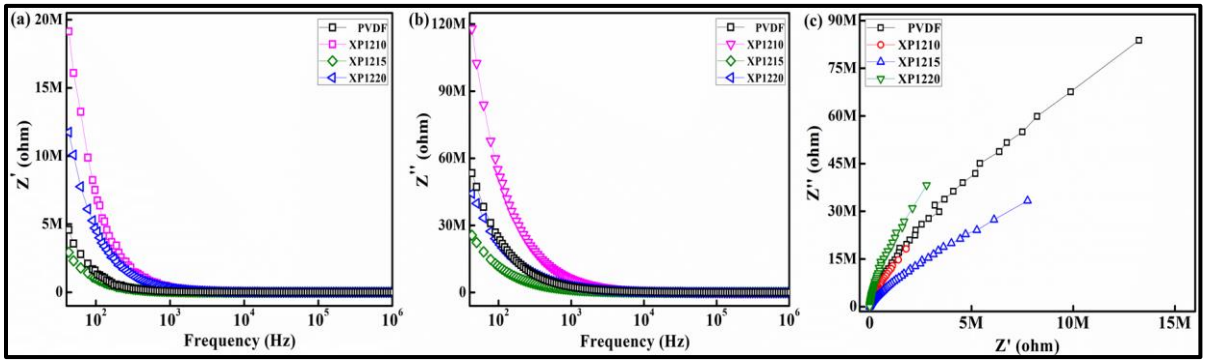

Figure 3.11: Variation of (a) real part of complex impedance (Z′), (b) imaginary parts of complex impedance (Z′′) and (c) Nyquist plot of XP1210, XP1215, XP1220 and bare PVDF nanocomposite films.

3.3.10 Study of EMI shielding property:

The shielding effectiveness study of the nanocomposite films (UP1410, UP1420, XP1210, XP1215, and XP1220) has been examined in the 4-18 GHz frequency range, where, 4-8 GHz knows as C-band, 8-12 GHz range known as X-band and 12–18 GHz represent the K_u-band of microwave radiation. The combined effects of shielding effectiveness by absorption (SE_A),

reflection (SE_R), and multiple reflection (SE_{MR}) phenomena resulted in the total shielding effectiveness (SE_T) of the nanocomposite films.

$$SE_T\ (dB) = -10 \log_{10}\left(\frac{P_t}{P_0}\right) = SE_A + SE_R + SE_{MR} \quad (3.12)$$

However, the shielding effectiveness by multiple reflections (SE_{MR}) can be neglected for these nanocomposite films as their thicknesses are more than the skin depth of the incident microwave radiation in the frequency range of 4-18 GHz. Thus, the total shielding effectiveness (SE_T) of nanocomposite films given in equation (12) can be further expressed as [33-35]

$$SE_T\ (dB) = -10 \log_{10}\left(\frac{P_t}{P_0}\right) = SE_A + SE_R \quad (3.13)$$

Where, P_t represents the transmitted power and P_0 represents the incident power of microwave radiations. The estimation of shielding effectiveness as SE_A and SE_R in the frequency range of 4-18 GHz can be done by the following equations [33-35]

$$SE_A\ (dB) = -10 \log_{10}\left(\frac{1 - |S_{11}|^2}{|S_{12}|^2}\right) \quad (3.14)$$

$$SE_R\ (dB) = -10 \log_{10}\left(\frac{1}{1 - |S_{11}|^2}\right) \quad (3.15)$$

Here, S represent the scattering parameters i.e., S_{11} (reflection coefficient) and S_{21} transmission coefficient) and the respective S represent have been extracted using the PNA Series Network Analyzer. Now, the interaction between EM wave and the material medium has been appeared due to three different phenomena and these phenomena are reflection, absorption and transmission. The interactions between the magnetic field vector of the incident EM wave with magnetic dipoles and electric field vector of the incident EM wave with electric dipole induced charge carriers convert this microwave radiation into thermal energy and these interactions are responsible for the improvement of the absorptivity of the materials [33]. On the other hand, the reflection phenomenon would be maximum from the surface of the material if it contains

conduction electron, whereas the absorption phenomenon would be maximum inside the volume of the material if it contains different forms of dipoles such as magnetic dipoles and electric dipoles [33]. The interaction between the electric field vector of the incident EM wave and the quantum particles (conduction electron) reflects the incident EM wave are responsible for the improvement of the reflectivity of the materials. Figure 3.12(a and d) and Figure 3.13(a, d, and g) shows the shielding effectiveness due to absorption (SE_A) of UP1410, UP1420, XP1210, XP1215, and XP1220 nanocomposite films in C-band, X-band and K_u-band of microwave frequency range. And Figure 3.12(b and e) and Figure 3.13(b, e, and h) shows the shielding effectiveness due reflection (SE_R) of UP1410, UP1420, XP1210, XP1215, and XP1220 nanocomposite films within the same frequency range of microwave radiation. In Figure 3.12(c and f) and Figure 3.13(c, f, and i) maximum shielding effectiveness due to absorption (SE_A) is -54 dB at -13.9 GHz in matching frequency of K_u-band for UP1420. On the other hand, -57.65 dB at 14.1 GHz in matching frequency of K_u-band corresponding XP1215 nanocomposite films have been observed. Now, in the present study high value of SE_A has been observed due to the presence of Co_2U and Co_2X-hexaferrite inside the matrix of PVDF. The significant amount of interaction between magnetic field vector of microwave radiation (4-18 GHz) with the magnetic dipoles of Co_2U and Co_2X-hexaferrite magnetic nanofillers of high magnetic response is responsible for the generation of this high value of shielding effectiveness by absorption (SE_A) of UP1410, UP1420, XP1210, XP1215, and XP1220 nanocomposite films. Also, the presence of various electric dipolar effects in each of the composite materials due to the successful incorporation of the Co_2U and Co_2X-hexaferrite inside the matrix of PVDF can generate the high value of shielding effectiveness due absorption (SE_A). Again, the maximum SE_R of -33 dB at 14.7 GHz in matching frequency of K_u-band for UP1420 and -32.67 dB at 15.30 GHz in matching frequency of K_u-band for XP1215 nanocomposite films. The presence

of Co_2U and Co_2X-hexaferrite inside PVDF matrix can generate induced carrier charges at the surface of the nanocomposite films. Now, these induced carrier charges when interacts with the electric field vector of the incident EM radiation, reflect them back to the first medium right from the surface of the nanocomposite films and thereby improves the SE_R of UP1410, UP1420, XP1210, XP1215, and XP1220 nanocomposite films in the frequency range of 4-18 GHz. Here, it is noticeable that for both the Co_2U and Co_2X-hexaferrite the absorption (SE_A) property of the materials is quite high as compare to the shielding effectiveness due to reflection (SE_R) and it gives us a clear idea that, both the materials have high capability to absorb the EM radiation. Finally, the maximum value of SE_T of -83 dB at 14.2 GHz in the matching frequency of K_u-band for UP1420 have been found -84.65 dB at 12.44 GHz in the matching frequency of K_u-band for XP1220.

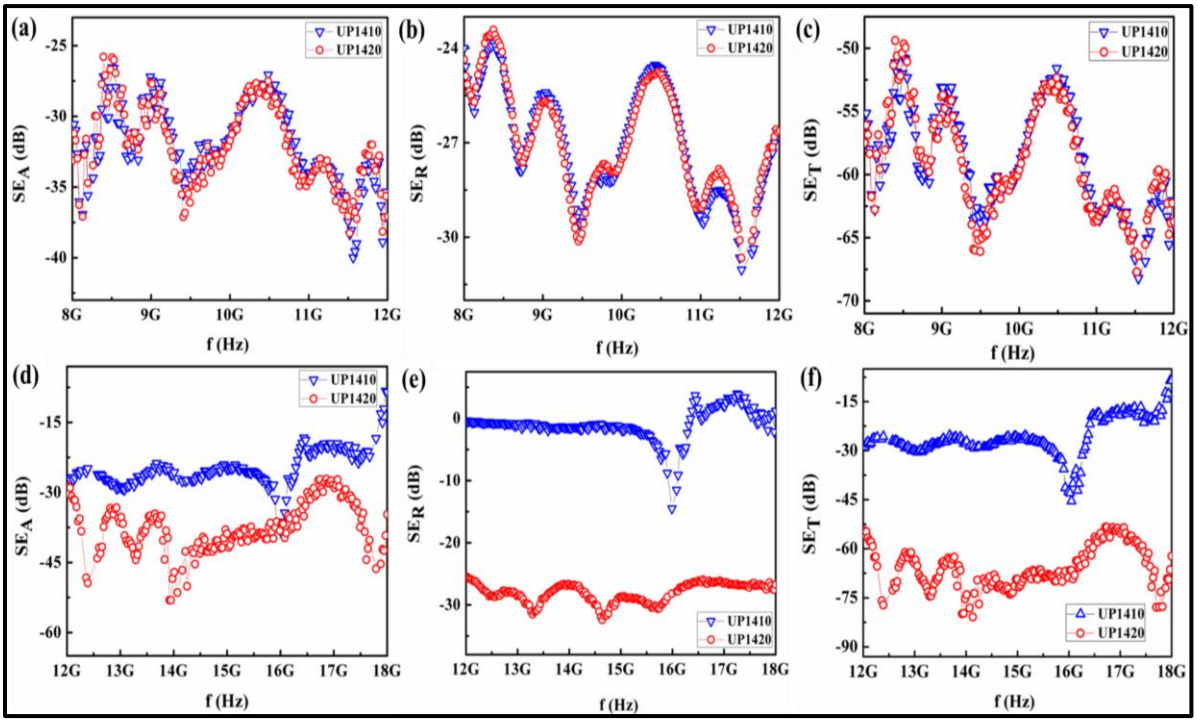

Figure 3.12: Shielding effectiveness by absorption (SE_A), reflection (SE_R), Total Shielding effectiveness (SE_T) in the frequency range of (a-c) 8–12 GHz of the X-band and (d-f) 12–18

GHz of the K_u-band for UP1410 and UP1420 nanocomposite films.

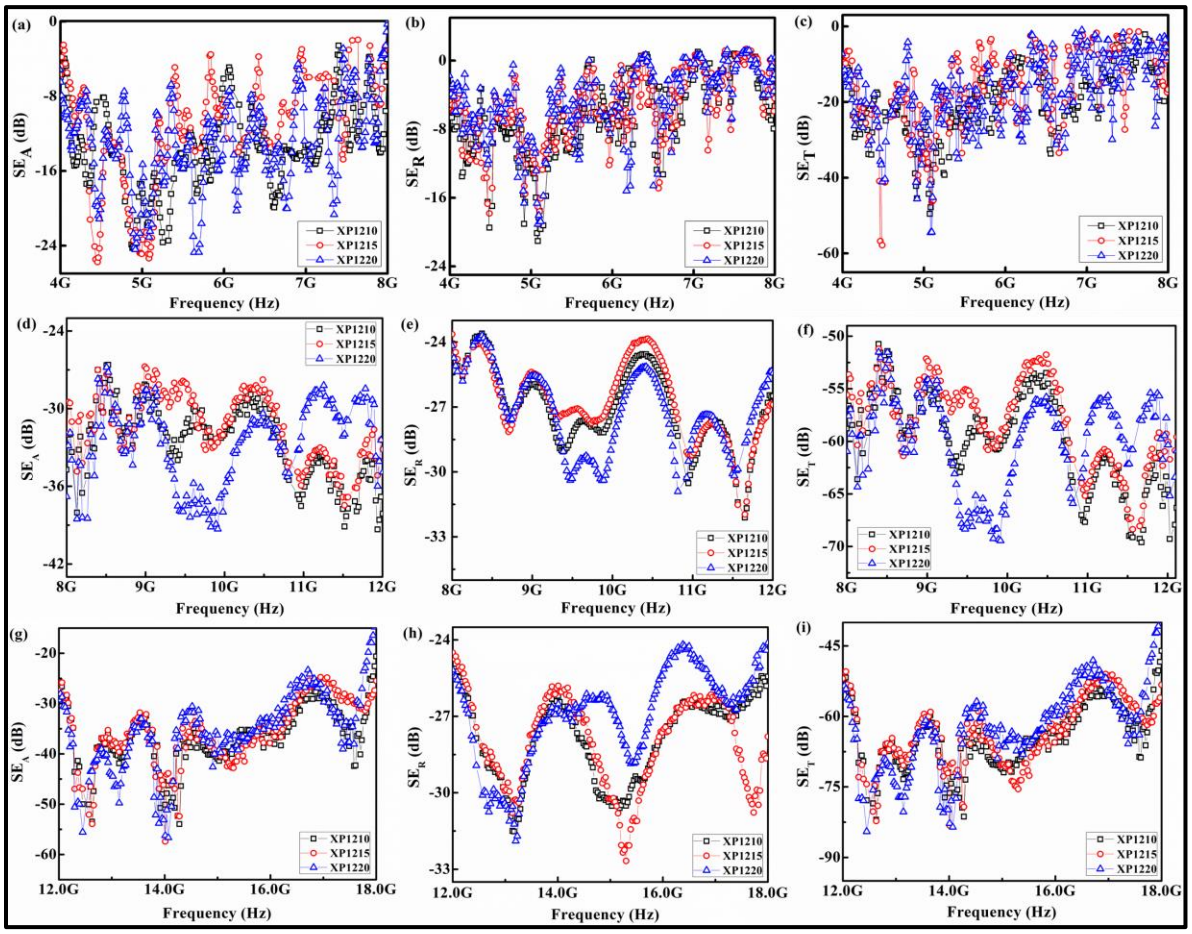

Figure 3.13: Shielding effectiveness by absorption (SE_A), reflection (SE_R), Total Shielding effectiveness (SE_T) in the frequency range of (a-c) 4-8 GHz of the C-band, (d-f) 8-12 GHz of the X-band and (g-i) 12-18 GHz of the K_u-band for XP1210, XP1215 and XP1220 nanocomposite films.

The high value of SE_T for these Co_2U-PVDF composite materials with an attenuation of >99.999999% corresponding to the UP1420 and >99.999999% for XP1220 lies in the large band width of 6 GHz. The attenuation percentage has been depicted in Fig. 3.14(a-c) for C-band, X-band and K_u-band respectively. Therefore, from the maximum values of SE_A, SE_R and SE_T of all the nanocomposite films (UP1410, UP1420, XP1210, XP1215, and XP1220) with the corresponding frequency) plays a significant role for the fabrication of superior microwave

absorbers that helps to reduce electromagnetic pollution and make our society free from all the hazards of EM pollution.

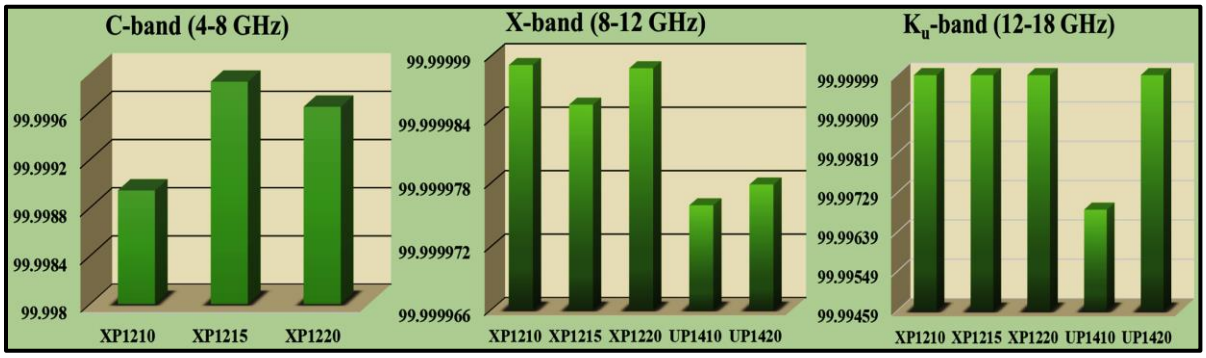

Figure 3.14: Attenuation percentage of XP1210, XP1215, XP1220, UP1410 and UP1420 nanocomposite films.

3.4 Conclusion:

The Co_2U and Co_2X-hexaferrites incorporated PVDF nanocomposite films have been reported in this study for shielding effectiveness applications in the GHz frequency range with comprehensive details. The incorporation of Co_2U and Co_2X-hexaferrite inside PVDF has been proved by substantiating the multiphase nature of the resultant Co_2U-PVDF and Co_2X-hexaferrite-PVDF nanocomposite films in XRD analysis. The coexistence of the dielectric and magnetic properties inside the nanocomposite films of Co_2U-PVDF and Co_2X-hexaferrite-PVDF have been substantiated from the dielectric and magnetic response study. The significant dielectric improvement of the nanocomposite films due to the generation of large area of interfaces between the Co_2U and Co_2X-hexaferrites and the PVDF matrix has been observed here. The simultaneous existence of both dielectric and magnetic responses of the nanocomposite films plays the most important role for the improvement of SE_A, SE_R and SE_T of Co_2U-PVDF and Co_2X-hexaferrite-PVDF nanocomposite films. The high EMI shielding effectiveness with high attenuation >99.999999% of the nanocomposite films of Co_2U-PVDF

and Co_2X-PVDF system have been observed in this chapter. The high shielding effectiveness of magnetic nanofiller incorporated PVDF based nanocomposite films made of Co_2U and Co_2X nanomaterials is very useful to design the efficient electromagnetic pollution reducers.

3.5 References:

1. R. Dangi, P. Lalwan, G. Choudhar, I. You, G. Pau, Sensors 22(1) 26 (2022) .

2. R. Gallego-Martínez, F. J. Muñoz-Gutiérrez, A. Alejandro Rodríguez-Gómez, Expert Systems with Applications 207, 118088 (2022).

3. D. Panagopoulos, O. Johansson, G. Carlo, Sci. Rep. 5, 14914 (2015).

4. Y. H. Hao, L. Zhao, R. Y. Peng, Mil. Med. Res. 2, 4 (2015).

5. R. Zhu, H. Wang, X. Xu, L. Zhao, J. Zhang, J. Dong, B. Yao, H. Wang, H. Zhou, Y. Gao, R. Peng, Sci. Rep. 11, 10061 (2021).

6. C. Blackman, Pathophysiology 16, 205-216 (2009).

7. J. Dong, R. Y. Peng, S. M. Wang, Y. B. Gao, L. F. Wang, L. Zhao, Mil. Med. Sci. 35 347-50 (2011).

8. Y. Lu, W. You, C. Cai, X. Yu, Y. Zhao, X. Liu, X. Zhang, W. Zeng, R. Che, Journal of Magnetism and Magnetic Materials 475, 24-29 (2019).

9. R. C. Pullar, Progress in Materials Science 57(7) 1191-1334 (2012).

10. A. Peleš, O. Aleksić, V. P. Pavlović, V. Djoković, R. Dojcˇilović, Z. Nikolić, F. Marinković, M. Mitrić, V. Blagojević, B. Vlahović, V. B. Pavlović, Physica Scripta 93 105801 (2018).

11. M.Y. Lodhi, M.A. Khan, M.N. Akhtar, M.F. Warsi, A. Mahmood, S.M. Ramay, Ceramics International 44, 2968–75 (2018).

12. V. S. Bystrov, I. K. Bdikin, M. V. Silibin, J. Nanomed Nanotechnol. 5(2) (2017) 049.

13. S. Sutradhar, K. Mukhopadhyay, S. Pati, S. Das, D. Das, P.K. Chakrabarti, J. Alloys Compd. 576, 126–133 (2013).

14. F. S. Gill, D. Uniyal, B. Prasad, S. Saluja, A. Mishra, R. K. Bachheti, S. Juyal, Journal of Molecular Structure 1267, 133541 (2022).

15. Abhishek Sasmal, Shrabanee Sen, Arout Chelvane, A. Arockiarajan, Polymer Volume 281, 126141 (2023).

16. Z. Su, S. Bennett, B. Hu, Y. Chen, and V. G. Harris, J. Appl. Phys. 115, 17A504 (2014).

17. P. Saha, S. Das, and S. Sutradhar, J. Appl. Phys. 124, 045303 (2018).

18. B. Liu, Y. Bando, A. Wu, X. Jiang, B. Dierre, T. Sekiguchi, C. Tang, M. Mitome, D. Golberg, Nanotechnology 21, 075708 (2010).

19. J. Lo´pez, L.F. Gonza´lez-Bahamo´n, J. Prado, J.C. Caicedo, G. Zambrano, M.E. Go´mez, J. Esteve, P. Prieto, Journal of Magnetism and Magnetic Materials, 324, 394-402 (2012).

20. S. M. Lebedev, O. S. Gefle, S. N. J. Tkachenko, Electrost. 68, 122–127 (2010).

21. M.O. Ilatovskaia, S.I. Sinyova, R.V. Starykh, Calphad. 59, 31-39 (2017).

22. T. Prabhakaran, J. Hemalatha, Science of Advanced Materials 6, 1313–21 (2014).

23. C. Xiaomei, L. Tingping, S. Daoheng, L. Liwei, RSC Advances 7, 15382–89 (2017).

24. B. Dutta, N. Bose, E. Kar, S. Das, S. Mukherjee, Journal of Polymer Research 24, 1–15 (2017).

25. M. Chireh, M. Naseria, H. Ghaedamini, Advanced Powder Technology 32(14) (2021).

26. S. Dwivedi, M. Badole, K. Gangwar, S. Kumar, Polymer, 232, 124164 (2021).

27. S. Das, A. Bandyopadhyay, P. Saha, S. Das, S. Sutradhar, Journal of Alloys and Compounds. 749, 1–9 (2018).

28. S.A. Ansari, A. Nisar, B. Fatma, W. Khan, M. Chaman, A. Azam, A.H. Naqvi, Materials Research Bulletin 47, 4161–68 (2012).

29. W.A. Yager, Physics 7, 434 (2004).

30. J. Maxwell, Electric and Magnetism 2, Oxford University Press, New York (1973).

31. C.G. Koops, Physical Review 83, 121 (1951).

32. Zheludev, I.S., Physics of Crystalline Dielectrics. Springer, 455–532 (1971).

33. S. Anand, S. Pauline, Advanced Materials Interfaces 8, 2001810 (2021).

34. Prodromakis T., Papavassiliou C., Applied Surface Science, 255, 6989–94 (2009).

35. D.D.L. Chung, Carbon 39, 279–85 (2001).

Chapter: 4

Synthesis of magnetic-semiconducting binary nanofillers and their conjugated structure with PVDF for superior EMI shielding behaviour

Chapter 4:

4.1 Introduction:

In the previous chapter (Chapter 3), the importance of highly magnetic hexaferrite nanofillers incorporated PVDF nanocomposite films has been studied for the EMI shielding applications. The impressive MW/RF wave absorption property of the magnetic nanofillers incorporated PVDF nanocomposite films confirms that, the nanocomposite material has sufficiently high magnetic (permeability) losses or dielectric (permittivity) losses or the simultaneous presence of both the loss factors therein, which are greatly helpful to reduce the electromagnetic pollution from our environment [1-4]. Therefore, the various forms of magnetic loss factors have appeared in the nanocomposite films due to the presence of hexagonal ferrites such as Co_2X-hexaferrite, Co_2U-hexafettite etc. inside the matrix of PVDF [5-8]. Also, the various forms of dielectric loss/polarization loss factors have appeared in the nanocomposite films due the presence of polar β-phase of modified PVDF matrix in the nanocomposite structure. Thus, the enhancement of the magnetic responses of the magnetic nanofillers and the enhancement of the dielectric responses of polar β-phase improved PVDF matrix can contribute to more shielding effectiveness (SE) just by producing more interaction with the magnetic field vectors and electric field vectors of incident EM radiation. So, in this chapter, to improve the SE of the nanocomposite films by the improvement of the magnetic loss contribution as well as the dielectric loss contribution of the nanocomposite films we have incorporated the semiconducting fillers of C_3N_4 in the matrix of PVDF along with the magnetic fillers such as Co_2X-hexafettite and Ni-Zn-Cu-ferrite (NZCF). Since, spinel ferrite such as Ni-Zn-Cu-ferrite can possess high permeability loss like magnetic hexaferrites in the MW/RF wave region, it is expected to get significant MW absorption behaviour from this spinel ferrite nanoparticles.

Among all the different semiconducting filler materials, C_3N_4, can be the most interesting filler material because of its large aspect ratio and flexibility. The semiconducting fillers of C_3N_4 of band gap energy ~2.7 eV in association with the magnetic materials such as Co_2X-hexafettite and Ni-Zn-Cu-ferrite can improve the EM shielding effectiveness of these Co_2X-C_3N_4 and NZCF-C_3N_4 binary composite materials just by allowing the generation of current loops inside the binary composite structures at RT, called eddy current, since semiconducting C_3N_4 filler can modulate its charge conduction property depending on temperature and doping [9]. Here in this present study C_3N_4 acts as a charge source and as a result of which there are more charge accumulations at the interfaces which enhances the dielectric response. This is to be mentioned here that the fabrication of nanocomposite materials with good shielding effectiveness in terms of reflection (SE_R), absorption (SE_A) and total shielding effectiveness (SE_T), a good dielectric and magnetic response is very crucial, especially the complex relative permittivity (ε^*) and complex relative permeability (μ^*) play the most significant role. The eddy current inside the nanocomposite structures of Co_2X-hexafettite and NZCF-C_3N_4 may be appeared due to the magnetic flux linked with the respective magnetic filler materials and it leads to the large absorption of EM radiation in the RF/MW region. Thus, below the percolation threshold this semiconducting filler i.e. C_3N_4 along with the magnetic fillers can improve the overall loss factors of this composite structure with enhanced shielding effectiveness. Now, inside the polar PVDF matrix the heterogeneous dispersion of semiconducting and magnetic binary filler materials leads to the synergistic absorption as well as total shielding effectiveness of MW radiation by these nanocomposite films.

4.2 Experimental Details:

4.2.1 Materials:

The required chemicals to synthesize Co_2X-C_3N_4 and NZCF-C_3N_4 binary fillers are barium (II) nitrate $Ba(NO_3)_2$ (Merck Germany, 99%), cobalt (II) nitrate $Co(NO_3)_2$, iron (III) nitrate nonahydrate $Fe(NO_3)_3.9H_2O$ (Merck Germany, 99%), citric acid ($C_6H_8O_7$), nickel (II) acetate tetrahydrate $Ni(CH_3COO)_2{\cdot}4H_2O$ (Sigma Aldrich, 99%), zinc (II) acetate dihydrate $Zn(CH_3COO)_2{\cdot}2H_2O$ (Sigma Aldrich, 99%), copper (II) acetate monohydrate $Cu(CH_3COO)_2{\cdot}H_2O$ (Sigma Aldrich, 99%), melamine ($C_3H_6N_6$) and ethyl alcohol (C_2H_5OH). After synthesized Co_2X-C_3N_4 and NZCF-C_3N_4 binary fillers, to get the Co_2X-C_3N_4-PVDF and NZCF-C_3N_4-PVDF nanocomposite films poly(vinylidene fluoride) pellets (molecular weight Mw: 275,000 (hpc), Mn: 107,000, Aldrich, Germany), N,N-dimethyl formamide (DMF) (Merck, India) have been used.

4.2.2 Synthesis of Co_2X-hexaferrite and NZCF spinel ferrite:

Synthesis of Co_2X-hexaferrite and NZCF spinel ferrite with the stoichiometry ratio of $Ba_2Co_2Fe_{28}O_{46}$ and $Ni_{0.50}Zn_{0.30}Cu_{0.20}Fe_2O_4$ have been done using simple sol-gel method. The details of the synthesis procedure have already been discussed in chapter 2 (**Section: 2.2.1** Synthesis of magnetic hexaferrite and ferrite nanoparticles by sol-gel method). After collecting the as prepared Co_2X-hexaferrite and NZCF spinel ferrite, Co_2X-hexaferrite was annealed at 1200 °C and NZCF spinel ferrite was annealed at 400 °C in a hot air oven to get the proper crystallographic phase.

4.2.3 Synthesis of C_3N_4 semiconducting fillers:

The semiconducting C_3N_4 nanofillers was prepared by one-step solid state reaction method. The desired product was obtained via heat treatment of 10 g melamine in a 7 ml curved bottom

silica crucible and calcined at 500 ^{o}C for 4 hrs with a heating rate of 3 ^{o}C/min. The detailed synthesis procedure has been mentioned in chapter 2 (**Section: 2.2.2.1** Synthesis of carbon nitrate (C_3N_4) by solid state reaction method).

4.2.4 Synthesis of Co_2X-hexaferrite-C_3N_4 and NZCF-C_3N_4-PVDF nanocomposite films:

Before synthesizing the nanocomposite films the binary fillers of Co_2X hexaferrite-C_3N_4 and NZCF-C_3N_4 have been prepared by solid-state reaction method, and the details of the solid-state reaction method have been discussed in chapter 2 (**Section: 2.2.2.4** Synthesis of binary nanocomposite by grinding-mixing method). To get the flexible, free-standing Co_2X hexaferrite-C_3N_4 and NZCF-C_3N_4-PVDF nanocomposite films, cost effective solution casting method has been used. The detailed procedure of solution casting method has been mentioned in chapter 2 (**Section: 2.2.2.5** Synthesis of nanofillers-polymer nanocomposite film by solution casting method). The prepared XCP732, XCP733, NFCP732, NFCP733, NFCP552 and NFCP553 nanocomposite films are cut into the proper dimensions to conduct all the measurement.

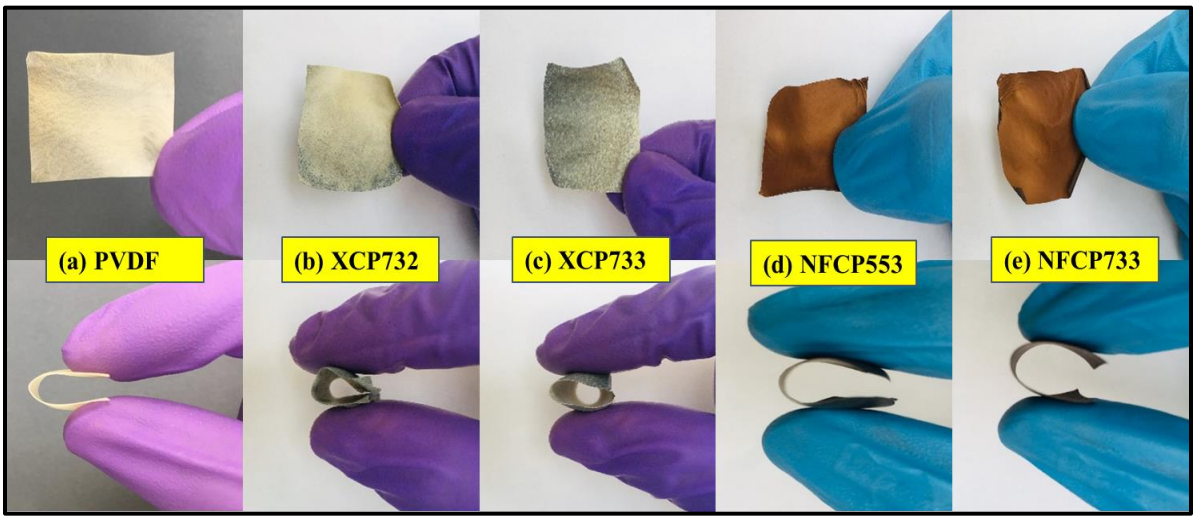

Figure 4.1: Free standing and flexible images of (a) PVDF, (b) XCP732, (c) XCP733, (d) NFCP553, (e) NFCP733 nanocomposite films.

4.3 Result and Discussions

4.3.1 Crystallographic phase analysis:

The X-ray diffraction (XRD) analysis of Co_2X-hexaferrite, NZCF, C_3N_4, bare PVDF and XCP732, XCP733, NFCP732, NFCP733, NFCP552 and NFCP553 nanocomposite films in the range of 10^o to 80^o, that confirms the crystallographic phases and the presence of all the crystallographic phases corresponding to the phase of Co_2X-hexaferrite-C_3N_4 and NZCF-C_3N_4 binary fillers inside the matrix of PVDF in the heterojunction multiphase nanocomposite films. The crystallographic phases corresponding to Co_2X-hexaferrite, NZCF nanoparticles, C_3N_4 and bare PVDF have been matched well with the crystallographic phases of the respective samples given in their JCPDS files 78-0135, 84-0757, 87-1526, and 42-1650, respectively. Co_2X-hexaferrite has two types of mixed phases i.e. Co_2W and Co_2M-hexaferiite so that the JCPDS number of 78-0135, 84-0757 belongs to Co_2W and Co_2M-hexaferiite respectively. The simultaneous existence of Co_2X-hexaferrite-C_3N_4 and NZCF-C_3N_4 binary fillers inside the structure of PVDF and the identification of their crystallographic phases along with the phase of laminated PVDF matrix make this study more significant from the shielding effectiveness point of view. Figure 4.2(I and II) shows the XRD pattern of Co_2X-hexaferrite, NZCF, C_3N_4, bare PVDF and the laminated nanocomposite films, i.e., XCP732, XCP733, NFCP732, NFCP733, NFCP552 and NFCP553. Thus, this XRD analysis will help us to understand the formation of the composite form of the resultant materials with proper multi-phase nature. The average crystallite diameter of Co_2X-hexaferrite and NZCF nanoparticles has been estimated from the broadening of the 100% intense peak of Co_2X-hexaferrite and NZCF nanoparticles, by applying the Debye-Scherrer equation [10]

$$< D >= \frac{0.9\lambda}{\beta_{\frac{1}{2}}\cos\theta} \tag{4.1}$$

Here, D is the average crystallite size, λ is the incident X-ray wavelength, θ is the Braggs angle and the corresponding full width at half maximum (FWHM) is designated as $\beta_{\frac{1}{2}}$. The crystalline diameter of Co_2X-hexaferrite and NZCF nanoparticles are ~ 28 nm and ~ 34 nm, respectively. Also, the formation of non-polar α, polar β and γ-phase crystallizations of the resultant nanocomposite films indicate that Co_2X-hexaferrite-C_3N_4 and NZCF-C_3N_4 binary fillers have formed successful interfaces in the PVDF matrix through electrostatic interaction. Also, it has been noticed that as compare to bare PVDF the non-polar α-phase is suppressed and the polar β-phase are quite prominent in case of nanocomposite films. The interaction between the binary fillers and PVDF is responsible for the formation of all trans-planar zig-zag (TTTT) conformation inside the nanocomposite films.

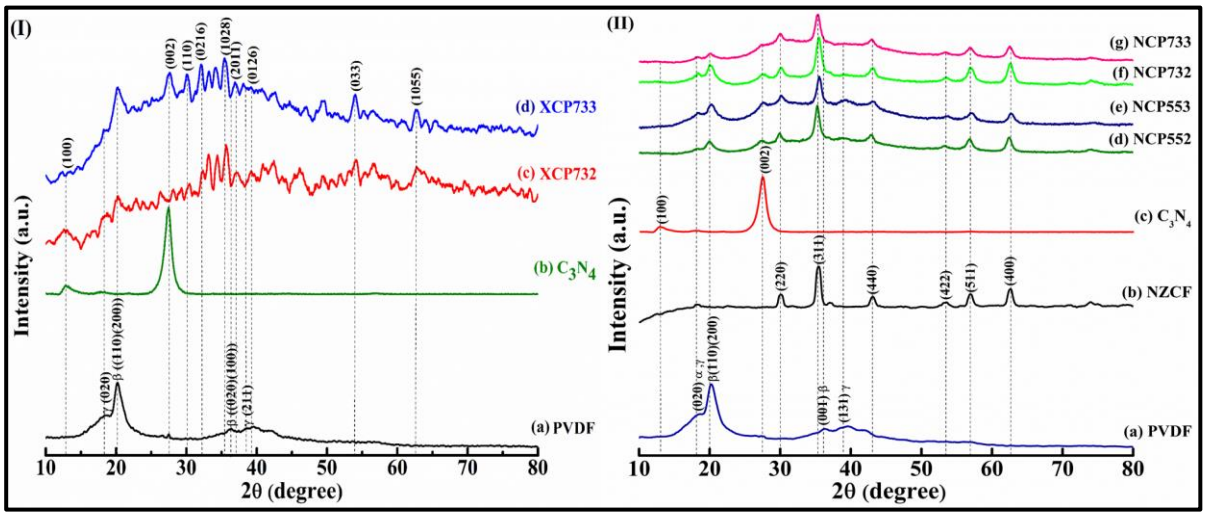

Figure 4.2: XRD patterns of (I) bare PVDF, Co_2X-hexaferrite, NZCF nanoparticles, C_3N_4 nanofillers, and (II) the nanocomposite films of XCP732, XCP733, NFCP552, NFCP553, NFCP732 and NFCP733.

4.3.2 Study of surface morphology:

The surface morphology study of Co_2X-hexaferrite-C_3N_4 and NZCF-C_3N_4 binary fillers and

some selected nanocomposite films (NFCP552, NFCP732, XCP732, and XCP733) has been depicted in Figure 4.3(a-l). The spherulite nature with the presence of prominent bubble type structures has been observed for the nanocomposite films. Also, the presence of radial lamellar structure has been found in the nanocomposite films, but the fractional contribution of the radial lamellar structure in the nanocomposite films is less. It has already been mentioned in the previous chapter that the presence of spherulite structure of bubble type in nature over the surface of NFCP552, NFCP732, XCP732, and XCP733 nanocomposite films indicates the presence of polar/electroactive β-phase crystallization of PVDF matrix, whereas, the radial lamellar structure over the surface of NFCP552, NFCP732, XCP732, and XCP733 nanocomposite films is attributed to non-polar α-phase [11, 12]. From Figure 4.3(b, c, e, f, h, i, k and l) of the given micrographs clearly show that the binary fillers are present inside the PVDF matrix. The insertion of Co_2X-hexaferrite-C_3N_4 and NZCF-C_3N_4 binary fillers inside the matrix of PVDF is responsible for the formation of nanofiller-PVDF interfaces inside nanocomposite films and the formation of such interfaces improves the overall electroactivity of the nanocomposite films and therefore, the polar/electroactive β-phase has been developed. Again, the energy dissipative spectroscopy (EDX) and elemental mapping study for the NFCP552 nanocomposite film have been done as a representative among the other nanocomposite films. The EDX and elemental mapping of NFCP552 are shown in Figure 4.3(m and n), respectively. The presence of nickel (Ni), zinc (Zn), copper (Cu), iron (Fe) and oxygen (O) ions in the NFCP552 nanocomposite film is confirmed by the EDX and elemental mapping study. Also, the peaks relating to gold (Au) in the EDX study has been observed due to the presence of gold coating over the surface of NFCP552 composite film during the preparation of the samples for FESEM imaging. The carbon and nitrogen peaks have not been considered

in EDX study since the FESEM observation was conducted keeping NFCP552 nanocomposite film over the surface of carbon tape which can make the carbon (C) peak corresponding to both C_3N_4 and carbon tape indistinguishable. Also, the elemental area mapping of NFCP552 nanocomposite film shows a nearly uniform distribution of all the ions, namely nickel (Ni), zinc (Zn), copper (Cu), iron (Fe) and oxygen (O), inside the composite film. From this morphological analysis it is quite clear that both magnetic NZCF nanoparticles and the semiconducting C_3N_4 layer structures are present simultaneously inside the NFCP552 and NFCP732 nanocomposite films and it is expected that these two components and more specifically the insertion of C_3N_4 semiconducting fillers inside the matrix of PVDF will put some addition impact to improve the shielding effectiveness due to absorption (SE_A) of the nanocomposite films.

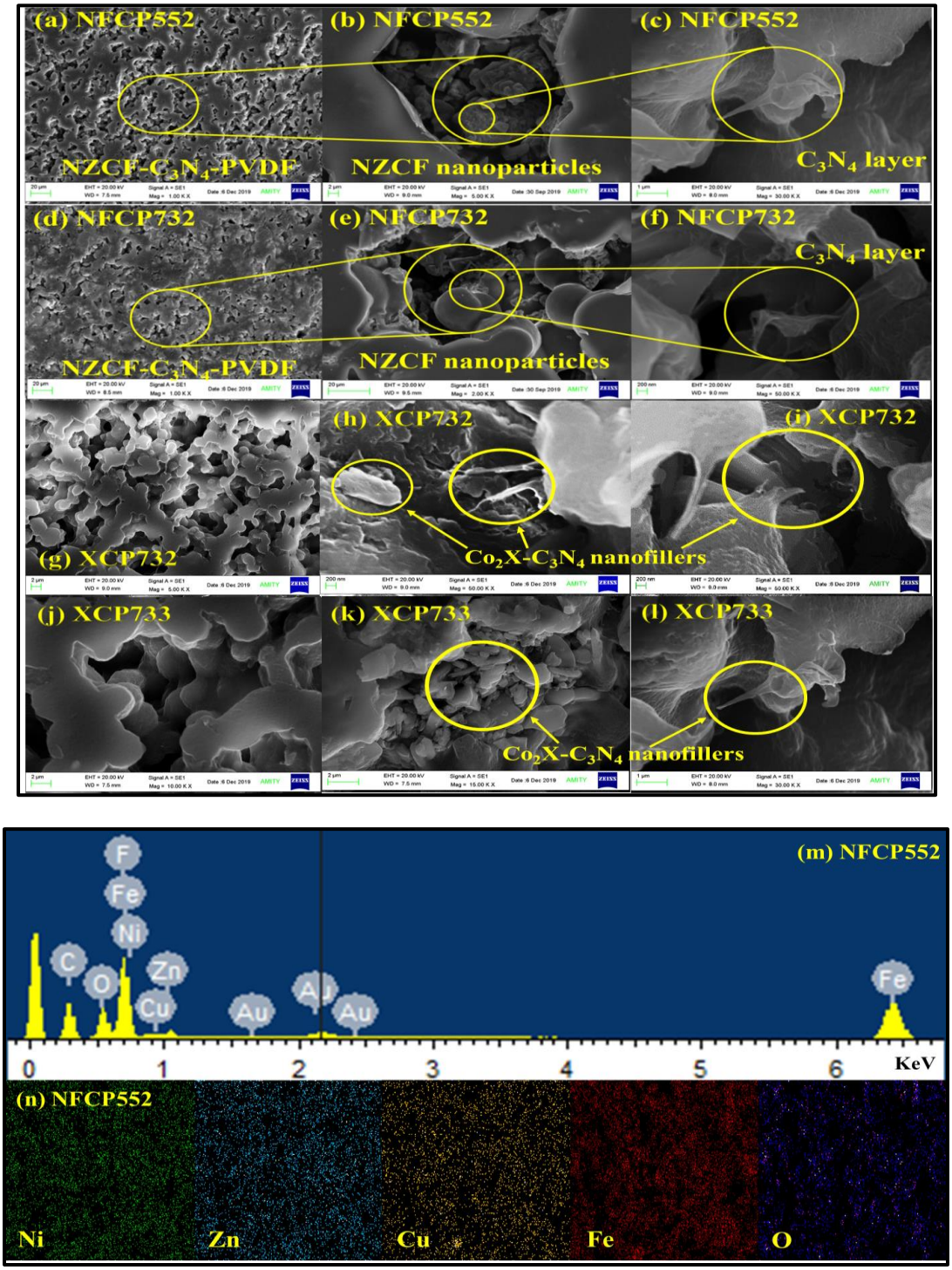

Figure 4.3: FESEM images of (a-c) NFCP552, (d-f) NFCP732, (g-i) XCP732, and (j-l) XCP733 nanocomposite films, (m, n) EDX spectra of NFCP552 and elemental mapping of NFCP552 nanocomposite film.

4.3.3 Chemical property study:

The FTIR study of bare PVDF and the nanocomposite films have been displayed in Figure 4.4(I and II), the presence of non-polar α-phase and the polar β-phase of the nanocomposite films have been observed and the corresponding peaks are also assigned in the given figure in the range of 1200-400 cm^{-1}. The different mode characteristic peaks of non-polar α-and polar β-phase of XCP732, XCP733, NFCP552, NFCP553, NFCP732 and NFCP733 have been listed and given in Table 4.1 [13-16]. Also, it is to be mentioned here that the several strong bands have been observed for all the nanocomposite films within the range of 2000–1100 cm^{-1}, signify the presence of stretching modes of CN heterocycles [17, 18]. The presence of these strong bands of XCP732, XCP733, NFCP552, NFCP553, NFCP732 and NFCP733 nanocomposite films clearly indicate that C_3N_4 semiconducting fillers are present inside the structure of PVDF. Now, the presence of both Co_2X-hexaferrite-C_3N_4 and NZCF-C_3N_4 nanoparticles with C_3N_4 semiconducting fillers are responsible for the formation of interfaces between the Co_2X-hexaferrite-C_3N_4 and NZCF-C_3N_4 binary fillers and the PVDF matrix. This electrostatic interaction between the Co_2X-hexaferrite-C_3N_4 and NZCF-C_3N_4 binary fillers and the PVDF matrix leads to the formation of aligned chains with all-trans-planar zig-zag (TTTT) conformation of all the nano composite films (XCP732, XCP733, NFCP552, NFCP553, NFCP732 and NFCP733), which on the other hand improves the fractional contribution of polar β-phase of PVDF in the nanocomposite films as compared to the non-polar α-phase. The β-phase fraction [F(β)%] of bare PVDF, XCP732, XCP733, NFCP552, NFCP553, NFCP732 and NFCP733 has been estimated using Lambert−Beer law

$$F(\beta) = \frac{A_\beta}{\left(\frac{K_\beta}{K_\alpha}\right)A_\alpha + A_\beta} \tag{4.2}$$

Here A_α and A_β are the absorbance at 773 cm^{-1} and 847 cm^{-1}, respectively, and K_α (6.1×10^4 cm^2mol^{-1}) and K_β (7.7×10^4 cm^2mol^{-1}) are the absorption coefficients at their respective wavenumbers. The enhancement of β-phase fraction [F(β)%] of the nanocomposite films has been observed due to the formation of more areas of interfaces between the Co_2X-hexaferrite-C_3N_4 and NZCF-C_3N_4 binary fillers and the PVDF matrix. Basically, the electrostatic interaction between the binary fillers and the CH_2 groups of PVDF matrix can produce a significant amount of aligned chains with all-trans-planar zigzag (TTTT) conformation, which will further enhance the β-phase fraction [F(β)%] of XCP732, XCP733, NFCP552, NFCP553, NFCP732 and NFCP733 nanocomposite materials as compared to the bare PVDF. This electrostatic interaction is mainly responsible for the enhancement of the polarization effect as well as the electroactive behaviour of XCP732 and XCP733 composite materials.

Table 4.1: FTIR peaks and corresponding data of bare PVDF, XCP732, XCP733, NFCP552, NFCP553, NFCP732 and NFCP733 nanocomposite films.

Sl. No.	**Sample name**	**α-phase (cm^{-1})**	**β-phase (cm^{-1})**	**CN absorption band (cm^{-1})**	***(F(β)%)***
1.	**PVDF**	496 (CF_2 waging)	520 (CF_2 stretching)	846 1081	36.9
		537 (CF_2 bending)	608 (CF_2 waging)	-	
		617 (CF_2 bending)	848 (CH_2 rocking, CF_2 stretching and skeletal C-C stretching)	-	
		768 (CF_2 skeletal bending)	1079 (CH_2 and CF_2 groups generated from the CH_2 rocking and CF_2 stretching)	-	

		815 (CH_2 rocking)		-	
		895 (CH_2 rocking)		-	
		970 (CH_2 rocking)		-	
2.	XCP732	same as above	same as above	1211 1289 1334 1344 1432 1550 1678	38.9
3.	XCP733	same as above	same as above	same as above	40.2
4.	NFCP552	same as above	same as above	1290 1340 1437 1685	44.3
5.	NFCP553	same as above	same as above	same as above	44.5
6.	NFCP732	same as above	same as above	same as above	45.2
7.	NFCP733	same as above	same as above	same as above	44.6

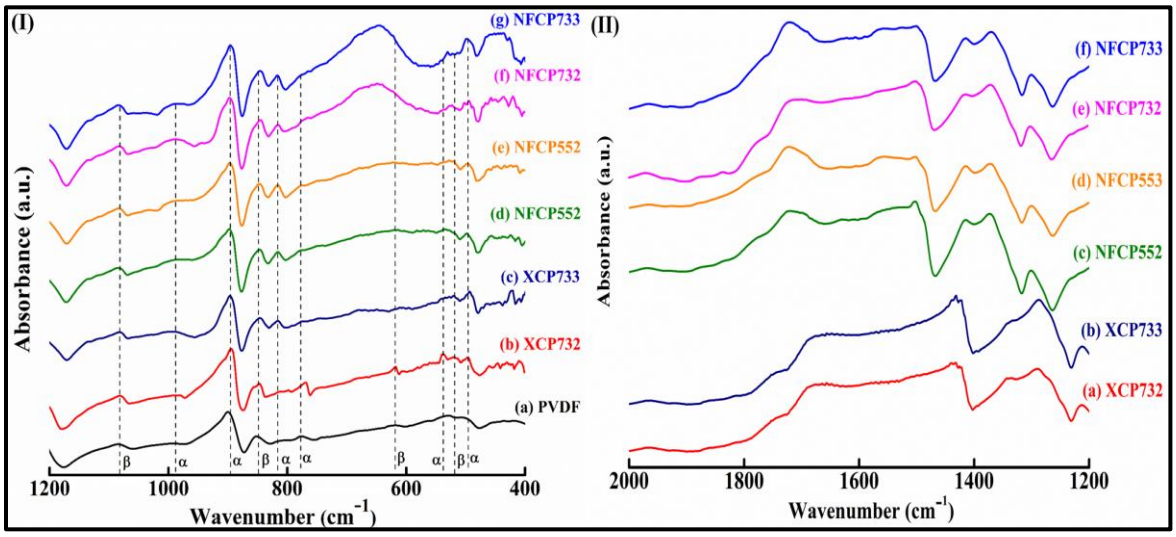

Figure 4.4: (I) FTIR spectra of (a) bare PVDF, (b) XCP732, (c) XCP73 (d) NFCP552, (e) NFCP553, (f) NFCP732 and (g) NFCP733 nanocomposite films in the range of 1200-400 cm^{-1} and (II) FTIR spectra of (a) XCP732, (b) XCP73 (c) NFCP552, (d) NFCP553, (e) NFCP732 and (f) NFCP733 nanocomposite films in the range of 2000-1100 cm^{-1}.

4.3.4 Magnetic property study:

In this chapter the magnetic response of Co_2X-hexaferrite-C_3N_4-PVDF and NZCF-C_3N_4-PVDF (XCP732, XCP733, NFCP553, NFCP7333) nanocomposite films have been investigated. The nanocomposite films show a clear hysteresis loop at RT which is clear evidence of having magnetic ordering in the representative nanocomposite films depicted in Figure 4.5(I and II). It has already been discussed in the experimental section of chapter 2 (**section 2.2.2.5**) that XCP733 and NFCP733 consist larger loading percentage of magnetic nanofillers as compared to NFCP553. So, it is expected to get a better magnetic response in NFCP733 as compared to XCP732 and NFCP553 nanocomposite films. In Figure 4.5(I)(a and b) it is observable that the M-H loops of XCP732, XCP733 are not completely saturated even when the applied magnetic field strength was 50,000 Oe but it has large coercive field this type of behaviour of the

magnetic nanocomposite films indicates the ferromagnetic behaviour. On the other hand Figure 4.5(II)(a and b) i.e. NFCP553, NFCP733 nanocomposite films shows relatively low coercivity and low retentivity, that indicates the superparamagnetic (SPM) behaviour of the nanocomposite films. The extracted magnetic information like, maximum magnetization, coercivity, and retentivity of XCP732, XCP733, NFCP553, NFCP733 have been listed in Table 4.2. The variation of maximum magnetization and coercivity of these magnetic nanocomposite films appears due to the variation of the Co_2X-hexaferrite and NZCF loading percentage in the matrix of PVDF. From the magnetic response study of these two representative nanocomposite films one thing can be confirmed that the other two nanocomposite films are also magnetic in nature at RT. This magnetic nature of the nanocomposite films signifies that all the nanocomposite films consist magnetic dipoles at RT and when these magnetic dipoles interact with the magnetic field vector of EM radiation attribute shielding effectiveness due to absorption (SE_A). The sufficiently high maximum magnetization and coercivity of the nanocomposite films make them a very good candidate for such kind of specific application in EM radiation absorption to combat against the pollution of excessive exposure of EM radiation in the GHz frequency range.

Table 4.2: Various magnetic parameters of XCP732, XCP733, NFCP553, NFCP733 nanocomposite films.

Sl. No.	Sample name	M_m (emu/g)	Hc (Oe)	Mr (emu/g)
1.	XCP732	9.63	1445	3.87
2.	XCP733	16.79	3366	10.29
3.	NFCP553	1.9	23	0.033

4.	NFCP733	9.7	24	0.190

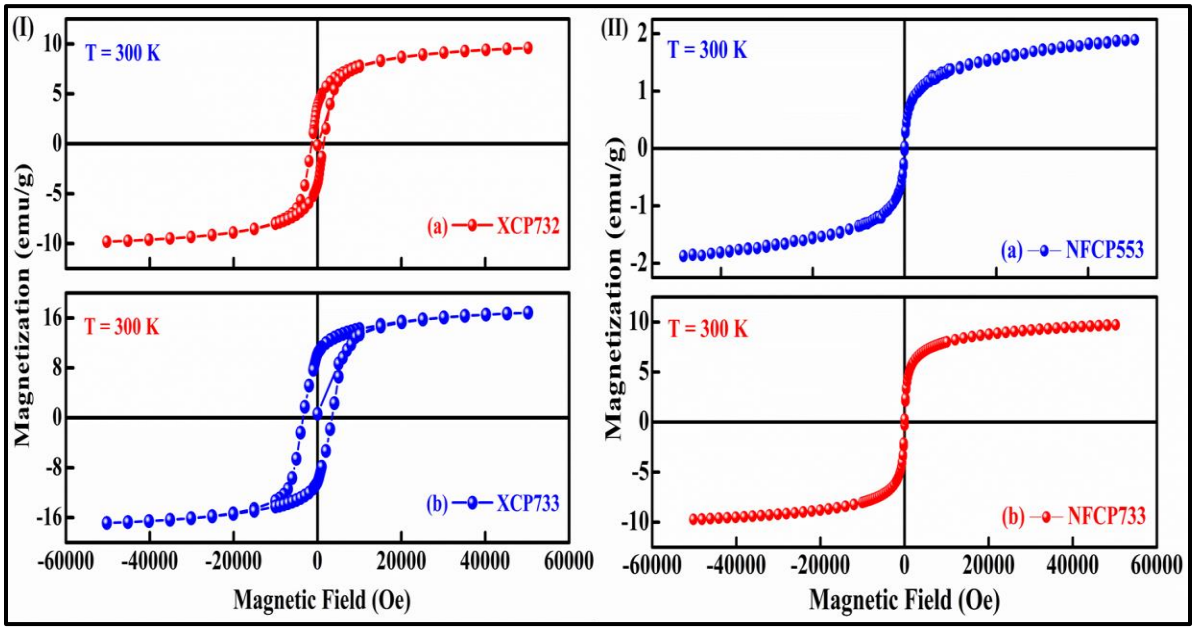

Figure 4.5: Magnetic M-H loops of (I) (a) XCP732, (b) XCP733, (II) (a) NFCP553 and (b) NFCP733 nanocomposite films at RT.

4.3.5 Dielectric response study:

The presence of complex dielectric permittivity and the types of polarizations responsible for the enhancement of the complex dielectric permittivity in bare PVDF and in the nanocomposite films (XCP732, XCP733, NFCP552, NFCP553, NFCP732 and NFCP733) have been investigated in this dielectric study. The variation of the real part of complex dielectric permittivity (ε′) and the imaginary part of complex dielectric permittivity (ε″) of the nanocomposite with respect to frequency of the external electric field (40 Hz to 10^6 Hz) at three different temperatures (30, 50, and 100 °C). The real part of complex dielectric permittivity (ε′) and the imaginary part of complex dielectric permittivity (ε″) of all the samples have been calculated by using the formula [19]

$$\varepsilon' = \frac{Cd}{\varepsilon_0 A} \tag{4.3}$$

$$\text{and } \varepsilon'' = \varepsilon' \times tan\delta \tag{4.4}$$

Here, C is the capacitance of the films, d and A are the thickness and area, respectively, of the films and ε_0 is the free space permittivity. Usually, the frequency dependent dielectric permittivity of the PVDF based nanocomposite films can be explained by two major phenomena such as the improvement of electroactive β-phase crystallization of nanofillers incorporated PVDF nanocomposite films and the second one is the Maxwell-Wagner-Sillers interfacial polarization [20-23]. In this particular synthesis procedure (the solution casting method also known as doctor's blade method), the formation of space charge polarization and other types of polarization at the interfaces inside the nanocomposite films are responsible for the variation of the electroactive β-phase crystallization. The nanocomposite films and bare PVDF show a significant dielectric response in the low frequency region, and as the temperature increases from 30 °C to 100 °C, the value of ε′ has been enhanced for all the materials keeping their nature of variation constant. Therefore, it can be inferred that all the materials have significant amount of frequency response dielectric polarizations. The value of ε′ of NFCP553 and NFCP552 shows enhancement as compared to the bare PVDF due to the improvement of the polar β-phase crystallization of the PVDF matrix in the nanocomposite films as well as the improvement of space charge polarization at the interfaces of the composite materials corresponding to the Maxwell-Wagner-Sillers interfacial polarization effect. In NFCP552 and NFCP553 nanocomposite films, the greater loading percentage of C_3N_4 semiconducting fillers inside the matrix of PVDF as compared to the NFCP732 and NFCP733 can provide more conduction charges at the interfaces of the NZCF-C_3N_4-PVDF nanocomposite films and this

can make the dielectric permittivity significantly high for NFCP552 and NFCP553. With the increase in temperature from 30 ^{o}C to 100 ^{o}C, C_3N_4 semiconducting fillers inside NFCP552 and NFCP553 nanocomposite films can contribute more conduction electron at the interfaces and thereby improves the dielectric permittivity of these nanocomposite films largely as shown in Figures 4.6(I). This conduction charge contribution by the C_3N_4 semiconducting fillers at RT inside the matrix of PVDF improves the resultant polarization effect of the nanocomposite films and it could help us to get better response in the field of magneto-dielectric applications. Also, according to the Debye theory, the real part of complex permittivity can be related to temperature as [24],

$$\varepsilon' = \varepsilon_\infty + \frac{\varepsilon_S - \varepsilon_\infty}{1-\omega^2\tau(T)^2} \tag{4.5}$$

$$\tau(T) = \tau_0 e^{(E_a/kT)} \tag{4.6}$$

where ε' is the real part of complex permittivity, ε_∞ is the high frequency limit of permittivity, ε_s is the static permittivity, ω is the angular frequency, E_a is the activation energy and τ_0 and $\tau(T)$ represents pre-factor and temperature dependent relaxation time and k is the Boltzmann's constant.

The variation of the imaginary part of complex dielectric permittivity (ε″) as a function of frequency at three different temperatures (30, 50, and 100 °C) has been depicted in Figure 4.6(II). The high value of ε″, specifically for a NFCP552 and NFCP553 nanocomposite films at low frequencies and its reduction with the increase in the frequency, also substantiates the presence of various forms of the electric dipolar polarization effect inside the structure of the nanocomposite films. The response of the electric dipoles under the influence of the frequency can generate thermal energy at the cost of the electrical energy corresponding to the external

electric field, and this loss of electrical energy in the form of thermal energy inside the structure of the nanocomposite films is responsible for the improvement of the shielding effectiveness of absorption of the nanocomposite films.

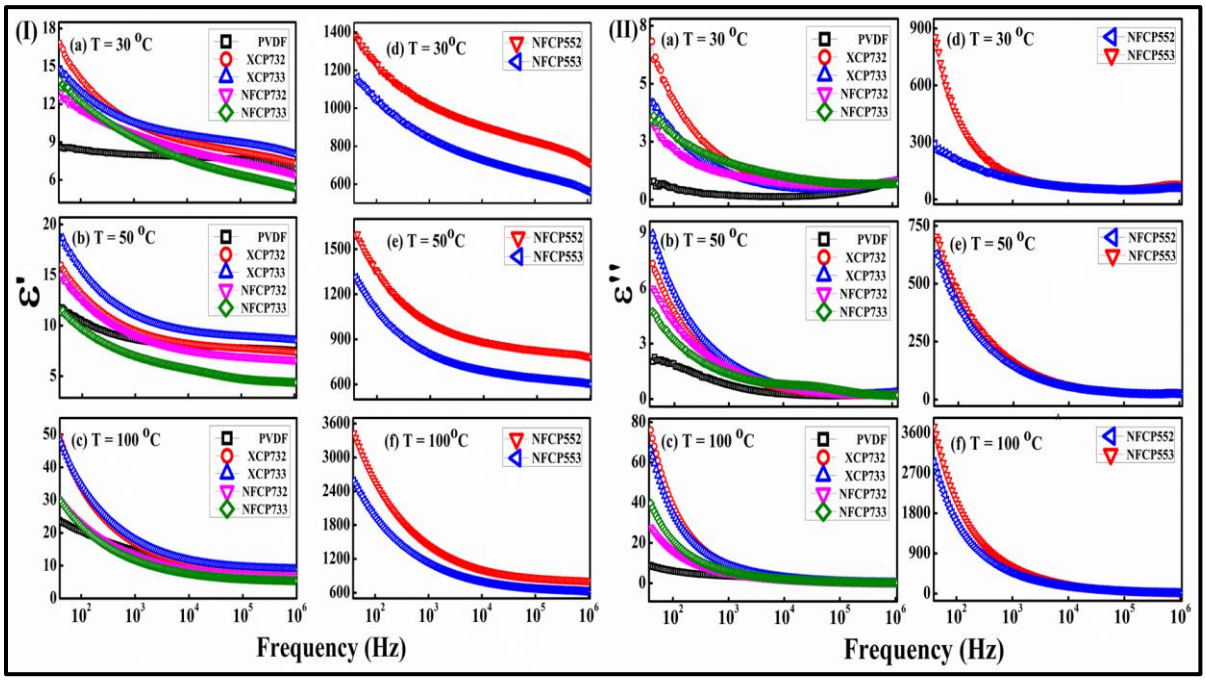

Figure 4.6: (I) Variation of real part of dielectric constant (ε′) and (II) imaginary part of dielectric constant (ε″) with frequency of bare PVDF, XCP732, XCP733, NFCP552, NFCP553, NFCP732 and NFCP733 nanocomposite films at (a) 30 °C, (b) 50 °C and (c) 100 °C and NFCP552 and NFCP553 nanocomposite films at (d) 30 °C, (e) 50 °C and (f) 100 °C.

The dielectric dissipation factor or the loss tangent (tan δ) and the ac conductivity (σ_{ac}) responses of bare PVDF and the nanocomposite films (XCP732, XCP733, NFCP552, NFCP553, NFCP732 and NFCP733) as a function of frequency of the external electric field at three different temperatures (30, 50, and 100 °C) and the corresponding graphs are depicted in Figure 4.7(I). The loss tangent (tan δ) and the ac conductivity (σ_{ac}) of the nanocomposite films have been estimated by using the formula [25]

$$tan\delta = \frac{\varepsilon''}{\varepsilon'} \quad (4.7)$$

$$\sigma_{ac} = 2\pi f \varepsilon_0 \varepsilon' \tan\delta \quad (4.8)$$

Where, f is the applied frequency of external ac field. The observed variation of frequency dependent dielectric loss tangent (tan δ) depends on the induced space charge polarization. From the tanδ study it is quite clear to us that all the nanocomposite films are highly responsive in the frequency range of 40 Hz to 10^6 Hz at three different temperatures (30, 50 and 100 ^oC), the value of tanδ decrease with increase of frequency but with the increase of loading percentage of semiconducting fillers (C_3N_4) inside the matrix of PVDF the value of tanδ increase significantly. Now the comparatively high value of tanδ for Co_2X-hexaferrite-C_3N_4-PVDF and NZCF-C_3N_4-PVDF nanocomposite films is due to the presence of C_3N_4 acts as a 2-D semiconducting material and this semiconducting material improves the polarization loss corresponding to the space charge polarization at the interfaces as well as the conduction loss inside the composite structures. Thus, the presence of C_3N_4 semiconducting fillers inside the matrix of PVDF is actually responsible for the enhancement of the tan δ of the nanocomposite films at all three different temperatures and the improvement of the tanδ can make these Co_2X-hexaferrite-C_3N_4-PVDF and NZCF-C_3N_4-PVDF nanocomposite films suitable for the shielding effectiveness in the microwave region of frequency.

The ac conductivity (σ_{ac}) of Co_2X-hexaferrite-C_3N_4-PVDF and NZCF-C_3N_4-PVDF nanocomposite films and bare PVDF has been observed from Figure 4.7(II). At the frequency region of 40 to 10^6 Hz corresponding to all three different temperatures the value of σ_{ac} has been enhanced largely at high frequency region. Firstly, the observed variation of σ_{ac} is short range conductivity in nature and this type of conductivity can be found when the charge carriers move inside the material structure under the influence of external alternating electric field. It is

now clear to us that C_3N_4 semiconducting fillers inside PVDF matrix can act as the charge source at RT and thereby it can provide charge carriers at the interfaces of the nanocomposite films. This entire process can improve the dipolar polarization effects. Now, the dipolar polarizations inside nanocomposite films can generate short-range σ_{ac} in the frequency range of 40 Hz to 10^6 Hz at all different temperatures, though, with the increase in temperature from 30 ^oC to 100 ^oC this short-range σ_{ac} get decreased. The variation of short-range σ_{ac} in the lower frequency range has been appeared due to the interfacial polarization effect of Co_2X-hexaferrite-C_3N_4-PVDF and NZCF-C_3N_4-PVDF nanocomposite films and it has been enhanced at high frequency range due to presence of other types of dipolar polarization effects such as ionic polarization, electronic polarization, which are temporary in nature. Also, this short-range σ_{ac} in the frequency range of 40 Hz to 10^6 Hz depends on both Maxwell-Wagner-Sillers interfacial polarization as well as other types of dipolar responses due to the presence of and influenced by the semiconducting C_3N_4 fillers inside the matrix of PVDF. Thus, from the dielectric response study, it is quite clear that the incorporation of semiconducting C_3N_4 fillers with different loading percentage inside PVDF matrix generates various dipolar effects due to which the EMI shielding ability of nanocomposite films is expected to be more in the GHz frequency range.

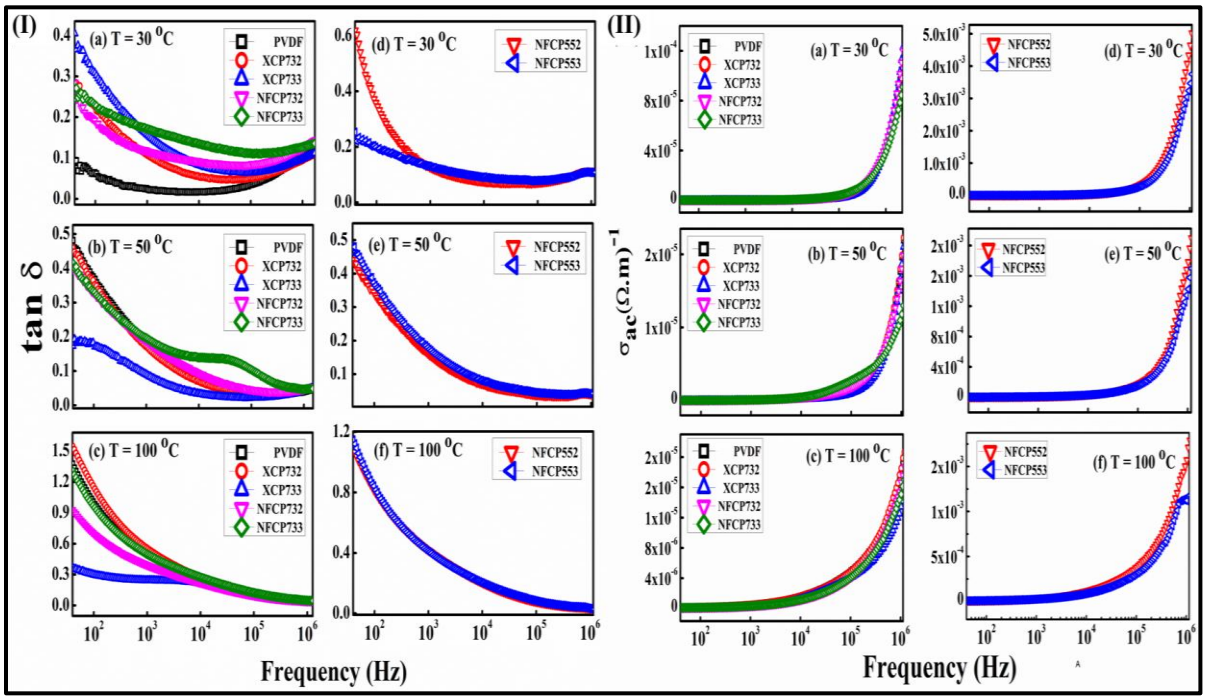

Figure 4.7: (I) Variation of tangent loss (tanδ) and ac conductivity (σ_{ac}) with frequency of bare PVDF, XCP732, XCP733, NFCP552, NFCP553, NFCP732 and NFCP733 nanocomposite films at (a) 30 ^{o}C, (b) 50 ^{o}C and (c) 100 ^{o}C and NFCP552 and NFCP553 nanocomposite films at (d) 30 ^{o}C, (e) 50 ^{o}C and (f) 100 ^{o}C.

4.3.6 Study of EMI shielding property:

In order to get a proper understanding about the usefulness of the nanocomposite films (XCP732, XCP733, NFCP552, NFCP553, NFCP732 and NFCP733) for shielding effectiveness against electromagnetic radiation as well as to understand the importance of different component materials and their contributions for the same. The shielding effectiveness study has been conducted in this chapter for X-band (8-12 GHz) and K_u-band (12-18 GHz) of microwave radiation. This frequency range i.e., 8-18 GHz is technically known as super high frequency (SHF) region. In this chapter the shielding effectiveness of the nanocomposite films has been considered for shielding effectiveness due to absorption (SE_A), shielding effectiveness due to

reflection (SE_R) and shielding effectiveness for multiple reflections (SE_{MR}) [26]. The overall shielding effectiveness of the nanocomposite films can be displayed in three different ways and they are shielding effectiveness due to absorption (SE_A), shielding effectiveness due to reflection (SE_R) and the total shielding effectiveness (SE_T). The SE_T of the nanocomposite films has been estimated by using the equation

$$SE_T\ (dB) = -10 \log_{10}\left(\frac{P_t}{P_0}\right) = SE_A + SE_R + SE_{MR} \quad (4.9)$$

However, the shielding effectiveness by multiple reflections (SE_{MR}) can be neglected for these nanocomposite films as their thicknesses are more than the skin depth of the incident microwave radiation in the frequency range of 8-18 GHz. Thus, the total shielding effectiveness (SE_T) of nanocomposite films given in equation (9) can be further expressed as [27, 28]

$$SE_T\ (dB) = -10 \log_{10}\left(\frac{P_t}{P_0}\right) = SE_A + SE_R \quad (4.10)$$

Where, P_t represents the transmitted power and P_0 represents the incident power of microwave radiations. The estimation of shielding effectiveness as SE_A and SE_R in the frequency range of 4-18 GHz can be done by the following equations [29]

$$SE_A\ (dB) = -10 \log_{10}\left(\frac{1 - |S_{11}|^2}{|S_{12}|^2}\right) \quad (4.11)$$

$$SE_R\ (dB) = -10 \log_{10}\left(\frac{1}{1 - |S_{11}|^2}\right) \quad (4.12)$$

Here, S represent the scattering parameters i.e., S_{11} (reflection coefficient) and S_{21} transmission coefficient). Figure 4.8(a, d, g, and j) represent the SE_A of XCP732, XCP733, NFCP552, NFCP553, NFCP732 and NFCP733 nanocomposite films for X-band and K_u-band in the frequency range of 8-18 GHz. The maximum SE_A values of -41.8 dB at a matching frequency of 9.9 GHz and -62.41 dB at a matching frequency of 14 GHz have been observed for XCP733 and XCP732 nanocomposite films, respectively and the maximum value of SE_A is -44.23 dB

has been observed for NFCP552 at a matching frequency of 11.9 GHz -61.00 dB has been observed for NFCP552 at a matching frequency of 14.1 GHz. These values are sufficiently larger than those of the shielding effectiveness of approximately -37.50 dB at a matching frequency of 11.5 GHz and -47.02 dB at a matching frequency of 14.5 GHz for the only Co_2X-hexaferrite nanofiller-incorporated PVDF matrix (XP). It is very interesting to mention here that the improvement in SE_A for XCP732 and XCP733 nanocomposite films as well as NFCP552 as compared to the XP nanocomposite film has been found due the presence of C_3N_4 nanofillers along with the Co_2X-hexaferrite and NZCF nanofillers inside the PVDF matrix. Now, the interaction between the magnetic field vector of microwave radiation and the magnetic dipoles of Co_2X-hexaferrite and NZCF nanoparticles is responsible for the generation of this high value of shielding effectiveness due to absorption (SE_A) of nanocomposite films. The significant amount of complex relative permeability (μ^*) and relative complex permittivity (ε^*) of Co_2X-hexaferrite and NZCF nanoparticles in this GHz frequency very much effective in interacting with EM radiation in the GHz frequency range and therefore converting the EM energy into heat energy by producing the absorption phenomenon. Also, the formation of electric dipolar polarization due to the presence of semiconducting C_3N_4 nanofillers in the matrix of PVDF can interact with the electric field vector of microwave radiation and, therefore, this interaction can also convert a significant amount of electromagnetic energy into heat energy. Therefore, the presence of C_3N_4 semiconducting fillers inside the matrix of PVDF in association with magnetic Co_2X-hexaferrite and NZCF nanoparticles can produce eddies of carrier charges and the corresponding eddy current loss inside the structure of PVDF [30]. Thus, for the overall improvement in SE_A of XCP732, XCP733, NFCP552, NFCP553, NFCP732 and NFCP733 nanocomposite films, the composition of Co_2X-hexaferrite-C_3N_4 and NZCF-C_3N_4

binary fillers plays a significant role. Now, from Figure 4.8(b, e, h, and k), the maximum SE_R of -33.64 dB at matching frequencies of 11.7 GHz for XCP733 and -33.81 dB at matching frequencies of 13.05 GHz for XCP732 nanocomposite films, on the other hand, -32.20 dB at a matching frequency of 11.99 GHz for NFCP732 and -33.91 dB has been found for NFCP552 at a matching frequency of 15.80 GHz has been found. The interaction between the surface charges and the electric field vector of the incident EM radiation generates resonance at a certain frequency of external EM radiation of the bound charges present on the surface and improves the shielding effectiveness due to reflection (SE_R) of XCP732, XCP733, NFCP552, NFCP553, NFCP732 and NFCP733 nanocomposite films. Usually, high reflection phenomenon depends on the matching of the frequency of the incident EM radiation with the plasmonic oscillation related to the surface conduction electron. This effect will be found maximum for the materials that consist large conduction electron at the surface and these surface conduction electrons related plasma oscillation [31]. In the present case, moderate amount of conduction charges is found right below the surface of the Co_2X-hexaferrite-C_3N_4-PVDF and NZCF-C_3N_4-PVDF nanocomposite films due to the presence of the C_3N_4 semiconducting fillers and this effect is even significant in the present case due to the presence of large surface to volume ratio of the binary fillers [30]. Now, the interaction between the electric field vector of the incident EM radiation and the conduction electron can produce reflection (SE_R) phenomena but the value of reflection (SE_R) is quite low as compared to the shielding effectiveness due to absorption (SE_A), and that confirm that the nanocomposite films (XCP732, XCP733, NFCP552, NFCP553, NFCP732 and NFCP733) are very good material for absorbing the EM radiation. Finally, the maximum values of SE_T observed from Figure 4.8(c, f, i, and l), -72.5 dB at a matching frequency of 9.9 GHz and -88 dB at a matching frequency of 14 GHz for XCP733 and XCP732

nanocomposite films, respectively, and -73.01 dB at a matching frequency of 9.5 GHz and -89.42 dB at a matching frequency of 14.1 GHz has been observed for NFCP732 and NFCP552 nanocomposite films. All the values of respective samples for SE_A, SE_R and SE_T have been given in Table 4.3. Thus, the presence of larger loading percentage of C_3N_4 semiconducting fillers inside the structure of nanocomposite films helps to provide better response of SE_T at comparatively high frequency region. Therefore, undoubtedly it can be conferred that these high shielding effectiveness corresponding to the absorption (SE_A), reflection (SE_R) and the total shielding effectiveness (SE_T) of these nanocomposite films not only resulted due to the presence of magnetic nanofiller with the PVDF matrix but the unique idea of introduction of C_3N_4 semiconducting fillers materials inside the matrix of PVDF along with Co_2X-hexaferrite and NZCF magnetic nanofiller has made all these nanocomposite films highly efficient for the fabrication of advanced microwave absorbers to fight against the pollution of excessive exposure of EM radiation in the GHz frequency range.

Table 4.3: Various parameters related to shielding effectiveness study of XP, XCP732, XCP733, NFCP552, NFCP553, NFCP732 and NFCP733 nanocomposite films.

Sl. No.	Sample name	Shielding effectiveness (dB)	X-band (8-12 GHz)	K_u-band (12-18 GHz)
1.	XP	$SE_{A(max)}$	-37.50	-47.10
		$SE_{R(max)}$	-32.00	-32.50
		$SE_{T(max)}$	-65.50	-75.00
2.	XCP732	$SE_{A(max)}$	-41.80	-62.41
		$SE_{R(max)}$	-31.35	-33.81
		$SE_{T(max)}$	69.72	-88.00
3.	XCP733	$SE_{A(max)}$	-39.43	-60.00
		$SE_{R(max)}$	-33.64	-33.89

		$SE_{T(max)}$	-72.50	-87.30
4.	NFCP552	$SE_{A(max)}$	-44.23	-61.00
		$SE_{R(max)}$	-31.66	-33.91
		$SE_{T(max)}$	-70.95	-89.42
5.	NFCP553	$SE_{A(max)}$	-38.72	-56.17
		$SE_{R(max)}$	-30.91	-33.10
		$SE_{T(max)}$	-68.31	-83.94
6.	NFCP732	$SE_{A(max)}$	-42.66	-58.82
		$SE_{R(max)}$	-32.20	-32.73
		$SE_{T(max)}$	-73.01	-85.74
7.	NFCP733	$SE_{A(max)}$	-40.85	-53.47
		$SE_{R(max)}$	-31.06	-33.47
		$SE_{T(max)}$	-68.92	-80.23

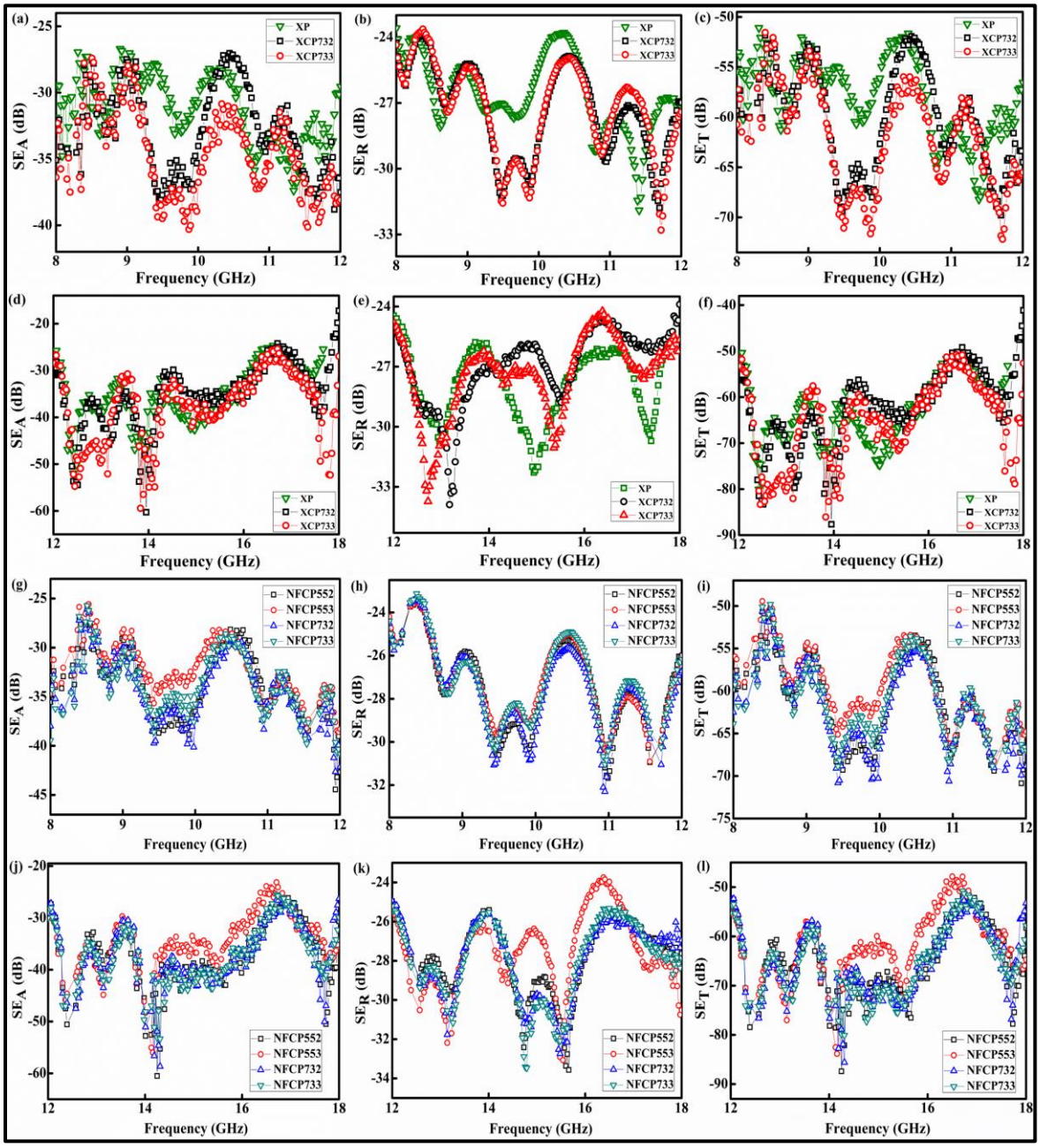

Figure 4.8: (a, d, g, and j) Shielding effectiveness by absorption (SE_A), (b, e, h, and k) shielding effectiveness by reflection (SE_R), and (c, f, i, and l) total shielding effectiveness (SE_T) of XP, XCP732, XCP733, NFCP552, NFCP553, NFCP732 and NFCP733 nanocomposite films in frequency ranges of 8-12 and 12-18 GHz.

4.4 Conclusion:

In this chapter, Co_2X-hexaferrite-C_3N_4 and NZCF-C_3N_4 binary fillers incorporated PVDF nanocomposite system has been prepared by a very simple solution casting method and structural, microstructural, and chemical investigations have been done. All these measurements show that the nanocomposite films have been formed with proper crystallographic phase, morphology, and chemical nature. The high permeability of Co_2X-hexaferrite-C_3N_4-PVDF and NZCF-C_3N_4-PVDF nanocomposite films simultaneously act to improve the shielding effectiveness due to absorption (SE_A). A maximum SE_A of -62.41 dB at a matching frequency of 14 GHz and SE_T of -89.42 dB at a matching frequency of 14.1 GHz for the nanocomposite films has been observed with attenuation of >99.999999%. S0, the presence of Thus, the presence of larger loading percentage of C_3N_4 semiconducting fillers inside the structure of nanocomposite films helps to provide better response of SE_T at comparatively high frequency region. Thus, indisputably it can be concluded that the high value of total shielding effectiveness (SE_T) of the present nanocomposite films not only appeared due to the presence of magnetic nanofiller (Co_2X-hexaferrite and NZCF nanoparticles) with the PVDF matrix but the exceptional idea of consideration of C_3N_4 semiconducting fillers inside the matrix of PVDF along with magnetic nanofiller has made Co_2X-hexaferrite-C_3N_4-PVDF and NZCF-C_3N_4-PVDF nanocomposite films highly efficient for the fabrication of microwave absorber to fight against electromagnetic pollution.

4.5 References:

[1] Zhao B, Zhao C, Li R, Hamidinejad SM, Park CB., ACS Appl. Mater. Interfaces, 9:20873-84 (2006).

[2] Li B.-W, Shen Y, Yue Z.-X, Nan C.-W., Appl. Phys. Lett., 89:132504-06 (2006).

[3] Phadtare V.D, Parale V.G, Lee K.-Y, Kim T, Puri V.R, Park H.H., J. Alloys Compd., 805:120-9 (2019).

[4] Ismail M.M, Rafeeq S.N, Sulaiman J.M.A, Mandal A., Appl. Phys. A., 124:380-392 (2018).

[5] Caltun O.F, Spinu L, Stancu A., OPTOELECTRON ADV MAT.,4(2):337-40 (2002).

[6] Xuan Y, Li Q, Yang G., J. Magn. Magn. Mater., 312(2):464-69 (2007).

[7] Li Q, Song J, Saura-Múzquiz M, Besenbacher F, Christensen M, Dong M, Scientific Reports, 6:25985-91 (2016).

[8] Kaur T, Kumar S, Bhat B.H, Srivastava A.K., J. Mater. Research, 30:2753-62 (2015).

[9] Sareshkeh A.T, Dorraji M.S.S, Rasoulifard M.H., Progress in Organic Coatings, 125:472-80 (2018).

[10] Sutradhar S, Das S, Roychowdhury A, Das D, Chakrabarti P.K., Mater. Sci. Eng. B, 196:44-52 (2015).

[11] Saha P, Das S, Sutradhar S., J. Appl. Phys., 124:045303-12 (2018).

[12] Saha P, Debnath T, Das S, Chatterjee S, Sutradhar S., Mater. Sci. Eng. B., 245:17-29 (2019).

[13] Prabhakaran T, Hemalatha J., Sci. Adv. Mater., 6(7):1313-21 (2014).

[14] Cai X, Lei T, Sun D, Lin L., RSC Adv., 7:15382-89 (2017).

[15] Prabhakaran T, Hemalatha J., RSC Adv.,6:1-7 (2016).

[16] Prabhakaran T, Hemalatha J., J. Mater. Chem. Phys., 137:781-87 (2013).

[17] Dong F, Li Y, Wang Z, Ho W.-K., Appl. Surf. Sci., 358:393-403 (2015).

[18] Zhu B, Xia P, Li Y, Ho W, Yu J., Appl. Surf. Sci., 391:175-83 (2016).

[19] Das S, Bandyopadhyay A, Saha P, Das S, Sutradhar S., J. Alloys Compd.,749:1-9 (2018).

[20] Wagner K.W., Ann. Phys., 40:817-19 (1973).

[21] Maxwell, J., Oxford University Press, New York (1973).

[22] Koops C.G., Phys. Rev., 83:121-24 (1951).

[23] Prodromakis T, Papavassiliou C., Appl. Surf. Sci., 255(15):6989-94 (2009).

[24] A. K. Jonscher, J. Phys. D: Appl. Phys. 32, R57 (1999).

[25] Ansari S.A, Nisar A, Fatma B, Khan W, Chaman M, Azam A, Naqvi A.H., Mater. Res. Bull., 47:4161-68 (2012).

[26] Hekmatara H, Seifi M, Forooraghi K, Mirzaee S., Phys. Chem. Chem. Phys., 16:24069-75 (2014).

[27] Ohlan A, Singh K, Chandra A, Dhawan S.K., ACS Appl. Mater. Interfaces, 2:927-33 (2010).

[28] Chung DDL., Carbon, 39(2):279-85 (2001).

[29] Bhattacharjee Y, Chatterjee D, Bose S., ACS Appl. Mater. Interfaces, 10:30762-73 (2018).

[30] Song W.L, Gong C, Li H, Cheng X.-D, Chen M, Yuan X, Chen H, Yang Y, Fang D., ACS Appl. Mater. Interfaces, 9:36119-29 (2017).

[31] Biswas S, Kar G.P, Bose S., Phys. Chem. Chem. Phys., 17:27698-712 (2015).

Chapter: 5

Synthesis of multi-layer structure of hexaferrite-rGO binary nanofillers incorporated PVDF nanocomposite system and the study of their EMI shielding behaviour

Chapter 5:

5.1 Introduction:

Electromagnetic (EM) pollution associated with the microwave radiation coming out from wireless telecommunication systems and electronic devices is responsible for many health issues of humans, animals and plants that we have already discusses in the previous chapter. However, these adversative effects of EM pollution on biological systems can be restricted effectively by the use of microwave absorber or EMI shielding materials. Moreover, the requirement of camouflage/stealth mechanism for military equipment (i.e., reduction of radar signature associated with ships, aircrafts, submarines, and tanks) and the protection of commercial equipment (i.e.; low EMI among various components of printed circuit board (PCB)) has enhanced the research and development (R&D) on the materials having EM wave absorption property. Polymer based nanocomposite films containing inorganic components have more suitable due to some of its excellent features needed for the generation of high microwave absorption (MA) or shielding effectiveness (SE) [1, 2]. In the field of shielding effectiveness research work, magnetic nanofillers such as ferrite and/or hexaferrite based polymer nanocomposite films have been extensively studied with significantly large EMI shielding effectiveness and attenuation [3, 4]. In the previous chapter (Chapter 4) the importance of conducting nanofillers along with magnetic ferrite/hexaferrites for the EMI shielding study has been discussed. Now, the specific hexaferrite material i.e. Co_2Z ($Ba_3Co_2Fe_{24}O_{41}$) is highly significant in the realm of microwave absorption because of its exceptional magnetic characteristics at elevated frequencies. The Co_2Z-hexaferrite is highly intriguing for microwave research due to its spontaneous polarization and planar magnetic anisotropy. Along with Co_2Z-hexaferrite, the reduced graphene oxide (rGO) of conducting in

nature has been considered due to its notable functional features that include strong chemical reactivity, mechanical strength, optical and electrical adjustability, thermally conducting, and large specific area [5]. Internal network has been developed by the overlapping rGO layers decorated with Co_2Z-hexaferrite amidst the local contact regions made with PVDF chain for all the corresponding nanocomposite films [6]. In order to achieve dielectric losses in the GHz frequency range and maximize the interfacial area inside PVDF matrix, reduced graphene oxide (rGO) is the most suitable material to accompany the magnetic Co_2Z-hexaferrites for microwave shielding applications. The high frequency permeability and permittivity is an important study to determine the EMI shielding performance of the materials. So, the synergistic effects of Co_2Z-hexaferrite, rGO and PVDF contributes highly to enhance the permeability and permittivity of the nanocomposite films at GHz frequency range. Therefore, we have enriched the EMI shielding effectiveness in term of absorption (SE_A) by using the appropriate proportion of Co_2Z-hexaferrite and rGO binary nanofillers in the PVDF matrix. Interestingly, along with permeability and permittivity the proper thickness of the nanocomposite film can also improve the shielding effectiveness due to absorption (SE_A). Due to this reason, in this chapter we have used multi-layer nanocomposite film to improve the SE_A of the nanocomposite films for this unique composition.

These multi-layer rGO-Co_2Z-PVDF laminated nanocomposite film for superior SE_A can be made possible by the selection of proper thickness of the resultant nanocomposite materials. The multi-layer rGO-Co_2Z-PVDF nanocomposite film facilitates the presence of extra interfaces between each layer, resulting in an increase of polarization-assisted losses. Such additional dissipative mechanisms are absent for a mono-layer of these shielding materials. Furthermore, the main advantage of employing multiple layers within a particular frequency

range, as opposed to a single layer with a specific quantity of filler material, is the capacity to modify the absorption loss (SE_A) in decibels (dB) which is written as $SE_A = 20\log(e^{-\gamma d})$ where, γ represents the complex wave propagation constant and d represents thickness of the shielding materials [7]. Therefore, the multi-layer exhibits superior absorption performance compared to the mono-layer. When an electromagnetic wave enters between the layers of consecutive mono-layer structure, it will experience internal reflections as it passes through each subsequent interior layer. The internal reflection of EM waves from each layer present inside the multi-layer structure will cease after the wave is absorbed by the subsequent internal layers of multi-layer structure of rGO-Co_2Z-PVDF nanocomposite systems. In this study multi-layer laminated nanocomposite film can be considered over the same of mono-layer to find their effect on shielding effectiveness behaviour. Therefore, in this study mono-layer and novel multi-layer laminated nanocomposite films containing binary nanofillers of rGO and Co_2Z-hexaferrite have been fabricated and their EMI shielding effectiveness properties have also been investigated. This study also shows the superior EMI shielding effectiveness in the frequency range of 12-18 GHz corresponding to the multi-layer structures of rGO-Co_2Z-PVDF laminated nanocomposite films.

5.2 Experimental:

5.2.1 Materials:

The reduced Graphene oxide (rGO) were synthesised by reducing graphene oxide with the help of the following chemicals for preparation: graphite fine powder (Loba Chemie), Sodium nitrate $NaNO_3$ (Merck Germany, purified), sulphuric acid (H_2SO_4) (98% concentrated, Merck), potassium permanganate ($KMnO_4$) (Loba Chemie India, 99%), hydrogen peroxide (H_2O_2) (30% concentrated, Merck), hydrochloric acid (HCl) (35% concentrated, Merck), Hydrazine

hydrate (made in Germany, Sigma-Aldrich). Co_2Z-hexaferrite having the composition $Ba_3Co_2Fe_{24}O_{41}$ were fabricated using sol-gel route of synthesis method. The chemicals used for this route synthesis include iron (III) nitrate nonahydrate ($Fe(NO_3)_3.9H_2O$) (Merck Germany, 99%), cobalt (II) nitrate hexahydrate ($Co(NO_3)_2.6H_2O$) (Merck Germany, 99%), barium (II) nitrate ($Ba(NO_3)_2$) (Merck Germany, 99%), citric acid ($C_6H_8O_7$) and ethanol (C_2H_5OH). Thus, the binary fillers rGO-Co_2Z incorporated inside the matrix of PVDF to obtain the laminated nanocomposite film, using solution casting method, involving the chemicals Poly(vinylidene) difluoride (PVDF) pellets (molecular weight Mn: 107,000, Mw: 275,000 (hpc), Aldrich, Germany) and N, N-dimethyl formamide (DMF) (Merck, India). All the chemicals used for synthesis are of analytical grade.

5.2.2 Synthesis of chemically reduced graphene oxide:

Graphene oxide (GO) was fabricated via modified Hummer's method [8], The details of this process have been discussed in in chapter 2 (**section: 22.2.2.2** Synthesis of reduce graphene oxide (rGO) by modified Hummer's method). The dried GO powder was dispersed in milli-Q (1 mg/ml) and hydrazine hydrate (1ml for 50 mg of GO) was added to the solution under continuous stirring and maintaining the temperature around 80 °C. After 12 h stirring, the resultant suspension was washed with distilled water to adjust the pH of the sample. The resultant sample was then finally dried in a hot air oven, and thus reduced graphene oxide (rGO) was obtained.

5.2.3 Synthesis of Co_2Z-hexaferrite:

The Co_2Z-hexaferrite were synthesised via sol-gel mode of synthesis. The stoichiometry ratio of the Co_2Z-hexaferrite is $Ba_3Co_2Fe_{24}O_{41}$. The detailed synthesis procedure has already been discussed in chapter 2 (**Section: 2.2.1** Synthesis of magnetic hexaferrite and ferrite

nanoparticles by sol-gel method). The sample after being mortared into a fine powder, was calcinated at a temperature of about 1200 °C in a high-vacuum furnace, to ensure structural integrity, along with phase formation, and enhanced magnetic domain size.

5.2.4 Synthesis of rGO-Co_2Z-PVDF nanocomposite films:

Before the synthesis of rGO-Co_2Z-PVDF nanocomposite films, 50:50 and 30:70 wt% of rGO:Co_2Z binary fillers have been prepared using grinding-mixing method which were named as rZ55 and rZ37, the details of the grinding-mixing method has been discussed in chapter 2 (**Section: 2.2.2.4** Synthesis of binary nanocomposite by grinding-mixing method). The obtained powders were then used in preparing rGO-Co_2Z-PVDF nanocomposite films, with varying loading percentages of the binary fillers using the solution casting method [5]. The detailed procedure of solution casting method mentioned in chapter 2 (**Section: 2.2.2.5** Synthesis of nanofillers-polymer nanocomposite film by solution casting method). Finally, all the nanocomposite films (rZP552, rZP553, rZP372 and rZP373) have been collected. After that, to prepare the multi-layer structure, we have taken six mono-layer films one above other of each nanocomposite film and stacked tightly by using hot press technique. The multi-layer structure formed successfully without having any gap within the layers and the effect of hot press is equally distributed throughout the layers of nanocomposite films during the making of multi-layer structure. Finally, the prepared mono-layer and multi-layer nanocomposite films are taken for different studies. The details of the nanocomposite films are mentioned in chapter 2, Table 2.2. Figures 5.1(I and II) show the free standing and flexibility of the mono-layer and multi-layer nanocomposite films respectively. Therefore, the flexibility of the nanocomposite films is not compromised in the process of going from mono-layer structure to a multi-layer one.

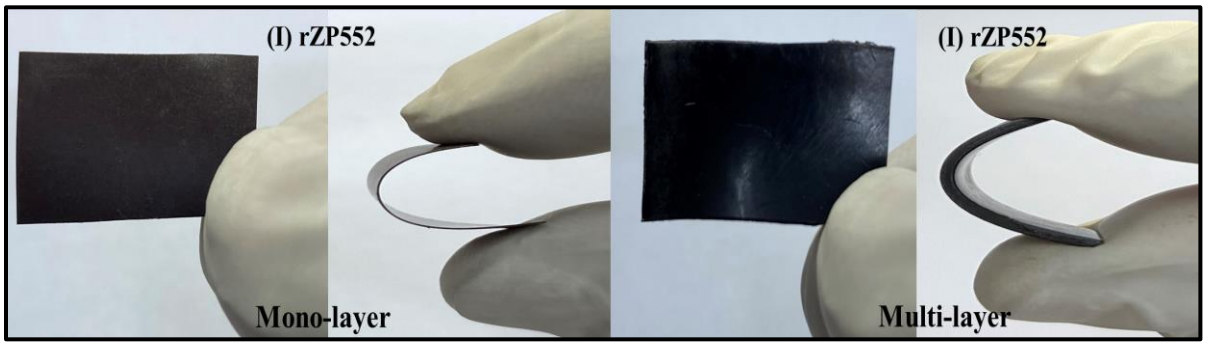

Figure 5.1: Free standing and flexible images of mono-layer and multi-layer rZP552 nanocomposite film.

5.2.5 Formation mechanism of rGO-Co_2Z-PVDF nanocomposite films:

The structural representation of rGO-Co_2Z-PVDF nanocomposite film is given in Figure 5.2. Co_2Z-hexaferrite has been studied as one of the most promising microwave-absorbing ferrites, mainly due to the existence of the strong magnetic property, as a consequence of the c-plane anisotropy especially at higher frequencies [3, 9]. Co_2Z-hexaferrite is a complex structure, because of the combination of two different types of hexaferrites (Co_2Y and Co_2M). The basic structure of Co_2Z-hexaferrite unit cell comprises of mainly three blocks, namely S-(spinel) block, R-(hexagonal) block, and T-(hexagonal) block. (Also included are their 180° rotational variants about the c-axis S*, R* and T*) [10]. The S- block does not contain any barium ions, the R-block contains barium ions with two oxygen layers, while the T-block comprises of barium ions along with four oxygen layers. These Co_2Z-hexaferrites are incorporated in the matrix of reduced Graphene oxide (rGO) via electrostatic forces of attraction between them due to the partially negative charges present on the surface of the hexaferrite, and the overall partial positive charge developed over the matrix of rGO. Poly(vinylidene fluoride) (PVDF), a piezoelectric polymer exists in the nanocomposite in the β-phase having the zigzag (TTTT) conformation. Alternatively layering doped rGO and PVDF matrices gives rise to a sandwich

configuration, which opens the prospect of the formation of multi-layered structures, while giving rise to a significant increase in piezoelectric parameters [38]. This connection results through the electrostatic forces of attraction, ultimately leads to the binding of PVDF with the rGO sheets on either side, consequently resulting in the sandwich structure of rGO-Co_2Z-PVDF nanocomposite films [11].

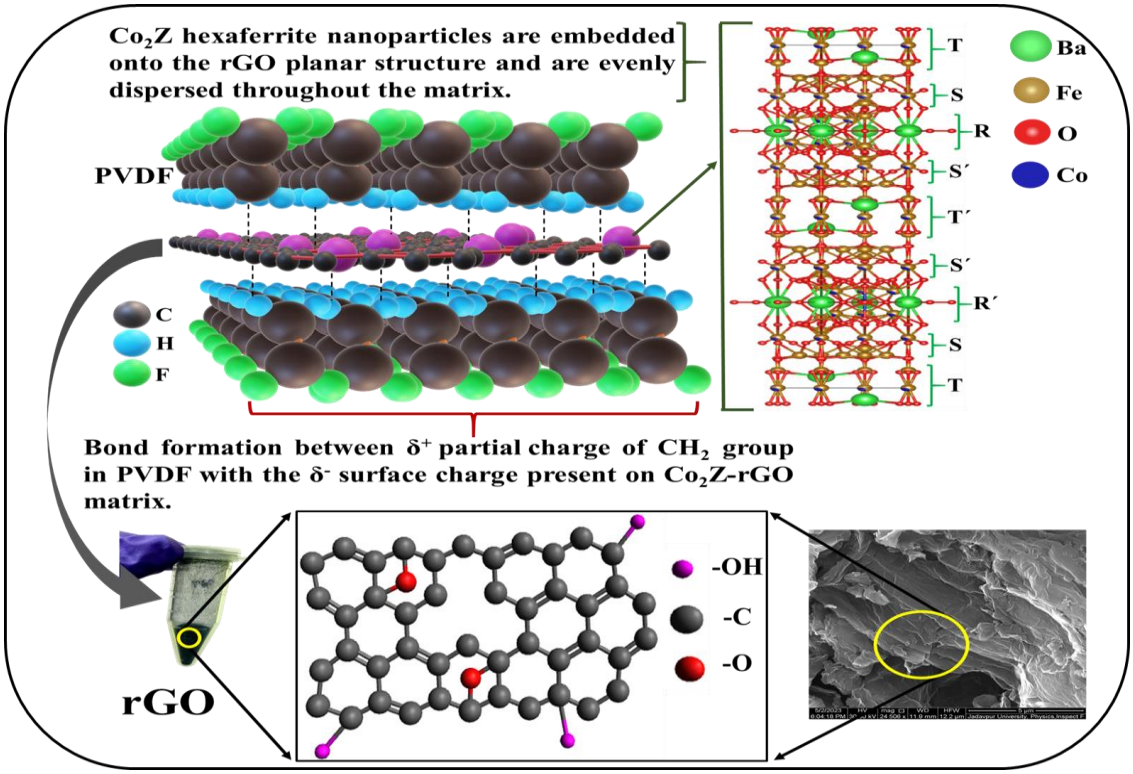

Figure 5.2: Schematic diagram for the structural build-up of rGO-Co_2Z-PVDF nanocomposite film.

5.3. Results and Discussions:

5.3.1 Crystallographic phase analysis:

The XRD profile of the rZP373, rZP372, rZP553, rZP552 nanocomposite films can determine the crystallographic phases related to the phase of rGO, Co_2Z-hexaferrite and the phase of PVDF in the nanocomposite systems. Figure 5.3(I) depicts the outcome of XRD analysis for bare PVDF film, rGO and Co_2Z-hexaferrite. The XRD patterns of rZP373, rZP372, rZP553,

rZP552 nanocomposite films are depicted in Figure 5.3(II). All the crystallographic phases in XRD patterns of rGO-Co_2Z-hexaferrite-PVDF nanocomposites are assigned by using JCPDS file number 42-1650, 78-0131 and 82-0472 respectively. The observed Co_2Z-hexaferrite crystallographic phase conforms to P63/mmc space group [12]. Now, in the XRD patterns of rZP373, rZP372, rZP553, rZP552 nanocomposite films, the appearance of matching phases of Co_2Z-hexaferrite, rGO and bare PVDF in the 2θ range of 10° to 80° has been found. The average crystallite diameter of Co_2Z-hexaferrite has been calculated from the broadening of the 100% intense peak (110) by Debye-Scherrer equation (1).

$$< D >_{(110)} = \frac{0.9\lambda}{\beta_{\frac{1}{2}} \cos\theta} \tag{5.1}$$

Here, D is the average crystallite size, λ is the incident X-ray wavelength, θ is the Braggs angle corresponding to the central position of the XRD peak (110) and $\beta_{1/2}$ is assigned as full width at half maximum (FWHM) of the XRD peak (110). The average crystallite diameter of ~ 22 nm for Co_2Z-hexaferrite has been observed by the XRD analysis. Figure 5.3(III) shows the plot generated by Reitveld refinement of the Co_2Z-hexaferrite prepared via sol-gl synthesis route with the help of the refinement software MAUD. Initially the specifications such as the lattice parameters, space group, atomic coordinates were evaluated from the similar reference patterns available at Crystallography Open Database (COD). To get a good fitting, the background factor was corrected using cosine Fourier series with eight refinable coefficients and the Bragg reflection profile was characterized by Thompson-Cox-Hastings pseudo-Voigt function. Parameters such as width dimensions, unit cell dimensions, orientation, assymetry, structure factor, occupancy were refined. Impurity in the hexaferrites can be ruled out since no additional peaks are found in the refinement. Goodness of fitting (χ^2), discrepancy factor (R_{wp}), expected values (R_{exp}) of Co_2Z-hexaferrite has been evaluated and shown in the inset of Figure 5.3(III).

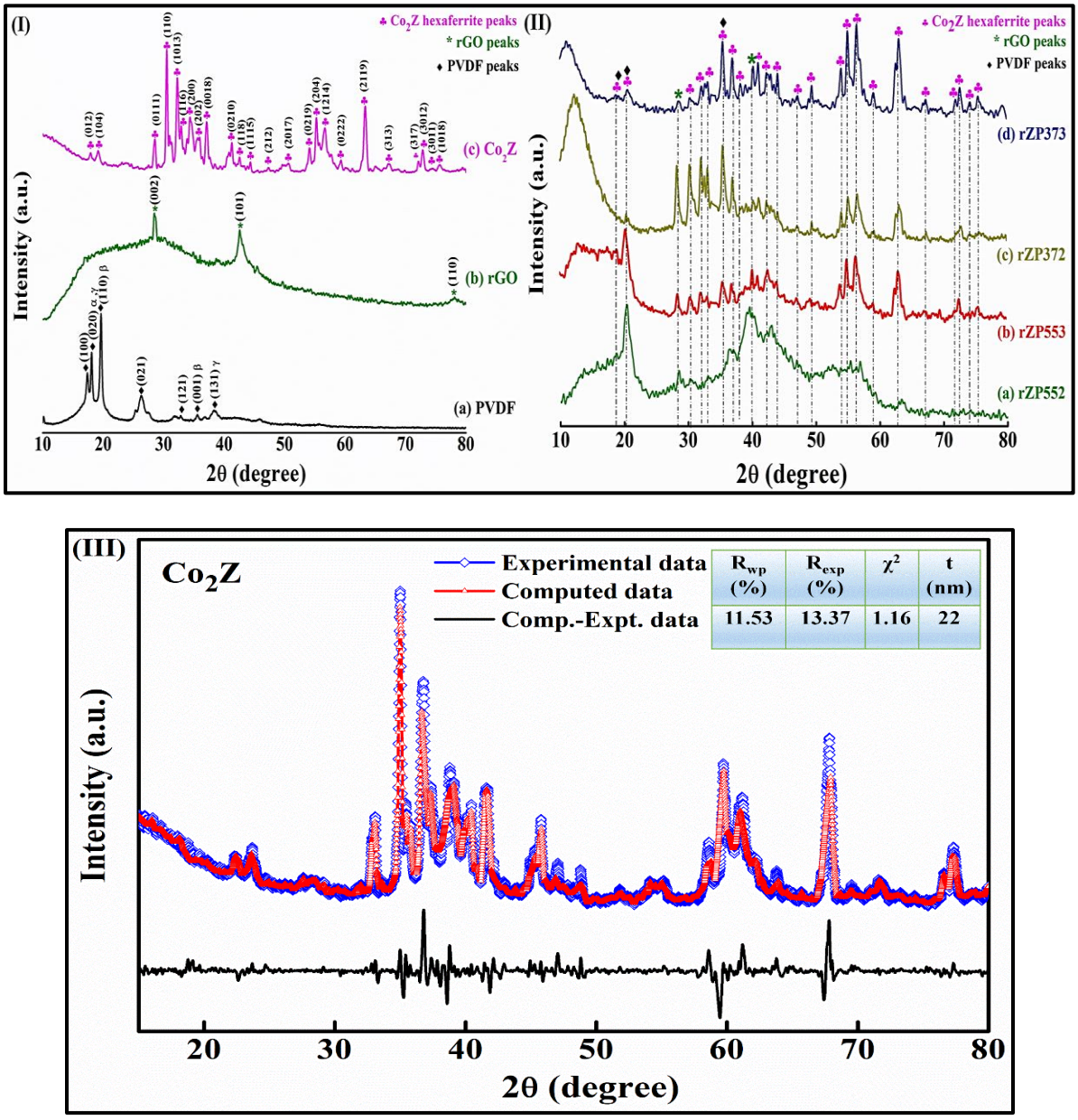

Figure 5.3: (I) XRD pattern of (a) PVDF, (b) rGO, (c) Co_2Z-hexaferrite (II) (a) rZP552, (b) rZP553, (c) rZP372 and (d) rZP373 nanocomposite films, (III) Rietveld refinement study of Co_2Z-hexaferrites.

5.3.2 Surface morphology study:

The morphological aspect of the rZP553 and rZP373 nanocomposite films has been characterized with the help of FESEM. The micrographs of bare PVDF film, Co_2Z-hexaferrite,

rGO, rZP553 and rZP373 nanocomposite films have been illustrated as Figures 5.4(a-g). The expected hexagonal crystal structure of the Co_2Z-hexaferrite has been achieved and depicted in Figure 5.4(c). Figure 5.4(d) shows the wrinkled structure of rGO. The wrinkles on the rGO surface develop with the restoration of sp^2 bonds between carbon and hence confirm the effective reduction of graphene oxide [13]. The FESEM micrographs given in Figures 5.4(e and f) reveal the successful inclusion of the binary rGO-Co_2Z hexaferrite binary fillers in the PVDF matrix. The binary fillers contained in the PVDF matrix will help in promoting the useful interfacial area between the binary fillers and the PVDF matrix which in turn enhances the polar β and γ-phases of the resultant rGO-Co_2Z-PVDF nanocomposite films [14, 15]. Also, Figure 5.4(g) represents the cross-sectional view of rZP373 multi-layer nanocomposite film. From the cross-sectional view of the representative nanocomposite film, it has been confirmed that the multi-layer structure formed successfully without having any gap within the layers and the FESEM image also shows that the thickness of each mono-layer film in multi-layer structure is nearly same. FESEM image shows that the thicknesses are very within the range of 100 μm to 144 μm. The Energy Dispersive X-ray Spectroscopy (EDS) study given in Figures 5.4(h and i), confirm the existence of all the elements, such as barium (Ba), cobalt (Co), iron (Fe), oxygen (O), carbon (C) and fluorine (F) in the rZP553 and rZP373 nanocomposite films. Elemental mapping images given in Figures 5.4(j and k), show the uniform distribution of the cations of Co_2Z-hexaferrite as well as the carbon and oxygen atoms of the rGO sheet inside the rZP553 and rZP373 nanocomposite samples.

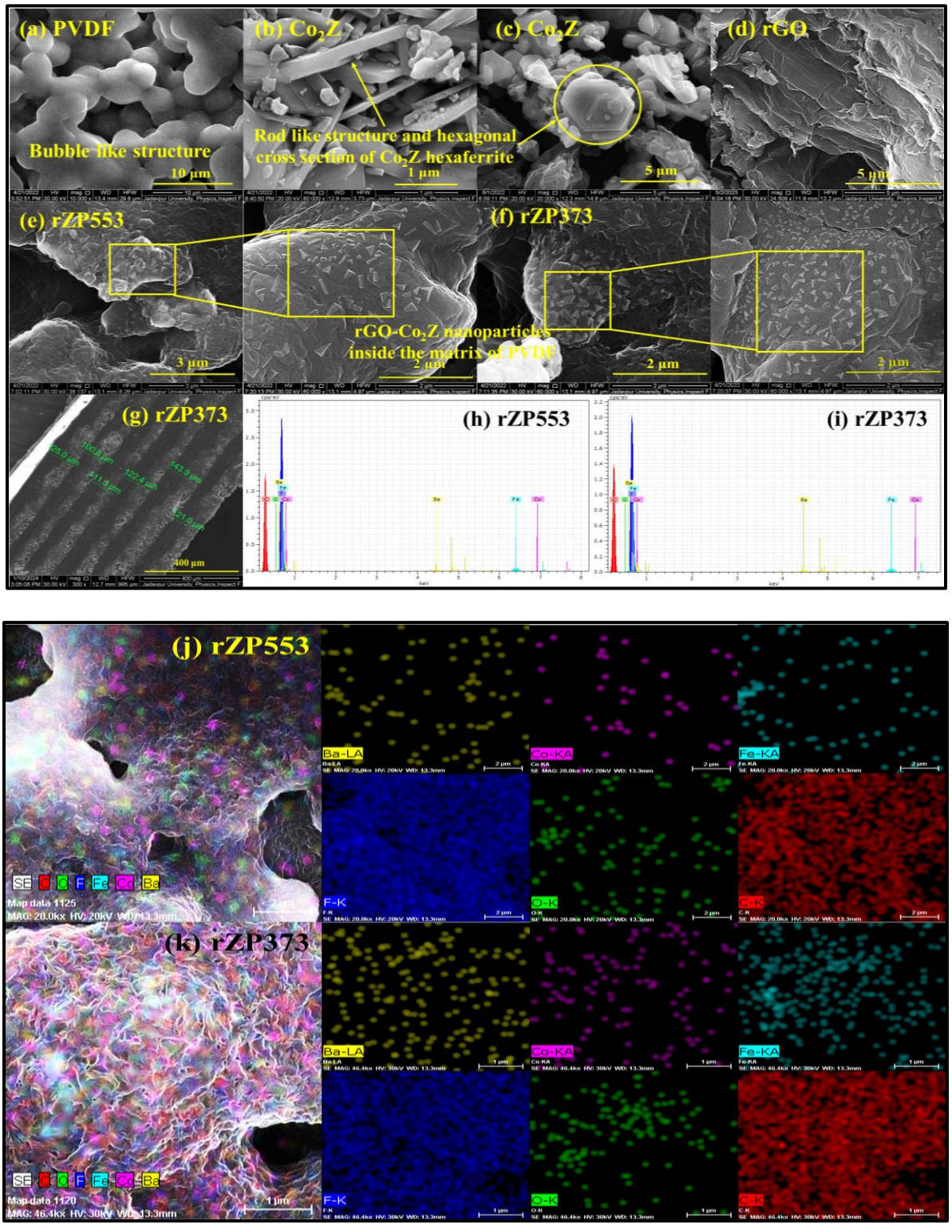

Figure 5.4: FESEM micrographs of (a) PVDF film, (b, c) Co_2Z-hexaferrite, (d) rGO, (e and f) rZP553 and rZP373 nanocomposite films, (g) cross sectional image of rZP373 nanocomposite

film (h and i) EDS spectra and (j and k) Elemental mapping and of rZP553 and rZP373 nanocomposite films respectively.

5.3.3 Study of RAMAN spectroscopy:

Figures 5.5(a-e) represent the Raman spectroscopy of rGO and rZP552, rZP553, rZP372, rZP373 nanocomposite films, respectively. To find the spectroscopy band of rGO, Raman spectroscopy is one of the fundamental studies. From respective graph both the D and G bands are visible at 1329 cm^{-1} and 1591 cm^{-1}, respectively. The existence of D band is found mainly due to the breathing mode of A_{1g} symmetry and it can also provide the defect number in rGO [40]. The activation reason of D band is disorder in carbon compound. For the first order scattering mode of E_{2g} phonons of sp^2 domains present in carbon atom observed from the presence of G band of rGO [16, 17]. So, the G band represents the tangential sheer mode of carbon atom corresponding to the stretching mode in the graphite plane [18]. The presence of both D and G bands are quite prominent in rZP552, rZP553, rZP372, rZP373 nanocomposite films and there is no shifting of peaks observed therein. The existence of 798 cm^{-1} and 879 cm^{-1} peaks represent the α and β–phases of PVDF, respectively. Also, the peak at around 683 cm^{-1} represents the Co_2Z-hexaferrite inside the matrix of PVDF [19]. Moreover, this study also provides information about the improvement of polar β–phase of the nanocomposite films. In Table 5.1 we have mentioned the band position, phase and group/vibrational mode of the rGO, PVDF and nanocomposite films rZP552, rZP553, rZP372 and rZP373, respectively.

Table 5.1: Details of Raman spectroscopy analysis

Sl. No.	Sample name	Band (cm^{-1})	Phase	group/Vibrational mode
1.	Co2Z	683	-	-
2.	rGO	1329 (D) 1591 (G)	-	-
3.	PVDF	798 879 1430 2971	α α, β	CH_2 r CC ν_s CH_2 δ, CH_2 ω CH_2 ν_s
4.	rZP552	same as above	same as above	same as above
5.	rZP553	same as above	same as above	same as above
6.	rZP372	same as above	same as above	same as above
7.	rZP373	same as above	same as above	same as above

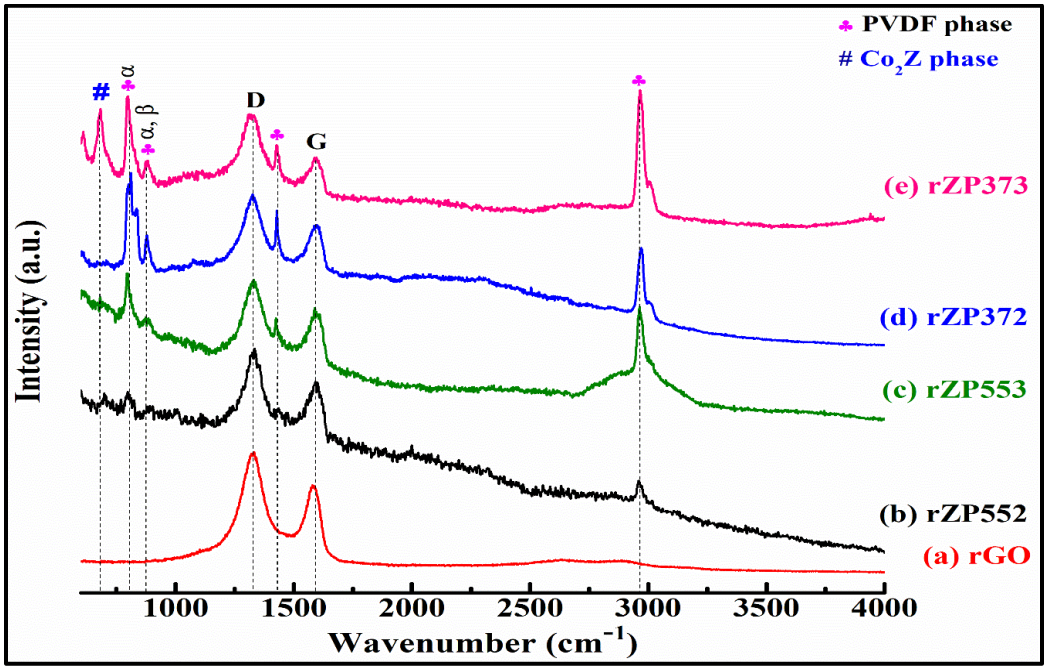

Figure 5.5: Raman spectra of (a) rGO (b) rZP552 (c) rZP553 (d) rZP372 and (e) rZP373 nanocomposite films.

5.3.4 XPS analysis:

The present study employs XPS measurements to examine the chemical states of each element in Co_2Z, rGO, rZ55, and rZ37. The 284.60 eV peak in the C 1s spectrum is utilized for binding energy calibration. The XPS survey spectra of Co_2Z-hexaferrite is presented in Figures 5.6(I)(a-e). The identified peaks include elements C, Ba, Fe, Co, and O only. The element binding energy analysis indicates that the Co_2Z-hexaferrites exhibit a single-phase composition without any additional impurity phases. The survey scan spectra in Figure 5.6(I)(a) exhibited peaks corresponding to Fe2p, Ba3d, Co2p, and O 1s in the material. The Ba $3d_{5/2}$ and Ba $3d_{3/2}$ peaks have binding energies of 779.32 and 796.34 eV respectively, as indicated in Figure 5.6(I)(b). Two separate prominent iron peaks are found and shown in Figure 5.6(I)(c). The initial prominent peak ($2p_{3/2}$) is divided into two distinct peaks, one at 710.32 eV which corresponds to the Fe^{2+} state and the other at 713.36 eV which is associated with the Fe^{3+} state [20]. Additionally, there are two satellite peaks located at 716.33 eV and 719.97 eV [20]. The second primary peak ($2p_{1/2}$) is also divided into two distinct peaks, with each peak occurring at 724.76 eV belonging to the Fe^{2+} oxidation state and 727.52 eV which corresponds to the Fe^{3+} oxidation state [20]. Further satellite peaks are observed at positions of 733 eV [21]. Figure 5.6(I)(d) displays two prominent peaks at 779.9 eV and 795.25 eV, corresponding to Co^{2+} $2p_{3/2}$ and Co^{2+} $2p_{1/2}$, respectively [20]. Figure 5.6(I)(e) displays the distinctive peak of O 1s, which has been divided into three distinct peaks. The peak at 529.92 eV (O^a) is caused by naturally occurring O^{2-} ions, whereas the peak at 532.7 eV (O^b) indicates the presence of oxygen vacancies and 533.5 eV (O^c) is due to O^{2-} ions that have been adsorbed during the processing of the sample [21]. Figures 5.6(II)(a-c) display the XPS analysis of rGO powder. The observation revealed two distinct and precise peaks at binding energies of approximately 288 eV and 529 eV,

corresponding to the C1s and O1s peaks respectively [22].

Figures 5.6(III) and (IV)(a) display the rZ55, rZ37, and whole-range XPS survey spectra, covering energies from 0 to 1200 eV. The identified peaks include elements C, Ba, Fe, Co, and O. The carbon peak observed in the rZ55 and rZ37 binary fillers is the most distinct and precise among all the other peaks of different elements. This indicates a successful reduction of graphene oxide (GO) to reduced graphene oxide (rGO). Figures 5.6(III) and (IV)(b-e) display the high-resolution scan of Fe2p, Ba3d, Co2p, and O1s in the rZ55 and rZ37 binary fillers. The presence of all the constituent elements (Ba, Fe, Co, and O) in the XPS scan of the binary fillers confirms that the Co_2Z-hexaferrites have been effectively incorporated in the matrix of rGO.

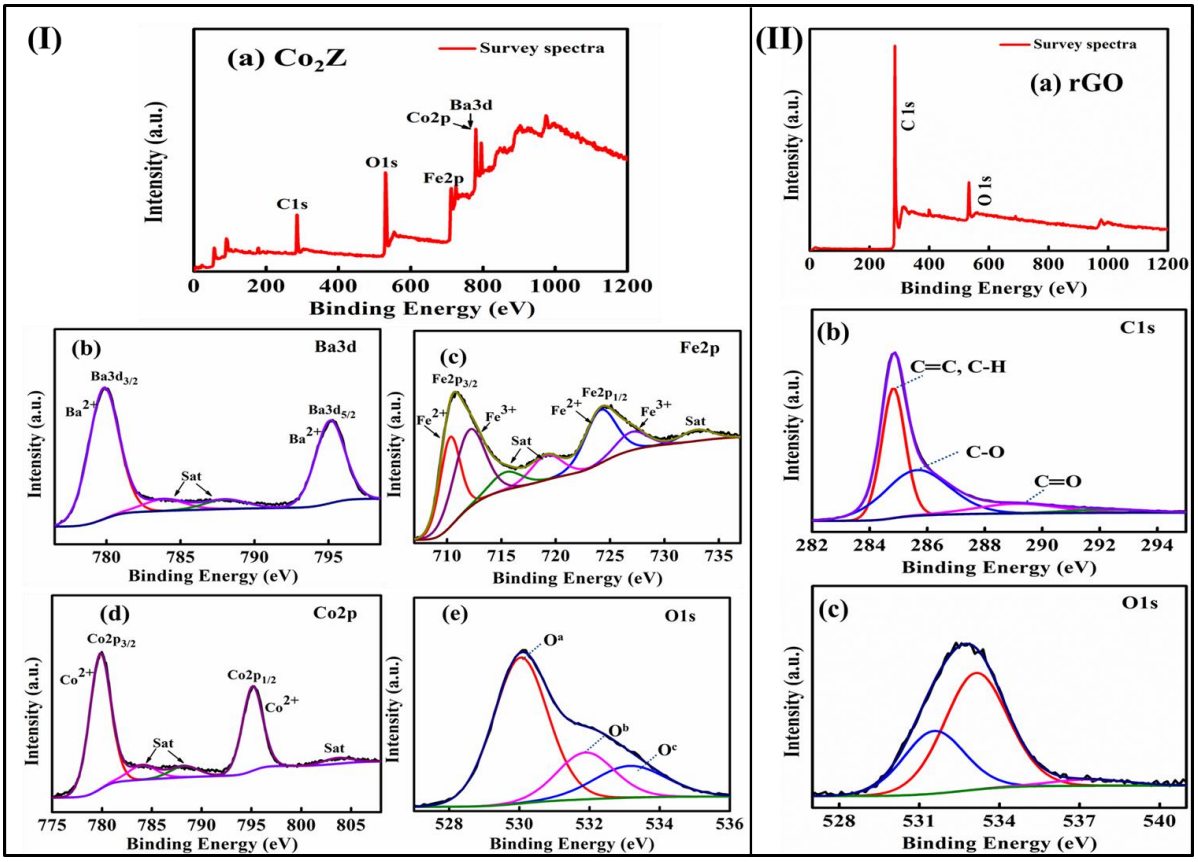

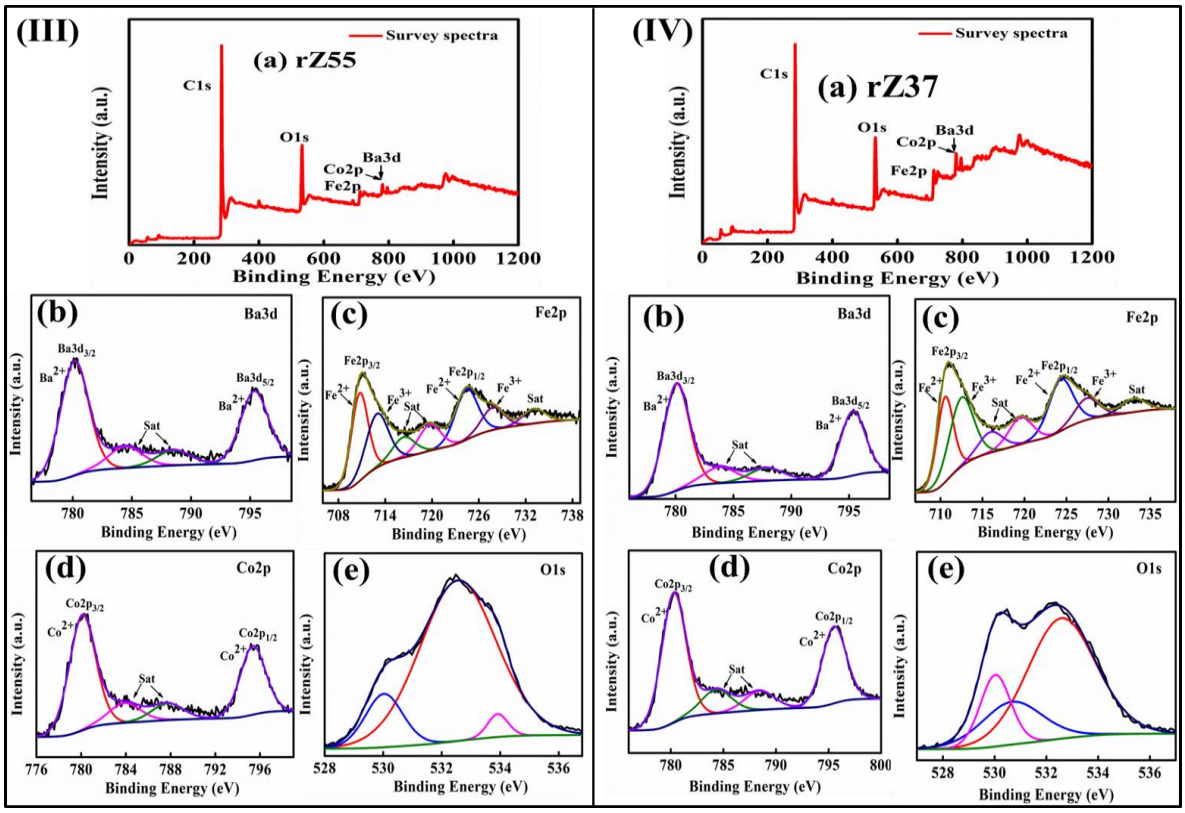

Figure 5.6: Full range XPS survey spectrum of (I)(a) Co_2Z, (II)(a) rGO, (III)(a) rZ55, and (IV)(a) rZ37, high-resolution spectrum for (I)(b) Ba3d, (c) Fe2p, (d) Co2p, and (e) O1s of Co_2Z, (II)(b) C1s, (c) O1s of rGO, (III) and (IV)(b) Ba3d, (c) Fe2p, (d) Co2p, and (e) O1s of rZ55 and rZ37 nanocomposites.

5.3.5 J-E characteristic study:

Figures 5.7(a-g) display current density (J) vs electric field (E) graph of bare PVDF, rGOP, Co_2ZP, rZP552, rZP553, rZP372 and rZP373 nanocomposite films under a circle of applied potential of ± 20 V. The room temperature J-E study was carried out to acquire the leakage current of the resultant nanocomposite films. Herein, Figure 5.7(h) represents the variation of maximum leakage current density (J) of different materials at 70 kV/m of applied electric field. The J-E curve of all the nanocomposite samples is seen to be non-linear in nature and it also shows butterfly nature of the loop. This butterfly nature and the non-traceability of the current

density indicates about the polarization property of the nanocomposite films [23]. The leakage current density of the bare PVDF is 1.0×10^{-7} A/m^2 which indicates that bare PVDF is insulating in nature. This elevation in the magnitude of current density with the increase of fillers in the PVDF matrix can be attributed to the increased number of conduction charges. However, they face restrictions in their path due to the presence of non-conducting PVDF matrix, since, the fillers are embedded inside of PVDF matrix. The leakage current density of the rGOP film is much higher 2.3×10^{-2} A/m^2 than that of all the nanocomposite films, because rGO is more conducting as compare to the Co_2Z-hexaferrites. Therefore, the tunnelling effect can be visible in case of rGOP film. Also due to the flaky and light weight property of the rGO, by increasing the nanofillers weight percentage in the PVDF matrix, agglomeration of fillers comes in effect which overcomes the restriction imposed by the PVDF matrix in the path of electrical conduction and that in return increases current density of the nanocomposite films with the applied potential difference [24, 25]. Now, the incorporation of Co_2Z and rGO in binary fillers with the wt % of 70:30 inside the PVDF matrix is found that the leakage current density is lower than rZP552 and rZP553 nanocomposite films. Also, the current density of all the nanocomposite films is very less in the order to 10^{-5} A/m^2. This minimum leakage current density even at ~90 kV/m external electric field shows significantly high electrical stability of the nanocomposite films and the conductivity of the nanocomposite films lies in the insulating region [26]. The high electrical stability can modulate the polarization property of the nanocomposite films at the presence of high external electric field without having any electrical breakdown. This may help to improve the shielding effectiveness due to the absorption (SE_A) of the nanocomposite films.

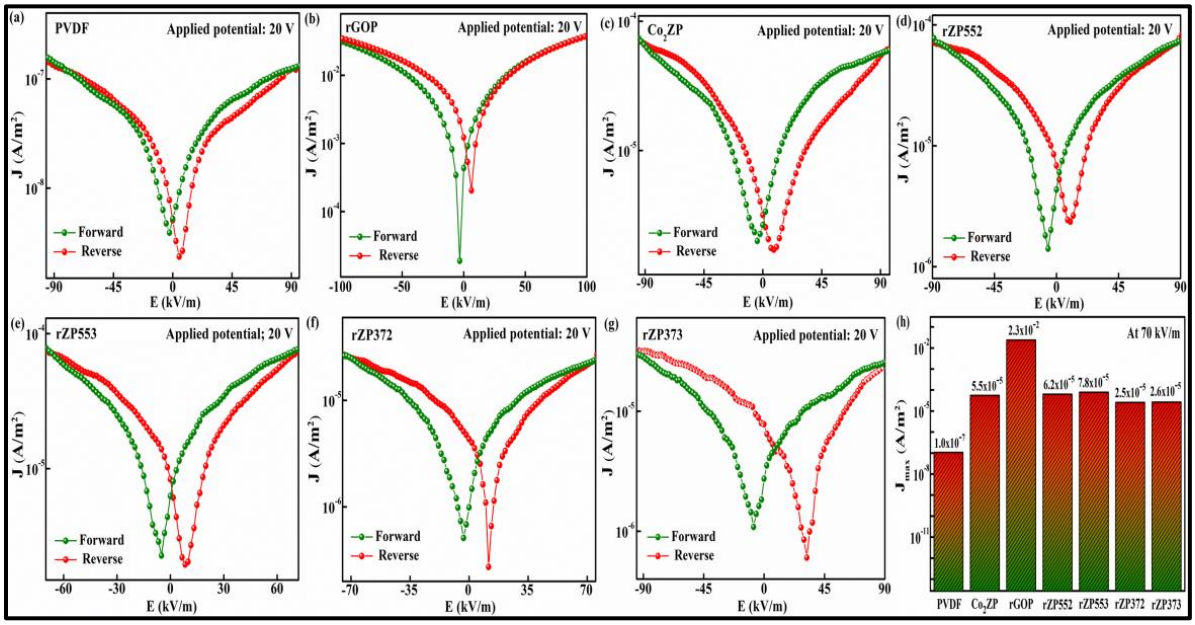

Figure 5.7: Variation of (a-g) current density (J) vs Electric field (E) and (h) maximum current density (J) of PVDF, rGO, Co_2ZP, rZP552, rZP553, rZP372, rZP373 nanocomposite films.

5.3.6. Magnetic property study:

Figures 5.8(a and d) show the field dependency of the magnetic moment (M-H loops) observed at 50 K and 300 K for the nanocomposite films of rZP553 and rZP373, where the maximum applied field was 30 kOe. These nanocomposites contain rGO-Co_2Z-hexaferrite binary fillers inside PVDF and this study has been made to understand the magnetic response of the nanocomposite materials which will have influence on shielding effectiveness due to absorption. The moderate coercive field and significant magnetization of nanocomposite films indicates the presence of the ordered magnetic phase, in this case strong ferrimagnetic nature in the prepared samples at RT. With the decrease of temperature from 300 K to 50 K, both the maximum magnetization and the coercive field increases in both the samples. This also signifies the presence of the ordered ferrimagnetic phase in the samples. Comparing Figures 5.8(a) and (d), the increase of loading percentage of the Co_2Z-hexaferrite inside the matrix of PVDF the magnetisation value has significantly increased. The values of maximum magnetisation (M_m),

coercive field (H_c) and remanence magnetisation (M_r) have been depicted in Figures 5.8(g and h) at 50 K and 300 K. However, the loops are not saturated even at 30 kOe of external magnetic field and there is a linear increase in magnetization value observed with increase of magnetic field even at 50 K. Firstly, it can happen due to the fractional presence of the superparamagnetic (SPM) particles in the prepared samples, secondly, due to the paramagnetic shell present over the magnetic core of each hexaferrite particles. The linear nature of magnetization data indicates that the linear increase of magnetization is not due to the SPM relaxation observed in case of magnetic nanoparticles. To further confirm this the temperature dependent magnetic study (M-T) of rZP553 and rZP373 nanocomposite films has been carried out during the field-cooled (FC) and zero-field-cooled (ZFC) process from 50 to 300 K depicted in Figure 5.8(b and e), respectively. From these data we observe that both rZP553 and rZP373 show a clear gap between the FC and ZFC magnetization data even at 300 K. This ensures that the blocking temperature of both the sample are much above RT. Thus, the chance of presence of SPM particles in these samples can be discarded. This confirms the linear increase in magnetization data is due to the paramagnetic shell present over ferrimagnetic core in the hexaferrite nanoparticles. In magnetic nanoparticles, it is found that a surface layer with disordered spin structure is found to form owing to the weak interaction between the particles at magnetic core and that at the surface. Since in nanoparticles the surface to volume ratio is quite high, so the presence of this disordered surface layer can affect the observed magnetization to some extent. Thus, the total magnetization observed in the samples arise due to ferrimagnetically ordered phase along with a paramagnetic phase present in the samples. To have a quantitative idea of both these contributions we tried to analyse the observed M-H loops using the following relation [27, 28];

$$M(H) = \left[2\frac{M_{FM}^{S}}{\pi} tan^{-1}\left\{\left(\frac{H \pm H_{ci}}{H_{ci}}\right) tan\left(\frac{\pi M_{FM}^{R}}{2M_{FM}^{S}}\right)\right\}\right] + \chi H \quad (5.2)$$

In this equation the first term represents the magnetization due to the ordered magnetic phase (in this case ferrimagnetic phase) and the second linear component is due to the paramagnetic contribution. Where, M_{FM}^{S}, M_{FM}^{R}, $H_{ci}$are respectively the ferrimagnetic saturation magnetization, remnant magnetization, intrinsic coercive field and χ is the paramagnetic susceptibility. The experimental magnetization, theoretical fit along with the simulated ferrimagnetic and paramagnetic contributions for 300 K data are shown in Figures 5.8(c and f). The extracted fitting parameters are tabulated in Table 5.2. The extracted parameters indicate that ~93% of the total magnetization observed in both the sample arises from the ferrimagnetic core of the prepared hexaferrites. This implies that rZP553 and rZP373 nanocomposite films exhibit ordered ferrimagnetism at RT with quite large coercive field which is mostly favourable to obtain the high shielding effectiveness due to absorption [29].

Table 5.2: Parameters obtained from M-H loop analysis

Sample name	**Temperature (K)**	**Observed Magnetization (emu/g)**	**Paramagnetic (PM) Contribution χ (emu/g Oe)**	**Ferromagnetic (FM) Contribution**		
				M_{FM}^{S} **(emu/g)**	M_{FM}^{R} **(emu/g)**	H_{ci} **(kOe)**
rZP553	300	6.425	2.399×10^{-5}	5.982	2.606	1.144
rZP373	300	8.907	3.324×10^{-5}	8.303	3.636	1.155

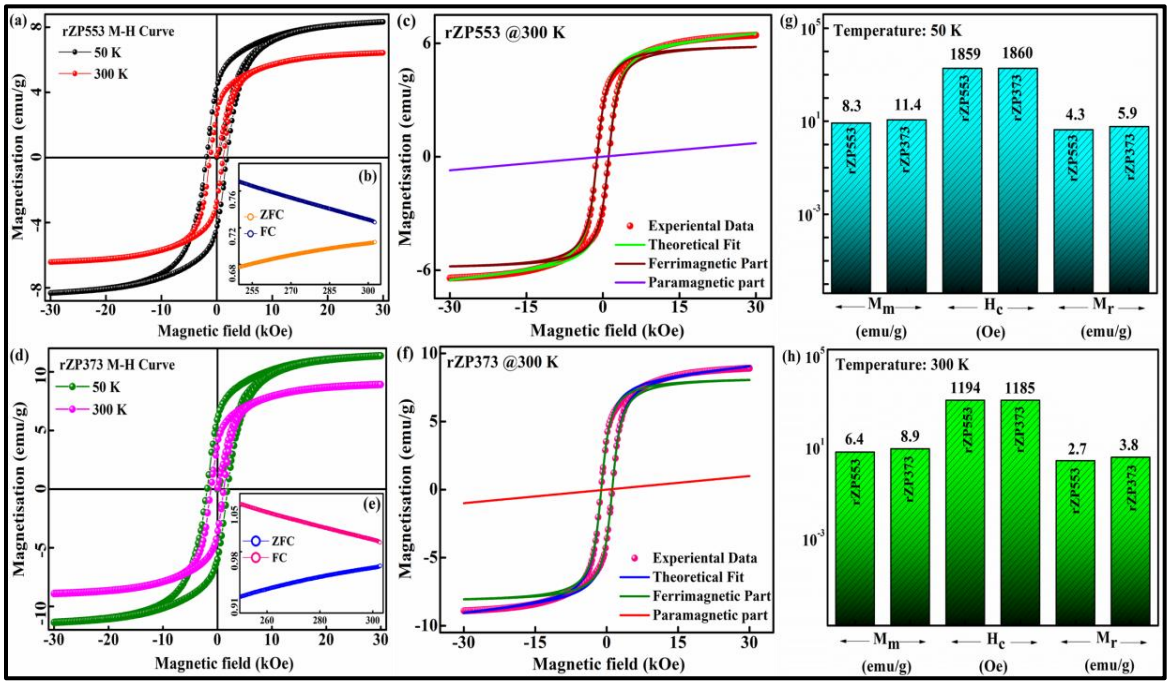

Figure 5.8: M-H loops of (a) rZP553 and (d) rZP373 at 50 K and 300 K, FC-ZFC curve of (b) rZP553 and (e) rZP373, Experimental and theoretically simulated curve of M-H loops of (c) rZP553 and (f) rZP373 at 300 K along with FM and PM contributions, comparison of various magnetic parameters of (g) rZP553 and (h) rZP373 at 50 and 300 K.

5.3.7. Study of shielding effectiveness property:

To understand the proper utilization of the rZP552, rZP553, rZP372 and rZP373 nanocomposite films for the EMI shielding applications, we have conducted shielding effectiveness study at the frequency range of 12-18 GHz (K_u-band). An electromagnetic wave is a combination of oscillatory and crossed electric and magnetic field. Materials which interact with one or both of this field can be utilized for fabrication of EMI shielding material. For effective microwave shielding the most direct characterization parameters are the complex permeability ($\mu_r = \mu' - j\mu''$) and permittivity ($\varepsilon_r = \varepsilon' - j\varepsilon''$). Here, μ' and μ''corresponds to the storing capacity and loss of magnetic energy whereas, ε' and ε'' corresponds to the storing capacity and loss of electric energy. The electromagnetic parameters complex permittivity ($\varepsilon_r = \varepsilon' + j\varepsilon''$) and

complex permeability ($\mu_r = \mu' + j\mu''$) of the sample are determined from the scattering parameters (S-parameters). The Nicolson-Ross-Weir (NRW) approach is often utilized for conducting this calculation [30-32]. The real and imaginary components of permeability, $\mu'$and μ'' strongly depends on the magnetization value of the magnetic material according to the following relation [33],

$$\mu' = 1 + \left(\frac{M}{H}\right)\cos\sigma \tag{5.3}$$

$$\mu'' = \left(\frac{M}{H}\right)\sin\sigma \tag{5.4}$$

Here, M is the magnetization, H is the external magnetic field and σ corresponds to the phase lag of magnetization with respect to the external magnetic field. Figures 5.9(I) (a-d) depict the real part of permittivity (ε') and permeability (μ'), Figures 5.9(II) (a-d) depict the imaginary part of permittivity (ε'') and permeability (μ''), and Figures 5.9(III) (a-d) depict the tangent of dielectric loss (tanδ_ε)and magnetic loss (tanδ_μ) of mono-layer and multi-layer nanocomposite films over the range of 12-18 GHz frequency. From the Figure 5.11(a, d) we see that the SE_A shows a high value at frequencies in which imaginary part of the permeability shows a peak. In addition to the permeability and permittivity value another factor affecting the shielding effectiveness is the impedance matching ratio (Z) between input impedance of the material (Z_{in}) and characteristic impedance of the free space (Z_0). Effective impedance matching confirms the entry of the incident electromagnetic wave in to the shielding material with nominal reflection from the air-material interface. To study that, we have calculated the impedance matching ratio (Z) from permeability and permittivity data using following relation [34],

$$Z_{in} = Z_0\sqrt{\frac{\mu_r}{\varepsilon_r}}\tanh\left[j\left(\frac{2\pi f d}{c}\right)\sqrt{\mu_r\varepsilon_r}\right] \tag{5.5}$$

$$Z = \frac{Z_{in}}{Z_0} \tag{5.6}$$

Here, d is the thickness of the material and c is speed of light and f is the frequency of the incident wave. The nature of variation of ratio of Z_{in} to Z_0 i.e. Z is shown in the Figures 5.9 (IV)(a, b). The absorption peaks are located near to the frequencies where the ratio of Z_{in} and Z_0 shows highest value. This is the same reason because of which the materials are showing high shielding absorption in the high frequency region even though μ'' and ε'' have smaller values there. To symbolizes the ability of integral attenuation of the incident electromagnetic wave inside the material the attenuation constant (α) is calculated from the real and imaginary component of relative permeability and permittivity using the following relation [34,35];

$$\alpha = \frac{\sqrt{2}\pi f}{c}\sqrt{(\mu''\varepsilon'' - \mu'\varepsilon') + \sqrt{(\mu''\varepsilon'' - \mu'\varepsilon')^2 + (\mu'\varepsilon'' + \mu''\varepsilon')^2}} \qquad (5.7)$$

where, f is the frequency of the incident wave and c is the speed of light. The frequency variation of the obtained data is shown in the Figures 5.9(IV)(c, d). From the figure we observe that frequency of the observed peaks of SE_A coincides with that of the peaks of α.

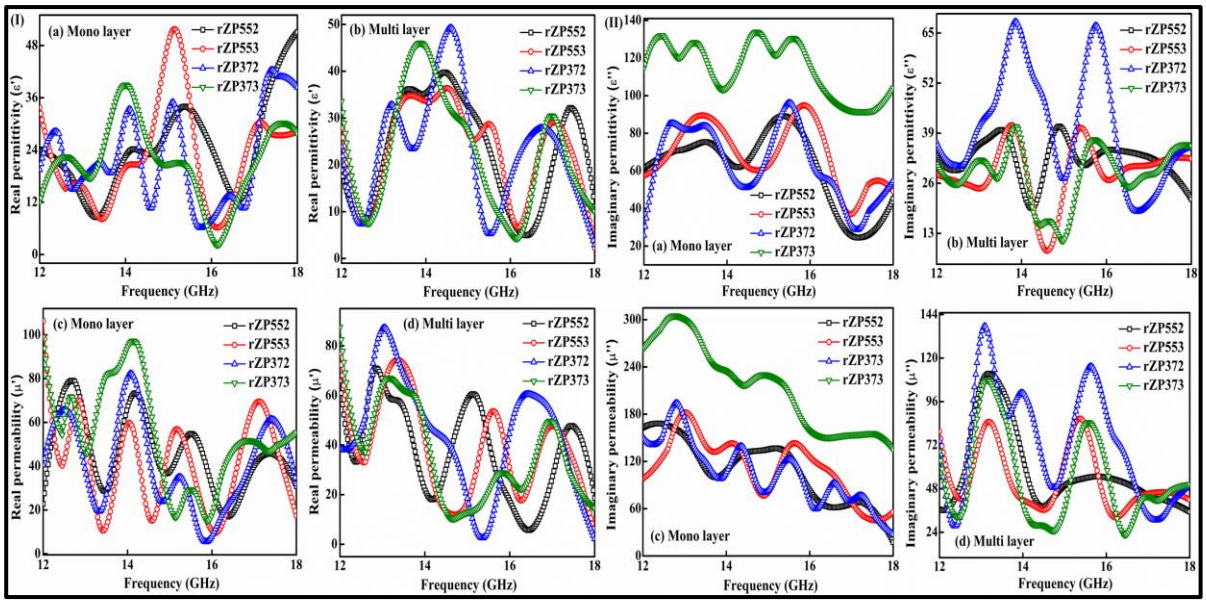

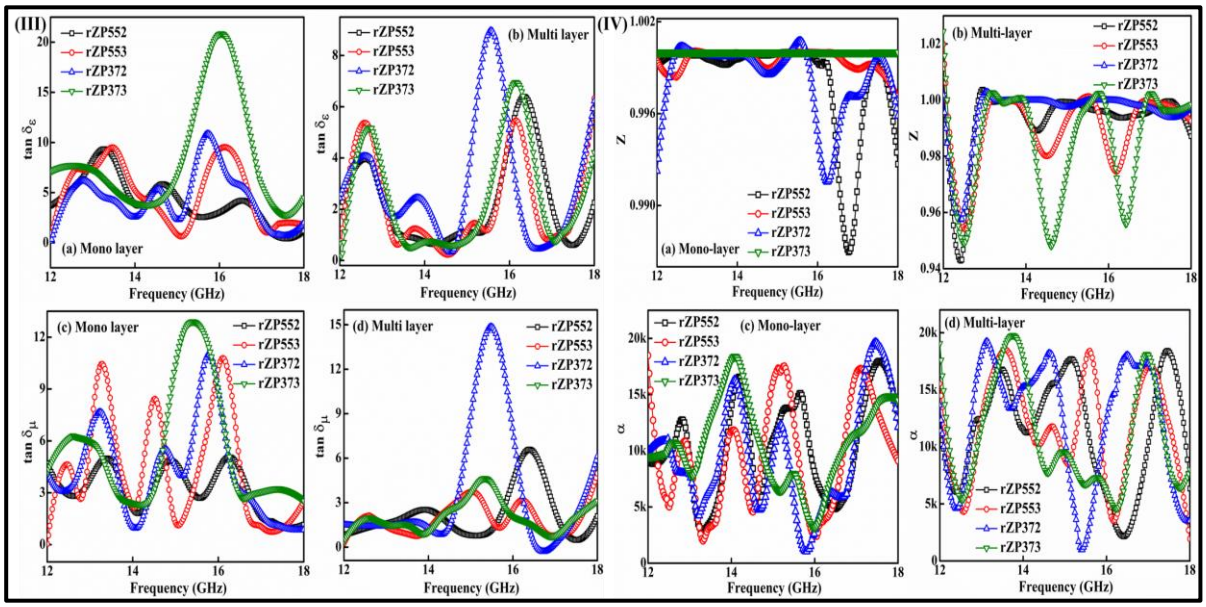

Figure 5.9: (I) (a, b) ε', (c, d) μ', (II) (a, b) ε'', (c, d) μ'', (III) (a, b) tanδ_ε, (c, d) tanδ_μ, (IV) (a, b) Z (c, d) α of mono-layer and multi-layer rZP552, rZP553, rZP372 and rZP373 nanocomposite films over 12-18 GHz.

The shielding effectiveness corresponding to absorption (SE_A), reflection (SE_R) and the total shielding effectiveness (SE_T) for both mono-layer and multi-layer structures of different nanocomposite films has been observed. Due to the large thickness and skin depth effect, we have tuned out the effect of shielding effectiveness due to multiple reflections (SE_{MR}) for both mono-layer and multi-layer nanocomposite films. So, the SE_A, SE_R is estimated to figure out the SE_T of the nanocomposite films and the respective equations are listed below

$$SE_T(dB) = -10\log_{10}\left(\frac{P_t}{P_0}\right) = SE_A + SE_R \tag{5.8}$$

$$SE_A(dB) = -10\log_{10}\left(\frac{1-|S_{11}|^2}{|S_{12}|^2}\right) \tag{5.9}$$

$$\text{and, } SE_R(dB) = -10\log_{10}\left(\frac{1}{1-|S_{11}|^2}\right) \tag{5.10}$$

Where, P_t represents the transmitted power and P_0 represents the incident power of microwave radiations. S_{11} and S_{21} are the reflection and transmission scattering parameters, respectively and known as scattering (S) parameters [36 ,37]. The thickness of nanocomposite film is increased with the formation of multi-layer structure of rGO-Co_2Z-PVDF nanocomposite film and the corresponding shielding mechanism has been depicted in Figure 5.10. As the EM wave passes through the rGO-Co_2Z-PVDF nanocomposite films, the wave gets interacted with the conducting rGO to counterpoise the electromagnetic wave, as a result the energy of EM radiation goes down. As EM wave incident on the layer structure, some of them will seep through the first layer onto the next layer. This escape of EM wave between the layers will undergo reflections between the consecutive internal layers. These reflections of waves will eventually terminate after the wave gets absorbed by the multi-layer structure of rGO-Co_2Z-PVDF nanocomposite films [38].

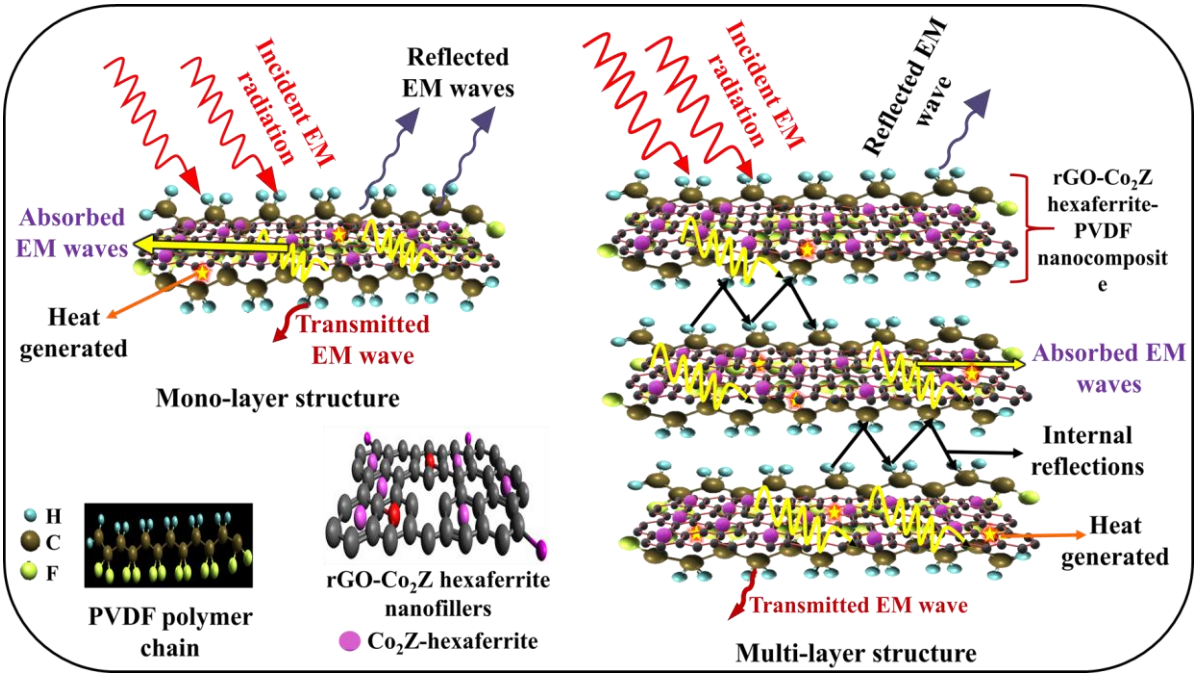

Figure 5.10: Plausible EMI shielding mechanism of mono-layer structure and multi-layered structure of rGO-Co_2Z hexaferrite-PVDF nanocomposite films.

Figure 5.11(a-f) depicts the SE_A, SE_R and SE_T of mono-layer and multi-layer structures of the nanocomposite films. For this work the focus has been given on the improvement of SE_A of EM wave and it has been observed the rising of SE_A over SE_R for both mono-layer and multi-layer structures. In case of mono-layer nanocomposite films the maximum value of SE_A is -27.03 dB at 12.38 GHz for rZP372 nanocomposite film, whereas, the maximum value of SE_R is -21.31 dB at 15.63 GHz for rZP553 nanocomposite film. This signifies that in mono-layer structure the nanocomposite film that consist a greater number of Co_2Z-hexaferrites the absorption (SE_A) value is high, on the other hand the nanocomposite film that consist a greater number of conducting nanofillers (rGO) shows high reflection (SE_R) value.

Now, the thickness of the nanocomposite films plays a significant role to improve the SE_A proposed mechanism [39].

$$SE_A(dB) = 20\log e^{\frac{d}{\sigma}} = 8.7(f\pi\sigma\mu)^{1/2} \propto d\sigma\mu \propto \alpha d \tag{5.11}$$

Where, d represent thickness of the material, σ is conductivity, f is frequency, μ is permeability and α signifies the attenuation constant of the material. The maximum value of SE_T is -47.03 dB at a matching frequency of 14.76 GHz for rZP373 nanocomposite film. Now, the maximum SE_A of multi-layer structure is -38.12 dB at 17.86 GHz for rZP373 nanocomposite film that consist maximum number of Co_2Z-hexaferrites and the maximum value of SE_R is -25.77 dB at 15.32 GHz for the rZP553 nanocomposite film which consist maximum number of conducting fillers (rGO). The maximum value of SE_T is -54.09 dB at 15.70 GHz for rZP372 nanocomposite film has been recorded. From this study we have clearly observed that SE_A is higher for both mono-layer and multi-layer nanocomposite films which containing more Co_2Z-hexaferrites as compare to rGO.

The improvement of SE_A for the nanocomposite films appears due to the interaction between induced electric dipoles with electric field vectors of the incoming EM radiation and the interaction between magnetic field vectors of the incoming EM radiation with the magnetic dipoles existing inside the nanocomposite films. The presence of rGO as conducting fillers inside the matrix of PVDF with Co_2Z hexaferrite can generate significant amount of conducting charges at the interface of the nanocomposite films. Due to the presence of rGO the conduction charges of rGO can generate short-range conductivity instead of long-range conductivity as these rGO fillers are surrounded by the non-conducting PVDF matrix and it creates charge pockets inside the matrix of PVDF. Due to the presence of magnetic Co_2Z- hexaferrite and magnetic field vector of incident EM radiation the magnetic flux will develop at charge pockets, as a result of which the conduction electrons will move circularly in the charge pockets. Thus, the rGO in binary fillers will generate small eddies inside the PVDF matrix and we will observe the attenuation of the EM radiation through absorption by this eddy current loss. Therefore, the electric dipoles and the formation of small eddies due to the bounded electrons of rGO in binary fillers improves SE_A of nanocomposite films. The improvement of SE_R values in the nanocomposite film are responsible due to the presence of conducting rGO nanofillers inside PVDF matrix. The reflection (SE_R) phenomena help to enhance the total shielding effectiveness (SE_T) of the nanocomposite films. Therefore, both the SE_A and SE_R are responsible to enhance the SE_T of rZP552, rZP553, rZP372 and rZP373 nanocomposite films which is shown in Figures 5.11(c and f), respectively. In case of rZP553 nanocomposite film the SE_A is less as compare to SE_R because the percentage of the rGO and Co_2Z-hexaferrite in binary fillers is 50:50 wt % and 30 wt % of these binary fillers are incorporated in the PVDF matrix. This rGO is highly conducting as well as flaky in nature. Due to the low density and high-volume ratio

may be more rGO sheet like structure are present at the surface of the nanocomposite film. This may improve the surface conductivity of the nanocomposite film. As a result, rZP553 nanocomposite film shows higher leakage current density as compare to the other nanocomposite films. For the shielding effectiveness study, the unique combination of conducting rGO and magnetic Co_2Z-hexaferrite and the formation of these nanocomposite films in multi-layer structure make them more efficient which comes out as a unique concept applied herein to improve the total shielding effectiveness (SE_T) of these laminated nanocomposite films. So, the variation of thickness of the nanocomposite films plays a significant role to improve the shielding effectiveness due to SE_A and it is also improved the overall total shielding effectiveness (SE_T).

The attenuation percentage of mono-layer and multi-layer structures of rGO-Co_2Z-PVDF nanocomposite films (rZP552, rZP553, rZP372 and rZP373) in the K_u-band region has been calculated and a high value of >99.999% attenuation was obtained. The attenuation graph of mono-layer and multi-layer structures of rGO-Co_2Z-PVDF nanocomposite films has been depicted in Figure 5.12. Here in Table 5.3 we have mentioned the maximum value of shielding effectiveness due to SE_A, SE_R, and SE_T and the corresponding attenuation % of rZP552, rZP553, rZP372 and rZP373 nanocomposite films respectively.

Table 5.3: Various parameters related to shielding effectiveness of rZP552, rZP553, rZP372 and rZP373 nanocomposite films

Sl. No	Sample name	Structure	$(SE)_{max}$ (dB)	Frequency (GHz)	Attenuation%
1	Co_2ZP	Mono-layer $(SE_A)_{max}$	-24.09	13.41	99.9833
		$(SE_R)_{max}$	-13.56	13.39	
		$(SE_T)_{max}$	-37.79	13.39	

2	rGOP	Mono-layer $(SE_A)_{max}$	-15.82	12.00	99.9451
		$(SE_R)_{max}$	-22.03	17.96	
		$(SE_T)_{max}$	-32.61	14.44	
3	rZP552	Mono-layer $(SE_A)_{max}$	-24.60	15.28	
		$(SE_R)_{max}$	-20.17	15.30	
		$(SE_T)_{max}$	-44.64	15.26	99.9966
		Multi-layer $(SE_A)_{max}$	-26.60	15.95	
		$(SE_R)_{max}$	-23.30	13.54	
		$(SE_T)_{max}$	-39.50	13.56	99.9888
4	rZP553	Mono-layer $(SE_A)_{max}$	-25.15	15.65	
		$(SE_R)_{max}$	-21.31	15.63	
		$(SE_T)_{max}$	-46.50	15.66	99.9978
		Multi-layer $(SE_A)_{max}$	-22.28	17.99	
		$(SE_R)_{max}$	-25.77	15.32	
		$(SE_T)_{max}$	-43.89	15.34	99.9917
5	rZP372	Mono-layer $(SE_A)_{max}$	-26.08	12.74	
		$(SE_R)_{max}$	-18.70	16.41	
		$(SE_T)_{max}$	-43.97	12.77	99.996
		Multi-layer $(SE_A)_{max}$	-31.92	15.71	
		$(SE_R)_{max}$	-24.08	15.69	
		$(SE_T)_{max}$	-54.09	15.70	99.9996
6	rZP373	Mono-layer $(SE_A)_{max}$	-27.03	12.38	
		$(SE_R)_{max}$	-19.37	14.79	
		$(SE_T)_{max}$	-47.03	14.76	99.998
		Multi-layer $(SE_A)_{max}$	-38.12	17.86	
		$(SE_R)_{max}$	-20.64	15.58	
		$(SE_T)_{max}$	-43.98	17.86	99.996

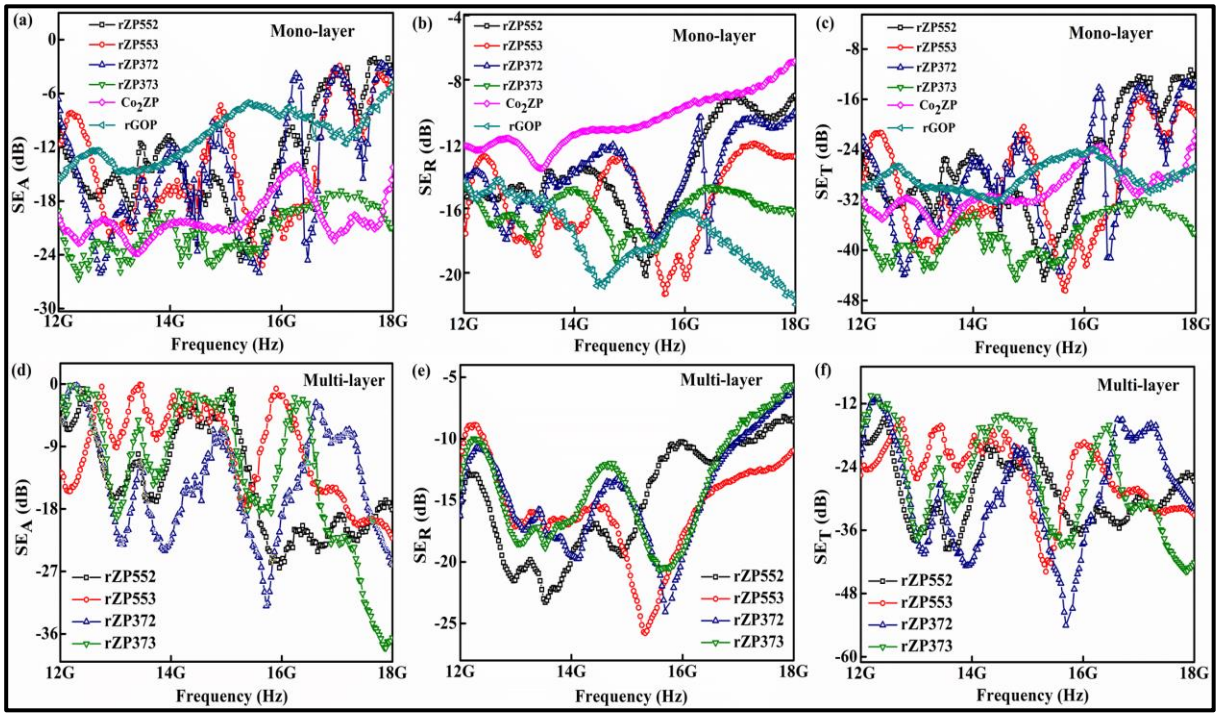

Figure 5.11: Shielding effectiveness due to absorption (SE_A) (a) mono-layer (b) multi-layer, reflection (SE_R) (c) mono-layer (d) multi-layer and total Shielding effectiveness (SE_T) (e) mono-layer (f) multi-layer of nanocomposite films for 12-18 GHz.

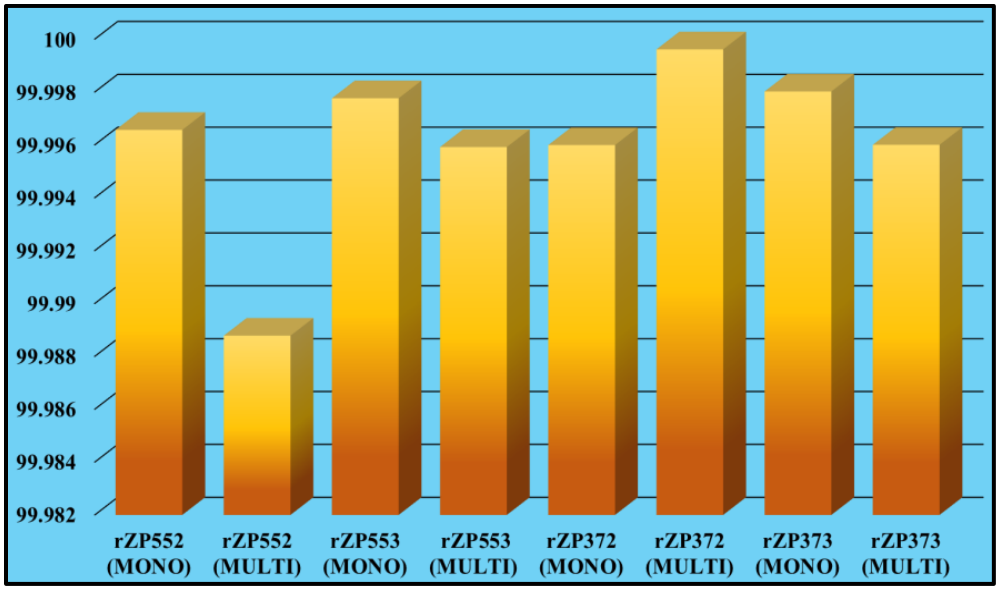

Here, MONO = Mono-layer, MULTI = Multi-layer

Figure 5.12: Attenuation percentage graph for mono and multi-layer rZP552, rZP553, rZP372 and rZP373 nanocomposite films.

5.4 Conclusion:

The strategic multiphase multi-layer structure of rGO-Co_2Z-PVDF nanocomposite films have been synthesized successfully by the cost-effective solution casting method. The XRD and Rietveld refinement study provide the necessary evidence of conducting rGO-magnetic Co_2Z-hexaferrite binary fillers inside the matrix of PVDF. The sheet like structure of rGO and hexagonal shape of Co_2Z-hexaferrite has been confirmed from FESEM observation. The cross-sectional micrographs indicate that, the thickness of mono-layer nanocomposite films lies within the range of 100 μm to 144 μm as well as the uniform thickness of each multi-layer nanocomposite film of 0.9 mm in average after the hot press method is applied. The presence of all the constituent elements (Ba, Fe, Co, C and O) in the XPS study of the rGO-Co_2Z binary fillers confirm the conjugation rGO and Co_2Z-hexaferrite in the binary fillers. The low leakage current density of 10^{-5} A/m^2 and the butterfly nature in each case represent the polarization behaviour of the nanocomposite film as observed in J-E characteristic study. The localized charge generating at the interface of the nanocomposite films plays a significant role for the EMI shielding application. The maximum magnetisation of the nanocomposite films is significantly high and the values of 6.4 and 8.9 emu/g for rZP553 and rZP373 have been found at 300 K. Here, the EMI shielding study of mono-layer structure, the multilayer structure exhibits greater absorption. The maximum SE_A of EM radiation by the mono-layer nanocomposite film is -27.03 dB at 12.38 GHz but in case of the multi-layer structure SE_A is increased to -38.12 dB at 17.86 GHz. Also, the maximum SE_T of the nanocomposite film is -54.09 dB at 15.70 GHz for multi-layer structure over the maximum SE_T -47.03 dB at 14.76

GHz in case of mono-layer structure. As a result, a high value of >99.999% attenuation has been obtained from the multi-layer nanocomposite film in EMI shielding study. Now, it has been confirmed the multi-layer structure of the nanocomposite films gives higher SE_A property as compare to mono-layer and the total SE_T study is significantly improved for the multi-layer structure of the nanocomposite films. So, these rGO-Co_2Z-PVDF nanocomposite films are the potential candidates for the microwave shielding applications such as EMI shielding jacket for radar radiation and health-care electronic body implants.

5.5 References:

1. Saha, P., Das, S. and Sutradhar, S., Journal of Applied Physics, 124(4) (2018).
2. Saha, P., Debnath, T., Das, S., Chatterjee, S. and Sutradhar, S., Materials Science and Engineering: B, 245, 17-29 (2019).
3. S. B. S. Magham, M. Sharma, S. R. Shannigrahi, H. R. Tan, V. Sharma, Y. S. Meng, S. Idapalpati, R. V. Ramanujan, D. V. M. Repaka, J. Magn. Magn. Mater. 441, 303-309 (2017).
4. S. Anand, S. Pauline, J. Phys. Chem. B. 112(10) 2775 (2020).
5. S. Pei, H. M. Cheng, Carbon 50(9) 3210-3228 (2012).
6. M. Chireh, M. Naseria, H. Ghaedamini, Advanced Powder Technology 32(14) (2021).
7. R.B. Schulz, V.C. Plantz and D.R. Brush, IEEE Transactions on Electromagnetic Compatibility 30(3) 187–201 (1988).
8. Y. H. Yang, H. J. Sun, T. J. Peng, Acta Phys-Chim. Sin. 27, 736 (2011).
9. S. Kolev, P. Peneva, K. Krezhov, T. Malakova, C. Ghelev, T. Koutzarova, D. Kovacheva, B. Vertruyen, R. Closset, L. T. Maria, A. Zaleski, Materials 13(10) 2355 (2020).

10. Q. Li, S. Yan, X. Wang, Y. Nie, Z. Feng, Z. Su, Y. Chen, V. G. Harris, Acta Materialia. 98, 190-6 (2015).
11. V. S. Bystrov, I. K. Bdikin, M. V. Silibin, J. Nanomed Nanotechnol. 5(2) 049 (2017).
12. L. Juan, L. Shuhui, F. Tao, S. Ning, C. Shenglei, J. Magn. Magn. Mater. 488, 165366 (2019).
13. N. M. S. Hidayah, W. W. Liu, C. W. Lai, N. Z. Noriman, C. S. Khe, U. Hashim, H. C. Lee, AIP Conf. Proc. 1892, 150002 (2017).
14. V. Sencadas, P. Martins, A. Pitães, M. Benelmekki, J. L. G. Ribelles, S. L. Méndez, Langmuir 27(11) 7241-9 (2011).
15. A. S. ELmezayyen, F. M. Reicha, I. M. El-Sherbiny, J. Zheng, C. Xu, Eur. Polym. J. 90, 195 (2017).
16. M. Iliut, C. Leordean, V. Canpean, C.M. Teodorescu, S. Astilean, J. Mater. Chem. C. 1(24) 4094-4104 (2013).
17. N. Sharma, V. Sharma, S. K. Sharma, K. Sachdev, Mater. Lett. 236, 444-447 (2019).
18. I. S. Elashmawi, L. H. Gaabour, Results Phys. 5, 105-110 (2015).
19. F. Kadlec, C. Kadlec, J. Vít, F. Borodavka, M. Kempa, J. Prokleška, J. Buršík, R. Uhrecký, S. Rols, Y. S. Chai, K. Zhai, Y. Sun, J. Drahokoupil, V. Goian, S. Kamba, Phys. Rev. B. 94, 024419 (2016).
20. E.E. Ateia, K. Elsayed, D. E. El-Nashar, Applied Physics A 129, 118 (2023).
21. P. Kaspar, D. Sobola, K. Částková, R. Dallaev, E. Šťastná, P. Sedlák, A. Knápek, T. Trčka, V. Holcman, Materials 14(6) 1428 (2021).
22. R. Joshi, A. D. Adhikari, A. Dey, I. Lahiri, Materials Science and Engineering: B 287 116128 (2023).

23. S. Sadhukhan, A. Mitra, A.S. Mahapatra, P. K. Chakrabarti, J. Alloys Compd. 956 170351 (2023).

24. S. Dwivedi, M. Badole, K. Gangwar, S. Kumar, Polymer. 231, 124164 (2021).

25. J. Mohapatra, M. Xing, J.P. Liu, Materials 12, 3208 (2019).

26. G. Wang, X. Huang, P. Jiang, ACS Appl. Mater. Interfaces 7, 18017−18027 (2015).

27. A. S. Mahapatra, A. Mitra, A. Mallick, A. Shaw, J. M. Greneche, P. K. Chakrabarti, J. Alloys Compd. 743, 274-282 (2018).

28. A. Ghasemi, MNT 125-299 (2022).

29. S. Lei, L. Liu, C. Wang, X. Shen, D. Guo, C. Wang, S. Zeng, B. Cheng, Y. Xiao, L. Zhou, CrystEngComm. 16, 1322 (2014).

30. A. M. Nicolson, G. Ross, IEEE Trans. Instrum. Meas., 19, 377-382 (1970).

31. W. B. Weir, Proc. IEEE, 62, 33-36 (1974).

32. A. H. Boughriet, C. Legrand, A. Chapoton, IEEE Trans. Microw. Theory Tech. 45 52–57 (1997).

33. H. Lv, G. Ji, H. Zhang, M. Li, Z. Zuo, Y. Zhao, B. Zhang, D. Tang, Y. Du, Scientific Reports 5, 18249 (2015).

34. H. Lv, H. Zhang, J. Zhao, G. Ji, Y. Du, Nano Res. 9, 1813–1822 (2016).

35. Z. Zhao, X. Zhou, K. Kou, H. Wu, Carbon 173, 80-90 (2021).

36. S. Biswas, G. P. Kar, S. Bose, J. Mater. Chem. A. 3, 12413 (2015).

37. R. Ravindren, S. Mondal, P. Bhawal, Sk. Md. N. Ali, N. C. Das, Polym. Compos. 40(4) 1404 (2018).

38. W. Cao, C. Ma, S. T. M. Ma, P. Wan, F. Chen, Nanomicro Lett. 11, 72 (2019).

39. Y. Bhattacharjee, S. Bose, ACS Appl. Nano Mater. 4 949−972 (2021).

Chapter: 6

Tailoring of EMI shielding behaviour by considering the coating of non-conducting polymer jacket over multi-layer hexaferrite-TMDC nanocomposite film

Chapter 6:

6.1 Introduction:

In Chapter 5, the stack up structure of multi-layered systems was used to improve MW absorption. The additional dissipation of microwave radiation at the interfaces between each layer has an impact on the forward and backward propagation of electromagnetic (EM) waves in these systems [1]. The mono-layer of these shielding materials does not possess any such additional dissipative mechanisms. The tunability of a mono-layer mainly depends on the filler quantity and the thickness of the sample. A multi-layer structure includes an additional adjustable mechanism: the ability to control the transmission of EM waves through several dielectric media interfaces, thereby directing or dispersing incoming EM radiation [1]. Nevertheless, it has been noted that the shielding efficiency due to reflection (SE_R) of the multi-layer rGO-Co_2Z-PVDF nanocomposite system, created via the hot-press process, is improved in certain instances when compared to its mono-layer equivalent. The rise of rGO on the surface, which has been influenced by temperature and pressure, is responsible for the increased surface reflection. In this study, an extra non-conducting surface has been added to the multi-layer structure to examine its ability to reduce reflection without affecting the desired absorption properties of the multi-layer nanocomposite films. To reduce surface reflection and improve impedance matching, extra layers of nonconducting PVDF have been added to both sides of the multi-layer nanocomposite films.

The originality of this study is the investigation of the synergistic influence of Ba-substituted Co_2Y-hexaferrite and MoS_2 binary nanofillers in a PVDF laminated nanocomposite structure on its ability to absorb EM radiation in the GHz frequency range. MoS_2 is a semiconducting material with a layered structure. It consists of one molybdenum (Mo) atom

sandwiched between two sulfur (S) atoms, which are joined by covalent links [2]. Moreover, the weak van der Waal forces aid in the vertical arrangement of MoS_2 nanosheets [3]. MoS_2, when in its bulk form, is categorized as an indirect bandgap semiconductor with a bandgap energy of ~ 1.2 eV [4]. This property enables the alteration of surface structure by utilizing the quantum confinement effect, resulting in improvements in its ability to absorb EM waves [5]. The ability of EM waves to decrease in intensity is due to the interfacial polarization at the interface and the loss of electrical energy displayed by thin layers of exfoliated MoS_2 nanosheets. Unlike graphene oxide, reduced graphene oxide and other two-dimensional (2D) materials, transition-metal chalcogenides have lower conductivity and a notable dielectric constant. This leads to less surface reflection, resulting in better impedance matching with free space and increased performance in absorbing microwaves [6]. These materials have unique attributes that make them appropriate for a diverse array of uses. This study fully exploits the magnetic properties of Ba substituted Co_2Y-hexaferrite and the polarization properties of MoS_2 nanofillers to achieve effective electromagnetic interference (EMI) shielding. These properties are utilized in the fabrication of polymer-based nanocomposite films. The main focus of this study is to investigate the comprehensive details of the EMI shielding capability and impedance matching condition of nanofiller-polymer nanocomposite films, both with and without a non-conducting PVDF jacket.

6.2 Experimental:

6.2.1 Materials:

The required chemicals to synthesize of Co_2Y hexaferrite-MoS_2-PVDF nanocomposite films are Molybdenum Oxide (MoO_3) (Sigma Aldrich, 99%) and Potassium Thiocyanate (KSCN) (Sigma Aldrich, 99%), iron (III) nitrate nonahydrate ($Fe(NO_3)_3.9H_2O$) (Merck Germany, 99%),

cobalt (II) nitrate hexahydrate ($Co(NO_3)_2.6H_2O$) (Merck Germany, 99%), barium (II) nitrate ($Ba(NO_3)_2$) (Merck Germany, 99%), and ethanol (C_2H_5OH), Poly (vinylidene fluoride-co-hexafluoropropylene) (PVDF-HFP) (average Mw: 455,000 Sigma Aldrich), N, N-dimethyl formamide (DMF) (Merck, India).

6.2.2 Synthesis of Co_2Y-hexaferrite:

Synthesis of Co_2Y-hexaferrite with the stoichiometry ration of $Ba_2Co_2Fe_{12}O_{22}$ has been done using simple sol-gel method. The details of the synthesis procedure have already been discussed in chapter 2 (**Section: 2.2.1** Synthesis of magnetic hexaferrite and ferrite nanoparticles by sol-gel method). After collecting the as prepared Co_2Y-hexaferrite, the powder was annealed at 1200 °C in a hot air oven to get the proper crystallographic phase.

6.2.3 Synthesis of MoS_2 semiconducting fillers:

The semiconducting MoS_2 nanofillers was prepared by hydrothermal method and the details of synthesis procedure has been mentioned in chapter 2 (**Section: 2.2.2.3** Synthesis of molybdenum sulphide (MoS_2) by hydrothermal method). The desired product was obtained via combining MoO_3 and KSCN are in a 1:2 molar ratio in distilled water medium. The hydrothermal system is subjected to a heat treatment of 200 °C for 24 hours. After washing and drying, the resultant powder was collected.

6.2.4 Synthesis of Co_2Y-hexaferrite-MoS_2-PVDF nanocomposite films:

Before synthesizing the polymer nanocomposite films the binary nanofillers of Co_2Y hexaferrite-MoS_2 has been prepared by solid-state reaction method, and the details of the solid-state reaction method has been discussed in chapter 2 (**Section: 2.2.2.4** Synthesis of binary nanocomposite by grinding-mixing method). To get the flexible, free-standing Co_2Y hexaferrite-MoS_2 nanocomposite films, cost effective solution casting method have been used.

The detailed procedure of solution casting method mentioned in chapter 2: (**Section: 2.2.2.5** Synthesis of nanofillers-polymer nanocomposite film by solution casting method). The prepared YMP552, YMP553, YMP912 and YMP913 nanocomposite films are cut into the proper dimensions to conduct all the measurement.

6.2.5. Formation mechanism of Co_2Y-hexaferrite-MoS_2-PVDF nanocomposite films

Figure 6.1(I) shows the schematic diagram of the Co_2Y hexaferrite-MoS_2-PVDF nanocomposite film. At RT, the Co_2Y-hexaferrite ($Ba_2Co_2Fe_{12}O_{22}$) shows a magnetization plane that is positioned at a right angle to the c-axis [7]. The Co_2Y-hexaferrite consists of one S unit and one L unit, resulting in a total of six layers. This hexaferrite crystal is classified under the R_3m space group [7]. Co_2Y-hexaferrite exhibits a decreased magnetic permeability in comparison to ferrites with uniaxial anisotropy. However, it demonstrates a substantial magnetization at high frequencies due to its possession of a magnetization plane that may rotate readily. MoS_2, a semiconducting 2D material, belongs to the category of transition-metal dichalcogenides. In the MoS_2 layer, a single Mo atom is situated between dual S atoms, connected by robust covalent bonds. 2D MoS_2 demonstrates exceptional EM wave attenuation capabilities as a result of its robust interfacial polarization and notable dielectric loss. This leads to a decrease in the amount of reflection on the surface and enhances the ability to match the impedance with open space [2-4]. The binary nanofillers Co_2Y hexaferrite-MoS_2 is first fabricated by the solid-state reaction approach. The nanocomposite system is then incorporated into the PVDF matrix separately by the solution-casting method. The positively charged hydrogen ligands in the PVDF matrix form an electrostatic connection with the binary nanofillers, which possess a negatively charged surface. The attachment is formed through the electrostatic forces of attraction, which helps in connecting PVDF with Co_2Y hexaferrite-MoS_2

on both sides, resulting in the successful integration of Co_2Y hexaferrite-MoS_2 nanofillers into the PVDF matrix. Furthermore, Figure 6.1(II) illustrates the free-standing and flexible nature of the nanocomposite films. The flexibility of the nanocomposite films remains intact even after the synthesis of multi-layer and polymer jacket coated nanocomposite films using the hot press process, without experiencing any physical damage.

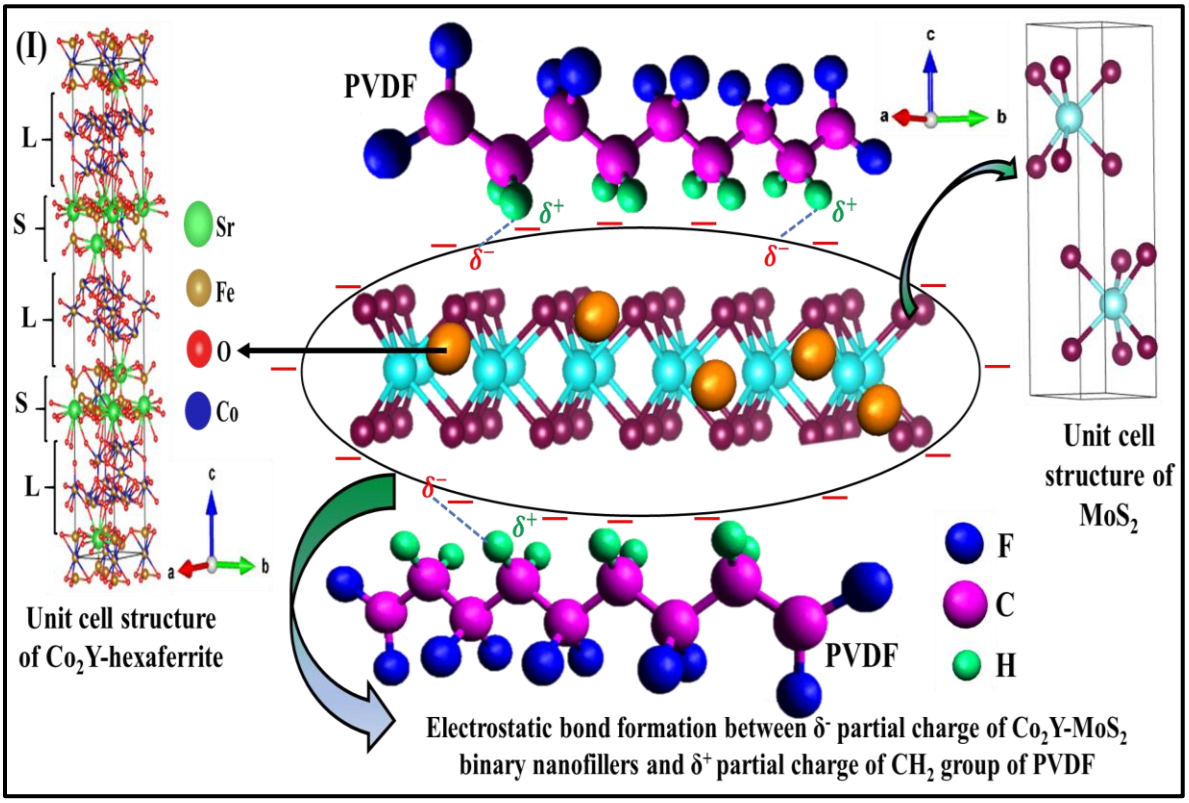

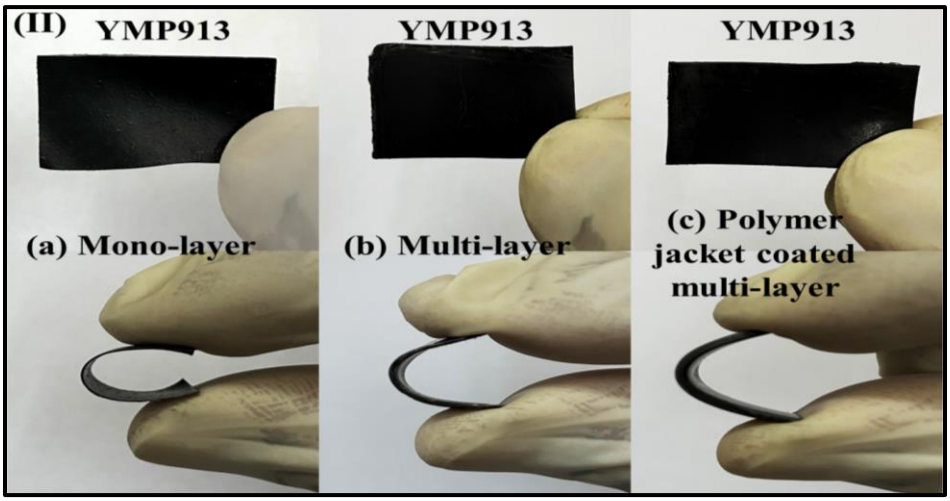

Figure 6.1: (I) Formation mechanism of Co_2Y-hexaferrite-MoS_2-PVDF nanocomposite film, (II) Free standing and flexible images of (a) mono-layer, (b) multi-layer and (c) polymer jacket coated multi-layer nanocomposite film.

6.3 Result and Discussions

6.3.1 Crystallographic phase analysis:

The X-ray diffraction (XRD) analysis was conducted on Co_2Y-hexaferrite, MoS_2, bare PVDF, and YMP552, YMP553, YMP912, and YMP913 nanocomposite films. The analysis covered a range of 10^o to 80^o and confirmed the presence of crystallographic phases corresponding to the Co_2Y-hexaferrite-MoS_2 binary fillers within the PVDF matrix in the heterojunction multiphase nanocomposite films. The crystallographic phases of Co_2Y-hexaferrite, MoS_2, and bare PVDF have been accurately correlated with the crystallographic phases of their respective samples as indicated in their JCPDS files 44-0206, 37-1492, and 42-1650. Figure 6.2(I and II) illustrates the results of Rietveld refinement for Co_2Y-hexaferrite and MoS_2 nanoparticles produced using the sol-gel and hydrothermal synthesis methods, respectively. Figure 6.2(III and IV) displays the X-ray diffraction (XRD) pattern of the III(a)bare PVDF film and (IV)(a-d) the nanocomposite films, specifically YMP552, YMP553, YMP912, and YMP913. Therefore, conducting this XRD analysis will enable us to comprehend the development of the composite structure of the resultant materials, exhibiting a well-defined multi-phase composition. The average size of Co_2Y-hexaferrite was determined by analyzing the most intense peak using the Debye-Scherrer equation [8]. This method allows for an estimation of the crystallite diameter.

$$< D >= \frac{0.9\lambda}{\beta_{\frac{1}{2}}\cos\theta} \tag{6.1}$$

In this context, D represents the mean size of the crystallites, λ stands for the wavelength of the

X-rays used, θ refers to the Bragg angle, and $\beta_{\frac{1}{2}}$ represents the full width at half maximum (FWHM). The Co_2Y-hexaferrite have a crystalline diameter of around 20 nm. The presence of non-polar α, polar β, and γ-phase crystallizations in the nanocomposite films suggests that successful interfaces have been created between the Co_2Y hexaferrite-MoS_2 binary fillers and the PVDF matrix. Furthermore, it has been observed that the non-polar α-phase is diminished and the polar β-phase is more evident in nanocomposite films compared to naked PVDF. This interaction is accountable for the creation of every trans-planar zig-zag (TTTT) conformation within the nanocomposite films.

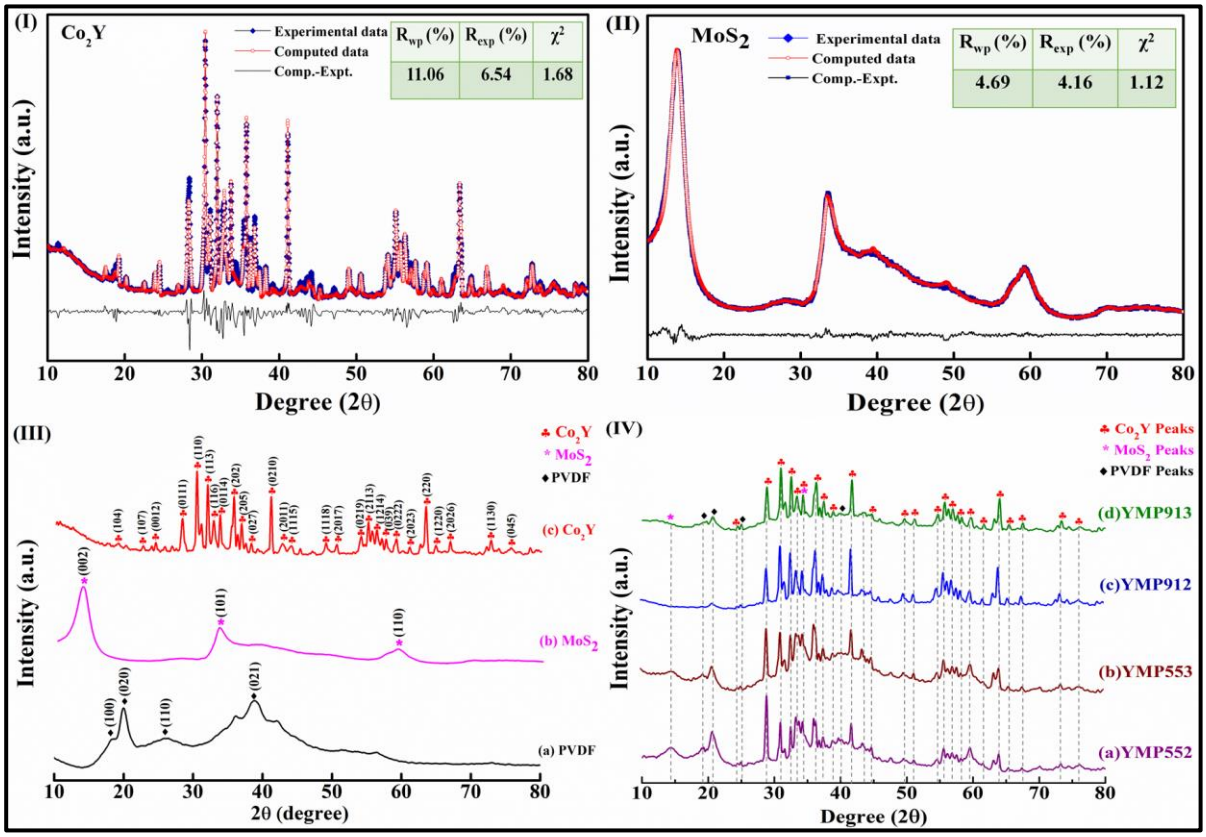

Figure 6.2: (I, II) Rietveld refinement of Co_2Y and MoS_2 nanoparticles, XRD patterns of (III) (a) bare PVDF-HFP, (b) MoS_2, (c) Co_2Y nanoparticles and (IV) (a) YMP552, (b) YMP553, (c) YMP912 and (d) YMP913 nanocomposite films.

6.3.2 Study of surface morphology:

Figure 6.3(a-h) illustrates the surface morphology analysis of Co_2Y hexaferrite-MoS_2 binary fillers and specific nanocomposite films (YMP553 and YMP913). The nanocomposite films have a spherulite nature, characterized by the presence of conspicuous bubble-like features. The previous chapter has already stated that the spherulite structure of bubble type found on the surface of YMP553 and YMP913 nanocomposite films shows the presence of polar/electroactive β-phase crystallization of the PVDF matrix. The micrographs in Figure 6.3(e, f, g and h) clearly indicate the presence of binary fillers within the PVDF matrix. The incorporation of Co_2Y hexaferrite-MoS_2 binary fillers into the PVDF matrix leads to the creation of nanofiller-PVDF interfaces within the nanocomposite films. These interfaces enhance the electroactivity of the films, resulting in the development of a more pronounced polar/electroactive β-phase. Figure 6.3(i-k) depicts the cross-sectional view of a nanocomposite film with several types of thicknesses: mono layer, multi-layer, and a non-conducting polymer jacket coated multi-layer structure. No leakage or gaps have been noticed with the transition from a mono-layer to a multi-layer construction, due to the improved thickness. The YMP553 and YMP913 composite films were analysed using energy dissipative spectroscopy (EDX) and elemental mapping. This study was conducted on YMP553 and YMP913 composite films as a representative example of the various nanocomposite films. Figure 6.3(l, m and n) displays the EDX and elemental mapping of YMP553 and YMP913, respectively. The EDX and elemental mapping studies have established the presence of barium (Ba), cobalt (Co), iron (Fe), fluorine (F), sulfur (S), molybdenum (Mo), oxygen (O), and carbon (C) ions in the YMP553 and YMP913 nanocomposite film. Remarkably, the enhanced combination of carbon (C) and fluorine (F) components is easily detectable. This can be due to the greater weight % of the

PVDF component in the nanocomposite film. The abundance of C and F elements corresponds to the composition of the polymer matrix, hence contributing to the overall elemental profile of the nanocomposite films. The morphological analysis reveals the coexistence of magnetic Co_2Y-hexaferrite and semiconducting MoS_2 layer structures in the YMP553 and YMP913 nanocomposite films.

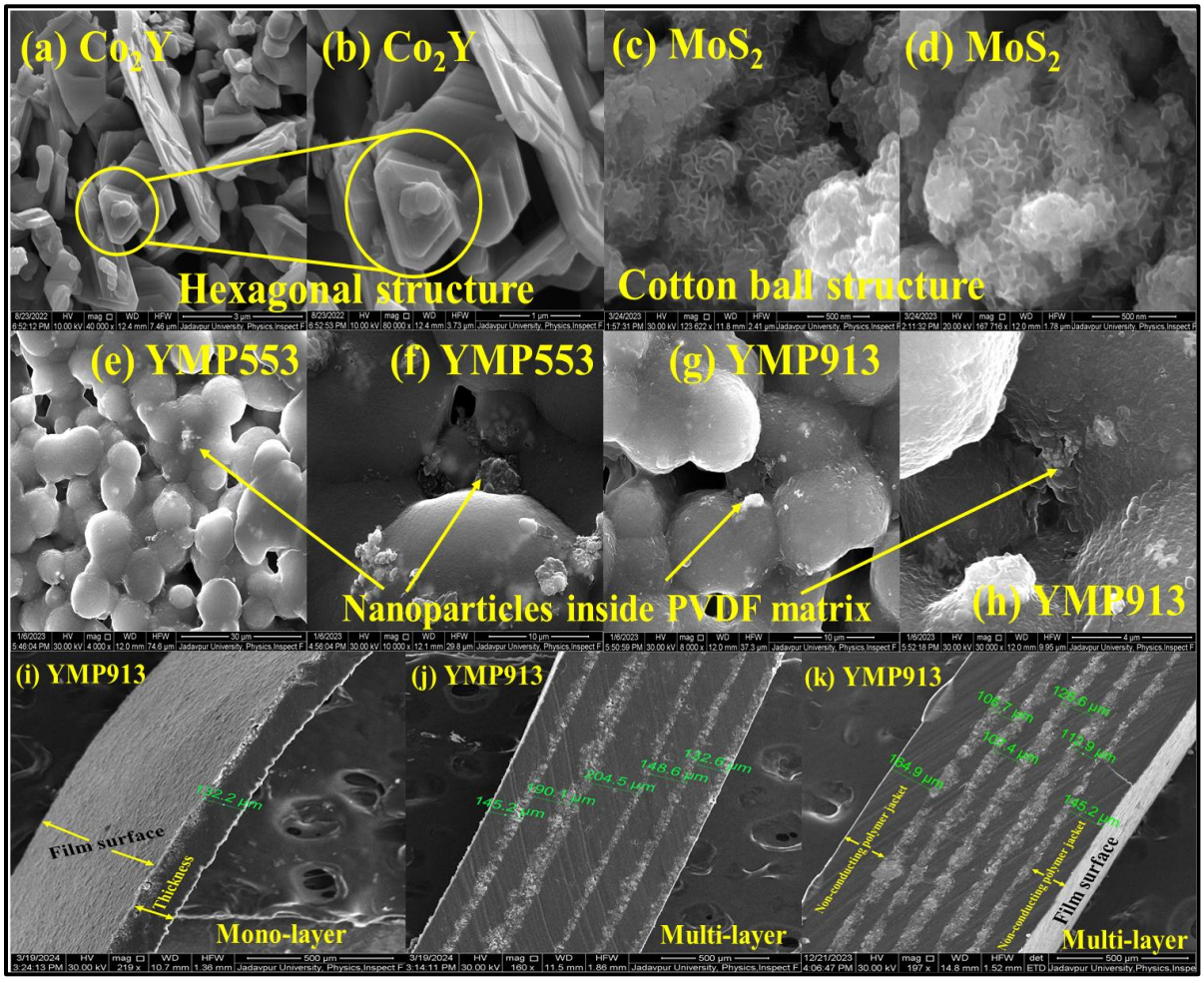

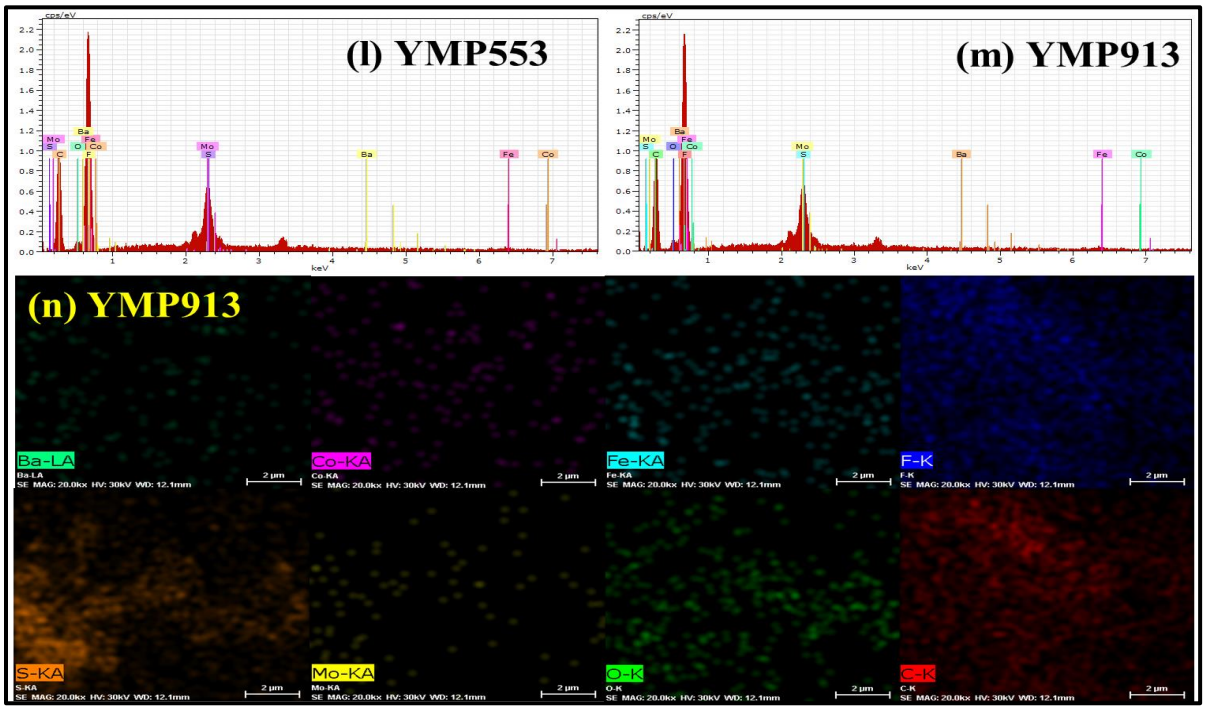

Figure 6.3: FESEM micrographs of (a, b) Co_2Y-hexaferrite, (c, d) MoS_2 nanoparticles, (e, f) YMP553, (g, h) YMP913 nanocomposite films, cross sectional images of (i) mono-layer, (j) multi-layer, (k) non-conducting polymer jacket coated multi-layer structure, (l, m) EDS study and (n) elemental mapping of YMP913 nanocomposite film.

6.3.3 J-E characteristic study:

Figures 6.4(a-g) depict the correlation between current density (J) and electric field (E) for several materials, namely bare PVDF, Co_2Y-hexaferrite, MoS_2, YMP552, YMP553, YMP912, and YMP913. These measurements were taken at RT and within a voltage range of ±20 V. Figure 6.4(h) illustrates the highest amount of current leakage seen in the nanoparticles and nanocomposite films when subjected to an electric field strength of 90 kV/m. The Figures 6.4(a-g) clearly demonstrate that the J-E curves do not follow the same path when tracing the voltage range. Instead, they exhibit a non-linear feature, generating a distinctive butterfly loop pattern. The presence of polarization effect in the samples is confirmed by the butterfly loop of the

curves [9]. The insulating properties of PVDF can be accurately described by its low current density, which is around 10^{-7} A/m^2. Co_2Y-hexaferrite and MoS_2 demonstrate significantly elevated leakage current when compared to other materials, as depicted in Figure 6.4(b) and (c), suggesting their semiconducting properties. Figures 6.4(a′-g′) display the I-V characteristics of the samples as an inset. The non-linear nature of the I-V curves, together with their deviation from intersecting at the origin, signifies their semiconducting characteristics [10]. The nanocomposite films consist of a 50:50 weight percentage of Co_2Y hexaferrite:MoS_2 binary fillers (YM55) demonstrate much greater leakage current densities in comparison to other nanocomposite films containing 90:10 wt.% of binary fillers (YM91). This provides compelling proof of the impact of MoS_2 within the PVDF matrix. Moreover, in Figure 6.4(h) the impact of the loading percentage of the binary nanofiller within the PVDF matrix (30 wt.%) demonstrates elevated magnitude of leakage current density.

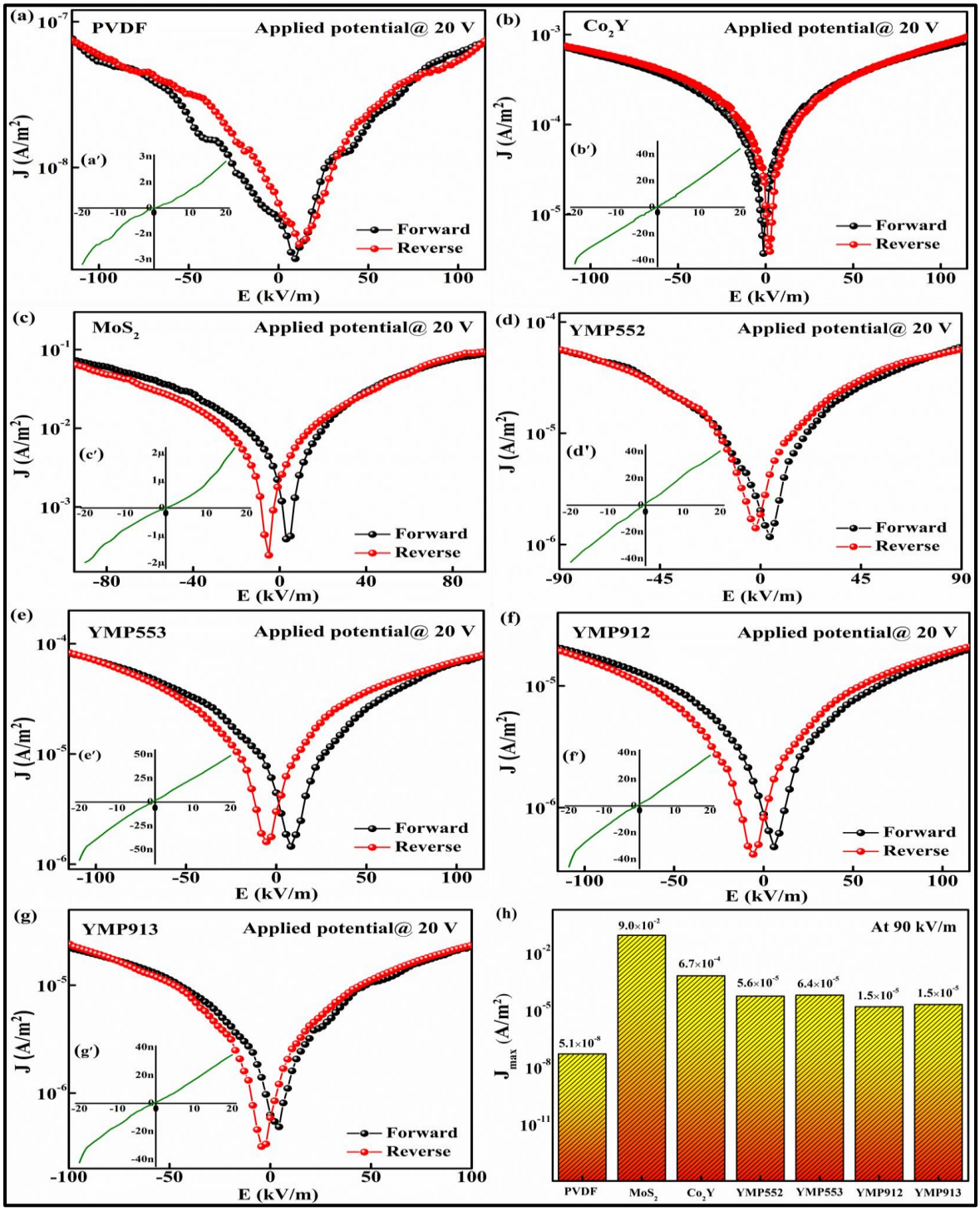

Figure 6.4: (a-g) J-E characteristic, (a′-g′) I-V characteristic and (h) variation of leakage current density of bare PVDF, Co_2Y-hexaferrite, MoS_2, YMP552, YMP553, YMP912, and YMP913 nanocomposite films.

6.3.4 Magnetic property study:

In this chapter the magnetic response of Co_2Y-hexaferrite at RT and a maximum applied field of 60000 Oe has been investigated. The hexaferrite show a clear hysteresis loop at RT which is clear evidence of having magnetic ordering in the representative nanocomposite films depicted in Figure 6.5. Figure 6.5 at 300 K provide the following information on the Co_2Y-hexaferrite: a saturation magnetisation (M_m) of 33.32 emu/g, a coercive field (H_c) of 647 Oe, and a remanence magnetisation (M_r) of 16.60 emu/g. The Co_2Y-hexaferrite crystal has Co^{2+} and Fe^{3+} ions with magnetic moments of 3 μB and 5 μB, respectively, located at the octahedral (B) sites. In contrast, Ba^{2+} ions are located at the tetrahedral (A) sites and have no magnetic moment [11]. The disparity in magnetic moment between the two sites results in a powerful interaction between the A-B sites, thereby enhancing the magnetization of the Co_2Y-hexaferrite [12]. The high saturation magnetisation of the Co_2Y-hexaferrite results in significant permeability values, making the nanocomposite films (YMP552, YMP553, YMP912, and YMP913) effective for studying EMI shielding in the microwave frequency range. To accurately quantify both of these factors, we endeavoured to examine the observed M-H loops utilizing the provided equation [13, 14].

$$M(H) = \left[2\frac{M_{FM}^{S}}{\pi}\, tan^{-1}\left\{\left(\frac{H \pm H_{ci}}{H_{ci}}\right) tan\left(\frac{\pi M_{FM}^{R}}{2M_{FM}^{S}}\right)\right\}\right] + \chi H \qquad (6.2)$$

The provided equation determines the magnetization, M(H), at a specified applied magnetic field, H. The equation comprises two terms. The first part refers to the magnetization that arises from the organized magnetic state, specifically the ferrimagnetic state. The second part is a linear component that originates from the paramagnetic contribution. In this equation M_{FM}^{S}, indicates the ferrimagnetic saturation magnetization, M_{FM}^{R}, represents remnant magnetization

and H_{ci} intrinsic coercive field, χ signifies the paramagnetic susceptibility. Figure 5 presents the experimental magnetization, theoretical fitting, and simulated ferrimagnetic and paramagnetic contributions for the data collected at 300 K.

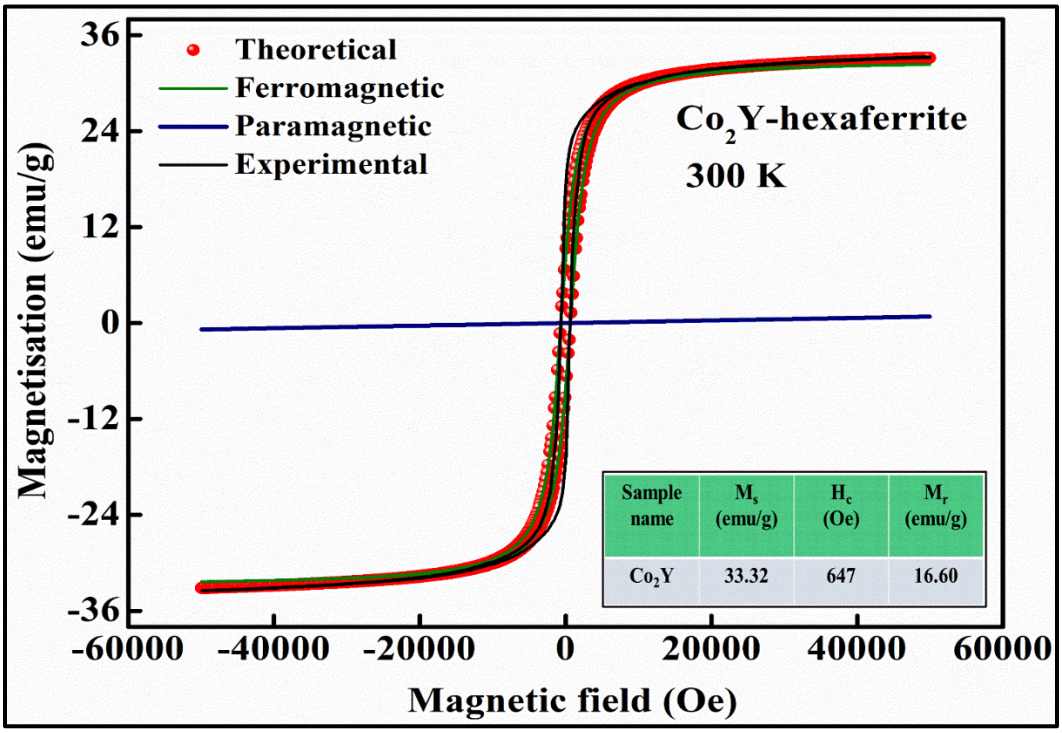

Figure 6.5: Experimental and theoretically simulated graph of M-H loop for Co_2Y-hexaferrite at 300 K.

6.3.5 High frequency complex permittivity and permeability study:

The permittivity and permeability characteristics of a material have a considerable impact on its EMI shielding efficiency. The permittivity and permeability of a material is its response to an external EM field in terms of its dielectric and magnetic properties. The nanocomposite films' complex permittivity ($\varepsilon^* = \varepsilon' + i\varepsilon''$) and permeability ($\mu^* = \mu' + i\mu''$) were found by computing them from the acquired S-parameters, specifically S_{11} (reflection coefficient) and S_{21} (transmission coefficient). The values were computed using the noniterative technique proposed by Boughriet et al. [15] which is based upon the NRW (Nicolson–Ross–Weir)

method. The real components of the complex permittivity and complex permeability (ε', μ') represent the ability of the material to store electric and magnetic energy, respectively inside the medium. The imaginary components of complex permittivity and complex permeability (ε'', μ'') represent the dielectric and magnetic losses resulting from various relaxation mechanisms, such as dipolar and ionic relaxations, domain wall resonance, and natural resonance. Tangent loss (tan δ) quantifies the level of energy dissipation that occurs when the dipoles of a material interact with EM waves. The shielding effectiveness of a substance is determined by its ability to match the impedance of the surrounding environment. Greater impedance matching enhances the absorption capacity of EM waves by materials, while lower matching results in reflection [16]. Therefore, it is crucial to align the permittivity and permeability of a material in the GHz frequency range in order to achieve a wide effective bandwidth for absorption.

Figure 6.6(a-f) displays the real component of the complex permittivity and permeability of the nanocomposite films. The notable increase in ε' in nanocomposite films as compared to PVDF can be attributed to the charge imbalance caused by the doping of a transition metal (Co) into hexaferrite [17], and the inclusion of semiconducting MoS_2 nanoparticles [18]. The Co_2Y-MoS_2 heterogeneous structure and the interfaces between the binary fillers and the polymer cause interfacial or space charge polarization. Figure 6.6(d-f) shows the real part of the complex permeability, which indicates that the nanocomposite films have a significantly greater capacity to store magnetic energy compared to their ability to store electric charge. The presence of Co_2Y-hexaferrite inside the nanocomposite systems is exclusively responsible for the considerable boost in μ' for the nanocomposite films [19, 20].

Figure 6.6(g-l) depicts the imaginary components of the complex permittivity and permeability ((ε'', μ''). Upon observation, it is evident that the dielectric loss is lower in

comparison to the magnetic loss. This indicates that the magnetic loss is the primary factor influencing the shielding efficiency of the nanocomposite films. Incorporating MoS_2 into the Co_2Y-hexaferrite-PVDF nanocomposite results in an enhanced localized electrical conductivity, leading to improvements in the imaginary permittivity and dielectric loss tangent [21]. In the microwave frequency range, the primary causes of magnetic losses are exchange resonance, natural resonance, and eddy current loss. The resistive characteristic of Co_2Y-hexaferrites ensures that Eddy current loss can be ignored [22]. Therefore, the identified resonance peaks are a consequence of both natural and exchange resonances. Furthermore, the major cause of the observed fluctuations is mostly attributed to the widespread occurrence of exchange resonance in the higher frequency range of 12-18 GHz [22].

Figure 6.6(m-r) shows the tangent loss of the dielectric ($tan\ \delta_\varepsilon = \ \varepsilon''/\varepsilon'$) and magnetic ($tan\ \delta_\mu = \ \mu''/\mu'$) components of the nanocomposite films. The dielectric tangent loss reduces as the frequency increases, but the magnetic tangent loss swings within a certain range due to exchange and natural resonances. Consequently, the magnetic hexaferrites and thickness of the nanocomposite films are the primary factors influencing the overall shielding efficiency of the films. In order for EM radiation to efficiently permeate into the absorber material, the surface impedance of the absorber material must be in accordance with the impedance of the surrounding medium, such as air. The impedance ratio (Z) of a material is determined by its EM properties, which can be expressed as follows [23].

$$Z = \frac{Z_{in}}{Z_0} = \sqrt{\frac{\mu_r}{\varepsilon_r}}\, tanh\left[j\left(\frac{2\pi f d}{c}\right)\sqrt{\mu_r \varepsilon_r}\right] \tag{6.3}$$

In equation (3), Z_{in} represents the impedance of the sample surface, Z_0 represents the impedance of air, ε_r represents the complex permittivity, and μ_r represents the complex

permeability. Figure 6.7(a) shows Z of the mono-layer nanocomposite films. Despite the fluctuations being close to unity, the presence of fluctuations suggests an inconsistency in impedance matching across the whole frequency range. Figures 6.7(b and c) depict the changes in impedance ratios in both the multi-layer and non-conducting polymer jacket coated multi-layer films over time. Within the lower to middle frequency range, Z is largely stable and is close to one. However, in the upper frequency spectrum, some dispersion becomes noticeable. The nanocomposite films demonstrate exceptional impedance matching across a broad frequency spectrum, indicating their strong ability to shield EM radiation. The attenuation constant of the nanocomposite films was determined by applying equation (10) [23].

$$\alpha = \frac{\sqrt{2}\pi f}{c}\sqrt{(\mu''\varepsilon'' - \mu'\varepsilon') + \sqrt{(\mu''\varepsilon'' - \mu'\varepsilon')^2 + (\mu'\varepsilon'' + \mu''\varepsilon')^2}} \quad (6.4)$$

In this context, the variable c represents the speed of light, whereas f indicates the frequency of the incident wave. The attenuation constant (α) is used as a measure to evaluate how well the nanocomposite films can block EM waves across the applicable frequency range. The Figures 6.7(d-f) show the α curve of the nanocomposite films in the frequency range of 12 to 18 GHz. This region corresponds to the highest values of SE_T for each sample. The undulating characteristics of the curves can be elucidated by the Z values found in Figures 6.7(a-c). The graphs clearly indicate that the attenuation constant of the nanocomposite films is greater in the frequency range of 12-18 GHz, where the Z values are nearly equal to one.

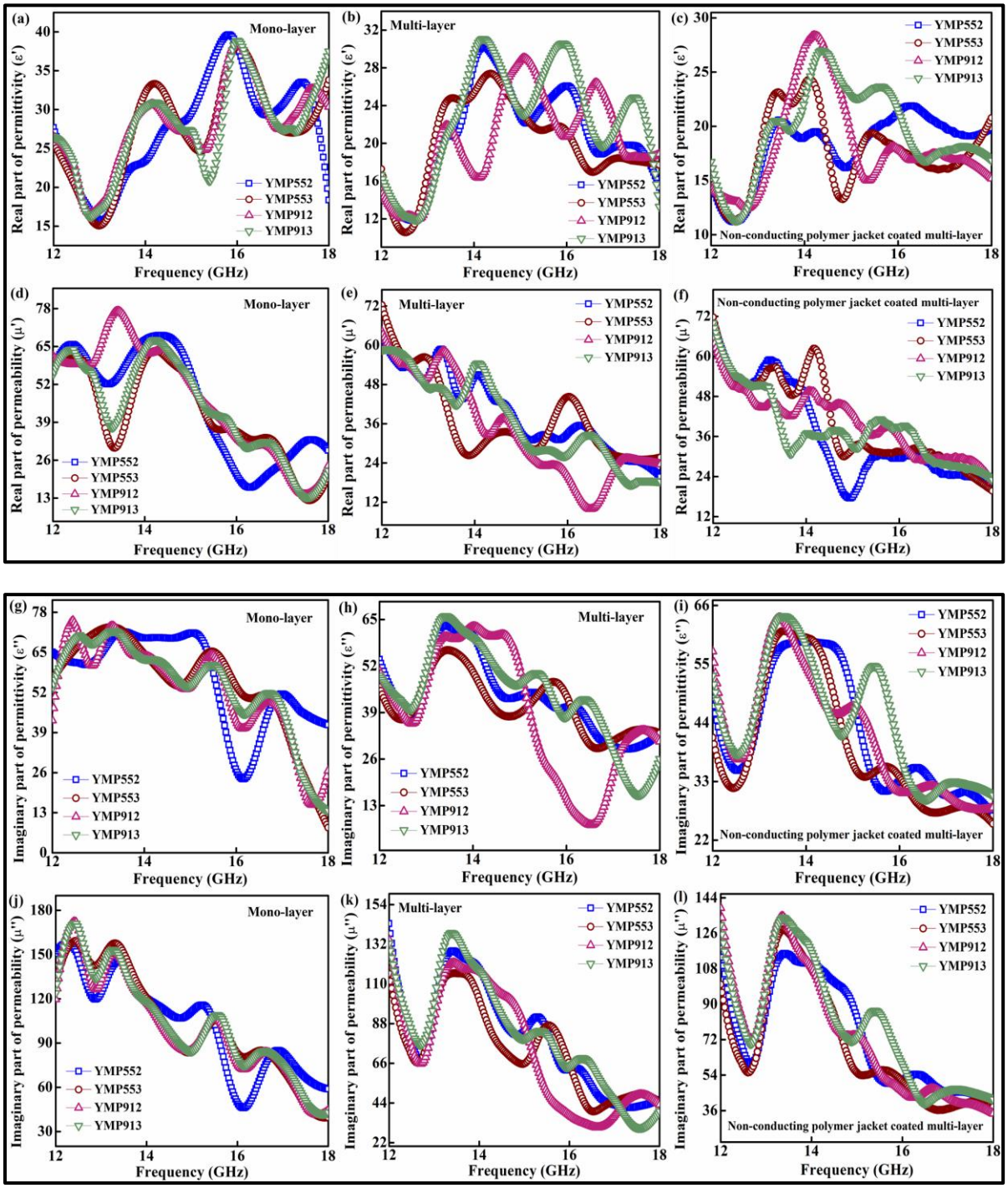
(a)
Mono-layer
Real part of permittivity (ε')
Frequency (GHz)
YMP552
YMP553
YMP912
YMP913
(b)
Multi-layer
(c)
Non-conducting polymer jacket coated multi-layer
(d)
Real part of permeability (μ')
(e)
(f)
(g)
Imaginary part of permittivity (ε'')
(h)
(i)
(j)
Imaginary part of permeability (μ'')
(k)
(l)

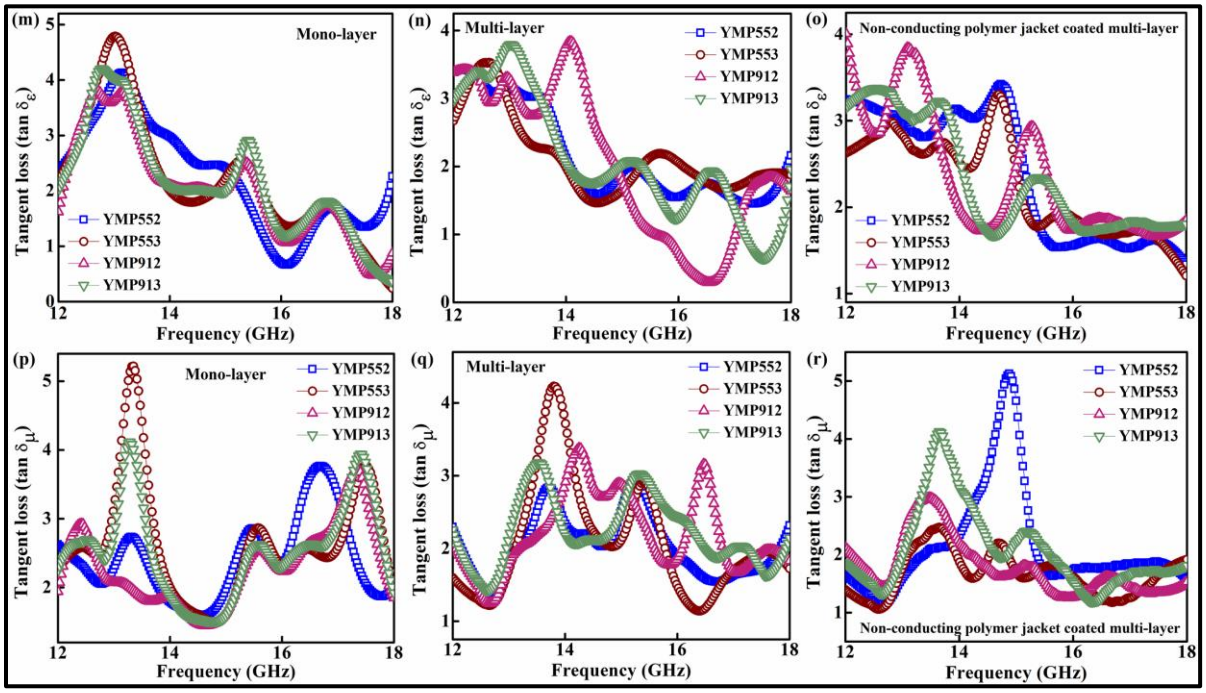

Figure 6.6: (a-c) ε', (d-f) μ', (g-i) ε'', (j-l) μ'', (m-o) tanδ_ε, (p-r) tanδ_μ of mono-layer, multi-layer and non-conducting polymer jacket coated multi-layer YMP552, YMP553, YMP912, and YMP913 nanocomposite films at 12-18 GHz.

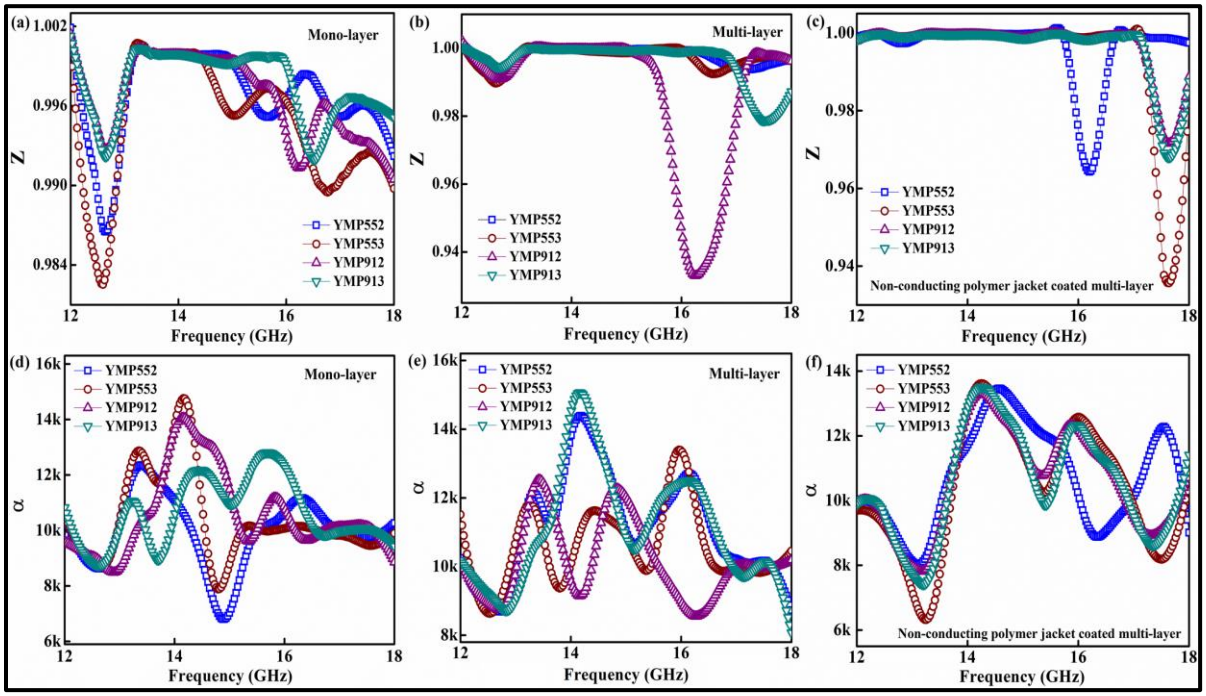

Figure 6.7: (a-c) impedance (Z), (d-f) attenuation constant (α) of mono-layer, multi-layer and non-conducting polymer jacket coated multi-layer YMP552, YMP553, YMP912, and YMP913 nanocomposite films at 12-18 GHz.

6.3.6 Study of EMI shielding property:

In this chapter, the EMI shielding effectiveness due to absorption by the fabrication of the multi-layer and a novel non-conducting polymer jacket coated multi-layer structure along with unique combination of different weight percentage of Co_2Y hexaferrite-MoS_2 binary fillers inside the PVDF-HFP matrix (YMP552, YMP553, YMP912, YMP913 nanocomposite films) have been focused. The shielding effectiveness study has been conducted in this chapter for K_u-band (12-18 GHz) of microwave radiation. Here, the shielding effectiveness of the nanocomposite films has been considered for shielding effectiveness due to absorption (SE_A), shielding effectiveness due to reflection (SE_R) and shielding effectiveness for multiple reflections (SE_{MR}) [24]. The overall shielding effectiveness of the nanocomposite films can be displayed in three different ways and they are shielding effectiveness due to absorption (SE_A), shielding effectiveness due to reflection (SE_R) and the total shielding effectiveness (SE_T). The SE_T of the nanocomposite films has been estimated by using the equation

$$SE_T\ (dB) = -10 \log_{10}\left(\frac{P_t}{P_0}\right) = SE_A + SE_R + SE_{MR} \qquad (6.5)$$

However, the shielding effectiveness by multiple reflections (SE_{MR}) can be neglected for these nanocomposite films as their thicknesses are more than the skin depth of the incident microwave radiation in the frequency range of 12-18 GHz. Thus, the total shielding effectiveness (SE_T) of nanocomposite films given in equation (9) can be further expressed as [25, 26]

$$SE_T\ (dB) = -10 \log_{10}\left(\frac{P_t}{P_0}\right) = SE_A + SE_R \qquad (6.6)$$

Where, P_t represents the transmitted power and P_0 represents the incident power of microwave radiations. The estimation of shielding effectiveness as SE_A and SE_R in the frequency range of 12-18 GHz can be done by the following equations [16]

$$SE_A\ (dB) = -10 \log_{10} \left(\frac{1 - |S_{11}|^2}{|S_{12}|^2} \right) \quad (6.7)$$

$$SE_R\ (dB) = -10 \log_{10} \left(\frac{1}{1 - |S_{11}|^2} \right) \quad (6.8)$$

Here, S represent the scattering parameters i.e., S_{11} (reflection coefficient) and S_{21} transmission coefficient). Figure 6.9(a and c) demonstrates that Co_2YP nanocomposite film exhibits high absorption (SE_A) compared to the MoS_2P nanocomposite film. Conversely, the MoS_2P nanocomposite film shows high reflection (SE_R) in comparison to the Co_2YP nanocomposite film. The data clearly demonstrates that the magnetic fillers (Co_2Y) have the greatest impact on enhancing the SE_A of the nanocomposite films, while the semiconducting nanofillers (MoS_2) contribute to SE_R. Figure 6.9(d-f) illustrates the shielding efficiency of mono-layer nanocomposite films, namely due to absorption (SE_A), reflection (SE_R), and the total shielding effectiveness (SE_T). It has been observed that the nanocomposite films with higher concentration of magnetic fillers exhibit enhanced absorption (SE_A). Specifically, the SE_A for YMP913 (consisting of 90 wt.% Co_2Y-hexaferrite and 10 wt.% MoS_2) is -32.91 dB at 15.51 GHz, which is superior to other films. However, YMP553, which consists of 50 wt.% of Co_2Y-hexaferrite and 50 wt.% of MoS_2, has a significantly increased reflection (SE_R) of -29.74 dB at 13.16 GHz compared to other films. This enhancement can be attributed to the inclusion of semiconducting MoS_2 nanofillers within the PVDF matrix. The YMP913 nanocomposite film exhibits SE_T of -59.44 dB at a frequency of 15.51 GHz. The absorption property of shielding materials is determined by the interaction between the electric dipoles of the system and the

electric field vectors of the incident EM radiation, as well as the interaction between the magnetic dipoles of the system and the magnetic field vectors of the incident EM radiation. The PVDF matrix contains magnetic dipoles caused by the inclusion of magnetic Co_2Y-hexaferrite, as well as electrical dipoles caused by the inclusion of semiconducting MoS_2 nanofillers. The inclusion of semiconducting MoS_2 within the PVDF matrix enables accumulation of charges that can generate electric dipoles when exposed to an electric field vector from incident radiation. The coexistence of these two fillers within the PVDF matrix can interact and result in resonance occurring at a corresponding frequency range of 12-18 GHz, which can effectively enhance the absorption (SE_A) of the nanocomposite films. Furthermore, the introduction of MoS_2 into the PVDF-HFP matrix can generate eddies caused by the movement of conducting electrons when exposed to the magnetic field of the incoming EM radiation [27]. The inclusion of Co_2Y hexaferrite-MoS_2 binary fillers within the PVDF matrix induces the formation of eddies, resulting in the absorption of incident EM radiation by eddy current losses. Thus, both effects contribute concurrently to improving the absorption property of the nanocomposite films.

In the previous chapter, it is already established that thickness helps in improving SE_A. In Figure 6.9(g), it was observed that the absorption of the nanocomposite films increased as the thickness of the films increased, in comparison to the mono-layer system. The nanocomposite film YPM913 has a maximum absorption (SE_A) of -36.14 dB at a frequency of 13.42 GHz. SE_R also increases for multi-layer structures in addition to their absorption properties. The wt.% of conducting MoS_2 nanofillers increases on the surface of the nanocomposite films as the thickness of the multi-layer structure grows. This leads to a greater intensity of EM radiation compared to the mono-layer structure. Figure 6.9(h and i) shows that the YMP913

nanocomposite film has a maximum reflection (SE_R) of -31.41 dB at a frequency of 13.43 GHz, and a maximum total shielding effectiveness (SE_T) of -66.61 dB at a frequency of 13.41 GHz. In order to enhance the thickness of the nanocomposite films, a multi-layer stacking process employing the hot-press method have been used. In this approach, the created nanocomposite films retain their elasticity and all the layers are tightly bonded without any presence of air gaps. In this study, a distinctive approach to enhance the EMI shielding efficacy by prioritizing absorption rather than reflection in the nanocomposite films have been employed. In this approach, a layer of non-conducting PVDF on both sides of the multi-layer structure have been applied. Consequently, when EM waves encounter the surface of the nanocomposite film, only a minimal portion of the waves are reflected, while the majority of the waves pass through the first layer (PVDF) of the film. This occurrence may be attributed to the absence of any nanofillers on the surface of the non-conductive PVDF jacket coated nanocomposite films. Upon entering the first layer of the nanocomposite films, the EM wave interacts with each subsequent layer of Co_2Y hexaferrite-MoS_2-PVDF nanocomposite films. This interaction persists across all the layers of the nanocomposite films. Therefore, only a minimal portion of the EM wave is reflected off the surface of the non-conductive polymer jacket covered multi-layer nanocomposite films. The PVDF jacket permits the transmission of the incoming microwave radiation and guides the waves towards the succeeding layers of nanocomposite films. Moreover, the PVDF jacket effectively contains the waves within the nanocomposite system, resulting in a reduction of both surface reflection and wave transmission. Figure 6.8 illustrates the potential EMI shielding mechanism between the molo-layer, multi-layer, and polymer jacket coated multi-layer structure.

The absorption of the non-conducting polymer jacket coated multi-layer nanocomposite films

in Figure 6.9(j) exhibits a substantial increase compared to both the multi-layer and mono-layer architectures. The non-conducting polymer jacket coated multi-layer nanocomposite film achieves a maximum absorption (SE_A) of -51.23 dB at a frequency of 14.03 GHz for YMP913. However, Figures 6.9(k and l) show that YMP553 has a maximum reflection (SE_R) of -28.93 dB at 13.38 GHz, whereas YMP913 has a maximum SE_T of -74.51 dB at 13.23 GHz. It has been observed that the non-conducting polymer jacket coated multi-layer nanocomposite films have a lower reflection (SE_R) compared to the multi-layer and mono-layer structure. This phenomenon occurs as a result of the internal reflections of EM waves at the successive layers of the nanocomposite films. These reflections cease after the EM wave is absorbed by the multi-layer structure that is coated with a jacket made of nano-conducting polymer. Figure 6.10(I-III) illustrates the changes in the maximum absorption (SE_A), reflection (SE_R), and total shielding effectiveness (SE_T) of the nanocomposite films. Figure 6.10(IV) illustrated the percentage of attenuation for the mono-layer, multi-layer, and non-conducting polymer jacket covered multi-layer construction. The non-conducting polymer jacket coated Co_2Y hexaferrrite-MoS_2-PVDF nanocomposite film has obtained an attenuation percentage more than 99.9999% in the high frequency range of 12-18 GHz (Ku-band). Hence, the utilization of Co_2Y hexaferrrite-MoS_2-PVDF nanocomposite films, along with the innovative technique of coating non-conducting polymer jackets on multi-layer nanocomposite films, presents a distinctive concept for enhancing the absorption (SE_A) in EMI shielding applications.

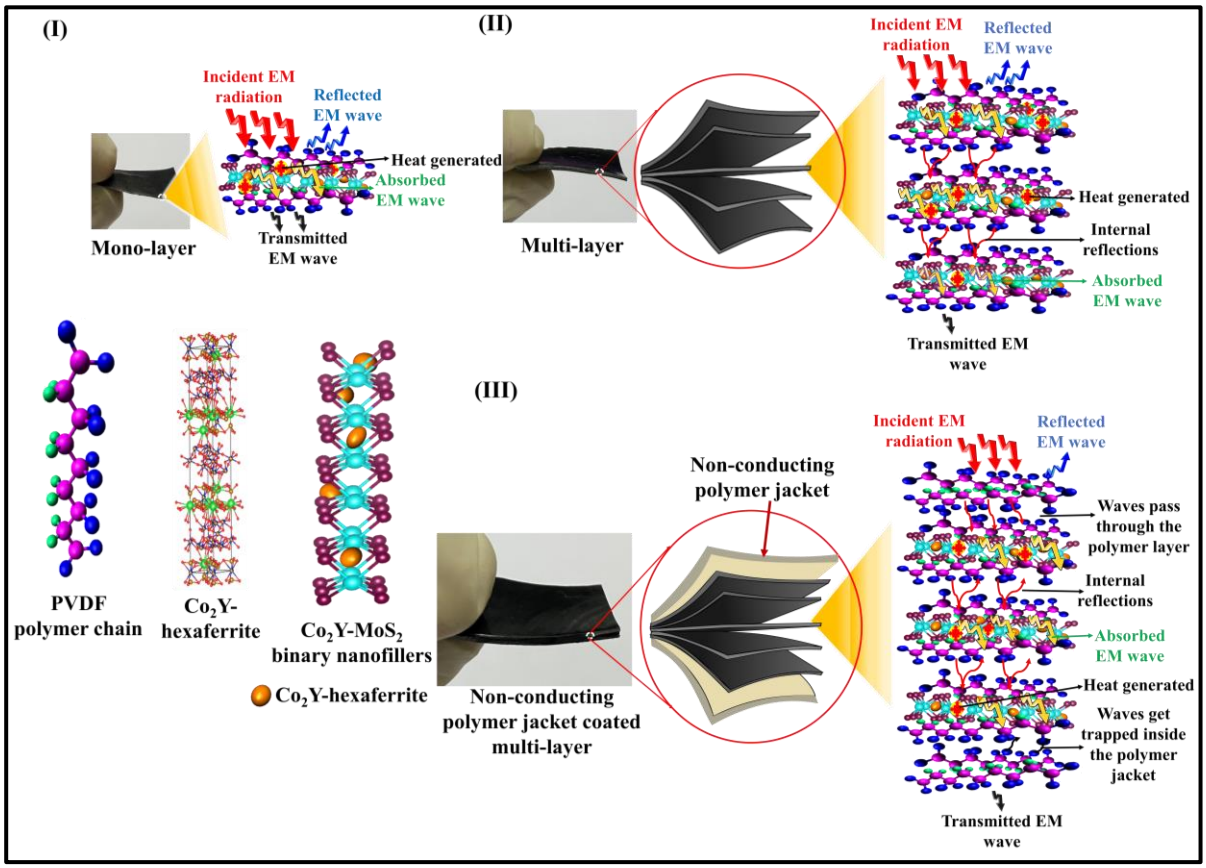

Figure 6.8: EMI shielding mechanism in (I) mono-layer, (II) multi-layer and (III) polymer jacket coated multi-layer structure.

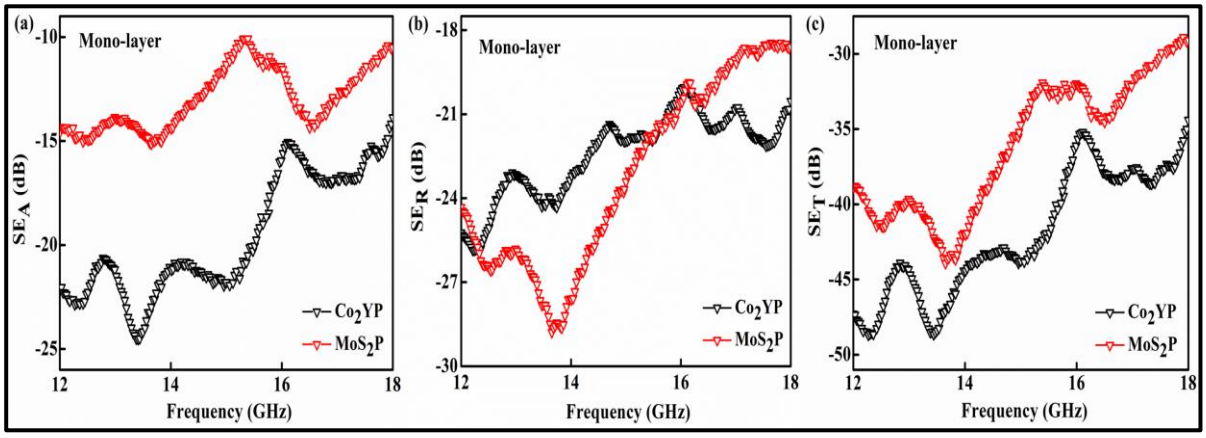

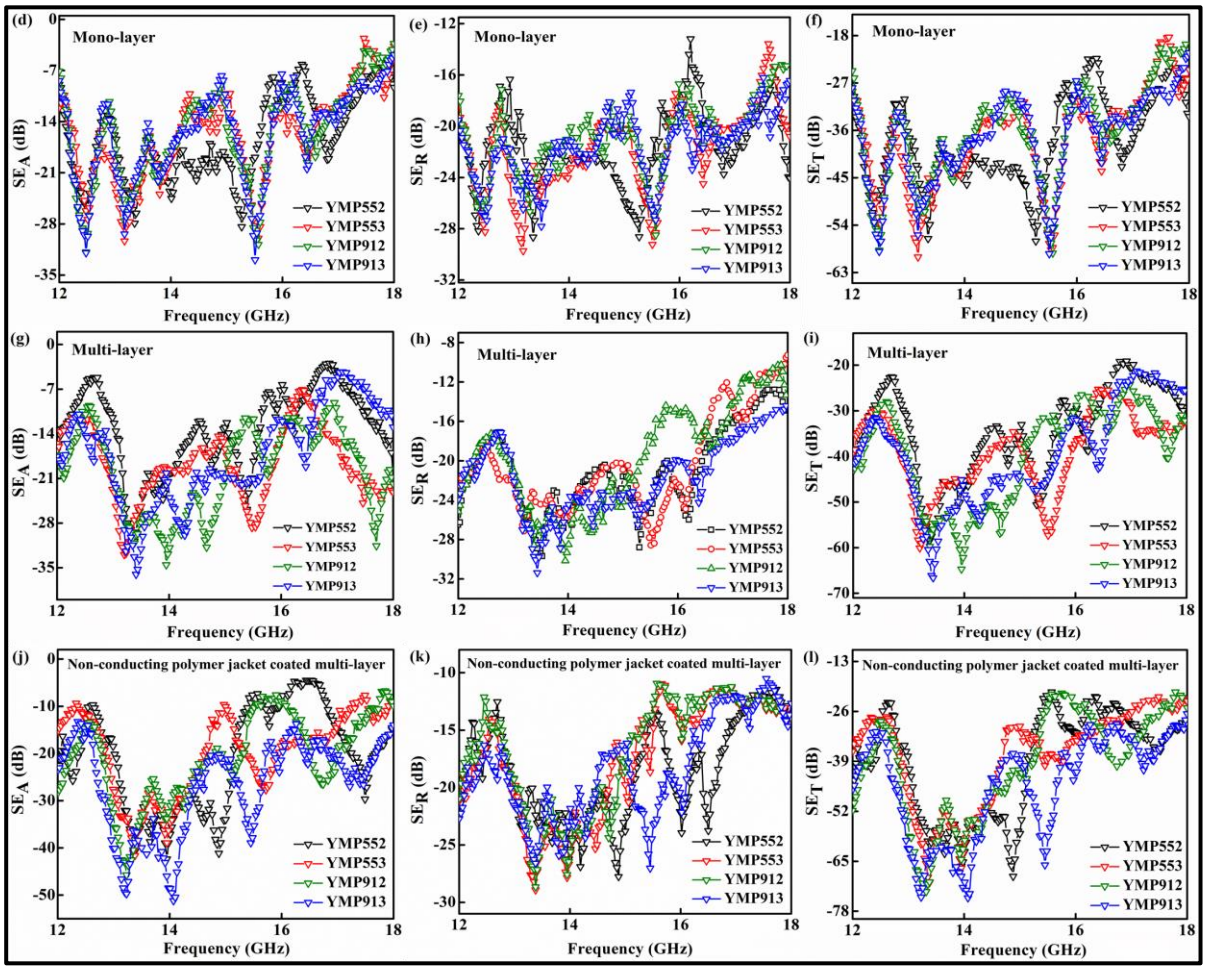

Figure 6.9: Shielding effectiveness due to (a, d, g and j) absorption (SE_A), (b, e, h and k) reflection (SE_R), and (c, f, I, and l) total Shielding effectiveness (SE_T) for mono-layer, multi-layer, and non-conducting polymer jacket coated multi-layer nanocomposite films at 12-18 GHz.

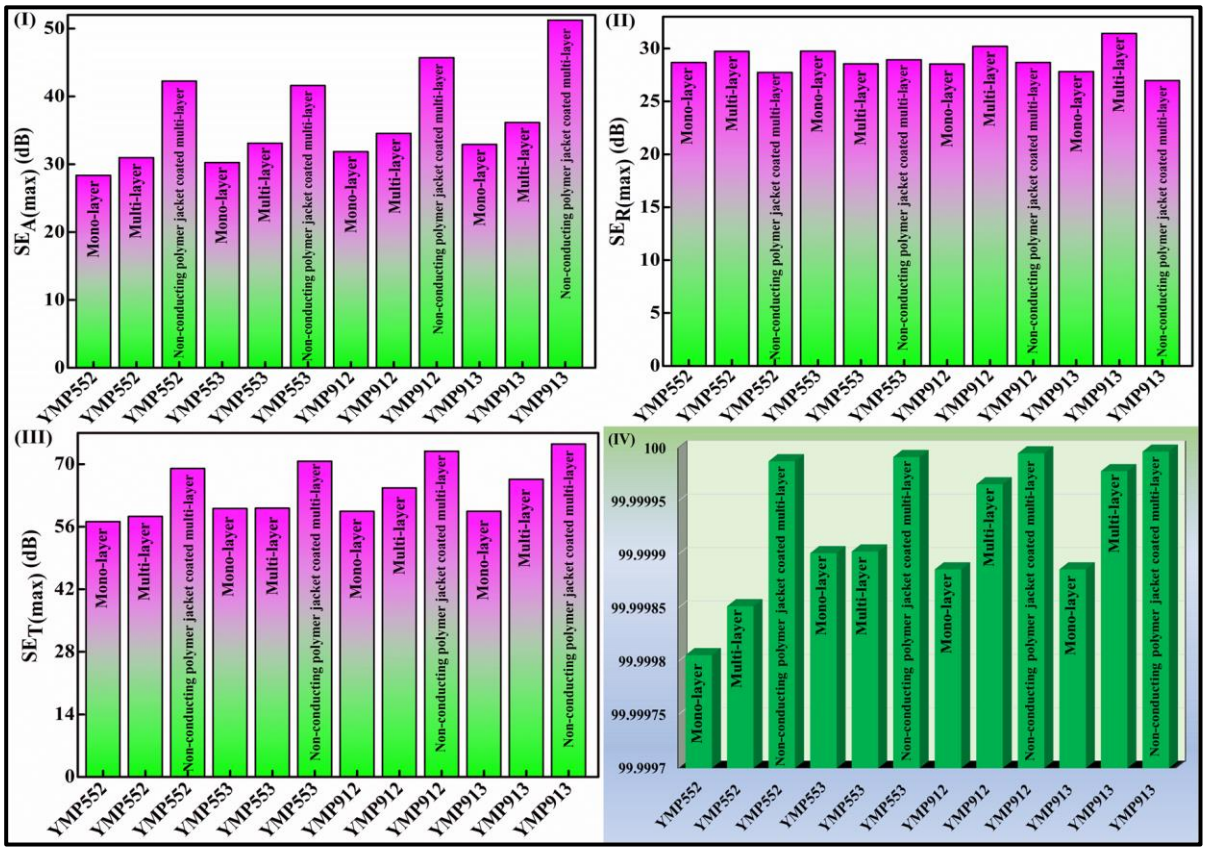

Figure 6.10: (I-III) variation of maximum absorption (SE_A), reflection (SE_R) and the total shielding effectiveness (SE_T) and (IV) attenuation percentage of mono-layer, multi-layer, and non-conducting polymer jacket coated multi-layer of the nanocomposite films.

6.4 Conclusion:

The multi-layer structures of Co_2Y hexaferrite-MoS_2-PVDF nanocomposite films have been fabricated by employing a hot-press process. These films were synthesized by a simple solution casting procedure and were coated with non-conducting polymer jacket. The XRD measurement revealed an average crystalline diameter of 20 nm for the Co_2Y-hexaferrite, as well as the presence of multi phases in the nanocomposite films. The Rietveld refinement verifies the existence of all the required crystallographic phases of Co_2Y-hexaferrite and MoS_2, without any contaminants. FESEM shows that Co_2Y-hexaferrite exhibits a hexagonal shape,

whereas MoS_2 has a cotton-ball structure. Additionally, the presence of Co_2Y hexaferrite-MoS_2 binary nanofillers within the PVDF matrix is clearly evident in the study. The cross-sectional view reveals the creation of tightly bounded layers of the nanocomposite films, which are coated with a non-conducting polymer jacket. The Co_2Y-hexaferrite exhibits a maximum magnetization of 33.32 emu/g at a magnetic field strength of 50000 Oe and a coercive field (Hc) of 647 Oe. This observation was made during the M-H loop study conducted at RT. The enhanced magnetic permeability of the Co_2Y hexaferrite -MoS_2-PVDF nanocomposite films contribute to the improvement in the shielding effectiveness due to absorption (SE_A). The ability of a material to shield against EMI is determined by its impedance matching property. Non-conducting polymer jacket coated multi-layer nanocomposite films provide a high degree of impedance matching when the value of Z is close to unity. In contrast, mono-layer nanocomposite films show a significant departure of Z from unity. Based on the study on the effectiveness of EMI shielding, it has been observed that all the nanocomposite films show a significant increase in SE_A compared to their SE_R in the frequency range of 12-18 GHz. The non-conducting polymer jacket coated multi-layer nanocomposite films have been reported to have a maximum SE_A of -51.23 dB at 14.03 GHz. This is higher than the maximum SE_A values of -32.91 dB at 15.51 GHz for mono-layer nanocomposite films and -36.14 dB at 13.42 GHz for multi-layer nanocomposite films. Thus, non-conducting polymer jacket coated multi-layer structures of Co_2Y-MoS_2-PVDF nanocomposite films nanocomposite films are highly efficient for the fabrication of microwave absorber to fight against electromagnetic pollution.

4.5 References:

1. R.B. Schulz, V.C. Plantz, D.R. Brush, IEEE Transactions on Electromagnetic Compatibility 30, 187–201 (1988).

2. N. A. Alarfaj, M. F. El-Tohamy, H. Oraby, New Journal of Chemistry 42, 11046–11053 (2018).

3. M.A. Bissett, I.A. Kinloch, R.A.W. Dryfe, ACS Appl. Mater. Interfaces 7, 17388–17398 (2015).

4. S. Kumar, V. Sharma, K. Bhattacharyya, V. Krishnan, New Journal of Chemistry 40 5185-5197 (2016).

5. X. Su, J. Ning, Y. Jia, Y. Liu, NANO 13, 1850084 (2018).

6. M. Hu, N. Zhang, G. Shan, J. Gao, J. Liu, R.K.Y. Li, Front. Phys. 13, 138113 (2018).

7. J. (Jan) Smit, H.P.J. Wijn, (1959).

8. Sutradhar S, Das S, Roychowdhury A, Das D, Chakrabarti P.K., Mater. Sci. Eng. B, 196:44-52 (2015).

9. S. Sadhukhan, A. Mitra, A.S. Mahapatra, P.K. Chakrabarti, Journal of Alloys and Compounds 956, 170351 (2023).

10. J. Prasad, A.K. Singh, J. Shah, R.K. Kotnala, K. Singh, Mater. Res. Express 5, 055028 (2018).

11. E.J. Carlson, Materials Performance 29, 76–80 (1990).

12. M. Chireh, M. Naseri, H. Ghaedamini, Advanced Powder Technology 32, 4697–4710 (2021).

13. A. Ghasemi, Magnetic Ferrites and Related Nanocomposites, Elsevier, 125–299 (2022).

14. S. Lei, L. Liu, C. Wang, X. Shen, D. Guo, C. Wang, S. Zeng, B. Cheng, Y. Xiao, L. Zhou, CrystEngComm 16, 1322–1333 (2014).

15. A.-H. Boughriet, C. Legrand, A. Chapoton, IEEE Transactions on Microwave Theory and Techniques 45, 52–57 (1997).

16. Y. Bhattacharjee, S. Bose, ACS Appl. Nano Mater. 4, 949–972 (2021).

[17] C.A. Stergiou, G. Litsardakis, Journal of Magnetism and Magnetic Materials 405, 54–61 (2016).

18. X. Wang, W. Xing, X. Feng, L. Song, Y. Hu, Polymer Reviews 57, 440–466 (2017).

19. Y. Liu, C. Ji, X. Su, X. He, J. Xu, Y. Li, Journal of Magnetism and Magnetic Materials 511, 166961 (2020).

20. J. Wang, X. Lin, Z. Chu, Z. Huang, T. Guo, L. Yang, S. Li, Nanotechnology 31, 135602 (2020).

21. E. Samadpour, E. Kiani, M. Hosein Shams, Materials Science and Engineering: B 298 116825 (2023).

22. G. Guan, K. Zhang, L. Gong, X. Chen, X. Li, Q. Wang, Y. Wang, J. Xiang, Journal of Alloys and Compounds 814, 152302 (2020).

23. S. Biswas, G. Prasanna Kar, S. Bose, Journal of Materials Chemistry A 3, 12413–12426 (2015).

24. Hekmatara H, Seifi M, Forooraghi K, Mirzaee S., Phys. Chem. Chem. Phys., 16:24069-75 (2014).

25. Ohlan A, Singh K, Chandra A, Dhawan S.K., ACS Appl. Mater. Interfaces, 2:927-33 (2010).

26. Chung DDL., Carbon ,39(2):279-85 (2001).

27. M. Javid, X. Qu, F. Huang, X. Li, A. Farid, A. Shah, Y. Duan, Z. Zhang, X. Dong, L. Pan, Carbon 171, 785–797 (2021).

Chapter: 7
Conclusion

Chapter 7:

7.1 Conclusion with outcomes:

In the present study different smart materials have been developed as laminated polymer-based nanocomposite systems with large shielding effectiveness, wide frequency bandwidth in the RF/MW region, as well as flexible and large surface area. So far, in this study based on shielding effectiveness property, magnetic-conducting/semiconducting-PVDF based nanocomposite systems have been considered for large magnetic and dielectric loss factors. Four different synthesis mechanism have been employed to obtain the smart nanocomposite systems which have been discussed in chapter 2; firstly, ferrite and hexaferrite materials have been prepared by sol-gel synthesis route. Then they are taken in PVDF matrix by simple solution casting method. After that to enhance the dielectric loss factors of the resultant nanocomposite systems, different conducting and semiconducting nanomaterials have been prepared and taken along with magnetic materials by solid state reaction technique and further incorporated in the PVDF matrix. To improve the shielding effectiveness due to absorption (SE_A) the thickness of the laminated films has been modulated. Several mono-layer nanocomposite films have been stacked together tightly by hot-press method to increase the thickness of the resultant nanocomposite systems without compromising the flexibility of the system. After that to increase the impedance matching condition of the resultant nanocomposite films, non-conducting polymer have been coated over the multi-layer nanocomposite systems to make the films more permeable to the incident EMR in the MW region. Thus, the tailor-made nanocomposite systems with the inclusion of spinel ferrite or hexagonal ferrite materials along with conducting/semiconducting nanofillers inside the matrix of PVDF improves the shielding effectiveness in the form of SE_A and SE_T of the

resultant nanocomposite materials, which is very important for the aim and objective of the present study.

In chapter 3 Co_2U- and Co_2X-hexaferrite nanomaterials incorporated PVDF nanocomposite films have been studied for shielding effectiveness applications in the GHz frequency range with comprehensive details. The incorporation of Co_2U- and Co_2X-hexaferrite inside PVDF has been proved by substantiating the multiphase nature of the resultant Co_2U-PVDF and Co_2X-PVDF nanocomposite films in XRD analysis. The coexistence of the dielectric and magnetic properties inside the nanocomposite films of Co_2U-PVDF and Co_2X-PVDF have been substantiated from the dielectric and magnetic response study. The significant dielectric improvement of the nanocomposite films due to the generation of large area of interfaces between the Co_2U- and Co_2X-hexaferrite and the PVDF matrix has been observed here. The simultaneous existence of both dielectric and magnetic responses of the nanocomposite films plays the most important role for the improvement of shielding effectiveness of Co_2U-PVDF and Co_2X-PVDF nanocomposite films. The high EMI shielding effectiveness with high attenuation >99.999999% of the nanocomposite films of Co_2U-PVDF and Co_2X-PVDF system have been observed in this chapter. The high shielding effectiveness of magnetic nanofiller incorporated PVDF based nanocomposite films made of Co_2U and Co_2X materials is very useful to design the efficient EM pollution reducers.

In chapter 4 the addition of semiconducting nanofillers along with the magnetic materials as binary fillers incorporated PVDF nanocomposite films can also improve the shielding effectiveness due to absorption (SE_A) as well as total shielding effectiveness (SE_A). Co_2X-C_3N_4 and NZCF-C_3N_4 binary nanofillers incorporated PVDF nanocomposite systems have been prepared by a very simple solution casting method and structural, microstructural, and chemical investigations have been done. All these measurements show that the

nanocomposite films have been formed with proper crystallographic phase, morphology, and chemical structure. The high permeability of Co_2X-C_3N_4-PVDF and NZCF-C_3N_4-PVDF nanocomposite films simultaneously act to improve the shielding effectiveness due to absorption (SE_A). A maximum SE_A of -62.41 dB at a matching frequency of 14 GHz and SE_T of -89.42 dB at a matching frequency of 14.1 GHz for the nanocomposite films has been observed with attenuation of >99.999999%. So, the loading percentage of semiconducting C_3N_4 nanofillers inside the structure of nanocomposite films helps to provide better response of SE_T at comparatively high frequency region. Thus, indisputably it can be concluded that the high value of total shielding effectiveness (SE_T) of the present nanocomposite films not only appeared due to the presence of magnetic nanofiller (Co_2X-hexaferrite and NZCF nanoparticles) with the PVDF matrix but the exceptional idea of addition of semiconducting C_3N_4 nanofillers inside the matrix of PVDF along with magnetic nanofiller has made Co_2X-C_3N_4-PVDF and NZCF-C_3N_4-PVDF nanocomposite films highly efficient for the fabrication of microwave absorber to fight against electromagnetic pollution.

In chapter 5 the strategic multiphase thick multi-layer structure of rGO-Co_2Z hexaferrite-PVDF nanocomposite films have been synthesized successfully for the application of EMI shielding property to reduce EM radiation. The cross-sectional micrographs indicate that, the thickness of mono-layer nanocomposite films lies within the range of 100 μm to 144 μm as well as the uniform thickness of each multi-layer nanocomposite film of 0.9 mm in average has been achieved after the hot press method is applied. The maximum magnetisation of the nanocomposite films is significantly high and the values of 6.4 and 8.9 emu/g for rZP553 and rZP373 have been found at 300 K. Here, in the EMI shielding study, the multilayer structure exhibits greater absorption than the mono-layer structure. The maximum SE_A of EM radiation by the mono-layer nanocomposite film is -27.03 dB at 12.38 GHz but in case of the

multi-layer structure SE_A is increased to -38.12 dB at 17.86 GHz. Also, the maximum SE_T of the nanocomposite film is -54.09 dB at 15.70 GHz for multi-layer structure over the maximum SE_T -47.03 dB at 14.76 GHz in case of mono-layer structure. As a result, a high value of >99.999% attenuation has been obtained from the multi-layer nanocomposite film in EMI shielding study. Now, it has been confirmed that the multi-layer structure of the nanocomposite films gives higher SE_A property as compared to mono-layer and the total SE_T study is significantly improved for the multi-layer structure of the nanocomposite films due to the increase of thickness of the nanocomposite films. So, these rGO-Co_2Z-PVDF nanocomposite films are the potential candidates for the microwave shielding applications.

In chapter 6, the hexagonal shape of Co_2Y-hexaferrite and cotton-ball structure of MoS_2 has been confirmed from the surface morphology study. The cross-sectional view reveals the creation of tightly bounded layers of the nanocomposite films, which are coated with a non-conducting polymer jacket. The Co_2Y-hexaferrite exhibits a maximum magnetization of 33.32 emu/g at a magnetic field strength of 50000 Oe and a coercive field (Hc) of 647 Oe was measured from the M-H loop study conducted at RT. The enhanced magnetic permeability of the Co_2Y hexaferrite-MoS_2-PVDF nanocomposite films contribute to the improvement in the shielding effectiveness due to absorption (SE_A). The ability of a material to shield against EMI is determined by its impedance matching property. Non-conducting polymer jacket coated multi-layer nanocomposite films provide a high degree of impedance matching where the value of Z is close to unity. In contrast, mono-layer nanocomposite films show a significant departure of Z from unity. Based on the study on the effectiveness of EMI shielding, it has been observed that all the nanocomposite films show a significant increase in SE_A compared to their SE_R in the frequency range of 12-18 GHz (K_u-band). The non-conducting polymer jacket coated multi-layer nanocomposite films have been

reported to have a maximum SE_T of -51.23 dB at 14.03 GHz. This is higher than the maximum SE_A values of -32.91 dB at 15.51 GHz for mono-layer nanocomposite films and -36.14 dB at 13.42 GHz for multi-layer nanocomposite films. And here it is noticeable that, due to the nonconducting polymer jacket coating, no surface conductivity effect has been observed. So, the issues that has been observed from the chapter 5 due to the surface conductivity effect 50:50 wt. % rGO: Co_2Z binary nanocomposite system which has shown comparatively high SE_R from SE_A has been resolved by using this nonconducting polymer jacket coated nanocomposite films. Thus, non-conducting polymer jacket coated multi-layer structures of Co_2Y-MoS_2-PVDF nanocomposite films nanocomposite films are highly efficient for the fabrication of microwave absorber to fight against electromagnetic pollution.

Thus, this thesis has validated that the magnetic, conducting/semiconducting binary nanofillers incorporated PVDF nanocomposite system are very efficient to combat against the EM pollution by absorbing the EMR in the MW frequency range. Also, the controllable thickness, area and the flexibility of the nanocomposite films are helpful for different EMI shielding application as well as it can be useful as potential stealth material in defence technology.

SEMINARS ATTENDED

A one-day seminar in

"COMMEMORATION OF CENTENARY BIRTH ANNIVERSARY OF PROF. SHYAMAL SENGUPTA"

Condensed Matter Physics Research Centre
Estd. 1990

Organised by

Condensed Matter Physics Research Centre & Department of Physics, Jadavpur University

CERTIFICATE OF PARTICIPATION

This certificate has been awarded to ***Tanmoy Chakraborty*** *of Dept. Of Physics, Jadavpur University in appreciation of his poster presentation titled* ***Enhanced microwave absorption of multilayer structures for EMI shielding applications*** *at the one day seminar in "Commemoration Of Centenary Birth Anniversary Of Prof. Shyamal Sengupta" held at Jadavpur University, Kolkata, India on 7th February 2024.*

07.02.2024

H.O.D. Dept. Of Physics, JU

7/02/2024

Co-Ordinator CMPRC, JU

ANVESHAN

Ganpat University
॥ विद्यया समाजोत्कर्षः ॥

National Student Research Convention
March 16-17, 2023

THIRD PRIZE

Certificate of Merit

This is to Certify that Mr / Ms / Dr. Tanmoy Chakraborty

affiliated with Jadavpur University

participated in **Anveshan: National Student Research Convention** organized by **Association of Indian Universities, New Delhi** and hosted by **Ganpat University, Gujarat** during March 16-17, 2023.

His/Her research project titled Superior Microwave absorption of layered structured for EMI shielding application under the category of Engineering & Technology has won **THIRD PRIZE.**

Dr. Kiran Amin
Anveshan Co-convener
Deputy Pro Vice Chancellor
Ganpat University

Dr. Ajay Gupta
Anveshan Convener
Director - R&D
Ganpat University

Dr. Amarendra Pani
Anveshan Convener
Joint Director (Research)
Association of Indian Universities

Dr. Mahendra Sharma
Pro-Chancellor & Director General
Ganpat University

Powered by ONGC | G20 | INSTITUTION'S INNOVATION COUNCIL (Ministry of HRD Initiative) | PROJECTSET

ASSOCIATION OF INDIAN UNIVERSITIES, DELHI
&
THE ASSAM ROYAL GLOBAL UNIVERSITY, GUWAHATI

THE ASSAM ROYAL GLOBAL UNIVERSITY GUWAHATI

ANVESHAN 2022

EAST ZONE STUDENT RESEARCH CONVENTION

CERTIFICATE

This is to certify that

Mr./Ms./Dr. Tanmoy Chakraborty

Son/Daughter of Shri Ranjit Chakraborty **enrolled in.** PhD

Department / Faculty of Physics **of** Jadavpur University

University / Institute participated in East Zone Student Research Convention held at The Assam Royal Global University, Guwahati during March 01-02, 2023.

His/Her proposal/project entitled Synthesis, Microwave Absorption ... Shielding application

under the category of ENGINEERING - 2nd

Dr. Usha Rai Negi
Assistant Director (Research)
Association of Indian Universities,
New Delhi

Prof. (Dr.) Rohit Singh
Pro Vice Chancellor
Zonal Coordinator- Anveshan 22
The Assam Royal Global University, Guwahati

Prof. (Dr.) S.P. Singh
Vice Chancellor
The Assam Royal Global University
Guwahati

NATIONAL INSTITUTE OF TECHNOLOGY ROURKELA

(An Institution of National Importance)

CHEMSMART-22

Certificate of Participation

This is to Certify that the Paper titled

Ni-Zn-Cu-Ferrite-PVDF Multiphase Nanocomposite Material for the Application of Multiferroics and Improved EMI Shielding Effectiveness

has been presented by the author(s)

Tanmoy Chakraborty

from

Jadavpur University

In one of the technical sessions of An International Conference on ADVANCES IN SMART MATERIALS, CHEMICAL & BIOCHEMICAL ENGINEERING (CHEMSMART-22) organized by the Department of **Chemical Engineering, NIT Rourkela,** during **December 16-18, 2022.**

Dr. Krunal Gangawane
Convener–CHEMSMART-22

Prof. Abanti Sahoo
Chairman –CHEMSMART-22

29th National Conference on Condensed Matter Physics (CMDAYS 2021)

Certificate of Participation

This is to certify that **Mr. Tanmoy Chakraborty** of Amity University Kolkata has presented a paper (e-POSTER) entitled ´´Possible Health Issues of Electromagnetic Pollution and the Corresponding Remedies´´ in **the 29th National (Virtual) Conference on Condensed Matter Physics ´´(CMDAYS2021)´´** was held during December 10-12, 2021, at the Department of Physics, Central University of Jharkhand, Ranchi, Jharkhand.

Dr. Basudev Pradhan
DoEE, Joint Convener

Dr. Avijit Ghosh
DoP, Convener

Third International Conference on Material Science

(ICMS2020)

04-06 March, 2020

Organized by

Department of Physics

Tripura University (A Central University)

Suryamaninagar-799022, Tripura, India

Certificate of Participation

Certified that Prof./Dr./Mr./Ms. Tanmoy Chakraborty

has participated / presented a paper entitled "Multiferroic Behaviour of Multiphase Mn-Zn-Co-ferrite-PVDF bclero composite film."

in the **Third International Conference on Material Science (ICMS2020)** organized by **Department of Physics, Tripura University (A Central University)** during **04-06 March, 2020.**

(Prof. Debajyoti Bhattacharjee)
Chairman
Local Organizing Committee

(Dr. Syed Arshad Hussain)
Convener
Local Organizing Committee

IEM IC: 66

IEMPHYS-19

International Conference on

Condensed Matter Physics

organized by

Institute of Engineering & Management

in collaboration with

IEM – Society of Physics Student Chapter (AIP)

INSTITUTE OF ENGINEERING & MANAGEMENT
Good Education, Good Jobs

Certificate of Appreciation

This is to certify that Prof./Dr./Mr./Mrs./Ms. ...Tanmay....Chakraborty.....

of .....Amity...University..,Kolkata.....

has given an oral/poster presentation on the paper titled

"..Influence..of..the..C_3N_4..Conducting..Network..inside..the..composite..Network..of..Ni-Zn-Cu-Ferrite.-

-..Poly(vinylidene..flouride)..Films...for..the...improvement...of...the..EMI..shielding..effectiveness"

in IEMPHYS-19 held on 14th-16th November, 2019 at Institute of Engineering & Management, Kolkata.

Prabir Kr Das

Prabir Kumar Das
Conference Chair,
Institute of Engineering & Management, Kolkata

Spal

Soumyadipta Pal
Convener,
Institute of Engineering & Management, Kolkata

Koyel Ganguly

Koyel Ganguly
Convener,
Institute of Engineering & Management, Kolkata